Investigations on Protein Charge Transfer Spectra among charged amino acids and monomeric proteins

A Thesis Submitted in Partial Fulfillment of the

Requirements for the Degree of

Doctor of Philosophy

By

Amrendra Kumar

Roll No. 136106010

Department of Biosciences and Bioengineering
Indian Institute of Technology Guwahati
Guwahati, Assam- 781039, India

March 2020

INDIAN INSTITUTE OF TECHNOLOGY
GUWAHATI, Assam, India

Department of Biosciences and Bioengineering

STATEMENT

I do hereby declare that the matter embodied in this thesis is the result of investigations carried out by me in the Department of Biosciences and Bioengineering, Indian Institute of Technology Guwahati, India, under the guidance of Prof. Rajaram Swaminathan.

In keeping with the general practice of reporting scientific observations, due acknowledgements have been made wherever the work described is based on the findings of other investigators.

IIT Guwahati — Amrendra Kumar

March 2020

INDIAN INSTITUTE OF TECHNOLOGY
GUWAHATI, Assam, India

Department of Biosciences and Bioengineering

CERTIFICATE

It is certified that the work described in this thesis, entitled "***Investigations on Protein Charge Transfer Spectra among charged amino acids and monomeric proteins***" done by **Amrendra Kumar** for the award of degree of Doctor of Philosophy is an authentic record of the results obtained from the research work carried out under my supervision in the Department of Biosciences and Bioengineering, Indian Institute of Technology Guwahati, India. This work has not been submitted elsewhere for a degree.

IIT Guwahati
March, 2020

Prof. Rajaram Swaminathan
Department of BSBE
IIT Guwahati

Dedicated to my Family

ACKNOWLEDGEMENTS

I am extremely happy to be in this position after facing many ups and downs throughout these six years. I would like to express my sincere gratitude to all those persons who helped me out through this tough time.

First and foremost, I want to express my deepest respect and sincere gratitude to my supervisor Prof. Rajaram Swaminathan for giving me an opportunity to work under his supervision. His continuous support, patience, enthusiasm, immense scientific ideas and motivation helped me in all the times of research and to explore the domains of work assembled in this thesis. He has been a great mentor, from whom I have learnt a lot. He encouraged me not only to grow as a researcher but also as a person. I am indebted to him, for his faith in me and providing the right direction whenever I needed it the most.

Besides my advisor, I would also like to extend my sincere thanks to the Doctoral Committee members, Prof. Utpal Bora, Prof. Vishal Trivedi and Dr. Debapratim Das for their encouragement, timely evaluation of my Ph.D. work and insightful suggestions, which helped me a lot in the betterment of this thesis.

I also thank Dr. Raghu Padinjat (National Center for Biological Sciences, Bangalore) and Prof. Chandrabhas Narayana (Jawaharlal Nehru Centre for Advanced Scientific Research, Bangalore) and Prof. Ajay B. Kunnumakkara (IIT Guwahati) for allowing me to work at their respective labs during the initial phase of my PhD.

Iwould also like to thank Prof. Mireille Clasessens and Dr. Aditya (University of Twente, The Netherlands) for providing purified α-Synuclein protein.

I would like to thank staff members of BSBE department for their co-operative nature and kind support. Thanks to IIT Guwahati and its administration for all the facilities that were made available to me and the Ministry of Human Resource Development (MHRD), India for the financial support.

Next, I wish to express my sincere thanks to my lab seniors Tulsi Swain, Saumya Prasad, Shrutidhara Biswas and Mohd. Ziauddin Ansari for their enormous help and suggestions during my Ph.D. I would like to thank specially Mohd. Ziauddin for providing purified

proteins for my work. For making the lab a great place to work, I express my deep sense of gratitude to all my extraordinary juniors Dileep, Anurag, Ekramul, Alka, Heeramoni, Nuzelu, Simangka, Vinay, Nayan, Aditya, Garima, Subhajit, Abheek, Harikrishna and Niteesh.

I would also like to express my sincere thanks to all my friends Ankit, Ashish, Rakesh, Reshmi, Karukriti and Ms. Swati for their constant support and timely help. I thank them for making my stay at IIT Guwahati a memorable one.

My Ph.D. endeavor could not have been completed without the endless love, unending support, tolerance and blessings from my family. My deepest gratitude to my parents whose enormous sacrifice, unconditional love in every stage of my life motivated me to overcome all the challenges. Especially my father, whose firm belief in me and his encouragement has given me all the strength to move through all the difficulties in my life. I am also grateful to my elder brother for his unending love and emotional support at all the times. I owe every bit of my achievement to my family.

There were many other people who helped me both personally and professionally. Although it is not possible to pen down each of their names, I would like to thank each one of them for helping me in some or the other way during different stages of my Ph.D.

Last but not the least; I am thankful to Almighty God for his continuous blessing during my research career to achieve these remarkable steps.

Amrendra Kumar *March 2020*

LIST OF ABBREVIATIONS

CT	Charge Transfer
ET	Electron Transfer
ProCharTS	Protein Charge Transfer Spectra
PBS CT	Peptide Backbone to Sidechain Charge Transfer
SS CT	Sidechain to Sidechain Charge Transfer
NATA	N-acetyl Tryptophan Amide
HuSA	Human Serum Albumin
HEWL	Hen Egg White Lysozyme
DTT	1,4-Dithiothreitol
Dansyl	2-dimethyl aminonaphthalene 6-sulfonyl
Gdn.HCl	Guanidine Hydrochloride
MEM	Maximum Entropy Method
BSA	Bovine Serum Albumin
ThT	Thioflavin T
UV-Vis	Ultraviolet-Visible

Thesis Abstract

Charge transfer is an intricate and crucial part of many biological systems and functions. This drives the crucial functions from life dependent processes like photosynthesis and cellular respiration to life saving and sustaining functions like UV DNA-damage repair and enzyme catalysis. The phenomena of charge transfer have been reported in almost all the biological macromolecules including DNA/RNA, peptides and proteins. Here in this thesis, phenomena of photo-induced charge transfer among charged, non-aromatic amino acids and proteins rich in charged residues are presented as an intrinsic chromophore in proteins with special emphasis on their emissive nature.

Conventionally, intrinsic chromophores present in proteins are only limited to aromatic amino acids (Trp, Tyr and Phe) and enzyme cofactors like NADH, FMN and FAD. Chromophore in the green fluorescent proteins (GFP) are also intrinsic in nature, where the actual chromophore is generated in an autocatalytic way out of its proximally located Ser, Tyr and Gly residues. Apart from these, no other intrinsic chromophores are known to exist in proteins. However, in 2001 our group has reported the anomalous absorption (in the range 230–500 nm) and fluorescence (at λ_{ex} 355 nm) from the concentrated solutions of L-Lysine monohydrochloride. Similar absorption spectra was also observed in proteins rich in lysine residues like, human serum albumin and calf thymus histone. The origin of such anomalous spectra was then postulated to arise due to inter/intramolecular interactions of proximally located lysine side chains. Later in 2017, using experimental as well as theoretical calculations on a synthetic protein (α_3C) rich in Lysine and Glutamate residues, the exact phenomena behind such an observation was elucidated as photo-induced charge transfer involving peptide backbone and side chains of charged residues. The charged amino ($NH3^+$)/ carboxylate (COO^-) group of lysine/glutamate side chain acts as electronic charge acceptor/donor for photo-induced electron transfer either from/to the polypeptide backbone or to each other. The absorption spectrum arising from such charge transfer transitions was coined as Protein Charge Transfer Spectra (ProCharTS). Apart from Lysine and Glutamate, other charged amino acids like His, Asp and Arg and phosphorylated amino acids like pTyr, pSer and pThr are also reported to participate in similar charge transfer (CT) transitions.

The present thesis work is an attempt to unravel the luminescence (and its characteristics) arising from charge transfer states of ProCharTS among charged amino acids (Lysine and Glutamate) and monomeric proteins rich in charged amino acids. These charged amino acids (Lysine, Lysine·HCl and Glutamate) are found to be luminescent not only in the region where aromatic amino acids are reported to exhibit fluorescence but also in the visible region up to 600 nm. However, the luminescence yield at longer excitation wavelength are found to be much lower than at shorter excitation wavelengths. Similarly, monomeric proteins moderately rich in charged residues like, human serum albumin (HuSA), PEST fragments of c-Myc and α-Synuclein are also intrinsically luminescent in the similar wavelength region. Such luminescence are considered to result from electron-hole charge recombination. The luminescence is characterized with lower quantum yield (~0.01 – 0.05 at λ_{ex} 355 nm) and lower luminescence mean lifetime (1 – 2.4 ns at λ_{ex} 340 nm) indicating lower efficiency/rate of charge recombination. However, the luminescence from charge transfer states show huge Stokes shift (10000 – 14000 cm^{-1} at λ_{ex} 280 nm) which indicates considerable change in the excited state dipole moment revealing its high sensitivity towards solvent polarity. Apart from this, the exceptionally higher extinction coefficient of proteins (between 325-800 nm) as compared to charged amino acids exhibited the crucial role of spatial proximity of side chains of charged residues for charge transfer transitions to happen. In spite of higher extinction coefficient, the quantum yield of proteins are similar to that of charged amino acids, which suggests the major contribution of extinction coefficient behind the much higher luminescence observed from charge transfer states in proteins.

Due to the prominent luminescence throughout the UV-Visible region, the effect of luminescence form charge transfer states are also explored on to the intrinsic and extrinsic probes in proteins. The presence of charged residue in the vicinity of indole in the NATA (N-acetyl tryptophan amide) not only quenched the fluorescence of NATA (at λ_{ex} 295 nm) but also changed the nature of fluorescence intensity decay from mono to bi-exponential. This may provide a clue to the unsolved mystery of the multi-exponential decay of Trp in proteins. Apart from this, the luminescence from charge transfer states are also observed to decrease the fluorescence lifetime of extrinsic probe like Dansyl (at λ_{ex} 340 nm) labelled to a moderately charged monomeric protein, HuSA.

The rest part of this thesis is attempted to establish applications of ProCharTS in tracking molecular events like protein unfolding and protein aggregation. With protein unfolding, the unfolded conformation can separate or result in loss of proximity between the side chains of charged residues. This could bring down the ProCharTS absorption and automatically the luminescence from charge transfer states. As anticipated, the unfolding of HuSA resulted in decrease of ProCharTS absorption (between 325-800 nm) as well as luminescence (at λ_{ex} 355 nm) and luminescence lifetime (at λ_{ex} 340 nm).

Contrary to above, the protein aggregation can create new intermolecular contacts between the aggregating entities leading to an increase in the population and density of interacting side chains of charged amino acids. This can eventually result in an increase in ProCharTS absorbance as well as luminescence from CT states. Surprisingly, ProCharTS absorption and luminescence shows a concomitant increase with the aging of HEWL (hen egg white lysozyme) aggregates. The increase in ProCharTS absorption was indeed due to aggregation, as the inhibition of aggregation resulted in no net increase of ProCharTS. Moreover, ProCharTS was found to be more sensitive in detecting oligomeric aggregates in comparison to other molecular probes like ThT (Thioflavin T). Further, decrease in luminescence lifetime and quantum yield upon aggregation in spite of their increasing luminescence with time, reveals a major role of extinction coefficient (extinction coefficient of older day aggregates are much higher than monomers) behind the intrinsic luminescence observed from aggregates. Apart from this, blue shift observed in the luminescence spectra of compact fibrillar HEWL aggregates formed at pH 2 (at $\lambda_{ex} \geq 330$ nm) depicts the sensitivity of emissions from CT states towards the solvent polarity. This could be used as a signature for the presence of fibrillar aggregates since oligomeric aggregates formed at pH 5 did not show any shift in the luminescence spectra.

Taken together, the charged amino acids and proteins rich in charged amino acids do show ProCharTS and the associated charge transfer states are emissive in nature. The weak luminescence from charge transfer states are excitation wavelength dependent and spans throughout the UV-Visible region. As a result, such luminescence can affect the fluorescence of other intrinsic or extrinsic fluorophores present in protein. Finally, ProCharTS can serve as a label-free tool to study and detect structural transitions and oligomerization/aggregation of proteins where the only prerequisite is the moderate richness and proximity of charged

residues in protein. This would be more advantageous for the proteins that lack or are scarce in aromatic chromophores but are rich in charged residues, viz. intrinsically disordered proteins (IDPs).

Table of Contents

		Page
	Acknowledgements	*i*
	List of Abbreviations	*iii*
	Abstract	*iv*

Chapter 1: Introduction and Literature Review

	Introduction	1-1
1.1	Charge Transfer	1-1
1.2	Charge Transfer in Biological Systems	1-4
	1.2.1 Charge transfer deriving the photosynthesis	1-5
	1.2.2 Charge transfer and the respiratory chain	1-8
	1.2.3 Charge transfer in nucleic acids	1-9
	1.2.4 Charge transfer in peptides and proteins	1-13
	1.2.5 Protein Charge Transfer Spectra (ProCharTS)	1-17
	Objectives of the thesis work	1-25

Chapter 2: Experimental Techniques and Materials & Methods

2.1	Experimental Techniques	2-1
	2.1.1. Spectroscopy	2-1
	2.1.2 Absorption Spectroscopy	2-2
	2.1.2.1 Basics of UV-Visible Spectroscopy	2-4
	2.1.3 Fluorescence Spectroscopy	2-6
	2.1.3.1 Steady-state fluorescence	2-11
	2.1.3.2 Steady-state fluorescence anisotropy	2-12
	2.1.3.3 Time-resolved fluorescence	2-13
	2.1.3.4 Analysis of time-resolved fluorescence intensity decay	2-17
	2.1.3.5 Fluorescence quenching	2-20
2.2	Materials	2-22

2.3 Methods 2-24
2.3.1 Estimation of protein concentration 2-24
2.3.2 UV-Visible absorbance measurements 2-25
2.3.3 Steady-state fluorescence measurements 2-26
2.3.4 Steady-state anisotropy measurements 2-28
2.3.5 Stokes shift measurements 2-28
2.3.6 Quantum yield measurements 2-28
2.3.7 Time-resolved fluorescence measurements 2-29
2.3.8 Analysis of time-resolved fluorescence data 2-30
2.3.9 Protein unfolding 2-31
2.3.10 Labelling of protein with Dansyl Chloride 2-31
2.3.11 Aggregation of HEWL 2-31
2.3.12 Thioflavin T assay 2-32

Chapter 3: Intrinsic luminescence from charged, non-aromatic amino acids and charged monomeric proteins

3.1 Introduction 3-1
3.2 Results and Discussions 3-3
3.2.1 ProCharTS observed among Lysine, Lysine·HCl and Glutamate 3-3
3.2.2 ProCharTS observed among amino acids are emissive in nature 3-4
3.2.3 Luminescence from charge transfer states in amino acids mirrors the change in ProCharTS absorbance 3-5
3.2.4 Effect of addition of equimolar concentration of Lysine·HCl and Glutamate 3-6
3.2.5 Selection of different proteins rich in charged residues 3-7
3.2.6 Absorbance and extinction coefficient of different protein and amino acids 3-8
3.2.7 ProCharTS observed from monomeric proteins 3-10
3.2.8 Emission spectra of different proteins and amino acids 3-11
3.2.9 Excitation spectra of different proteins and amino acids 3-12

3.2.10 Stokes shift 3-13
3.2.11 Variation in luminescence yield with excitation wavelength 3-15
3.2.12 Quantum yield of different proteins and amino acids 3-17
3.2.13 Linearity in luminescence at λ_{ex} 355 nm 3-18
3.2.14 Relationship between the luminescence and product of ε and Φ 3-20
3.2.15 Luminescence lifetime of protein charge transfer states 3-21
3.2.15.1 Luminescence lifetime at λ_{ex} 340 nm 3-21
3.2.15.1 Luminescence lifetime at λ_{ex} 295 nm 3-25
3.3 Conclusions 3-30

Chapter 4: Human Serum Albumin (HuSA): A model protein to investigate ProCharTS

4.1 Introduction 4-1
4.2 Results and Discussions 4-3
4.2.1 Effect of pH and ionic strength of ProCharTS of HuSA 4-3
4.2.2 Prevalence of luminescence from charge transfer states in HuSA 4-4
4.2.3 Intrinsic luminescence observed from monomeric HuSA 4-5
4.2.4 Unfolding of HuSA decreases ProCharTS 4-9
4.3 Conclusions 4-14

Chapter 5: Effect of ProCharTS on extrinsic and intrinsic fluorescent probes in proteins

5.1 Introduction 5-1
5.2 Results and Discussions 5-3
5.2.1 Effect of ProCharTS on fluorescence of an extrinsic probe, Dansyl 5-3
5.2.2 Effect of ProCharTS on the fluorescence of intrinsic probes 5-9
5.2.2.1 Effect of Lysine on the fluorescence of NATA 5-9
5.2.2.2 Effect of Lysine·HCl on the fluorescence of NATA 5-13
5.2.2.3 Effect of Glutamate on the fluorescence of NATA 5-15
5.2.2.4 Effect of charged residues in protein on the fluorescence 5-21

of NATA

5.2.2.5 Effect of inserted Trp on the ProCharTS luminescence of PEST wt 5-23

5.3 Conclusions 5-25

Chapter 6: ProCharTS: A label-free approach to detect aggregation of hen egg white lysozyme (HEWL)

6.1 Introduction 6-1

6.2 Results and Discussions 6-2

6.2.1 Detection of HEWL aggregates by ProCharTS 6-3

6.2.1.1 ProCharTS of HEWL aggregates formed at alkaline pH 6-3

6.2.1.2 ProCharTS of HEWL aggregates formed at acidic pH 6-4

6.2.2 Intrinsic luminescence from HEWL aggregates 6-7

6.3 Conclusions 6.15

Chapter 7: Thesis Summary and Future Perspectives

7.1 Thesis Summary 7-1

7.2 Future Directions 7-2

Appendix

List of publications and conferences

References

Chapter 1

Introduction and Literature Review

Introduction

The electronic charge redistribution is one of the most important events in almost all the photo-induced processes for both the chemical and biological systems (May & Khun 2011). In addition, charge transfer at molecular level plays a fundamental role in many areas of chemistry, physics, and biology as well as material sciences(Wörner et al 2017). Among biological systems, charge transfer plays a vital role in many key mechanisms including UV DNA damage repair (Moughal Shahi & Domratcheva 2013, Weber 2005), energy harvesting (Strümpfer et al 2012), photosynthesis (Meech et al 1986, Wahadoszamen et al 2014), cellular respiration (Kaila Ville 2018, Martin & Matyushov 2017) and signaling through photoreceptor proteins like cryptochrome (Sjulstok et al 2015). Apart from these, their crucial role has also been established in metalloproteins like Azurin, Plastocyanin, Cytochrome C, Myoglobin, etc. (Gray & Winkler 2001, Liu et al 2014) as well as in the field of magnetic sensing among birds and animals (Johnsen & Lohmann 2008, Solov'yov et al 2014). Here, in this work charge transfer and its significance among different biological macromolecules and biological systems are presented with a special reference to charge transfer in proteins and amino acids.

1.1 Charge Transfer

Charge transfer is a process in which a charge is permanently relocated from a donor to an acceptor (Wörner et al 2017). Charge transfer, when referred are primarily thought to be associated with the Charge Transfer Complexes, which are supposed to be produced when one reagent is an electron donor (Lewis base) and the other is an electron acceptor, Lewis acid (Calatayud & Zamora 2013). The term charge transfer complex was introduced by Mulliken to define a new type of adduct that does not fall into the category of ionic, covalent, coordination or hydrogen bonding (Gutmann 1997, Mulliken & Person 1969). Charge transfer complexes are most commonly observed with the coordination compounds that possess one or multiple metal centers bound to ligands. The charge transfer in these compounds are mainly of two different types depending upon the transfer of electrons, ligand-to-metal-charge-transfer (LMCT) or metal-to-ligand-charge-transfer (MLCT) (Horváth & Stevenson 1993, Lever 1974). Here the electronic charge is essentially transferred either from the ligands towards the coordinating metal or from the coordinating metal to the ligands.

This type of transition in which an electron is transferred from metal to ligands or vice-versa, is called the charge transfer transition (Lever 1974). The charge transfer transitions are also defined as the electronic transitions in which a large fraction of an electronic charge is transferred from one region of a molecular entity, called electron donor, to another, called electron acceptor (Braslavsky 2007).

The electron transfer reactions between a donor (D) and acceptor (A) are mostly represented by the following scheme

$$D^{-}A \rightarrow DA^{-} \tag{1.1}$$

Here, D^{-} represents an excess of electrons localized on the donor and DA^{-} represents the product state formed after the electron has moved to the acceptor. When the donor and acceptor both belongs to the same molecule (as in case of proteins), the reaction is called the intramolecular or unimolecular electron transfer while in case where two distinct molecules are involved, the reaction is called intermolecular or bimolecular electron transfer. In spite of these differences, the common structure formed by the donor and acceptor enabling electron transfer to happen, is called the donor-acceptor (DA) complex (May & Khun 2011).

Figure 1.1 represents the energy diagram for the electron transfer reaction shown in equation 1.1. In simplest case of electron transfer reaction, the excess electron initially occupying the lowest unoccupied molecular orbital (LUMO) of the donor (donor state) moves to the LUMO of the acceptor (acceptor state). Alternatively, the transferred electron can also come from the excited state of the donor (D*). Post excitation of an electron of the donor is placed into the LUMO. Then the electron transfer happens between donor and acceptor LUMOs. This scheme of electron transfer (Figure 1.1b) is generally called the photoinduced electron transfer. However, in photoinduced hole transfer reactions, the electron from the HOMO of acceptor gets transferred to HOMO of donor, consequently transferring the hole from donor to acceptor (Figure 1.1c). (Bolton & Archer 1991, May & Khun 2011).

As far as work on electron transfer are concerned, it can broadly be subdivided into three categories (Bolton et al 1991):

a) Photo-induced electron transfer reactions in which both forward (charge separation) and reverse (charge recombination) intramolecular electron transfer can happen;
b) Charge-shift reaction in which an electron is introduced into one entity in the molecule and then undergoes intramolecular electron transfer to another entity, and

c) Bimolecular studies using uncombined donor and acceptor entities, in which it has been possible to infer the unimolecular rate constants for the charge recombination within the geminate radical ion pairs formed by charge separation at encounter between an excited molecule and quencher.

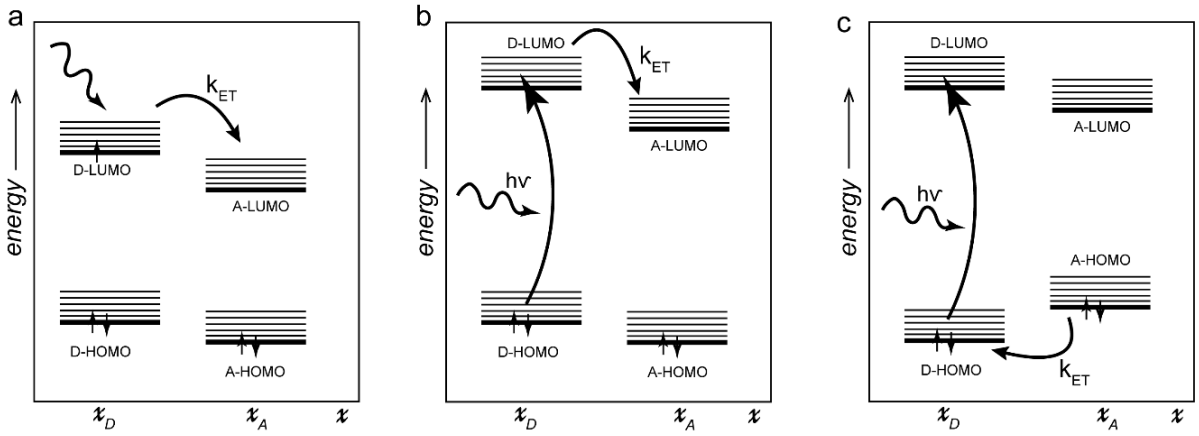

Figure 1.1: Panel **a** shows the electron transfer reaction of an excess electron in a donor-acceptor (DA) complex with spatial donor position x_D and acceptor position x_A (thick lines - electronic levels, thin lines - vibrational levels). The reactant state electron configuration is shown. The electron spin is represented by an upward/downward arrow, and the curved arrow indicates the pathway the transferred electron takes toward the product state. Panel **b** shows the photoinduced electron transfer reaction and panel **c** shows the photoinduced hole transfer reaction in DA complex. Reproduced from (May & Khun 2011) with permission from John Wiley & Sons.

The rate of intramolecular electron transfer depends upon the factors like, energy of the excited state, exergonicity $(-\Delta G^0)$, distance between the donor and the acceptor, orientation of donor with respect to acceptor, nature of bridge, nature of solvent and temperature (Bolton et al 1991). The rate of charge transfer can be understood well by the Marcus theory given by R. A. Marcus in 1956 (Marcus 1956a, Marcus 1956b, Marcus 1993). It describes the rate of overall charge transfer process, and includes the electronic and structural rearrangements on a time scale limited to that of nuclear motions. The energy potential surfaces in electron transfer reaction is represented in Figure 1.2.

The rate of charge transfer is given by

$$k_{CT} = A \exp\left(\frac{-\Delta G^*}{k_B T}\right) \tag{1.2}$$

where, ΔG^* is represented by

$$\Delta G^* = \frac{\lambda}{4}\left(1 + \frac{\Delta G^0}{\lambda}\right)^2 \quad (1.3)$$

The term A in equation 1.2 depends upon the nature of the electron transfer reaction (for example, bimolecular or intramolecular), k_B is Boltzmann constant, T is temperature, ΔG^0 is the standard free energy of reaction and λ is the reorganization term composed of solvation (λ_s) and vibrational (λ_v) components (Equation 1.4).

$$\lambda = \lambda_s + \lambda_v \quad (1.4)$$

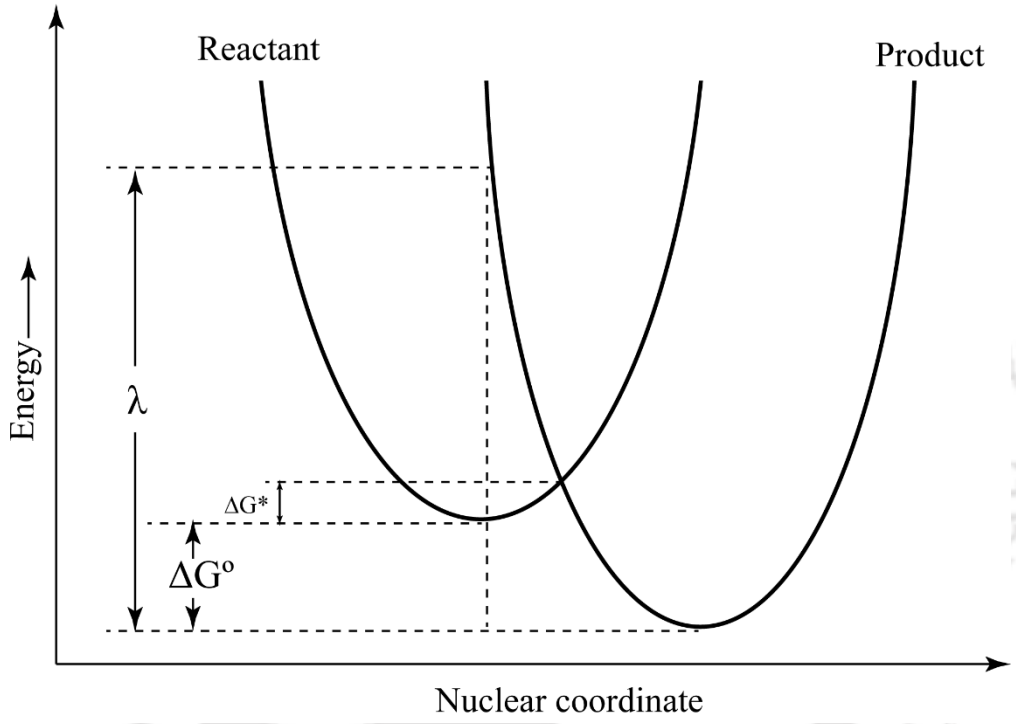

Figure 1.2: Schematic representation of reactant and product potential-energy surfaces in electron transfer reactions indicating the driving force (ΔG^0), the activation free energy (ΔG*) and the reorganization energy (λ). Adapted from (Gray & Winkler 1996) with permission from Annual Reviews.

The emission from the charge transfer states of coordination compounds generally originates from the energetically lowest triplet state and in rare cases fluorescence originating from the lowest-energy singlet are also observed (Vogler & Kunkely 1993).

1.2 Charge transfer in biological systems

The significance of non-covalent interactions among the biological molecules and macromolecules are key to their flexibility and specificity (Frieden 1975). Formation of charge transfer complex could help achieve the same. A vast amount of literature reports the formation and significance of charge transfer complex in biological systems. A few

noticeable examples are the charge transfer complex formation with purine, pyrimidines, nucleotide, nucleoside, DNA/RNA, amino acids, protein, porphyrins, saccharides, lipids, vitamins, neurotransmitters and even in microorganisms (Gutmann 1997). Apart from this, the core of charge transfer complex formation , that is, the electron transfer is heart and soul of biological processes like photosynthesis, electron transport chain in cellular respiration and various enzymatic mechanisms.

1.2.1 Charge transfer deriving the photosynthesis

Photosynthesis is the basis for all life forms on the earth. It converts the solar energy into the chemical forms inside the chloroplast of green plants and chromatophores (Lascelles 1962) in photosynthetic bacteria (Galston 1992). Specifically, the process of photosynthesis converts the absorbed light energy into a nanosecond-lived electronic excitation, to a charge-separated state, and finally to a membrane proton gradient which is ultimately harnessed to produce ATP (Breton et al 1986, Kirmaier et al 1991, Rochaix 2011, Strümpfer et al 2012). This process of electron transfer happens within the pigment-protein complex called reaction center (RC) (Deisenhofer et al 1985).

In a bacterial system, reaction center contains four bacteriochlorophyll (BChl) pigments and two bacteriopheophytin, $BPh_{1,2}$ (BChl with no magnesium) which help in absorption of light. The light energy absorbed by all the six pigments is transferred as an excitation to the central BChl pair, called Special Pair or P870 ($BChl_1$+$BChl_2$ = SP) (Strümpfer et al 2012). The excited state of P870* has an estimated excited state redox potential of -0.94 E_m (V) (Blankenship 2014, Blankenship & Prince 1985). This SP then initializes the charge separation by transferring an excited electron to the bacteriopheophytin (BPh_1) through $BChl_3$. The electron is subsequently transferred to a permanently bound molecule of quinone (Q_1) and finally to another, exchangeable quinone (Q_2) (Figure 1.3). Hence, a series of electron transfer establishes a charge transfer state, $Q_2^- + SP^+$ (Strümpfer et al 2012). Further, the cytochrome bc_1 complex catalyzes the transfer of electrons from the quinone to the cytochrome c and concomitantly translocate protons across the membranes (Xia et al 2013), generating proton motive force essential for ATP synthesis. Finally, the cytochrome c reduces the oxidized SP. This electron transfer inside the reaction center can be represented by the following scheme (Lin et al 2009, Meech et al 1986, Moser et al 1992):

$$SP\ BPh_1\ Q_2 \xrightarrow{h\nu} SP^*\ BPh_1\ Q_2 \longrightarrow SP^+\ BPh_1^-\ Q_2 \longrightarrow SP^+\ BPh_1\ Q_2^-$$

It should also be noted that the rate of charge recombination process (in which the electron directly returns from one of the acceptor to oxidized SP) is much slower (Figure 1.3b) due to higher rate constants for forward reaction and larger energy gaps involved. This steers the system towards the charge-separation reactions away from the wasteful recombination reactions, making the process of photosynthesis very efficient (Blankenship 2014).

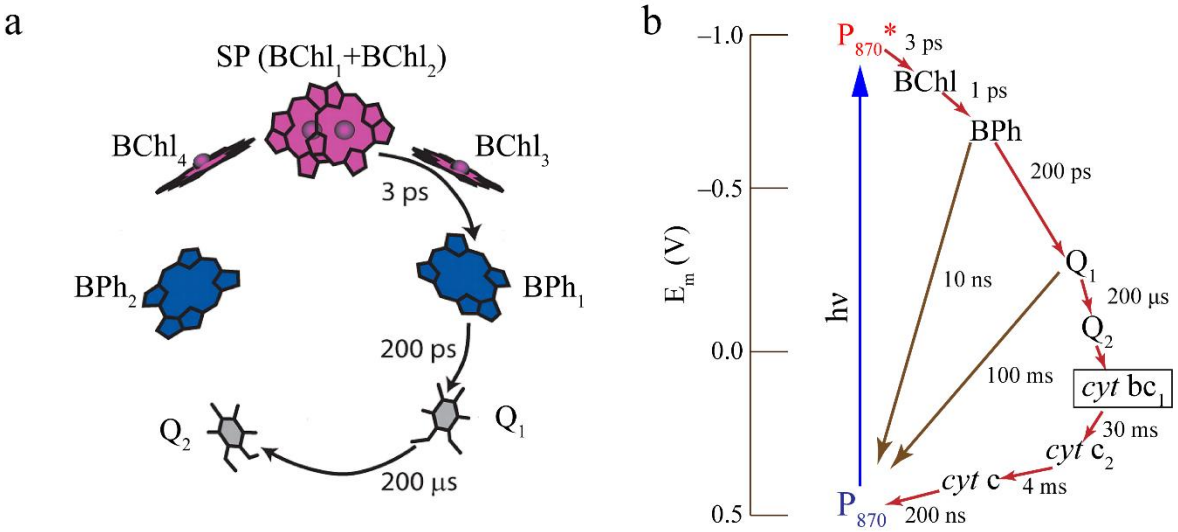

Figure 1.3: Panel **a** shows the arrangement of cofactors in *Rb. sphaeroides* reaction center. Arrow represents the electron transfer pathway. Adapted from (Lin et al 2009) with permission from National Academy of Sciences. Panel **b** shows the energy-kinetic diagram describing the energetics and reaction time for electron transfer processes in reaction center from *Rb. sphaeroides*. Reproduced from (Blankenship 1994) with permission from Springer Nature.

Similar to the electron transfer pathway shown above, the oxygenic photosynthesis also involves a complex of different proteins and cofactors that ultimately derive the formation of ATP. However, unlike the cyclic electron pathway described above for bacteria, the oxygenic photosynthesis involves two photosystems, namely Photosystem 1 (P700) and Photosystem 2 (P680). Figure 1.4 displays the scheme for electron transfer in oxygenic photosynthesis.

Another distinctive feature is the generation of molecular oxygen from the oxidation of water molecules at Photosystem 2. This is accomplished by the presence of Oxygen Evolving Complex (OEC) containing tetranuclear Mn cluster, which are capable of generating molecular oxygen by oxidising water molecules probably due to very high redox potential of $P680^+$ (+1.2 E_m (V)) as compared to water (+0.8 E_m (V)) (Blankenship 2014). The reduced OEC then transfers the electrons to $P680^+$. The rest of architecture of core

pigments, proteins and quinone reduction part is very similar to those discussed above for bacterial reaction centre. However, in this case cytochrome b_6f is present having a similar role as of cytochrome bc_1 complex. Here the cytochrome f is responsible for the reduction of oxidised $P700^+$ of photosystem 1 through a small copper protein, plastocyanin (PC).

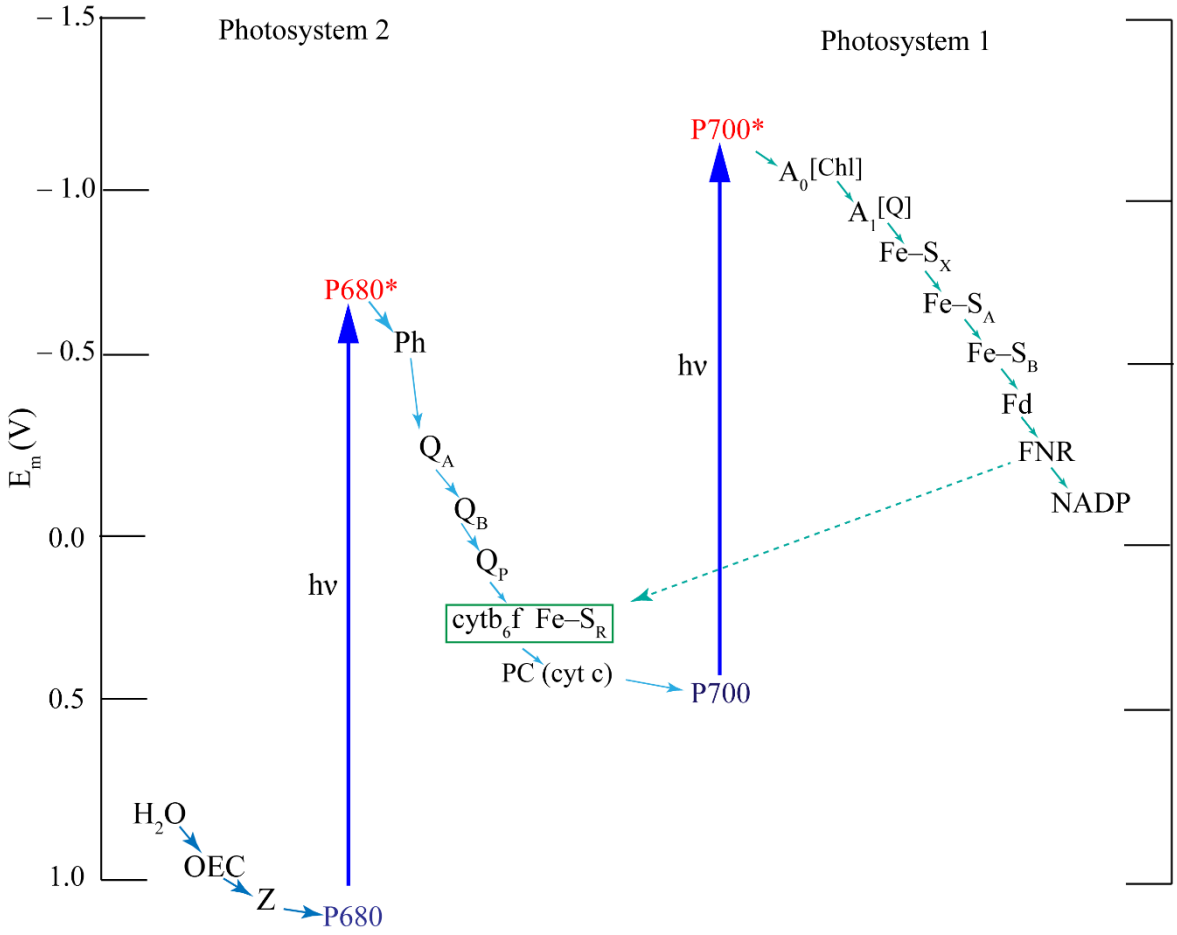

Figure 1.4: The Z scheme for oxygenic photosynthesis constructed using excited-state redox potentials. OEC, oxygen-evolving complex; Z, donor to photosystem II (PS II); P_{680}, reaction center chlorophyll of PS II; Ph, pheophytin acceptor of PS II; Q, quinone; cyt, cytochrome; FeS_R, Rieske iron-sulfur protein; PC, plastocyanin; P_{700}, reaction center chlorophyll of PS 1; A_0 and A_1, early acceptors of PSI (possibly chlorophyll and quinone species); FeS_X, FeS_A and FeS_B, bound iron-sulfur protein acceptors of PS 1; Fd, soluble ferredoxin; FNR ferredoxin-NADP reductase.. The dashed line indicates cyclic electron flow around PS I. Reproduced from (Blankenship & Prince 1985) with permission from Elsevier.

Photosystem 1, on the other hand has numerous cofactors and proteins and operates in a much reducing regime. The electron transfer process starts with the excitation of P700 where the excited electron is transferred to primary acceptor (another chlorophyll, called A_0 with redox potential approximately -1V). This electron is then transferred to one of the quinones (called A_1) in ~25 ps and from there the electron is transferred through three iron sulphur

clusters (Fe-S) to the soluble ferredoxin (Fd). Ferredoxin-NADP reductase (FNR) sequentially accepts two electron from the Fd and carries out the electron reduction of NADP+ to NADPH. The transfer of electrons from the FNR to the $cytb_6f$ complex give rise to the cyclic electron flow around PS1, which is coupled with proton translocation and ATP formation. (For more details, *Molecular Mechanism of Photosynthesis* by Robert E. Blankenship should be referred).

Hence, the process that started with the electronic excitation of photosystems and charge separation mediated by various proteins and cofactors results in generation of ATP and NADPH, which ultimately is utilized in fixation of CO_2 molecules by Calvin cycle (Quick & Neuhaus 1997).

1.2.2 Electron transfer and the respiratory chain

In the cellular respiration, the electrons are released from the NADH and $FADH_2$ and are eventually transferred to the oxygen (O_2), which results in the formation of water (H_2O) molecules along with the generation of proton gradient across the membrane. The respiratory chain accomplishes the whole process through its four major complexes, NADH-CoQ reductase complex, Succinate-CoQ reductase complex, CoQH2-Cytochrome c reductase complex and Cytochrome c oxidase complex. These are respectively called Complex I, II, III and IV.

The electrons released from the NADH at Complex I and from $FADH_2$ at Complex II are transferred to Coenzyme Q (CoQ) through the Iron-Sulfur (Fe-S) protein present within the respective complexes. The transfer of electrons from the NADH to CoQ through Complex I leads to the pumping of 4 hydrogen ions (H^+) out of the mitochondrial matrix. Further, Complex III catalyzes the transfer of electrons from the $CoQH_2$ to the Cytochrome c and concomitantly pump 2 protons out of the mitochondrial matrix. Finally, the Complex IV catalyzes the oxidation of reduced Cytochrome c and electrons are subsequently transferred to the ultimate electron acceptor, O_2 resulting in the formation of H_2O. During this process, 2 protons are translocated across the membrane (Figure 1.5). For more details *Molecular Cell Biology* (Lodish et al 2000) and *Biochemistry* (Berg et al 2006) should be referred.

The overall process involves an immense interplay and sequential transfer of electrons (hence, called the electron transport chain) generating electrochemical proton gradient across the membrane which ultimately drives the generation of ATP (oxidative phosphorylation) (Barbara et al 1996).

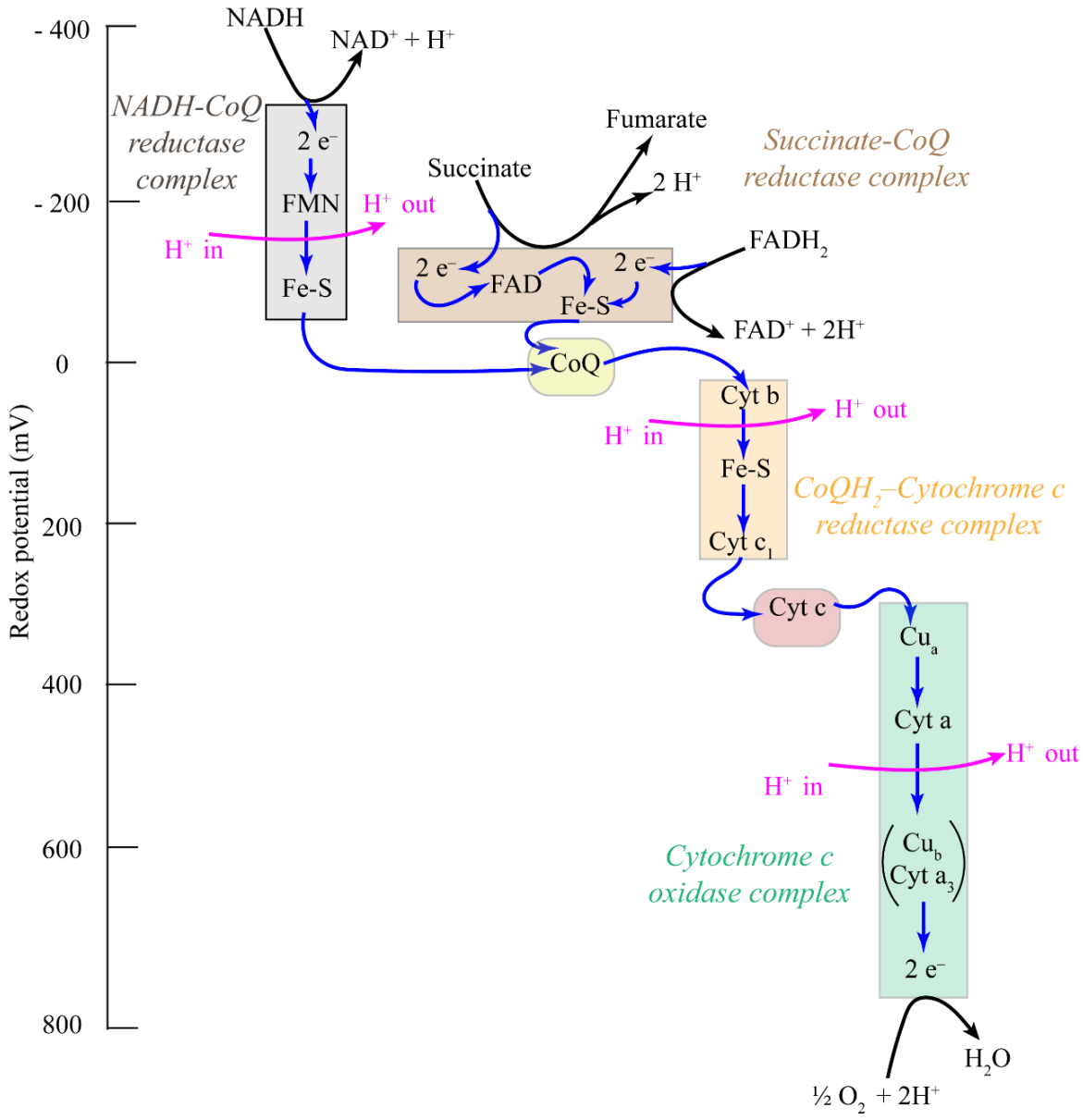

Figure 1.5: Schematic for sequential electron transfer through the electron transport chain from NADH, succinate and $FADH_2$ to O_2. The blue arrows represents the electron transfer while the magenta arrows displays the proton translocation across the membrane. Electrons passes in a sequence from carriers with a lower reduction potential to those with the higher potential. Adapted from (Lodish et al 2000) © 2000, W. H. Freeman and Company.

1.2.3 Charge transfer in nucleic acids

Nucleic acids are composed of pentose sugar units, phosphate backbone and π-stacked bases. These π-stacked bases are believed to be involved in the charge migration (Eley & Spivey 1962, Holmlin et al 1997). However, there is little or no role of sugar and phosphate backbone in electron transfer (Siriwong & Voityuk 2012). The electron transfer in DNA can affect most of the electronic and chemical properties of the polynucleotide chain (Clement

& Corongiu 1982) while structural fluctuations in DNA structure and the presence of counter ions and water molecules can affect the electron transfer process (Giese 2002a, Kubař & Elstner 2008, Voityuk et al 2004).

The charge transfer processes in DNA can be characterized into two types namely, oxidative hole transfer and reductive electron transfer processes. Both processes involve electron transfer reactions but in terms of orbital, they are distinct. The reductive electron transfer is associated with LUMO while the oxidative hole transfer is HOMO controlled process (Wagenknecht 2005) (as shown in Figure 1.1).

In oxidative hole transfer, the electrons are transferred from the final acceptor to the photoexcited donor while in reductive electron transfer the photoexcited electron of donor is transferred to final electron acceptor (Figure 1.1). Since, the oxidation potential of purine bases (adenine/A and guanine/G) are lower than that of pyrimidine bases (thymine/T and cytosine/C), the hole transfer in DNA can be deduced to the formation of cation radicals, G^+ and A^+. While on the other hand, in reductive electron transfer, radical anions of C and T are mainly involved as intermediate electron carrier (Siriwong & Voityuk 2012, Wagenknecht 2005).

Coming to the mechanisms of charge transfer in DNA, this can happen by two different ways: (*i*) superexchange-induced charge transfer and (*ii*) multistep charge transport via hopping (Jortner et al 1998). In case of superexchange, the charge tunnels in one coherent step from donor (D) to acceptor (A), avoiding the energetically higher states (higher than the photoexcited donor state) of DNA bridge (intermediate bases, B) between the D and A (Figure 1.6). This process is also called single-step hole transfer. The rate of hole transfer (k_{HT}) by this mechanism decreases exponentially with distance between D and A. Hence, this type of charge transfer is limited to only short distances (≤15 Å) (Siriwong & Voityuk 2012).

On contrary, in multistep charge transfer mechanism, the cation radical, G^+ plays an important role of intermediate charge carrier. Once the G^+ forms, another Guanine (G_2) can donate its electron to G^+, resulting in hole transfer from G^+ to G_2. The hole transfer to the distant G can happen either through the intermediate guanines (called G hopping) or through the intermediate adenine bases (called A hopping) as shown in Figure 1.7a (Giese 2002b). Moreover, in this case the energy states of the bridge (intermediate bases, G_n) are lower than that of photoexcited donor state allowing step by step hopping of charge from excited state

donor to final acceptor. This type of hole hopping can allow rapid transfer of radical cations over a distance of 200 Å (Berlin et al 2000, Genereux & Barton 2010).

Mechanism of reductive electron transfer are considered mainly to happen through electron hopping involving all the base pairs (A-T and G-C) and pyrimidine radical anions $C^{\bullet -}$ and $T^{\bullet -}$ (Giese 2002b). Similar hopping can occur in this case as described for hole hopping but through either cytosine (C-hopping) or thymine bases (T-hopping) (Figure 1.7b).

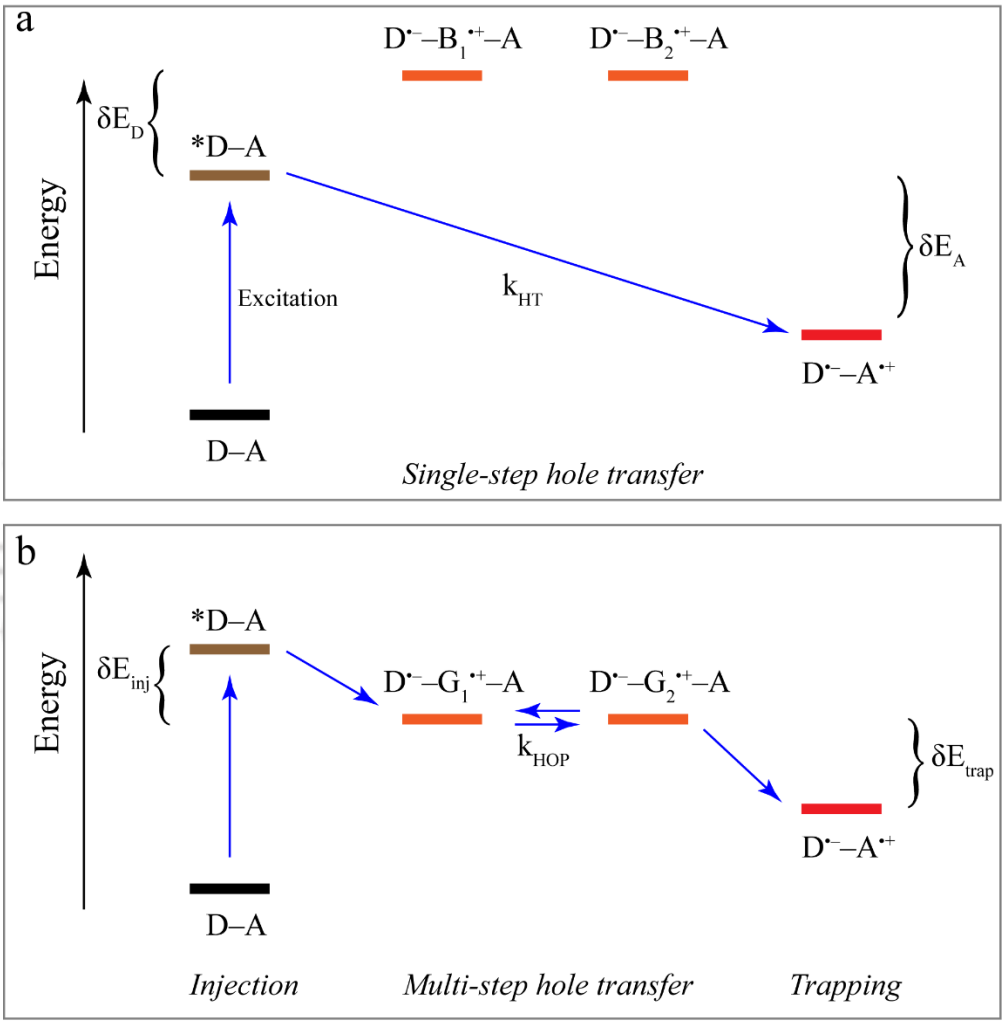

Figure 1.6: Comparision of (**a**) photoinduced DNA-mediated hole transfer via superexchange mechanism and (**b**) photoinduced hole transport via hopping (D = Donor; B = Base; A = Acceptor; HT = Hole Transfer; inj = injection; HOP = Hopping; trap = trapping. Reproduced from (Wagenknecht 2005) with permission from Wiley-VCH.

The importance of charge transfer in DNA can be understood by the various DNA-protein interactions, which modulate DNA mediated hole/electron transfer. For example, conformational changes brought about by TATA-box binding protein in the DNA helix, decreases the efficiency of hole transport while the proteins like endonuclease *PvuII* and

transcription factor ANTP (Antennapedia homeodomain protein) which stiffens the DNA conformation, facilitates the hole transport (Rajski & Barton 2001). Another classical example where electron transfer plays an important role is the action of enzyme photolyase in protecting DNA damage from T-T dimers (thymine dimers) formed by the action of UV irradiation (Brash 1997).

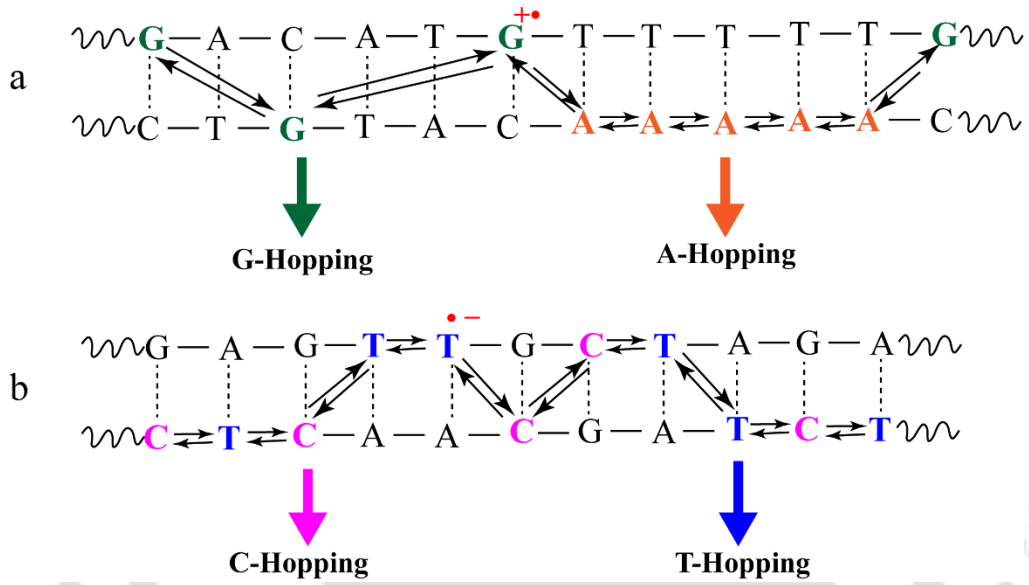

Figure 1.7: Schematics showing the (**a**) DNA-mediated hole transport via guanine and adenine hopping while (**b**) shows the DNA-mediated excess electron transport via cytosine and thymine hopping. Reproduced from (Wagenknecht 2005) with permission from Wiley-VCH.

The enzyme photolyase consists of two cofactors, one is the fully reduced Flavin adenine dinucleotide ($FADH^-$) and the other is deazaflavin or methenyltetrahydrate folate. The binding of enzyme to DNA is independent of light but the primary activation of first chromophore (deazaflavin) happens by the absorption of light between 350-450 nm. The excitation energy from this chromophore is transferred to the $FADH^-$ cofactor. The excited Flavin cofactor then transfers an electron to the Pyr< >Pyr dimer, generating a charge-separated radical pair ($FADH^{\bullet}$ + Pyr< >$Pyr^{\bullet -}$), which causes the split in the 5-5 and 6-6 bonds of cyclobutane, leading to the formation of a Pyr and a Pyr^-. Then the Pyr^- donates an electron back to the Flavin cofactor, regenerating $FADH^-$ and dissociation of enzyme from DNA (Sancar 1994, Sancar 1996).

The charge transfer in DNA could be utilized in several applications. Since, charge transfer in DNA is very sensitive to the base stacking, any perturbation and interruption in DNA base pairing caused by mismatches or DNA mutation could be detected by DNA chips and biosensors (Rawtani et al 2016, Wagenknecht 2005, Wong & Gooding 2006).

Apart from charge transfers discussed above, electron transfer in DNA-RNA hybrids (Kratochvílová et al 2013, Li et al 2016a, Li et al 2016b, Wong & Shao 2017), PNA; Protein nucleic acids (Wierzbinski et al 2012) and RNA (Hsiao et al 2013, Maie et al 2009, Takada et al 2011) have also been observed and investigated.

1.2.4 Charge transfer in peptides and proteins

As seen in previous sections, the role of electron transfer in the photosynthetic reaction centers and respiratory chain are very crucial for sustenance of these key physiological functions. However, the role of individual proteins in the electron transfer would be more revealing and could provide a better understanding of the phenomena of electron transfer at molecular level. Hence, in this section charge transfer among peptides and proteins and its mechanism along with their physiological relevance are presented.

Earlier studies of charge transfer in peptides were done with dipeptides of aromatic amino acids, Tyr and Trp (Prütz et al 1981), where the conversion of indolyl into phenoxy radicals was observed subsequent to one electron oxidation of TrpH residues with azide radicals ($N_3^{\bullet}$). The scheme of electron transfer is shown below:

$$Trp^{\cdot} - TyrOH \overset{k_1}{\rightarrow} TrpH - TyrO^{\cdot} \qquad k_1 = 7.3 \times 10^4\ s^{-1} \tag{1.5}$$

$$TyrOH - Trp^{\cdot} \overset{k_2}{\rightarrow} TyrO^{\cdot} - TrpH \qquad k_2 = 5.4 \times 10^4\ s^{-1} \tag{1.6}$$

Scheme of electron transfer between the Trp and Tyr in a dipeptide, post oxidation of TrpH with azide radicals ($N_3^{\bullet}$) (Prütz et al 1981).

Here, the phenomena of charge transfer across the peptide bond were reported supposedly through electron tunneling mechanism. This work was further extended in proteins, where similar electron transfer was observed directly between the aromatic side chains (Trp and Tyr), present at a distance from each other (Prűtz et al 1980, Prütz et al 1981). Similar observations of electron transfer were also reported in a number of different proteins like pepsin, trypsin, lysozyme, papain, chymotrypsin, concanavalin A and β-lactoglobulin (Butler et al 1982) and even in DNA photolyase of *A. nidulans* (Aubert et al 1999). The importance of proximal distance between the participating side chains involved in electron transfer was also established through the observations made for the decrease in transfer rate upon unfolding of β-lactoglobulin in presence of SDS (Butler et al 1982). For all these observations of intramolecular electron transfer, the role of hydrogen bonds and charge

conduction through the chain was negated (Butler et al 1982, Prűtz et al 1980) and electron transfer by direct superexchange like mechanism was suggested.

The mechanism of electron transfer among proteins and peptides has been postulated to be similar like that of discussed for nucleic acids, that is, either through single step superexchange mechanism or by multistep hopping mechanism (Figure 1.8).

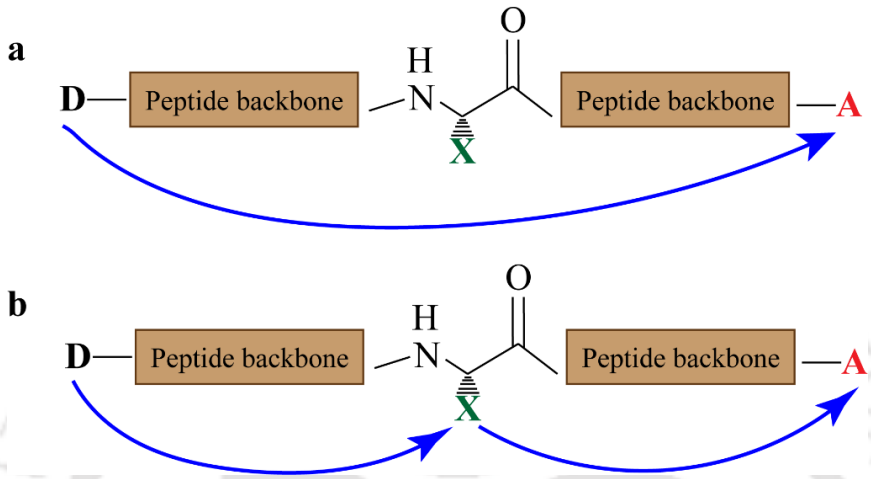

Figure 1.8: Possible electron pathways through peptides. (**a**) Electron transfer occurs via single step reaction if there is no redox-active side chain at position X between donor and acceptor is present while electron transport can happen in two-step hopping mechanism if an amino acid with redox-active side chain is present at position X (**b**). Reproduced from (Giese et al 2012) with permission from John Wiley & Sons.

The rate of electron transfer by superexchange mechanism depends exponentially upon the distance (r_{DA}) or peptide length between acceptor and donor

$$k_{ET} \propto e^{-\beta r_{DA}} \tag{1.7}$$

where β represents the influence of separating medium on the electron transfer rates (Hopfield 1974). On the other hand, the rate of electron transfer by hopping mechanism depends upon the number of hopping steps (N)

$$k_{ET} \propto N^{x} \tag{1.8}$$

where the value of x depends upon whether the steps are reversible or irreversible (Jortner et al 1998).

For hopping mechanism, where a step wise coupling of neighboring sites has been proposed (Baranov & Schlag 1999), the intermediate amino acids between the donor and acceptor acts as relay molecules or stepping stones through which the transfer of electrons happen. Amino acids with low redox potentials can play the role of relay stations, which include aromatic

as well as sulfur-containing aliphatic amino acids. For example, Tyr356, Tyr730 and Tyr731 act as relay amino acid in electron transfer observed in ribonucleotide reductase (Seyedsayamdost et al 2007, Seyedsayamdost et al 2006). However, the role of other amino acids, specially charged amino acids (glutamic acid, aspartic acid, lysine, arginine and histidine) in electron transfer have not been evaluated so far (Giese et al 2012) until recently (Mandal et al 2018, Prasad et al 2017).

Protein conformation also plays an important role in the electron transfer. The rate of electron transfer were also found to be dependent upon the dipole moment of the α-helical protein/peptide. The electron transfer rates are favored in the direction of diploe moment of α-helix while the rate are reduced in the opposite direction. In absence of net dipole moment like in a random coil polypeptide, the rate of electron transfer were found to be identical in both the directions (Figure 1.9) (Fox & Galoppini 1997, Galoppini & Fox 1996, Gatto et al 2008, Giese et al 2012).

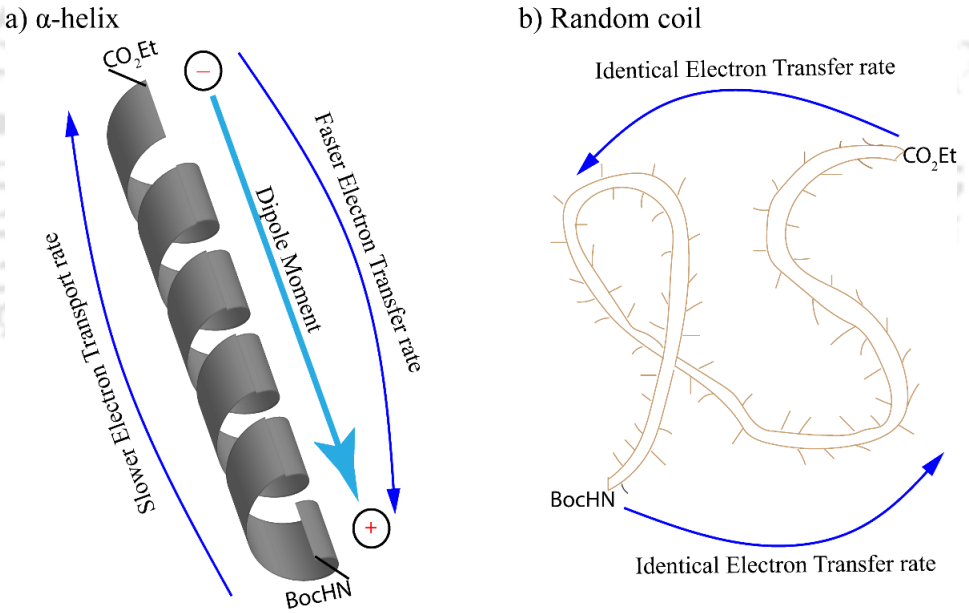

Figure 1.9: Comparison of electron transfer rate between the donor and acceptor across the (**a**) α-helix and (**b**) random coil. Here, 2-pyrenyl group acted as electron acceptor and N,N-dimethyl-p-anilino as electron donor group for peptides made of alternating Ala-Aib (Galoppini & Fox 1996). Reproduced from (Giese et al 2012) with permission from John Wiley & Sons.

The role of amide bonds in electron transfer process remains controversial (Shah et al 2015). However, at several instances the role of peptide bonds in intramolecular electron transfer has been exhibited. For example, a rotational motion was observed along the Ramachandran angles, aligning the adjacent CO group at a distance of 2.8 Å following localized

photoexcitation along the peptide chain (Schlag et al 2007) and in the intramolecular electron transfer in Azurin (Broo & Larsson 1991). Apart from this, long range electron transfer through the α-helical peptides has also been reported to use the amide bonds as intermediate relay junctions between donor and acceptor (Arikuma et al 2010, Kai et al 2008). Recently, the peptide bond has been reported to act like donor/acceptor for charge transfer to/from the charged amino acids (Prasad et al 2017).

Most of the understanding about the mechanism and rate constants of long-range electron transfer among proteins have come from the study of metalloproteins/enzymes. The Ruthenium- bipyridine (Ru-bpy) modified copper containing proteins (azurin, stellacyanin and plastocyanin), heme containing proteins (cytochrome c, b_5, b_{562} and myoglobin) and other iron-sulfur proteins have been studied for electron transfer reactions between the Ru-bpy complex (bound to specific side chains of amino acids like His/Lys/Cys) and metal center. Moreover, such complexes were also utilized to study several inter-protein electron transfer reactions (Gray & Winkler 1996, Gray & Winkler 2001, Gray & Winkler 2010). Such electron transfer processes laid the foundation for the investigation of reactive intermediates in proteins (Lam et al 2016) and increased our understanding towards functionality and activity of proteins and enzymes, which are dependent upon electron transfer reactions.

The activity of photolyase enzyme, as discussed in previous section is not only dependent upon the electron transfer from the $FADH^-$ to the thymine dimer, but the generation of $NADH^-$ itself is an example of intramolecular electron transfer mechanism within the enzyme. This is accomplished by the photoactivation of $FADH^\bullet$ and subsequent electron transfer over 15 Å through three highly conserved tryptophan residues (Trp382, Trp359, Trp306). The final deprotonation step of $TrpH306^{+\bullet}$ prevents the back flow of electron transfer and thus allow the catalytic cycle to happen (Brettel & Byrdin 2010) (Figure 1.10).

The understanding of electron transfer in peptides and proteins has led to the rationale engineering of electron transfer pathway towards the production of hydrogen as a cleaner alternative fuel (Barber 2009). This could be achieved by the coupling of hydrogenase to the acceptor end of the PSI that are capable of harvesting the photo-chemically produced electrons to reduce protons to hydrogen (Lubner et al 2010, Yacoby et al 2011). This has also motivated the construction of the electron transfer-based biosensors (Ghindilis et al 1997) and electrochemical immunological biosensors (Saen-Oon et al 2013).

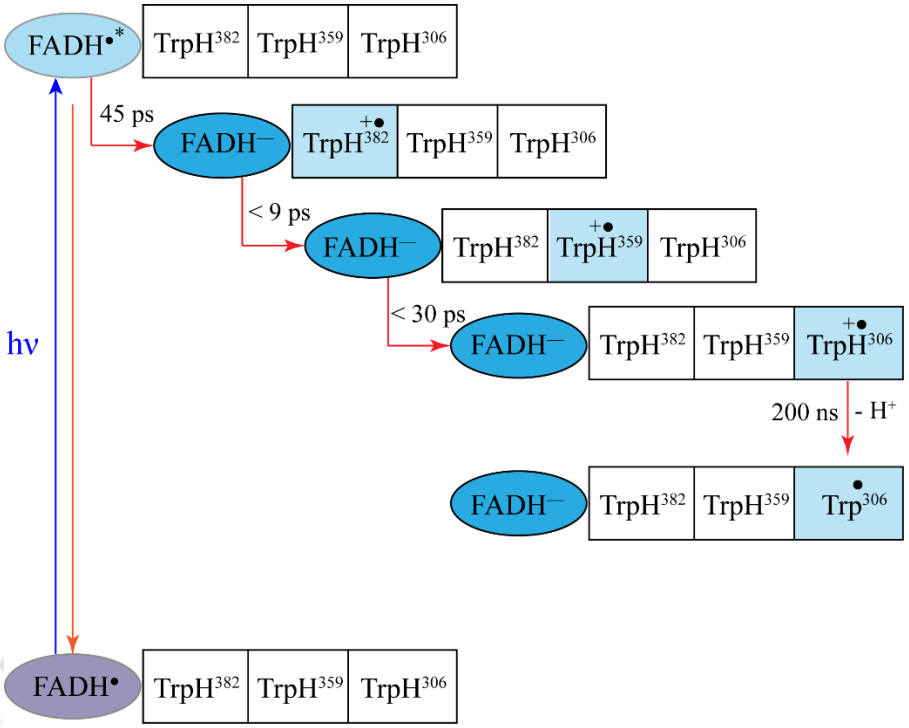

Figure 1.10: Mechanism of generation of $NADH^{-}$ from $NADH^{\bullet}$*, achieved through the electron transfer over three highly conserved Trp residues in DNA photolyase (Brettel & Byrdin 2010). Reproduced from (Giese et al 2012) with permission from John Wiley & Sons.

1.2.5: Protein Charge Transfer Spectra (ProCharTS)

So far, we have discussed the charge transfer phenomenon and its existence in the biological field from simple peptides to the complex networks of proteins and from base hoppings in nucleic acids to the life-saving mechanisms of enzymes. At the core of all these intriguing aspects of photo-induced electron transfer lies the transient absorption of light followed by a cascade of electronic activity. The transient absorption of light detected by simple spectroscopic techniques can deduce the whole range of information about the nature of chromophore and the types of transitions involved. On contrary to this, emission from the excited states can reveal the nature of environment in which the chromophore is present as well as about the excited state lifetime and factors affecting it.

Talking about the proteins, absorption spectra in the UV-visible region could arise due to the presence of any of the three most prominent aromatic chromophore (Trp, Tyr and Phe) or prosthetic groups (like heme, flavin, carotenoid, etc) or coenzymes (like FAD, NADH, NAD^{+}, etc). Among aromatic amino acids, Trp absorption is strongest (ε = 36,000 $M^{-1}cm^{-1}$ at 220 nm and 5,600 $M^{-1}cm^{-1}$ at 280 nm) followed by Tyr (ε = 9,000 $M^{-1}cm^{-1}$ at 222 nm and 1,300 $M^{-1}cm^{-1}$ at 280 nm) and Phe (ε = 9,600 $M^{-1}cm^{-1}$ at 205 nm and 200 $M^{-1}cm^{-1}$ at 250

nm). The peptide bonds (ε = 7,000 $M^{-1}cm^{-1}$ at 190 nm and 100 $M^{-1}cm^{-1}$ between 210-220 nm) and disulfide bonds (ε = 300 $M^{-1}cm^{-1}$ around 250 and 270 nm) also act like chromophores. Apart from this, histidine containing imidazole ring is also reported to absorb between 125-220 nm with ε = 6,000 $M^{-1}cm^{-1}$ at 212 nm and amino acids like Asp, Glu, Asn, Gln, and Arg show very weak absorption, weaker than peptide bonds at ~220 nm (Cantor & Schimmel 1980, Creed 1984, Weinryb & Steiner 1971, Wetlaufer 1963). Prosthetic group like heme shows intense band near 404 nm (ε = 1,70,000 $M^{-1}cm^{-1}$) due to the presence of porphyrin ring and among coenzymes, NAD^+ absorbs strongly at 259 nm (ε = 16,900 $M^{-1}cm^{-1}$), FAD at 450 nm (ε = 11,300 $M^{-1}cm^{-1}$) and NADH at 340 nm (ε = 6,220 $M^{-1}cm^{-1}$) (Aliverti et al 1999, Dawson et al 2002, Karnaukhova et al 2014). Hence, a naked protein without any prosthetic group or coenzyme is not expected to show any absorbance beyond 320 nm, since Trp at 300 nm has ε = 20 $M^{-1}cm^{-1}$ (Demchenko 1986). Additionally, in absence of any aromatic amino acids and disulfide bonds in protein, should make the absorption spectra optically silent beyond 250 nm. Similar absorption spectra can be expected from other non-aromatic amino acids in the UV-visible region.

However, contrary to this expectation, concentrated solutions of lysine-hydrochloride were reported to show an anomalous absorption spectra (ε = 0.34 $M^{-1}cm^{-1}$ at 270 nm) in the range of 230-500 nm (Homchaudhuri & Swaminathan 2001) which were further corroborated by other groups (Chai et al 2008, Chen et al 2018, Ryzhkina et al 2018). Similar observations were made for the proteins rich in lysine residues like human serum albumin and calf thymus histone. It was suggested that the lysine-lysine interactions (intermolecular interactions in case of lysine solutions and intramolecular interactions between proximally present lysine residues in case of proteins) are responsible for the origin of such spectra and the interacting groups are the side chains and not the amino or carboxyl groups (Homchaudhuri & Swaminathan 2004). In spite of this speculation, the exact nature of chromophore was not established. In the mean time, other research groups have come up with an idea of H-bonding and proton transfer behind the similar anomalous behavior for their luminescence observations made with protein powders, protein at high concentrations and protein aggregates (Chan et al 2013, Guptasarma 2008, Pinotsi et al 2013, Pinotsi et al 2016, Shukla et al 2004).

Our group initiated further investigations to unravel the role of lysine side chains and other charged amino acids, mainly glutamate using a monomeric synthetic protein α_3C (Tommos et al 2013). This protein is devoid of any aromatic amino acids but rich in lysine and

glutamate residues. Its structure is composed of three alpha-helix bundles and its protein sequence is 67 amino acids long harboring 54% charged residues including 17 Lys, 17 Glu and 2 Arg.

α_3C presents a broad absorption spectra spanning all the way from 250-800 nm. In spite of absence of any aromatic amino acids, there is an intense absorption in the range of 250-300 nm while a broad tail of absorption is followed beyond 300 nm until 800 nm (Figure 1.11a). The appearance of broad tail due to any artifact like scattering and higher extinction coefficient due to any intermolecular interactions were negated for such observations. Hence, the observed absorbance spectra was speculated to arise from monomeric α_3C molecules and definitely charged residues have a major role to play in it. It was also suggested that the three-dimensional structure of protein is crucial for the interaction between the side chains of charged residues, since the mixture of individual amino acids (those present in protein) show only negligible absorption in the same spectral region (Figure 1.11b).

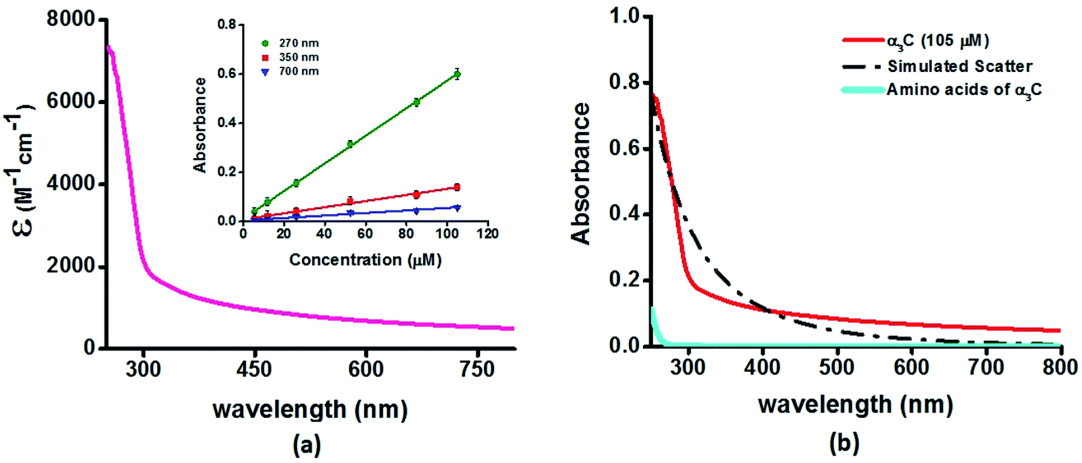

Figure 1.11: Panel (**a**) shows the absorption spectrum (250–800 nm) of α_3C in water. Inset shows a linear concentration dependence of absorbance at different wavelengths. Panel (**b**) shows the comparison of absorption spectrum (250–800 nm) of the intact α_3C protein with that of a solution mixture of constituent amino acids in α_3C. The concentration of individual amino acids are adjusted to match that of present in 105 μM α_3C. Simulated scatter is shown as dots and dashes. (Prasad et al 2017) Published by Royal Society of Chemistry.

The excess charge on the side chains of these charged amino acids can polarize the frontier orbitals to create a well-defined D-B-A (Donor-Bridge-Acceptor) complex in these systems (Mandal et al 2018). Here, the D groups are populated with filled orbitals while A groups have empty frontier orbitals. TDDFT (Time-dependent density functional theory) calculations and MD simulations done on these systems revealed the phenomena of charge-

transfer (CT) transitions between the D and A which are responsible for the origin of unusual absorption spectra observed for charged amino acids and protein rich in charged residues. This absorption spectra arising from CT transitions are termed as ProCharTS (Protein Charge Transfer Spectra) (Prasad et al 2017). These CT transitions are categorized as peptide backbone to side chain (PBS) CT transitions and side-chain to side-chain (SS) CT transitions.

The PBS CT transitions are low energy transitions and are well described in terms of ground state dipole moments of these chromophores. In these transitions, the photo-induced electron transfer happens either from the polypeptide backbone to the NH^{3+} in lysine or from COO^{-} in the glutamate to the polypeptide backbone through the connecting bridge. Here the carbon chain connecting the polypeptide backbone to the charged head group of side chains of Glu/Lys acts like a bridge (Figure 1.12) (Mandal et al 2018).

When the electrons are transferred from glutamate to polypeptide backbone, polypeptide backbone acts like an acceptor and COO^{-} in glutamate acts like donor while for the other transition from lysine to polypeptide backbone, lysine head group (NH^{3+}) acts like an acceptor and polypeptide backbone as donor (Figure 1.13).

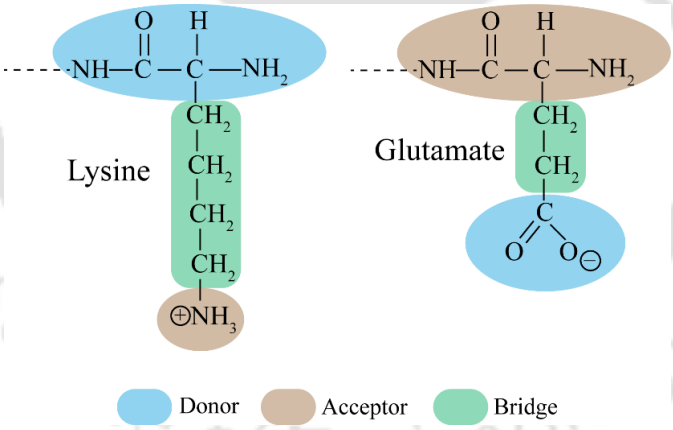

Figure 1.12: The colored segments represents the Donor (D), Acceptor (A) and Bridge (B) for the PBS CT transitions expected in polypeptide. Reproduced from (Mandal et al 2018) with permission from Royal Society of Chemistry.

For SS CT transitions, the electrons are transferred from the glutamate (COO^{-}) to the lysine (NH^{3+}). Hence, the glutamate side chain acts like a donor and lysine side chain as an acceptor (Figure 1.14). Here in this case, the bridge (B) component is variable and depends upon the solvent and the protein. Depending upon the proximity of donor and acceptor, the bridge could include variable number of water molecules or other side chain groups.

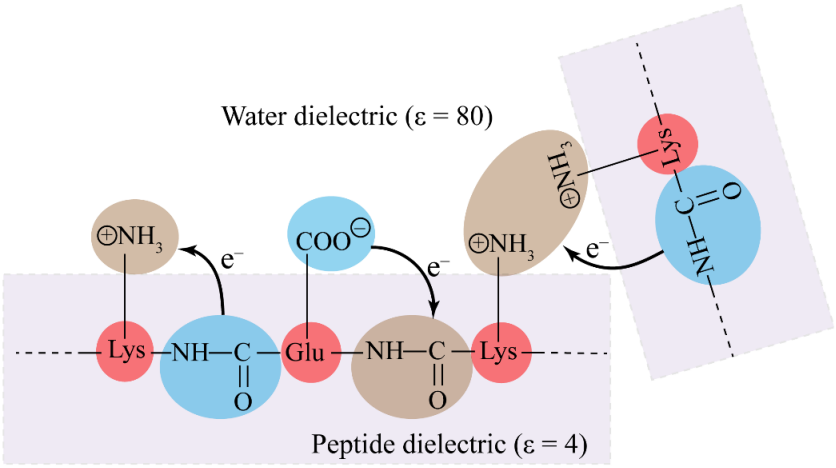

Figure 1.13: Schematic representing the Peptide Backbone- Sidechain (PBS) charge transfer transitions. Close interactions between sidechains with like charges lead to more delocalized A states and lower the CT transition energy. Adapted from (Prasad et al 2017). Published by Royal Society of Chemistry.

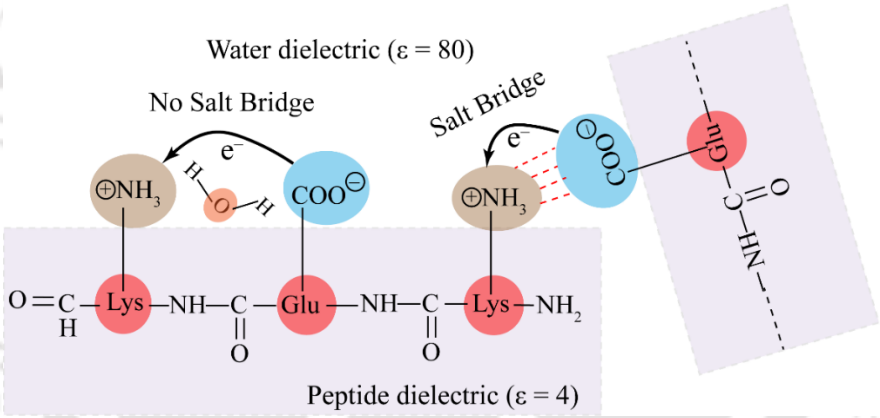

Figure 1.14: Schematic representing the Sidechain - Sidechain (SS) charge transfer transitions. Adapted from (Prasad et al 2017). Published by Royal Society of Chemistry.

The folded conformation of proteins can bring side chains of distantly located amino acids in close proximity, which can play a pivotal role in the CT transitions. When two charged side-chains are present in close proximity (Glu-Glu, Lys-Lys or Glu-Lys) can alter the relative stabilities of ground (Ψ_G) and excited state (Ψ_E) as a function of distance between the interacting pair. In case where Lys-Lys or Glu-Glu are in close proximity, the pair undergoes electrostatic repulsion, which destabilizes the ground state (Ψ_G) of the system, and at the same time the excited state (Ψ_E) of the system could be stabilized due to a higher probability of placing/removing electron from Lys-amino/Glu-carboxylate group. This stabilization of excited state brings down the energy gap between the HOMO and LUMO facilitating the PBS CT transitions (Figure 1.13, right). For example, when the proximal distance between Lys-Lys pair decreased from 6-7.5 Å to 3-4 Å, the energy gap between

HOMO-LUMO also decreased from 4.5 ± 0.8 eV to 3.4 ± 0.2 eV (Figure 1.15). A similar trend was observed for the Glu-Glu pair.

On the other hand, a closer proximity of Glu-Lys head groups, stabilizes the ground state (Ψ_G) of the system due to favorable electrostatics (formation of salt bridges) and also destabilizes the excited state (Ψ_E) due to charge neutralization. This causes the energy gap between the HOMO and LUMO to increase (Figure 1.15). However, when the Lys/Glu head groups are further apart, the energy gap decreases and could facilitate the SS CT transitions (Figure 1.14). For instance, with an increase in the distance between Lys-Glu pair from 2-3 Å to 5-6 Å, the HOMO-LUMO energy gap decreases from 6.2 ± 0.4 eV to 3.4 ± 0.3 eV (Figure 1.15)

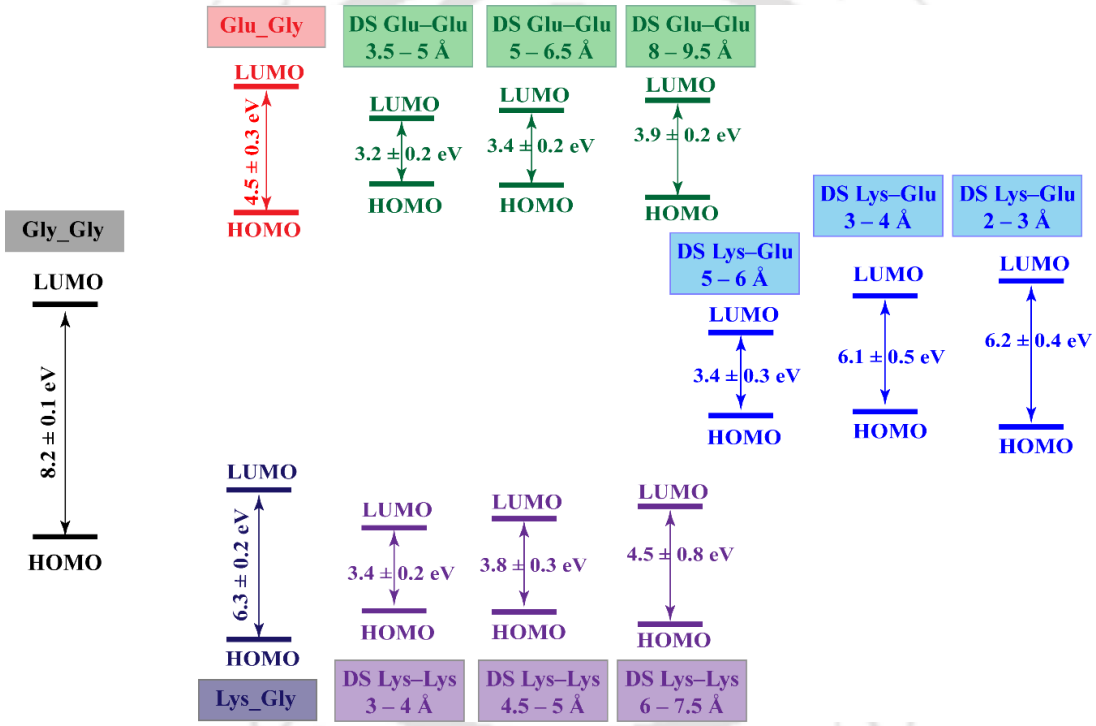

Figure 1.15: Average ground-state HOMO-LUMO gaps for different pairs calculated from 100 MD snapshots are presented. Here, different HOMO-LUMO gaps for the Lys-Lys, Glu-Glu and Lys-Glu are compared as a function of proximal distance between them. Energy gap for Gly-Gly, Lys-Gly and Glu-Gly are also shown as a control where no charged side-chain pair is present. DS stands for Distally Separated. Adapted from (Prasad et al 2017), Published by Royal Society of Chemistry.

With these insights upon the distance dependencies of CT transitions, a more detailed picture was generated with the visualization of TDDFT based simulated absorption spectra. This absorption spectra was generated for all three pairs, Lys-Lys, Glu-Glu and Lys-Glu as a function of increasing proximal distance between the partners (Figure 1.16). Both Lys-Lys and Glu-Glu, sidechain interactions displays low energy transitions. Spectral range for Lys-

Lys pair (Figure 1.16; 1a-3a) extends up to 550 nm (strong interactions), 500 nm (intermediate interactions) and 350 nm (weak interactions). Similarly, for Glu-Glu pair (Figure 1.16; 1b-3b), the spectral range extends up to 690 nm (strong interactions), 650 nm (intermediate interactions) and 500 nm (weak interactions). In contrast to Lys-Lys and Glu-Glu sidechain interactions, the extension of CT spectra was inversely proportional to the strength of the interacting Lys-Glu pair. For weakly interacting Lys-Glu pair, prominent transitions up to 800 nm (Figure 1.16; 3c) was observed while for the strong and intermediate interactions (Figure 1.16; 1c and 2c) between the pair limited the transitions to 350 nm. This limitation came from the neutralization of the charge by the formation of salt bridge between the pair, as discussed above.

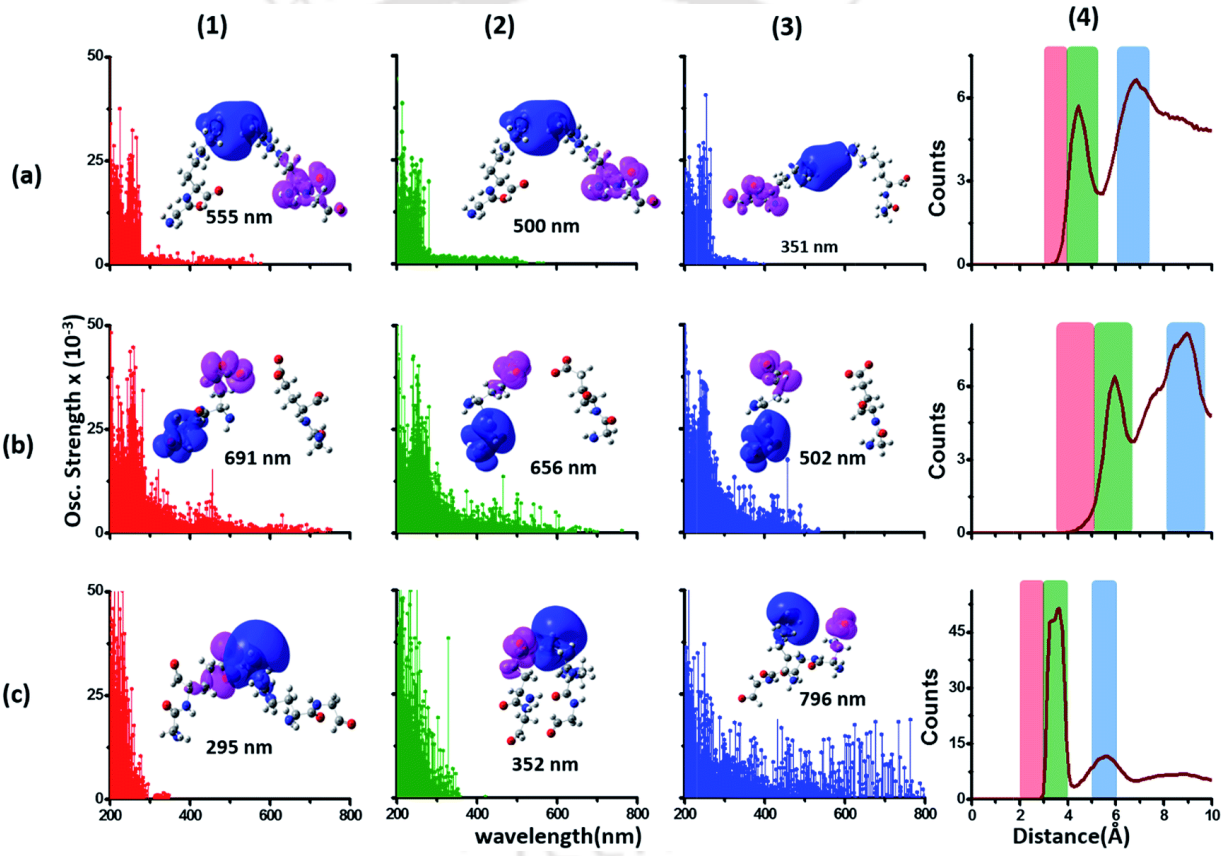

Figure 1.16: Simulated absorption spectra (wavelength vs. oscillator strength) for distally separated Lys–Lys (a1–a3), Glu–Glu (b1–b3), and Lys–Glu (c1–c3). Each panel displays spectra from 100 amino acid structures extracted from 100 ns MD trajectories of α_3C. The distance between the Lys–Lys (Row **a**), Glu-Glu (Row **b**) and Lys-Glu (Row **c**) head groups for which the CT transitions are displayed are chosen from the corresponding color coded regions of the RDF (radial distribution function) plots in last column. Precisely the distance are indicated in Figure 1.15. In each absorption spectra panel (a1–a3, b1–b3 and c1–c3) difference density plots show regions with decrease in electron density (pink lobes) and regions with increase in electron density (blue lobes) on Lys/Glu fragments for the lowest energy transitions in that panel. Adapted from (Prasad et al 2017). Published by Royal Society of Chemistry.

Apart from the Lysine and Glutamate, similar CT transitions are also reported with other charged amino acid residues like His, Arg, Asp and even among phosphorylated amino acids like, phosphorylated Ser (pSer), phosphorylated Thr (pThr) and phosphorylated Tyr (pTyr). (Mandal et al 2018).

From the above observations, it is clear that the ProCharTS arising from CT transitions are dependent upon the distance between the interacting side chains as well as on the sign of charge between interacting pairs or involved side chain. This makes the ProCharTS sensitive towards the effect of charge neutralization (due to presence of counter ions, pH variation or change in ionic strength of medium) and change in structural conformation of protein (induced by temperature fluctuations, presence of denaturing agents, mis-folding or aggregation). Hence, ProCharTS could be utilized to track these physiochemical effects on proteins and molecular events like denaturation and aggregation of proteins.

Apart from this, there are different aspects, which can be explored and detected by ProCharTS. Such possibilities can be appreciated by the abundance of charged amino acids across the proteome and their role towards several key biological function. Approximately 25% of proteome across the archea, bacteria and eukaryotes are rich in the charged amino acids (K, H, R, D and E) (Brüne et al 2018). There are many instances where this richness in the charged amino acids play a crucial role from functionality to even pathogenicity in proteins. For example, the presence of charge on nascent peptide determines the translation efficiency and protein expression (Charneski & Hurst 2013, Requião et al 2017) and alteration of the charge on side chain of amino acids induced by oxidative damage could lead to loss of protein stability and promotes aggregation (de Graff et al 2016).

Protein domains rich in D, E, K and R are involved in ribosome biogenesis and transcription regulation while H rich domain are involved in zinc transport and regulation (Cascarina & Ross 2018, Law et al 2006). Similarly, linker surrounding the DNA binding domains are rich in Ser, which acts as a target for phosphorylation, regulating the gene expression (Iakoucheva et al 2004). Apart from this, phosphorylated amino acids (pSer, pTyr, pThr) also play key role in signaling and cellular regulatory mechanisms in all organisms including Archaea (Ardito et al 2017, Kennelly 2014).

The charged amino acids also play an important role in protein-protein and protein-ligand interaction. This is signified by the moderate richness and conserved charged residues at the interfaces of protein involved in protein-protein and protein-ligand interaction (Mohamed et al 2015, Zhao et al 2011).

Intrinsically disordered proteins (IDPs) which are rich in charged residues but devoid of any aromatic amino acids (Bürgi et al 2016, Hansen et al 2006) presents another avenue where ProCharTS could be utilized from simple quantification of protein to as a tool for probing structural transitions and protein dynamics.

Moreover, the ProCharTS can also detect the intermolecular events like aggregation of proteins where new intermolecular contacts could form between the aggregating entities and could reflect more population of proximally present charge residues than its monomeric counterparts. Here, ProCharTS could be used to track time dependent growth kinetics of protein aggregates.

Hence, ProCharTS could be utilized as a label-free probe to study different molecular functions and aspects like protein structural transitions and protein-protein/protein-DNA interactions.

Objectives of the thesis work:

All we discussed above was about the mechanism of photo-induced electron transfer among proteins and amino acids and its consequent absorption spectra, ProCharTS. Apart from that, a briefing about the possibilities of ProCharTS as an intrinsic label-free tool is also made. The intriguing phenomenon of CT transitions and its applicability drove this thesis. A part of this thesis work is an attempt towards understand the intrinsic luminescence arising from the charge transfer states and how it can affect the fluorescence of other intrinsic and extrinsic chromophores in proteins. Another part of my thesis is devoted to the applications of ProCharTS where I have attempted to track down the molecular events like aggregation and unfolding of protein using ProCharTS as an intrinsic label-free tool.

Based upon this, objectives of this thesis work are outlined as:

1. Intrinsic luminescence from charged, non-aromatic amino acids and charged monomeric proteins
2. Human Serum Albumin (HuSA): A model protein to investigate ProCharTS
3. Effect of ProCharTS on extrinsic and intrinsic fluorescent probes in proteins
4. ProCharTS: A label-free approach to detect aggregation of Hen Egg White Lysozyme (HEWL)

Chapter 2

Experimental Techniques and Materials & Methods

2.1 Experimental techniques:

Under this thesis work, mainly two types of UV-Visible spectroscopic techniques are utilized to accomplish various experiments, namely absorption and fluorescence spectroscopy. The principles behind these techniques are explained under the following sections.

2.1.1 Spectroscopy

In broad terms, spectroscopy involves the study of interaction of light with matter (Cid & Bravo 2014, Knowles 1985). Light is a rapidly oscillating electromagnetic field and can disturb the distribution of charge and spins within a molecule exposed to light. With these perturbations, the electrical and magnetic properties of the molecule could change (Hof 2003). This change can be observed from the properties of the radiation that emerges from the sample. The simplest property that can be measured is the fraction of incident light absorbed by the sample. Optical absorption spectroscopy and Nuclear Magnetic Resonance (NMR) spectroscopy are solely dependent upon this measurement. Apart from this, radiation emitted by the samples at wavelengths other than that used for irradiation can also be examined which forms the basis of techniques like fluorescence, phosphorescence and Raman scattering. Moreover, techniques like fluorescence polarization and circular dichroism are dependent on the kind and degree of polarization of the emitted radiation from sample (Cantor & Schimmel 1980).

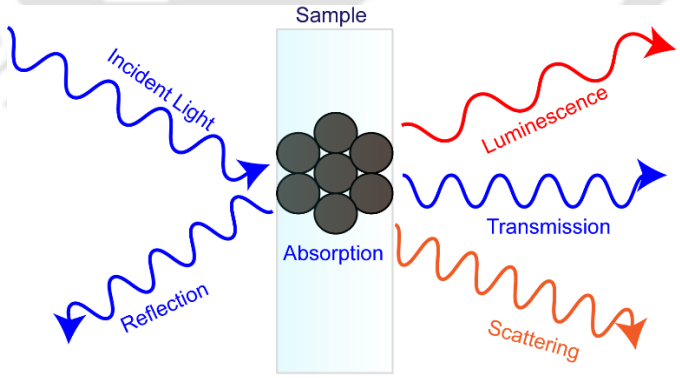

Figure 2.1: Illustration of interaction of light with matter

It is also worth noting that the energy of incident light has direct impact on the nature of perturbation caused within a molecule. For example, radiation with energy $3x10^{0}$ - $3x10^{-2}$

kcal mole^{-1} are sufficient to change the vibrational and rotational energy levels while the energy of 1x10^{2} - 50 kcal mole^{-1} can perturb the electronic energy levels. In the biological world, certain wavelengths are used to study specific aspects of molecular structure that can be detected by a particular spectroscopic technique. Table 2.1 shows the list of biologically useful spectroscopic regions and its associated techniques (Cantor & Schimmel 1980). As far as this thesis is concerned, we will be talking more about UV-Visible absorption and fluorescence spectroscopy.

Typical Wavelength (cm)	Approx. Energy (kcal mole^{-1})	Spectroscopic Region	Techniques and Applications
1 x 10^{-11}	3 x 10^{8}	γ-Ray	Mössbauer
1 x 10^{-8}	3 x 10^{5}	X-Ray	X-ray diffraction, scattering
1 x 10^{-5}	3 x 10^{2}	Vacuum UV	Electronic spectra
3 x 10^{-5}	1 x 10^{2}	Near UV	Electronic spectra
6 x 10^{-5}	5 x 10	Visible	Electronic spectra
1 x 10^{-3}	3 x 10^{0}	IR	Vibrational spectra
1 x 10^{-2}	3 x 10^{-1}	Far IR	Vibrational spectra
1 x 10^{-1}	3 x 10^{-2}	Microwave	Rotational spectra
1 x 10^{0}	3 x 10^{-3}	Microwave	Electronic paramagnetic resonance
1 x 10^{1}	3 x 10^{-4}	Radio frequency	Nuclear magnetic resonance

Table 2.1: Biologically useful spectroscopic regions. Adapted from Cantor and Schimmel 1980.

2.1.2 Absorption Spectroscopy

Absorption spectroscopy for biologists are generally concerned with the absorption of visible or ultraviolet radiation among the biomolecules. The process of absorption of a photon is extremely fast, happening in 10^{-15} s (Lakowicz 2013). The absorption of light causes perturbation in the energy levels of the molecule and molecule can be excited from the ground state to one of many rotational-vibrational energy levels of the excited electronic state, S_1 (Cantor & Schimmel 1980). Figure 2.2 shows the potential energy surfaces of two lowest electronic energy states of a simple molecule.

The energy spacing between the two electronic states S_0 and S_1 are typically 80 kcal mole^{-1} while energy spacing between the vibrational levels are ~10 kcal mole^{-1} and ~1 kcal mole^{-1}

between rotational energy levels. This implies that at room temperature, all the molecules in a solution are in the lowest electronic state, S_0 while lowest vibrational levels of S_0 and many rotational levels are populated. Owing to quantized nature of energy levels, excitation of molecules can only happen when light of frequency matching the energy gap between two energy levels is absorbed.

The total energy of the molecule is represented as the sum of the electronic, vibrational and rotational energy levels. Rotational levels are only relevant in gas phase. In condensed phases, the rotational motion is hindered and the vibrational levels are blurred.

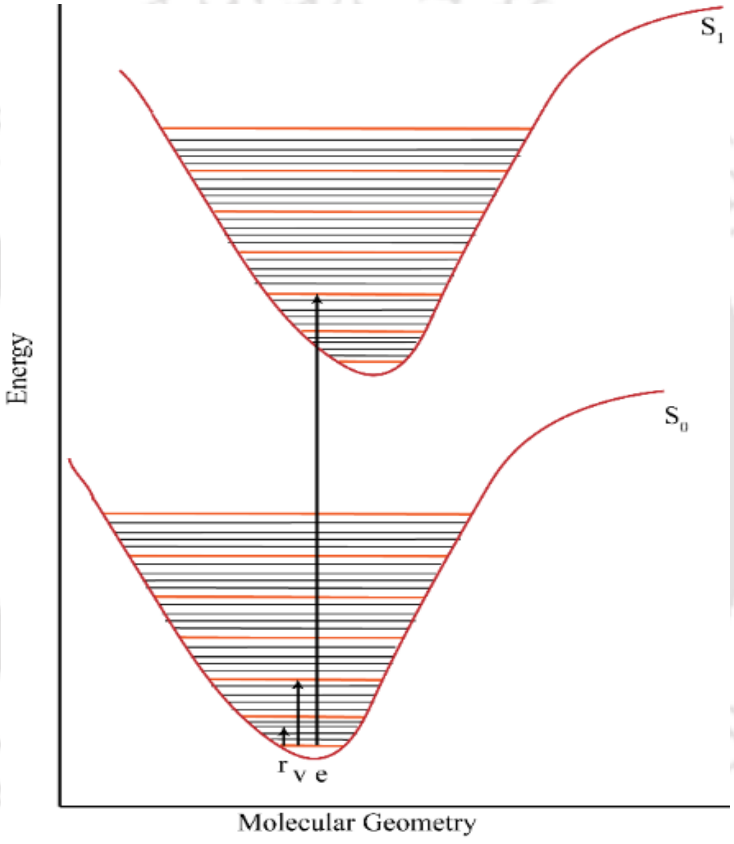

Figure 2.2: Illustration showing different energy levels and transitions between S_0 and S_1. Adapted from Cantor and Schimmel 1980. r, v and e represents the electronic, rotational and vibrational energy levels, respectively.

$$E_{total} = E_{elec} + E_{vib} + E_{rot} \quad (2.1)$$

During absorption process, the energy of the incident photon should be equal to the energy gap between the initial and final state of the molecule, given by

$$\Delta E = E_{final} - E_{initial} \quad (2.2)$$

where, $\Delta E = h\nu$ and h (Planck's constant) = 6.63×10^{-34} Js; ν = frequency of incident photon; E = energy of incident photon.

2.1.2.1 Basics of UV-Visible spectroscopy

When the light passes through the sample, the amount of light absorbed can be easily measured by a spectrophotometer. A simple schematic of a light-absorption measurement is represented in Figure 2.3.

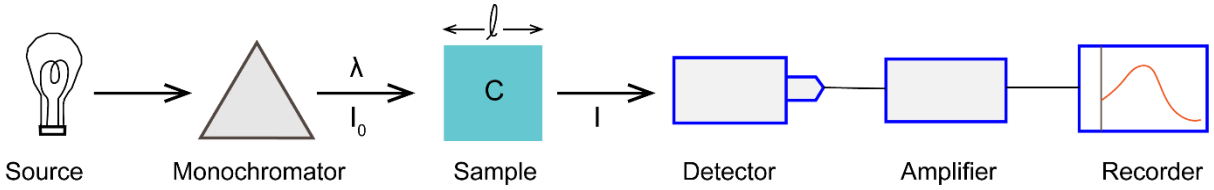

Figure 2.3: Schematics of spectroscopic experiments. Adapted from Cantor and Schimmel 1980.

When the light with intensity I_0 at wavelength λ impinges on a sample (with concentration C moles liter^{-1}) for a path length of *l* cm, a fraction of light is absorbed and rest is transmitted with intensity I. Now, for sufficiently thin layer of sample (*dl*) through which light is passing, the fraction of light absorbed (*dI/I*) should be proportional to the number of absorbing molecules. This relationship is given by

$$-\frac{dI}{I} = C\varepsilon' \, dl \tag{2.3}$$

where ε' is a proportionality constant called the molar extinction coefficient, *I* is the intensity of light of wavelength λ and *C* is the concentration of absorbing species in moles/liter. The above equation can be integrated from initial intensity (I_0) to final intensity (*I*) on the left hand side and from zero (0) to *l* on the right hand side to obtain

$$\ln (I_0/I) = C \, \varepsilon' l \tag{2.4}$$

The above equation can be converted to log base 10, as represented below

$$log \, (I_0/I) = C\varepsilon(\lambda)l = A(\lambda) \tag{2.5}$$

where $\varepsilon = \varepsilon'/2.303$ and A is called the absorbance or (sometimes) the optical density. This equation 2.5 is called the Beer-Lambert law, which states that the amount of light absorbed by the sample is proportional to the concentration of absorbing species, path length of the sample holder (cuvette) and the molar extinction coefficient.

The cross-section of absorbing molecules and extinction coefficient are inter-related. Consider a slab of solution with an area *A* (in cm^2) and a thickness *dl*. Considering the concentration of solute is *C*, the number of solute molecules per cm^3 will be $CN_0/1000$.

Therefore, the number of solute molecules in a thin slab of thickness *dl* will be $CAN_0dl/1000$. Now if the solute molecule has a radius of *r*, the fraction of cross-sectional area of the slab occupied by solute molecules is given by f_{max}, as shown in the Figure 2.4.

$$f_{\max} = (\pi r^2 \mathrm{CAN_0}\, dl/1000)/\mathrm{A}\, dl = \pi r^2 \mathrm{CN_0}/1000 \tag{2.6}$$

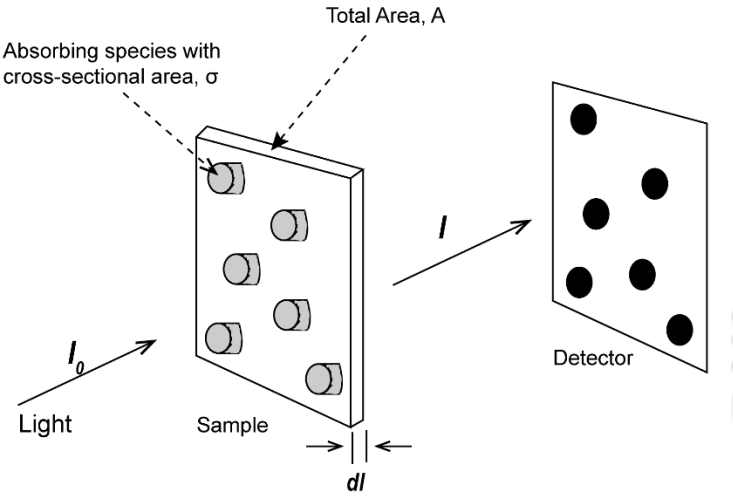

Figure 2.4: Illustration of light absorption by molecules within a very thin layer of sample. Adapted from Cantor and Schimmel 1980.

If the probability of absorption of light by the sample is P, then the fraction of light absorbed will be $f_{max}P$ and the contribution from individual molecule will be

$$\sigma = P\pi r^2 \tag{2.7}$$

Here, σ is the cross-section of the molecule. Now, the fraction of light absorbed can be written in terms of cross-section as

$$\frac{dI}{I} = (\sigma C N_0/1000)dl \tag{2.8}$$

With the above equations 2.3, 2.4 and 2.5, it can easily be shown that

$$\epsilon = (\sigma C N_0/1000)/2.303\mathrm{C} = \sigma N_0/2303 \tag{2.9}$$

which can be computed to obtain σ.

$$\sigma = 3.825 \text{ x } 10^{-21}\, \varepsilon\ (\mathrm{cm}^2) \tag{2.10}$$

The above equation derives the relationship between the molecular size and extinction coefficient. Moreover, it also states that the extinction coefficient is independent of sample concentration.

The molar extinction coefficient is related to Einstein coefficient for stimulated absorption as

$$B_{ab}=(1000c/N_0h)\int(\varepsilon'/\nu)\,d\nu \tag{2.11}$$

where N_0 is Avogadro's number, c is the velocity of the light and ν is frequency of light.

Using the equation 2.11, and converting ε' to ε, the following relationship can be obtained

$$|\langle\psi_b|\boldsymbol{\mu}|\psi_a\rangle|^2 = 9.180 \text{ x } 10^{-3}\int(\varepsilon'/\nu)\,d\nu = D_{ab} \quad (\text{debye}^2) \tag{2.12}$$

Here D_{ab} is called the dipole strength, which is a measure of the strength of transition dipole. Apart from this, another useful measure term is oscillator strength, f_{ab} which compares the intensity of absorption to that expected from a three dimensional harmonic oscillator, given by

$$f_{ab}= (8\pi^2mc/3h\nu)D_{ab}=4.315 \text{ x } 10^{-9}\int\varepsilon(\bar{\nu})d\bar{\nu} \quad (\text{dimensionless}) \tag{2.13}$$

where m is the mass of electron. For strongly allowed transitions f_{ab} are in the range of 0.1 to 1. Both the quantities, f_{ab} and D_{ab} are crucial in understanding the various special optical effects observed in polymers.

2.1.3 Fluorescence Spectroscopy

Fluorescence spectroscopy is one the major research tools used in biochemistry and biophysics. Ease of fluorescence detection and its sensitivity has made it a popular technique to be used in vastly expanding scientific research. Absorption occurs from equilibrium, so it cannot provide any information on the dynamics, while fluorescence, occurring from an out of equilibrium state can provide dynamical information at least in the nanosecond timescale (the typical fluorescence timescale). (Lakowicz 2013).

Fluorescence is a kind of luminescence. Luminescence is defined as spontaneous emission of radiation from an electronically excited species or from a vibrationally excited species which are not in thermal equilibrium with its environment (Berberan Santos & Valeur 2012). Optical transitions conserve the spin, so that if one starts from a singlet only transition towards singlet states are formally allowed. Indeed phosphorescence is a spin-forbidden transition, and for this reason its probability is very low and, accordingly, phosphorescence timescales are very long. These time scales are illustrated in Jablonski diagram (Figure 2.5).

After the light absorption, which happens in femtosecond (10^{-15} s) time scale, several processes usually occur. This includes the excitation of absorbing species/fluorophore to some higher vibrational levels of either S_1 or S_2. These excited state electrons rapidly relax to the lowest vibrational level of S_1 in a time scale of picoseconds (10^{-12} s) or less. This process is called internal conversion. The loss in energy is due to the vibrational relaxation or due to collision with solvent or other molecules. The lost energy is dissipated as heat into the solvent. This process of internal conversion is temperature dependent and increase in temperature can cause decrease in fluorescence emission. Moreover, the difference in time scale of fluorescence and internal conversion clearly points out that all the excited-state electrons are relaxed to lowest vibrational level of S_1 before commencement of any fluorescence emission.

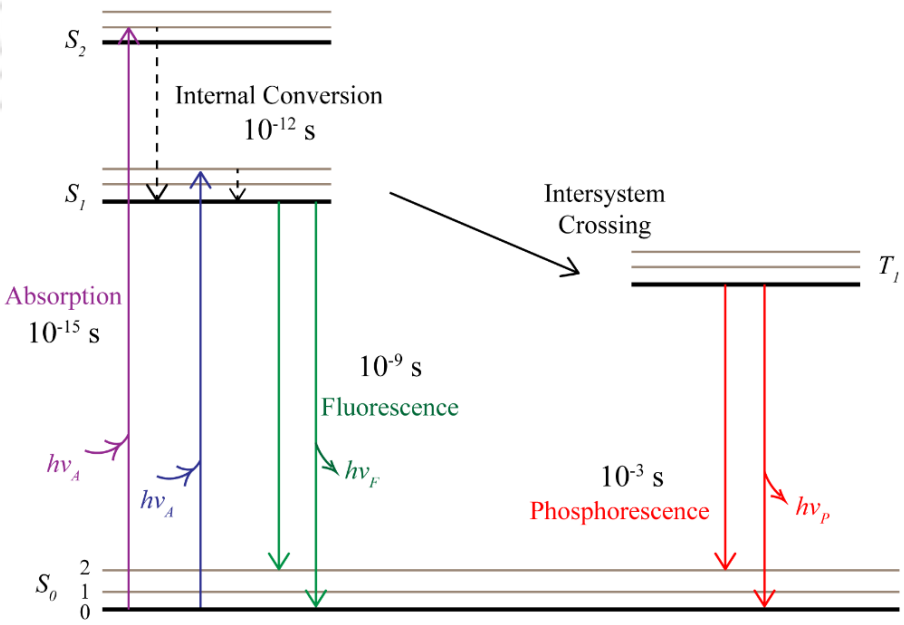

Figure 2.5: Simplified form of Jablonski diagram. Adapted from (Lakowicz 2013) with permission from Springer Nature.

The molecules in excited electronic state S_1 can also undergo a spin conversion to the first excited triplet state T_1. This process is known as intersystem crossing. The probability of intersystem crossing increases when the vibrational level of two states have overlapping energy. The heavy atoms like iodine and bromine facilitates intersystem crossing by spin orbit coupling. Transitions from T_1 to the singlet ground state is spin-forbidden, and as a result, the rate constant for triplet emissions are several orders of magnitude lower than the fluorescence. This also leads to the much longer lifetime of phosphorescence process, ~10^{-3} s. In addition, the emission from the T_1 is generally shifted to longer wavelengths as compared to fluorescence.

Apart from the intersystem crossing and internal conversion, the process of quenching also affects the rate of fluorescence emission. In general, any process that decreases the fluorescence intensity of a fluorophore is called as fluorescence quenching. Quenching can occur either by depopulating the excited state fluorophore or by forming a non-fluorescent complex with the ground state fluorophore. Different molecules like oxygen, halogens, amines and electron-deficient molecules like acrylamide can act as collisional quenchers and the process is diffusion limited. The quenching process can be represented as

$$S_b + Q \xrightarrow{k_q} S_a + Q + heat \tag{2.14}$$

where S_a is the ground state energy level and S_b is the excited state energy level of a molecule, Q is the quencher and k_q is the bimolecular quenching constant.

From the above discussions, it is obvious that these non- radiative processes (internal conversion and intersystem crossing) along with quenching, decreases the rate of fluorescence. The observed fluorescence lifetime (τ) can be defined as

$$\tau = 1/(k_r + k_{isc} + k_{ic} + k_q [Q]) \tag{2.15}$$

Here, k_r, k_{isc}, k_{ic} and k_q denotes the rate of decay of fluorescence, intersystem crossing, internal conversion and fluorescence quenching, respectively. [Q] represents the molar concentration of quencher. The above equation can be simplified by combining all the rates of non- radiative decay processes as k_{nr}.

$$\tau = 1/(k_r + k_{nr}) \tag{2.16}$$

The lifetime of the fluorophore in absence of any non-radiative process is called intrinsic or natural lifetime (τ_n), given by

$$\tau_n = 1/k_r \tag{2.17}$$

Since the fluorescence efficiency or the quantum yield (ϕ) is defined as

$$\phi = \frac{k_r}{k_r + k_{isc} + k_{ic} + k_q[Q]} = \frac{k_r}{k_r + k_{nr}} \tag{2.18}$$

The natural lifetime (τ_n) can also be calculated from the measured lifetime (τ) using equation

$$\tau_n = \tau/\phi \quad or \quad \phi = \tau/\tau_n \tag{2.19}$$

The above equation shows the relationship between the quantum yield and lifetime. According to the equation, a decrease in the quantum yield should be reflected with a decrease in fluorescence lifetime.

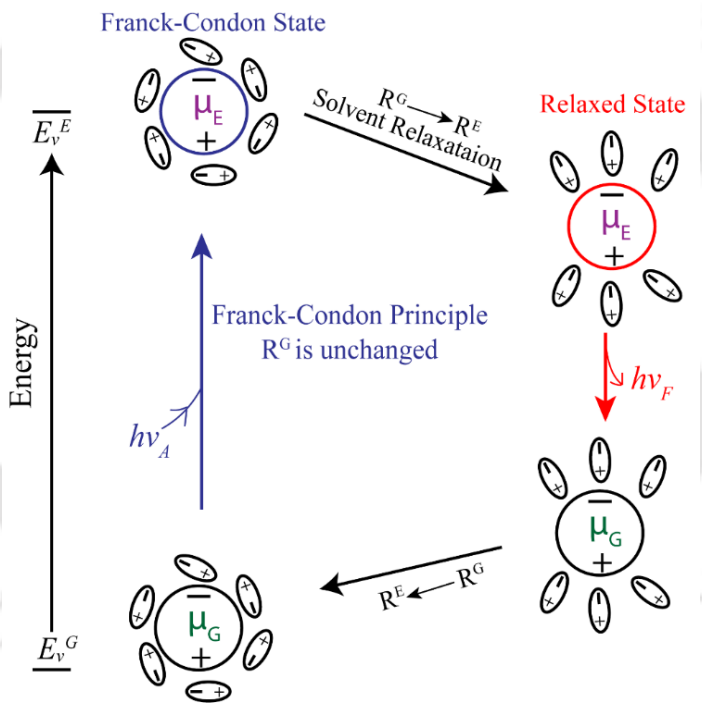

Figure 2.6: Effect of orientation reaction fields (R^G or R^E) on the energy of a dipole in a dielectric medium, $\mu_E > \mu_G$. The smaller circle represents the solvent molecules and their dipole moments. E_v represents the energy levels of fluorophores in vapor state Adapted from (Lakowicz 2013) with permission form Springer Nature.

Apart from the above listed modes of non-radiative decay, the polar solvent molecules like water can also affect the fluorescence of a chromophore. The relatively longer timescale of fluorescence allows the solvent molecules to have ample amount of time to interact and reorient around the excited-state fluorophores. Generally, the fluorophore has a larger dipole moment in excited state (μ_E) than in ground state (μ_G). Following the excitation of the

fluorophore, the solvent dipoles can reorient or relax around the excited-state dipole of fluorophore (μ_E). This reorientation or relaxation of solvent dipoles around the excited-state dipole of fluorophores, lowers the energy of excited state, as illustrated in Figure 2.6. This process is called solvent relaxation and happens in a time scale of ~1-10 ps.

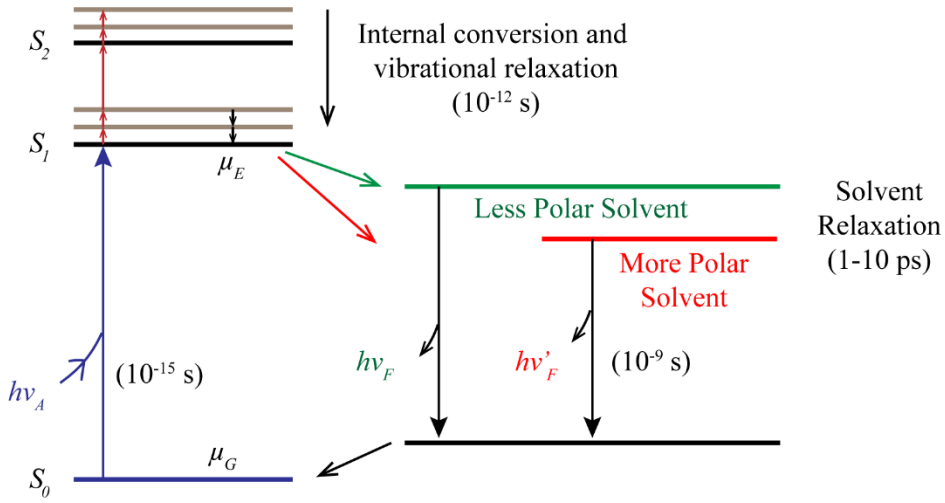

Figure 2.7: Jablonski diagram illustrating the effect of solvent relaxation on the energy of excited state. Adapted from (Lakowicz 2013) with permission from Springer Nature.

As illustrated in Figure 2.7, the lowering of the energy of the excited state, results in emissions at longer wavelengths (or at lower energies). This phenomenon of solvent relaxation results in the observed Stokes shift in the fluorescence spectra of any fluorophore. Here, the Stokes shift is the difference between the absorption maxima and the emission maxima of the fluorophore, represented as

$$Stokes\ shift, \Delta\bar{\nu} = \bar{\nu}_A - \bar{\nu}_F \qquad (cm^{-1}) \tag{2.20}$$

With an increase in solvent polarity, this effect becomes larger and can result in substantial Stokes shift. Polar fluorophores are more sensitive towards solvent polarity. The change in energy between the excited state and ground state due to solvent relaxation is described by the Lippert-Mataga equation as,

$$\bar{\nu}_A - \bar{\nu}_F = \frac{2}{hc}\left(\frac{\epsilon - 1}{2\epsilon + 1} - \frac{n^2 - 1}{2n^2 + 1}\right)\frac{(\mu_E - \mu_G)^2}{a^3} + constant \tag{2.21}$$

In the above equation h is the Plank's constant, c is the speed of light and a is the radius of the cavity in which the fluorophore resides. $\bar{\nu}_A$ and $\bar{\nu}_F$ are the wavenumber (cm^{-1}) of

absorption and emission, respectively while n is the refractive index and ϵ is the dielectric constant of the medium.

It should be noted that in Lippert-Mataga equation, the term $(\epsilon - 1/2\epsilon - 1)$ stands for the spectral shift due to redistribution of electrons in the solvent molecules as well as due to the reorientation of the solvent molecules. On the other hand, the term $(n^2 - 1/2n^2 - 1)$ accounts for only the redistribution of electrons in the solvent molecules. The difference between these two terms represents the spectral shifts due to reorientation of the solvent molecules. Hence, the difference between these two terms is also called as the orientation polarizability (Δf), i.e.

$$\Delta f = \left(\frac{\epsilon - 1}{2\epsilon + 1} - \frac{n^2 - 1}{2n^2 + 1}\right) \tag{2.22}$$

However, the constant term in the equation 2.21 accounts for the minimal losses at vibrational levels of excited state that is dissipated as heat in the solvent. This implies that even in most non-polar solvents, the absorption and emission maxima cannot coincide.

Fluorescence measurements can be done in two ways, that is either exciting the sample with a continuous beam of light or by a single short pulse of light. These two modes of excitation of fluorophores give rise to two different dimensions to the fluorescence spectroscopy, namely steady-state fluorescence and time-resolved fluorescence.

2.1.3.1: Steady-state fluorescence

In steady-state fluorescence, the sample is continuously illuminated with a continuous beam of light at particular wavelength and the fluorescence emitted by the fluorophores are detected as a function of wavelength. Here, the population of ground state molecules are in equilibrium with the excited state molecules. This kind of measurements provides time averaged parameters of fluorophores in excited state. A number of simple experiments like excitation and emission spectra, quantum yield, quenching of fluorescence, Förster Resonance Energy Transfer (FRET), steady state anisotropy and many more can be done using this methodology. Moreover, the variation in fluorescence intensity and emission maxima can provide valuable information about the solvent exposure and degree of polarity around the fluorophore. These information are quite relevant for the studies of many biological phenomena like protein folding/structural transitions.

2.1.3.2: Steady-state fluorescence anisotropy

In fluorescence anisotropy, the fluorophores are excited with vertically polarized light (along Ƶ axis) and the extent of polarization of the emission is described in terms of anisotropy (*r*). When a sample is excited with polarized light, the molecules with absorption transition dipole nearly parallel to the electric vector of the polarized light have the maximum probability of excitation. The probability of absorption is actually proportional to the $\cos^2\theta$, where θ is the angle between the absorption dipole and the electric vector of excitation light. This process is called the photoselection, which causes the population in excited state to be partially oriented. The depolarization of excited state fluorophores can happen due to rotational diffusion and this extent of depolarization is actually measured. The anisotropy of very fast tumbling molecules are close to zero. The schematic of fluorescence measurement is shown in Figure 2.8. The anisotropy is given by

$$r_{ss} = \frac{I_{VV} - GI_{VH}}{I_{VV} + 2GI_{VH}} \tag{2.23}$$

where G is known as geometric factor and defined as the ratio of monochromator and detector sensitivity to the intensity of vertically (S_V) and horizontally (S_H) polarized light. G factor is expressed as

$$G = \frac{S_V}{S_H} \tag{2.24}$$

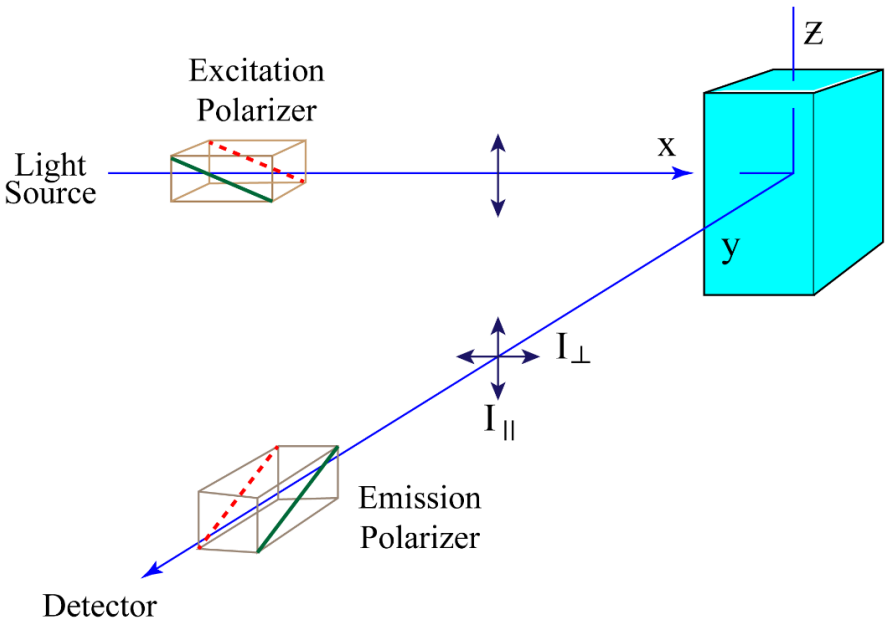

Figure 2.8: Illustration showing the schematic of fluorescence anisotropy measurement. Adapted from (Lakowicz 2013) with permission from Springer Nature.

Since the phenomena of depolarization of excited state fluorophore happens in the time period when the fluorophore is in excited state, the steady state anisotropy (r_{ss}) can also be defined as the average of anisotropy decay time over the intensity decay of the fluorophore. That is

$$r_{ss} = \frac{\int_0^\infty r(t)I(t)dt}{\int_0^\infty I(t)dt} \tag{2.25}$$

Anisotropy is a dimensionless quantity, which is independent of the total intensity of the sample. It reveals the information about the overall rotational motion, shape and size of the molecule. It can also be utilized to study protein-protein and protein-ligand interactions, protein aggregation, and protein folding and membrane fluidity. It should be noted that the anisotropy measurements should be carried out in dilute non-viscous media to avoid artefacts arising from scattering and energy transfer.

2.1.3.3: Time-resolved fluorescence

In time-resolved fluorescence, sample is excited with an ultrashort pulse of light and the resulting decay of fluorescence intensity is analyzed as a function of time. There are two methods of measuring the time-resolved fluorescence; the time-domain and frequency domain methods. Time-domain is also called the pulse fluorometry in which the samples are excited with a pulse of light with ultra-short duration. On the other hand, in frequency-domain or pulse-modulation method, the samples are excited with intensity modulated light, typically sine-wave modulation.

In time-domain fluorescence, the width of the excitation pulse is made as short as possible, and is preferably much shorter than the decay time (τ) of the sample. Generally, the pulse-width are in the rage of sub-nanoseconds to picoseconds. Following the excitation pulse, the decay time (τ) is calculated from the slope of the plot of log *I(t)* versus *t*, or from the time at which the intensity decreases to 1/*e* of the intensity at $t = 0$. The intensity decays are often measured through a polarizer oriented at 54.7° (illustrated in Figure 2.9) from the vertical *z*-axis to avoid the effects of rotational diffusion or anisotropy on the measured intensity decay.

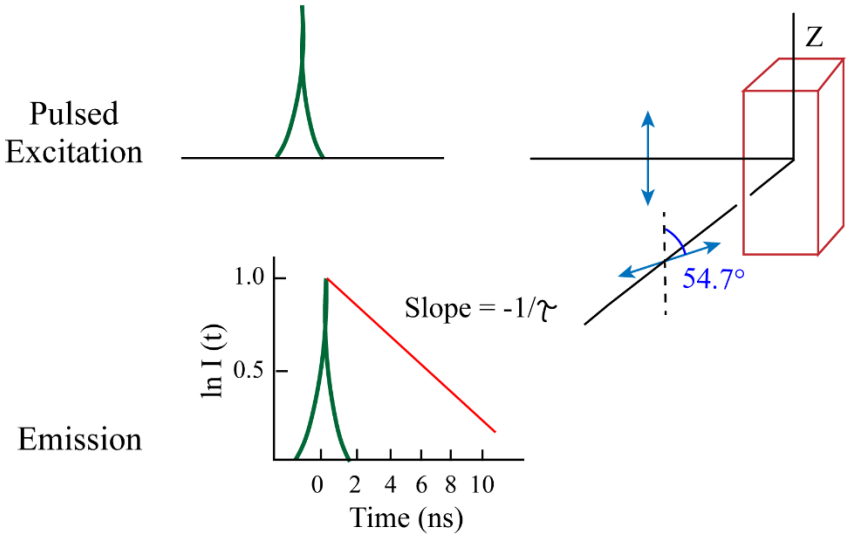

Figure 2.9: Illustration of time-domain lifetime measurement. Adapted from (Lakowicz 2013) with permission from Springer Nature.

Most commonly, time-domain measurements are performed using time-correlated single-photon counting (TCSPC) technique. Electronic schematic of TCSPC is represented in Figure 2.10. As discussed above, the samples are excited with a short pulse of light to observe numerous photons from many excited fluorophores but the TCSPC conditions are adjusted to observe less than one photon per pulse of excitation. This is achieved by deliberately keeping the fluorescence count rate at <1% of pulse repetition rate. A constant fraction discriminator (CFD) which precisely measures the arrival time of each excitation pulse is used. With the arrival of the excitation pulse, CFD sends a START signal to the time-to-amplitude converter (TAC), which generates a voltage ramp (voltage that increases linearly with time on the nanosecond timescale). Another CFD placed on the side of emission precisely determines the arrival time of pulse from the first detected fluorescence photon, which sends STOP signal to TAC to stop the voltage ramp. With this time delay (Δt) between the start and stop signal from CFDs, TAC now contains a voltage proportional to the time delay (Δt) between the excitation and emission signals. This voltage is amplified by the programmable gain amplifier (PGA) which is then converted to a numerical value by the analog-to-digital converter (ADC). A checkpoint is provided by the window discriminator (WD) to minimize false readings by suppressing the voltage signals that are out of the given range of voltages. The digital values from ADC are stored as a single event with the measured time delay. By repeating this process numerous times, a histogram of photon arrival times is generated representing the real time intensity decay of the sample.

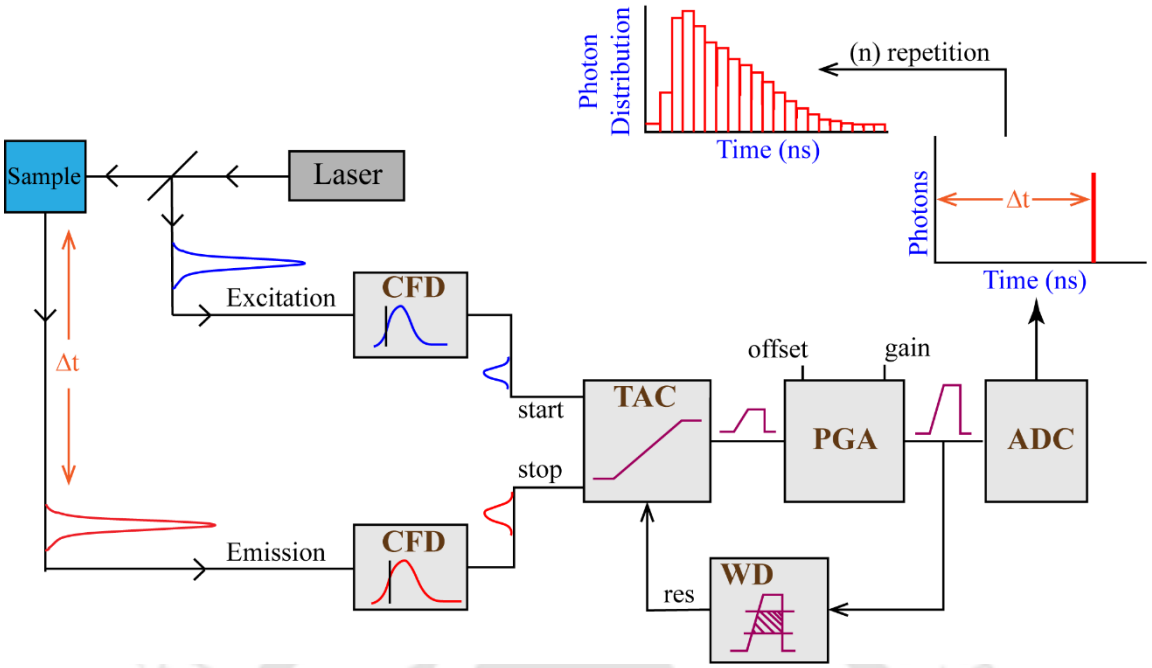

Figure 2.10: Schematic of electronics of TCSPC. Adapted from (Lakowicz 2013) with permission from Springer Nature.

As suggested by equation 2.16, the fluorescence lifetime can be written in terms of excited state population decay as

$$\frac{dn(t)}{dt} = -(k_r + k_{nr})n(t) \tag{2.26}$$

where *n(t)* is the number of excited state molecules at time t following excitation, k_r is the emissive rate and k_{nr} is the non-radiative decay rate. Since, emission is a random event and each excited state fluorophore has the same probability of emitting in a given time. The decay of the excited state population is exponential in nature and is represented by equation

$$n(t) = n_0 \exp(-t/\tau) \tag{2.27}$$

The above expression can be written in terms of fluorescence intensity because it is the intensity which is observed during experiments rather than the number of excited molecules:

$$I(t) = I_0 \exp(-t/\tau) \tag{2.28}$$

In the above equation, I_0 is the intensity at $t = 0$. The fluorescence lifetime is an average time a fluorophore remains in the excited state before emission of a photon. This average time <*t*> can be calculated by averaging the time t over the intensity decay of the sample:

$$< t >= \frac{\int_0^\infty tI(t)dt}{\int_0^\infty I(t)dt} = \frac{\int_0^\infty t\ exp(-t/\tau)dt}{\int_0^\infty exp(-t/\tau)dt} \tag{2.29}$$

The above equation can be solved to get $< t >= \tau^2/\tau$. This implies that for the single exponential decay the average time of fluorophore in excited state is equal to its lifetime:

$$< t >= \tau \tag{2.30}$$

For multi exponential decay, as seen for fluorophores present in different environments or due to presence of more than one fluorophore, the time dependent intensity can be expressed as

$$I(t) = \sum_{i=1}^{n} \alpha_i \exp(-t/\tau_i) \qquad n = 1, 2, 3 \tag{2.31}$$

where $\sum_i \alpha_i$ is normalized to unity and τ_i and α_i represents the i^{th} fractional lifetime and i^{th} fractional amplitude, respectively. The calculated mean lifetime of the fluorophore is proportional to the area under the intensity decay curve. The mean lifetime τ_m can be expressed as:

$$\tau_m = \sum_{i=1}^{n} \alpha_i \tau_i \qquad n = 1, 2, 3 \tag{2.32}$$

The relationship between the decay time and the steady-state intensity (I_{ss}) can be described as:

$$I_{ss} = \int_0^\infty I_0\ e^{-t/\tau}\ dt = I_0\tau \tag{2.33}$$

The fluorescence lifetime measurement has several advantages over the steady state fluorescence measurements. Unlike the steady-state, time-resolved fluorescence lifetime is independent of the fluorophore concentration, can distinguish between the static and dynamic quenching and most importantly it can provide crucial information upon the immediate micro-environment around the fluorophore.

2.1.3.4: Analysis of time-resolved fluorescence intensity decay

The information collected from the TCSPC is quite complex, as the lifetime and amplitude parameters cannot be extracted by simple graphical methods. At a first glance, the data from a time-resolved decay can be observed to consist of three different curves. First, the measured data, $N(t_k)$, the instrument response function (IRF), $L(t_k)$ and the calculated or fitted decay, $N_c(t_k)$. These functions are in term of discrete times (t_k) because the photons are collected in channels of known time (t_k) and width (Δt).

The IRF, $L(t_k)$ is the response of the instrument to the non-fluorescent sample or zero lifetime sample. It is collected using a dilute scattering solution like colloidal silica (Ludox) in absence of any emission filters. This decay represents the shortest time profile that can be measured by the instrument. The width of the IRF is due to the combination of the characteristics of the detector like transit-time spread and the timing electronics. Moreover, the measured intensity decay, $N(t_k)$ is a convolution of the IRF, $L(t_k)$ with actual intensity decay of the sample, $N_c(t_k)$.

The concept of convolution can be understood by assuming that the excitation pulses are a series of δ-functions with different amplitudes and each of these δ-functions excites an impulse response from the sample, with an intensity proportional to the height of the δ-function. This can be represented as

$$I_k(t) = L(t_k)I(t - t_k)\Delta t \qquad (t > t_k) \tag{2.34}$$

The above equation shows that the impulse response function excited at time t_k is proportional to the excitation intensity $L(t_k)$ occurring at the same moment. Since the impulse response started at $t_k = t$ and there is no emission from $I(t_k)$ before excitation, the term $(t - t_k)$ is utilized in the above equation. Now the measured intensity, $N(t_k)$ can be represented as the sum of all the impulse responses created by all the individual δ-function excitation pulses occurring till t_k.

$$N(t_k) = \sum_{t=0}^{t=t_k} L(t_k) I(t - t_k) \Delta t \tag{2.35}$$

For small value of Δt, the above equation can be expressed as an integral:

$$N(t) = \int_0^t L(t') I(t - t') dt' \tag{2.36}$$

According to the above equation, the experimentally measured intensity at time t is given by the sum of the intensities expected for all the δ-function excitation pulses occurring till time t. It should be noted that as long as there is non-zero intensity in $L(t_k)$ the new intensity decays are created in the sample. Because of this obvious reason, the intensity decay takes on the shape of IRF. This means the measured intensity decay, $N(t_k)$ contains significant contribution from IRF which has to be deconvoluted to determine the actual lifetime of the sample.

There are several methods to analyze the TCSPC data. These include non-linear least squares (NLLS), maximum entropy method (MEM), method-of-moments, Laplace transformation, phase plane method, and many more. Among all these, Marquardt's algorithm based NLLS method (Bevington et al 1993) is widely utilized to analyze the multi-exponential decay.

The least-square analysis starts with a model that is expected to be the best representation of the data. The goal is to obtain the parameter values for the model that provide the best match between the measured data, $N(t_k)$ and the calculated decay, $N_c(t_k)$, using assumed parameter values. This is accomplished by minimizing the goodness-of-fit parameter, χ^2 given by

$$\chi^2 = \sum_{k=1}^{n} \frac{1}{\sigma_k^2} [N(t_k) - N_c(t_k)]^2 = \sum_{k=1}^{n} \frac{[N(t_k) - N_c(t_k)]^2}{N(t_k)} \tag{2.37}$$

In the above expression, σ_k is the standard deviation at each data point and n is the total number of channels used for the analysis. Since, χ^2 depends upon the number of data points, it is not convenient to interpret. For this reason, the value of reduced χ^2 is utilized which can be expressed as:

$$\chi_R^2 = \frac{\chi^2}{n-p} = \frac{\chi^2}{v} \tag{2.38}$$

where n is the number of data points, p is the number of floating parameters and $v = n - p$ is the number of degrees of freedom.

The value of χ_R^2 is used to determine the goodness of fit. A value closer to unity shows a close match between the calculated and experimental decay data. When the selected model does not fit the data, the value of χ_R^2 is significantly greater than one. In the case of mismatch, new set of parameters are selected by modifying the older parameters. This process of matching and reconvolution is repeated iteratively until the value of χ_R^2 does not change significantly any further. Thus, this operation is termed as iterative reconvolution.

Apart from the χ_R^2, another parameter called the distribution of residuals or the deviation plots (D_k), also determine the quality of the fit. The deviation (D_k), is the difference between the measured and the calculated data, expressed as

$$D_k = \frac{I(t_k) - I_c(t_k)}{\sqrt{I(t_k)}} \tag{2.39}$$

The goodness of the fit can be judged by visually inspecting the randomness of residual distribution around zero whereas a badly fitted data would show some distinct pattern in the distribution of residuals.

The non-linear least square analysis assumes a model the decay should fit prior to analysis. In other words, it compels the data to fit in that very model. Therefore, a method of analysis that does not require the assumption of specific model would be more appropriate. This could be done with Maximum Entropy Method (MEM) analysis (Livesey & Brochon 1987). MEM is a model free system where all possible lifetimes in a given range of 0.01 ns to 20 ns or so have equal probability. The initial assumed distribution plot of probability or the amplitude versus lifetime is flat. After the analysis is completed, the flat distribution is transformed into structured distribution that adequately fits the experimental decay data.

In this case, each iteration is attempted to achieve a distribution of lifetimes by minimizing the χ^2 and maximizing the entropy, S (known as Shannon-Jaynes Entropy) given by:

$$S = \sum_i -p_i \log p_i \tag{2.40}$$

where, p_i is the probability (amplitude) for the i^{th} lifetime. All lifetimes in the distribution are assigned an equal amplitude (0.001) in the beginning. Among many possible distributions of p_i for a given value of χ^2, MEM gives the distribution for which entropy, S is maximum. Here, χ^2 is given by:

$$\chi^2 = \frac{\left(1/m\right) \sum_{i=1}^{m} [F_c(t_i) - F_e(t_i)]^2}{F_e\,(t_i)} \tag{2.41}$$

where, m is the number of data points and $F_c(t_i)$ and $F_e(t_i)$ are the calculated and experimental luminescence intensity, respectively at time t_i.

Here the goodness of fit is determined by the value of obtained reduced chi square (χ^2) value as well as the increased entropy value.

MEM is advantageous because it provides smooth α(τ) spectra that have enough detail to reveal the shape of the distribution. Moreover, it does not introduce α(τ) components unless they are needed to fit the data. A detailed explanation of the MEM analysis is provided elsewhere (Swaminathan et al 1994a, Swaminathan & Periasamy 1996, Swaminathan et al 1994b).

2.1.3.5: Fluorescence quenching

As discussed earlier, the fluorescence quenching is any process that decreases the fluorescence intensity of the sample. Quenching of a fluorophore can occur due to different molecular interactions like, excited-state reactions, molecular rearrangements, energy transfer, ground-state complex formation or collisional quenching. Therefore, quenching can be studied both as fundamental phenomenon and more importantly as a source of information about biochemical systems. Fluorescence of quenching can be categorized into two types depending upon the state (ground or excited) of fluorophore with which the quencher interacts: a) Static quenching, and b) Dynamic quenching.

2.1.3.5.1: Static quenching

Static quenching occurs because of the formation of non-fluorescent ground-state complex between the fluorophore and quencher. With absorption of light, this complex immediately returns to the ground state without emission of any photon. Therefore, static quenching eventually lead to the decrease in the concentration of fluorophore undergoing excitation.

This results in the decrease in the fluorescence intensity. Schematic representation of static quenching is represented below:

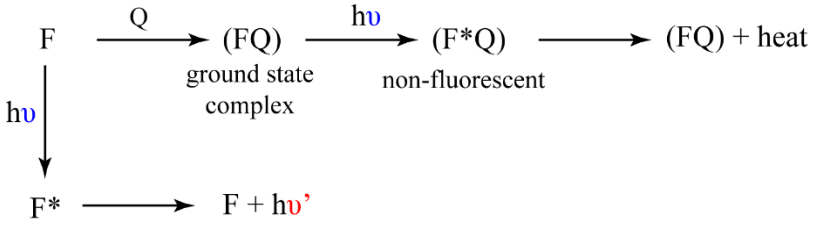

Here, F represents the fluorophore. Q represents the quencher and (FQ) represents the non-fluorescent ground state complex between the ground-state fluorophore and the quencher.

The static quenching is described by the given equation given below:

$$\frac{F_0}{F} = 1 + K_S[Q] \tag{2.42}$$

where, F_0 and F are the fluorescence intensity in absence and presence of quencher, respectively. K_s is the association constant for the non-fluorescent complex formation between the fluorophore and quencher; [Q] is the concentration of quencher in moles/liter.

However, the fluorophores present in free form exhibits normal excited state properties and normal fluorescence upon excitation. Hence, the lifetime of the fluorophore remains unchanged, that is $\tau_0/\tau = 1$, where τ is lifetime of fluorophore in presence of quencher and τ_0 is the lifetime of fluorophore in absence of quencher.

2.1.3.5.2: Dynamic or collisional quenching

Dynamic quenching of the fluorophore happens whenever a quencher collides with an excited state fluorophore. This collision causes the decrease in the lifetime of fluorophore by enhancing the decay of excited-state fluorophore. Therefore, $\tau_0/\tau > 1$, where τ and τ_0 are the lifetime of fluorophore in presence and absence of quencher, respectively. The energy of the excited state fluorophore is released as heat. Schematic representation of dynamic quenching is represented below:

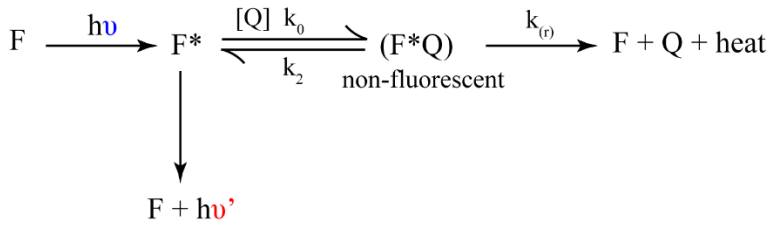

In the above scheme, k_0 is the bimolecular rate constant for the formation of *(F-Q)**. k_2 represents the rate constant for the dissociation of *(F-Q)** into *F** and *Q* while $k_{(r)}$ denotes the rate constant of decay of *(F-Q)** into *F* and *Q*. Therefore, the efficiency of quenching, E_Q can be expressed as:

$$E_Q = \frac{k_{(r)}}{k_2 + k_{(r)}} \tag{2.43}$$

The dynamic quenching is described by the Stern-Volmer equation as

$$\frac{F_0}{F} = 1 + K_{SV}[Q] = 1 + k_q \tau_0 [Q] \tag{2.44}$$

Here, F_0 and F are the fluorescence intensity in absence and presence of quencher, respectively. k_q is the bimolecular quenching rate constant, K_{SV} is the Stern-Volmer quenching constant, τ_0 is the lifetime of fluorophore in absence of quencher and *[Q]* is the concentration of quencher in moles/liter. Since, for dynamic quenching $\tau_0/\tau = F_0/F$, the above equation can also be written as

$$\frac{\tau_0}{\tau} = 1 + k_q \tau_0 [Q] \tag{2.45}$$

In the Stern-Volmer plot, k_q, bimolecular quenching rate constant describes the efficiency of quenching. For a diffusion controlled quenching, the value of k_q around 1×10^{10} $M^{-1}s^{-1}$ shows the maximum possible value of k_q in the solution. In addition, values smaller than this could result from the steric shielding of the fluorophore or a low quenching efficiency.

2.2 Materials:

Chemicals and reagents: Glycine (50046), L-Lysine monohydrochloride (L5626), L-Lysine (L5501), L-Glutamic acid monosodium salt (G1626), 1, 4-Dithiothreitol (D0632), Folin & Ciocalteu's phenol reagent (F9252), Guanidine hydrochloride (G3272), Thioflavin T (T3516), N-acetyl tryptophan amide (A6501), Hen Egg White Lysozyme (L6876), Human Serum Albumin (A1653), Bovine Serum Albumin (A3059), N-Acetyl-L-lysine methyl ester hydrochloride (859095) and N-Acetyl-L-glutamic acid (855642) were purchased form Sigma Aldrich Chemicals Pvt. Ltd., Bangalore, India. Dimethyl sulphoxide (61857), Citric

acid monohydrate (100244), Sodium acetate (17952), Potassium chloride (17792), Potassium iodide (17512), di-Sodium hydrogen phosphate (17549), Sodium di-hydrogen phosphate (93624), Dimethylformamide (17754) and Cyclohexane (1028220500) were all purchased from Merck India limited. 5-(Dimethylamino)naphthalene-1-sulfonyl chloride (D23) was purchased from Invitrogen, Molecular Probes, USA. PD-10 desalting columns (17-0851-01) were purchased from GE Healthcare. All the chemicals used were of analytical grade with purity ≥98 %.

Amino acid sequences of all the proteins used under this study is provided in Figure 2.11. The UniProt ID of Human c-Myc PEST region (residues 201-268) is P01106 while for Human Serum Albumin (HuSA), α-Synuclein and Hen Egg White Lysozyme (HEWL) are Q56G89, P37840 and P00698, respectively.

[A] PEST M1 (78 amino acids)

MDSSSPKSCA SQDSSAFSPS SDSLLSSTES SPQGSPEVL LHEETPPTTS SDSEEEQEDE
EEIDVVSVEW LEHHHHHH

[B] PEST wt (77 amino acids)

MDSSSPKSCA SQDSSAFSPS SDSLLSSTES SPQGSPEVL LHEETPPTTS SDSEEEQEDE
EEIDVVSVEL EHHHHHH

[C] α-synuclein (140 amino acids)

MDVFMKGLSK AKEGVVAAAE KTKQGVAEAA GKTKEGVLYV GSKTKEGVVH GVATVAEKTK
EQVTNVGGAV VTGVTAVAQK TVEGAGSIAA ATGFVKKDQL GKNEEGAPQE GILEDMPVDP
DNEAYEMPSE EGYQDYEPEA

[D] HuSA (585 amino acids)

DAHKSEVAHR FKDLGEENFK ALVLIAFAQY LQQCPFEDHV KLVNEVTEFA KTCVADESAE
NCDKSLHTLF GDKLCTVATL RETYGEMADC CAKQEPERNE CFLQHKDDNP NLPRLVRPEV
DVMCTAFHDN EETFLKKYLY EIARRHPYFY APELLFFAKR YKAAFTECCQ AADKAACLLP
KLDELRDEGK ASSAKQGLKC ASLQKFGERA FKAWAVARLS QRFPKAEFAE VSKLVTDLTK
VHTECCHGDL LECADDRADL AKYICENQDS ISSKLKECCE KPLLEKSHCI AEVENDEMPA
DLPSLAADFV GSKDVCKNYA EAKDVFLGMF LYEYARRHPD YSVVLLLRLA KTYETTLEKC
CAAADPHECY AKVFDEFKPL VEEPQNLIKQ NCELFEQLGE YKFQNALLVR YTKKVPQVST
PTLVEVSRNL GKVGSKCCKH PEAKRMPCAE DCLSVFLNQL CVLHEKTPVS DRVTKCCTES
LVNGRPCFSA LEVDETYVPK EFNAETFTFH ADICTLSEKE RQIKKQTALV ELVKHKPKAT
KEQLKAVMDD FAAFVEKCCK ADDKETCFAE EGKKLVAASQ AALGL

[E] HEWL (129 amino acids)

KVFGRCELAA AMKRHGLDNY RGYSLGNWVC AAKFESNFNT QATNRNTDGS TDYGILQINS
RWWCNDGRTP GSRNLCNIPC SALLSSDITA SVNCAKKIVS DGNGMNAWVA WRNRCKGTDV
QAWIRGCRL

Figure 2.11: Amino acid sequences of different proteins. Charged (blue) and aromatic amino acids (red) are highlighted in bold fonts.

Dr. Padmavathi Lolla, Center for DNA Fingerprinting and Diagnostics (CDFD), Hyderabad, did the cloning of PEST M1 and PEST wt. Both the clones were gifted to our lab by Dr. Rashna Bhandari, Laboratory of Cell Signaling, CDFD, Hyderabad. Dr. Mohd Ziauddin Ansari did the expression and purification of these two proteins in our lab. The details of which has been reported earlier (Ansari et al 2018).

Human α-synuclein was gifted by Mireille M. A. E. Claessens, University of Twente, Netherlands, in lyophilized form and was directly used for our experiments. The purification of this protein is described previously (Hoyer et al 2002).

The remaining proteins, HEWL and HuSA were procured from Sigma Aldrich, Bangalore, India, in lyophilized form. These proteins were directly used without any further processing or purification.

2.3 Methods:

2.3.1: Estimation of protein concentration

The protein concentration was estimated by the Lowry method (Hartree 1972, Lowry et al 1951) using Bovine Serum Albumin (BSA) as the standard protein. Standard curve was prepared using this protein. Different dilutions were made in the range of 0.05 mg/mL to 1 mg/mL from the 1 mg/mL stock of BSA. Stock solution was freshly prepared on the day experiment in deionized water.

0.1 mL of each of the dilutions of BSA along with each of the proteins to be measured is transferred to amber eppendorf vials. Each sample was prepared in duplicates. 1 mL of Reagent I (described in Appendix-I) was added to each vial and mixed thoroughly. Subsequently, all the samples were incubated at room temperature for 10 minutes. Then, 0.1 mL of Reagent II (described in Appendix-I) was added to each vial and incubated again for 30 minutes at room temperature. This incubation was carried out in total darkness. After this incubation period was over, absorbance of each of the sample was determined at 650 nm. For the absorbance measurements, similarly treated cocktail of Reagent I and II (without any protein) was taken as blank. The concentration of each of the protein was determined from the slope of BSA concentration versus absorbance plot.

Apart from the Lowry method, concentration of different proteins were also determined by measuring the absorbance in far-UV region. The protein concentration was determined by the equation reported by W. J. Waddell (Waddell 1956):

$$Protein\ concentration\ (\mu g/mL) = 144(A_{215} - A_{225}) \qquad (2.46)$$

Here, A_{215} and A_{225} are the absorbance values at 215 and 225 nm, respectively.

2.3.2: UV-Visible absorbance measurements

The electronic absorption spectra of all the proteins and amino acids were collected using a double beam Lambda-25 UV-Vis Spectrophotometer (Perkin Elmer, USA). The samples were scanned between the 250 nm to 800 nm with 1 nm bandwidth and a scan speed of 480 nm/min. Deionized water (Milli-Q) with resistivity of 18.2 MΩ.cm was taken as blank for background subtraction. All the samples (proteins and amino acids) were freshly prepared in deionized water and all the measurements were done at 25 °C using quartz cuvette of 10 mm path length (Hellma; Z600210). All the samples were made in triplicates and averaged absorbance values are presented. The extinction coefficient was calculated by measuring absorbance at multiple concentrations between 5—50 μM for proteins and 0.01—0.5 M for amino acids.

For measurement of linearity in absorbance with increasing concentration, among different amino acids, stock solution of 1 M L-Lysine monohydrochloride and Glutamic acid monosodium salt was freshly prepared in deionized water. For L-Lysine, 0.15 M stock solution was similarly prepared. For proteins, stock of 200 μM for HuSA, 100 μM of PEST M1 and wt and 50 μM of α-Synuclein was freshly prepared in deionized water.

For absorbance measurements done to study the effect of unfolding on the ProCharTS, the incubated HuSA samples were measured against the respective buffer blanks containing either 0, 3 or 6 M Gdn·HCl. All the solutions were buffered at pH 7.0 (50 mM phosphate buffer).

Absorption spectra for the HEWL aggregates formed at alkaline pH (12.2) were recorded after dilution in 0.1 M sodium bicarbonate buffer (pH 9.3) to keep the lysine side chain charged and protonated for ProCharTS. All the aggregated samples were centrifuged at 12,000g for 10 minutes prior to absorbance measurements to remove insoluble aggregates

that can cause scattering. For the HEWL aggregates formed at acidic pH (2 and 5), the spectra were recorded in the same buffer as for incubation.

2.3.3: Steady-state fluorescence measurements

Luminescence emission spectra for all the proteins and amino acids (Lysine·HCl, Glutamate and Lysine) were collected at different excitation wavelengths: 280, 310, 340, 355, 370 and 410 nm with slit width of 2 nm for excitation and 15 nm for emission. Emission spectra were collected between 300—550, 330—600, 360—650, 375—650, 390—650 and 430—750 nm for excitation wavelengths 280, 310, 340, 355, 370 and 410 nm, respectively. Subsequently, all the spectra were normalized to unity and plotted for comparison between various proteins and amino acids.

Excitation spectra were collected for all the samples at three different maximal intensity emission wavelengths: 425, 450 and 480 nm for excitation wavelength between 320—410, 430 and 460 nm, respectively. Excitation spectra were acquired with excitation slit width of 2 nm and emission slit width of 5 nm.

Relative luminescence yield was also measured at different excitation wavelengths between 280–500 nm for all the amino acids and proteins (proteins containing Trp are excluded for λ_{ex} 280 nm and 310 nm while proteins with Tyr are excluded for λ_{ex} 280 nm) under similar conditions.

Linearity in luminescence with increasing concentrations (up to 50 μM for proteins and up to 0.5 M for amino acids) was performed at λ_{ex} 355 nm. Spectra were similarly collected as stated above and integrated luminescence intensity was linearly fitted with increasing concentration using OriginPro 8.5 software.

Effect of unfolding of HuSA on the luminescence from charge transfer states was observed by exciting the natively folded and unfolded HuSA (in presence of 3 and 6 M Gdn-HCl) at λ_{ex} 355 nm with slit width of 2 nm and emission was collected between 375 nm to 650 nm with a slit width of 15 nm. Similarly, all the samples were also observed for the Trp fluorescence to affirm the event of unfolding. For this, samples were excited at λ_{ex} 295 nm with a slit width of 2 nm and emission was collected between 315 nm to 550 nm with a slit width of 5 nm. All the samples were buffered at pH 7.0 (50 mM phosphate buffer) to avoid any effect from mere change in pH.

Fluorescence for the Dansyl-labelled HuSA, samples were collected by exciting at 340 nm with excitation slit width of 2 nm and emission was collected between 370-650 nm with a slit width of 10 nm. For these measurements, 0.1 μM of Dansyl-HuSA was mixed with 5 and 10 μM of unlabeled HuSA (also, 1 μM of Dansyl-HuSA with 25, 50 and 100 μM of unlabeled HuSA). All these measurements were done in solution buffered at pH 7.0.

For studies upon the effect of amino acids on the fluorescence of NATA, different amino acids (either Lysine, Lysine-HCl or Glutamate) was mixed in different concentrations while keeping the concentration of NATA fixed at 20 μM. For L-Lysine, the concentration was varied between the 5 mM to 20 mM while for L-Lysine monohydrochloride and L-Glutamic acid, the concentration was varied between 50 mM to 300 mM; and 100 mM to 500 mM;, respectively. Steady-state fluorescence was collected at λ_{ex} 295 nm with slit width of 2 nm and emission was collected between 310 nm to 590 nm with a slit width of 10 nm. For determination of integrated fluorescence, integrated area under curve was collected between 320 nm to 360 nm. This range of fluorescence was selected since the bandpass filter (340±20 nm) has to be used for time-resolved measurements.

The intrinsic luminescence from HEWL aggregates (formed at pH 2 and pH 5) were observed by exciting the different day old aggregates at λ_{ex} 330 nm, 340 nm and 355 nm with excitation slit width of 2 nm and emission was collected with a slit width of 5 nm. Before the fluorescence measurements, all the samples were centrifuged at 10,000g for 10 minutes to remove any insoluble aggregates.

All spectra were acquired after applying corrections for excitation light intensity changes and detector wavelength sensitivity across the spectrum. All spectra were corrected for Raman scatter and background luminescence by subtracting the spectra of deionized water or respective buffer collected under identical conditions. Samples were always freshly dissolved in deionized water or respective buffer and all the measurements were done with 10 mm path length quartz cuvette (Hellma; Z802875) at 25 °C using FluoroMax3 (Jobin Yvon, Horiba). To acquire corrected emission spectra, data acquisition was done as S1c/R signal with an integration time of 0.1s and wavelength increment of 1 nm. The monochromator calibration was verified by cross checking the emission maxima of standard samples (N-acetyl tryptophan amide (NATA) at λ_{ex} 295 nm; Pyrene at λ_{ex} 310 nm and Fluorescein at λ_{ex} 492 nm) with the reported values.

2.3.4: Steady-state anisotropy measurements

The anisotropy of Dansyl labelled HuSA (Dansyl-HuSA) was measured at 340 nm and emission was collected at 415 nm. Excitation was done with 5 nm of slit width and emission was collected with 10 nm of slit width. The samples prepared for the measurements were similar to those described for steady-state fluorescence measurements. All the measurements were done in duplicates.

2.3.5: Stokes shift measurements

Excitation wavelength dependent changes in Stokes shift (in wavenumber units) was calculated from the emission spectra of all the samples when excited at 280, 310, 340, 355, 370 and 410 nm using the equation below

$$Stokes\ Shift\ \Delta(\bar{\nu}) = \bar{\nu}_{ex} - \bar{\nu}_{emm} \tag{2.47}$$

Here, $\bar{\nu}_{ex}$ and $\bar{\nu}_{emm}$ stands for the excitation wavelength and corresponding emission maximum, respectively (in cm^{-1}).

Similarly, the Stokes shift observed among the HEWL aggregates were also measured. Here, the samples were excited at 330, 340 and 355 nm.

2.3.6: Quantum yield measurements

Quantum yield for all the proteins and amino acids were calculated by excitation at 355 nm using the 9, 10 diphenyl anthracene (DPA) as reference (Brouwer Albert 2011). The quantum yield was calculated using equation

$$\Phi_f^i = \frac{F^i f_s n_i^2}{F^s f_i n_s^2} \Phi_f^s \tag{2.48}$$

Here Φ_f^i and Φ_f^s are the photoluminescence quantum yield of the sample and that of the standard, respectively. F^i and F^s are the integrated luminescence intensities of sample and standard spectra, respectively. f_i is the absorption factor (absorptance), the fraction of light impinging on the sample that is absorbed ($f_x = 1 - 10^{-A_x}$, where A = Absorbance). n_s and n_i are the refractive indices of the reference and the sample.

The 355 nm excitation was selected as it is close to maximal emission yield for all proteins and amino acids while being far red-shifted from intrinsic excitation bands of aromatic amino acids.

Absorbance spectra was measured as described above for all the proteins in deionized water while for the 9,10-DPA, measurement was done in cyclohexane (99%). The concentration of each sample was adjusted to match the absorbance value of reference (DPA) at 355 nm (0.01—0.03).

Similarly, luminescence spectra were measured in deionized water for all the proteins and amino acids while for 9,10-DPA (Diphenylanthracene) measurement was done in cyclohexane (99%). All the samples including standard were excited at 355 nm with a slit width of 1 nm and nearly full emission spectrum was collected between 370 - 690 nm with a slit width of 5 nm. Quantum yield calculations were corrected for difference in refractive index of cyclohexane (DPA) and aqueous samples. Integrated luminescence (area under complete emission spectrum) was calculated between 370-690 nm for all the samples for calculation of quantum yield. All the measurements were done at 25°C in triplicates and averaged. Quantum yield of different day old HEWL aggregates formed at pH 2.0 were also measured as indicated above.

2.3.7: Time-resolved fluorescence measurements

All the luminescence intensity decay measurements were done with time-correlated single photon counting (TCSPC) instrument, using DeltaPro equipped with motorized polarizer, supplied by Horiba Scientific, UK. The excitation source used were either 295 nm DeltaDiode (vertically polarized, ~810 ps FWHM Instrument Response Function (IRF); 20 MHz repetition rate) or 340 nm DeltaDiode (vertically polarized, ~800 ps FWHM IRF; 20 MHz repetition rate). Emission was collected at magic angle (54.7º) polarization to remove the artifacts of anisotropy decay from luminescence decay signals. Signal acquisition was done with a Photo Multiplier Tube (PPD-900; Horiba Scientific) subsequent to 320 nm long pass filter (Schott; WG320) or 370 nm long pass filter (KV370) for 295 nm or 340 nm excitation source, respectively. No monochromator was used as samples are weakly luminescent. IRF was collected at both excitation wavelengths using dilute suspension of finely grained chalk powder prepared freshly before the experiment.

All the samples were freshly prepared in deionized water or respective buffers and the absorbance for all the samples were kept ≤0.08 at the given excitation wavelengths to avoid inner filter effects. The luminescence intensity decay for all the samples were collected in 4096 channels with 28.38 ps/channel resolution. Peak counts collected were 15,000 for each decay and each data for sample was acquired independently 3-6 times. All measurements were done with 10 mm path length quartz cuvette (Hellma; Z802875) at 25 °C.

2.3.8: Analysis of time-resolved fluorescence data

All the luminescence intensity decay measurements were analyzed by both the discrete exponential analysis method (Swaminathan et al 1994b) and Maximum Entropy Method (MEM) (Swaminathan et al 1994a). For both analyses, software was kindly provided by Prof. N Periasamy. (Tata Institute of Fundamental Research, Mumbai, India).

For discrete analysis, observed luminescence intensity decays were analyzed by iterative reconvolution (Grinvald & Steinberg 1974). The observed decay was compared against convolution of chosen decay model (Equation 2.31) with the measured IRF. Non-linear least-squares analysis (Bevington et al 1993) was used to extract parameters (α_i and τ_i) in successive iterations for the best fit to the data. All the luminescence intensity decays were first tried with simpler model (i = 1 in Equation 2.31) before opting for higher models (i >1) to obtain adequate fit. Mean lifetime was calculated using Equation 2.32.

The number of time channels employed for the fit was chosen based on the completeness of the decay. The goodness of fit was determined by the reduced chi square (χ_R^2) value (Equation 2.38).

Goodness of fitted data was additionally ascertained by visual inspection of the randomness in residual distribution or residuals (D_k) given by Equation 2.39.

For each sample, at least three decays with adequate fits were used to determine the standard deviation in the tau (τ_i) values while the alpha (α_i) values were selected from the best fitted data.

Luminescence lifetime distributions were obtained by (MEM) maximum entropy method (Livesey & Brochon 1987). In MEM analysis, the decays were fitted to 100 exponentials with lifetime values between 0.01—20 ns, distributed uniformly in the logarithmic scale. Each iteration is attempted to achieve a distribution of lifetimes by minimizing the χ^2 and maximizing the entropy, S (known as Shannon-Jaynes Entropy) given by Equation 2.41 and

2.39, respectively. The goodness of fit was determined by the value of obtained reduced chi square (χ_R^2) value as well as the increased entropy value. At least three such fits were performed for each sample and the fits with best χ_R^2 values were selected.

2.3.9: Protein unfolding

To study the effect of protein unfolding on the ProCharTS, 25 µM of HuSA was incubated in presence of different concentrations (0, 3 and 6 M) of Gdn·HCl. DTT was avoided in these experiments because of its own absorption which could interfere with the measurements. Incubation was done at 25 °C for 36 hours. Different solutions of Guanidine·HCl were buffered at pH 7.0 (50 mM phosphate buffer). Absorbance, fluorescence and time-resolved fluorescence measurements were done as indicated in above sections. All the samples were prepared in triplicates and repeated twice.

2.3.10: Labelling of protein with Dansyl Chloride

Labelling of HuSA with Dansyl was done as described previously (Homchaudhuri et al 2006). 250 µM of HuSA was prepared in 0.1 M bicarbonate buffer (pH 9.3) and stock of 40 mM Dansyl chloride was prepared in dimethyl formamide (DMF). Labelling reaction was set by adding 25 µL from the stock of Dansyl chloride to 1 mL protein solution of above-mentioned concentration. This mixture was incubated at 4 °C for 3 hours with continuous steering. After incubation, the unlabeled dye was separated from labelled protein using PD-10 column (from GE Healthcare) pre-equilibrated with 50 mM Phosphate buffer, pH 7.0. Elution was done with 50 mM Phosphate buffer; pH 7. Protein and labelled-dye concentration was determined by measuring the absorbance values at 280 nm (for protein) and 339 nm (for dye). The extinction coefficient of HuSA at 280 nm is 35,700 $M^{-1}cm^{-1}$ (Leggio et al 2008, Pace et al 1995) while for conjugated dye the extinction coefficient at 339 nm is 3370 $M^{-1}cm^{-1}$ (Chen 1968, Levi & González Flecha 2003). The concentration of dye and protein were determined spectrophotometrically as described in upper sections. The dye per protein (D/P) ratio was determined to be around 0.59.

2.3.11: Aggregation of HEWL

A stock solution (0.4–4.5 mM) of HEWL monomer was made in deionized water. The desired concentrations of HEWL in the chosen buffer were prepared by diluting this stock. All the HEWL concentrations mentioned refer to monomer concentration only.

2.3.11.1 Aggregation at alkaline pH

HEWL (120 µM; 1 mL) was prepared in 50 mM sodium phosphate buffer (pH 12.2) and subsequently incubated at 23–25 °C without shaking for 10 days (Ravi et al 2014b). At the end of each day, an aliquot of sample was stored at 4 °C for further analysis or instantly diluted in 0.1 M bicarbonate buffer (pH 9.3), yielding 6–36 µM concentrations for absorbance measurements.

2.3.11.2 Aggregation at pH 5.0

Aggregation of HEWL (100 µM; 1 mL) was carried out in 0.1 M citrate buffer (pH 5.0), incubated at 65 °C with intermittent mixing for 5 days (Ahn et al 2016). At the end of each day aliquots of sample were stored at 4 °C for further analysis.

2.3.11.3 Aggregation at pH 2.0

Aggregation of HEWL (1.36 mM; 1 mL) was carried out in 10 mM glycine buffer (pH 2.0), incubated at 65 °C with intermittent mixing for 5 days (Chaari et al 2015, Krebs et al 2000). At the end of each day 100 µL aliquots of sample were collected and stored at 4 °C for further analysis. For collecting the absorbance and luminescence spectrum, the incubated sample was diluted to 100 µM in the same buffer.

2.3.11.4 Inhibition of HEWL aggregation

Inhibition of HEWL aggregation at alkaline pH was done in the presence of iodoacetamide as reported earlier (Ravi et al 2014a). Iodoacetamide was added at 2, 6, 12 and 24 hour time points. The final concentration of iodoacetamide after 24 hours in the incubated sample was 11.9 mM.

2.3.12: Thioflavin T Assay

For the determination of fibril formation under acidic conditions, a ThT assay was done as indicated previously, with some modifications (Ravi et al 2014a). Stock of ThT was prepared in water and subsequently filtered through 0.45 micron membrane filter. The concentration of ThT was determined by measuring the absorbance at 416 nm. The extinction coefficient of ThT at 416 nm in ethanol is 26,620 $M^{-1}cm^{-1}$ (Gade Malmos et al 2017, Ravi et al 2014a). For optimum binding of ThT to fibrils, the molar ratio of dye to fibril is kept 2:1 (Wall et al 1999). Hence, for fluorescence measurements, 10 µM of aggregated protein was mixed with 20 µM of ThT in aqueous medium buffered at pH 8.5. The sample was excited at 450 nm (slit width 1 nm) and the emission was collected between 470 nm and 550 nm (slit width 5 nm). The area under the emission spectrum was calculated between 470 nm and 550 nm after subtraction of the blank spectrum without ThT. All

fluorescence measurements were done in triplicate in a 1 mL quartz cuvette with a 10 mm path length [Hellma (Z600253)] using a Fluoromax-3 spectrofluorometer (Jobin-Yvon Horiba Inc., USA).

Chapter 3

Intrinsic luminescence from charged, non-aromatic amino acids and charged monomeric proteins

3.1 Introduction

The absorbance from the aromatic amino acids have been reported long back (Feraud et al 1935, Wetlaufer 1963) and the fluorescence signatures of aromatic amino acids in proteins are also well characterized (Demchenko 2013, Lakowicz 2013, Longworth 1971, Teale & Weber 1957). Apart from these aromatic amino acids, no other amino acid was expected to show absorption in the UV-visible region. However, in 2001 our group had reported on the novel absorption and fluorescence features of L-Lysine monohydrochloride (Homchaudhuri & Swaminathan 2001). Later other research groups also corroborated this finding (Chai et al 2008, Chen et al 2018, Ryzhkina et al 2018). The maximum absorption of Lysine·HCl was observed at ~270 nm while upon excitation at 355 nm fluorescence emission maxima was observed at ~435 nm. The reported absorption was characterized as featureless absorption spectra extending from 230 nm to all the way up to 500 nm. Similar observations were also made for the proteins rich in Lysine residues like human serum albumin, calf thymus histone and poly-L-Lysine (Homchaudhuri & Swaminathan 2004). With the similarity in absorption spectra of L-Lysine solutions and proteins rich in Lysine residues, it was speculated that such unusual absorbance spectra could originate due to inter/intra molecular interactions between the lysine residues. However, the exact chromophore could not be identified that time.

Later in 2017, using a combination of experimental and theoretical approaches upon a synthetic protein, α_3C, our group with the help of collaborators has deduced that such absorption spectra could originate due to charge transfer transitions involving the protein backbone and the charged residues in protein. Such transitions originate when charged amino/carboxylate groups in the side chains of Lys/Glu act as electronic charge acceptors/donors for photo-induced charge transfer either from/to the polypeptide backbone or to each other. The absorption spectrum originating from such charge transfer transitions was termed Protein Charge Transfer Spectra (ProCharTS). It was also revealed that the strength of these transitions are highly dependent upon the proximity of side chains of charged residues in proteins (Prasad et al 2017). α_3C is rich in charged amino acids (mainly Lys and Glu) and is devoid of any aromatic amino acid. In spite of absence of any aromatic amino acid, α_3C shows an intense ProCharTS absorption not only in the spectral region between 250-325 nm, where only aromatic amino acids are supposed to absorb but also shows an extended tail of absorption throughout the visible region until 800 nm. Further, it

was reported that apart from glutamate and lysine, other charged amino acids like, aspartate, histidine, arginine and even phosphorylated amino acids like phosphorylated-serine, threonine and tyrosine can also contribute to the charge transfer transitions (Mandal et al 2018).

Ample amount of work has been done so far (Homchaudhuri & Swaminathan 2001, Homchaudhuri & Swaminathan 2004, Prasad et al 2017) on the absorption arising from the charged amino acids. It has also been established that the ProCharTS among charged amino acids are dependent upon the pH and ionic strength of the solvent. Among all the charged amino acids, Lysine displays highest extinction coefficient (ε) at 270 nm followed by aspartate and glutamate salts (Prasad et al 2017). Apart from charged amino acids, rest of the amino acids show negligible ProCharTS.

This work was further extended to proteins rich in charged amino acids. Proteins like α_3C and intrinsically disordered proteins (IDPs) like DHN1 from *Zea mays* and PEST wt and its Trp mutant, PEST M1 from human c-Myc have been studied to reveal the effects of structural transition on the ProCharTS. Structural transitions brought about by changes in pH, ionic strength and temperature were reflected by changes in intensity of ProCharTS (Ansari et al 2018).

Apart from the absorbance studies, little work has been done upon the luminescence arising from ProCharTS. Previously, it has been observed that the concentrated solutions of L-Lysine (0.5 M) display luminescence when excited at different λ_{ex} between 290-410 nm (Homchaudhuri & Swaminathan 2004). This initial work upon the luminescence observed from charged, non-aromatic amino acid (L-Lysine) laid the foundation of this present work described in the current chapter. Here in this chapter, luminescence arising from charge transfer states among different charged, non-aromatic amino acids (Lysine, Lysine·HCl and Glutamate) are presented and discussed. Amino acids with capped amino/carboxy terminal are also studied in parallel to monitor the role of charge at N/C terminals in charge transfer transitions. Alongside the amino acids, different proteins rich in charged amino acid residues are also explored for the probable luminescence in their monomeric form. Employing steady state and time resolved fluorescence measurements; various luminescence features have been unraveled including the characteristic emission and excitation spectra, Stokes shift, quantum yield, and luminescence lifetime. Apart from this, the role of extinction coefficient is also addressed behind the origin of intrinsic luminescence from monomeric proteins.

3.2 Results and Discussions:

3.2.1 ProCharTS observed among Lysine, Lysine·HCl and Glutamate

The ProCharTS of all the above mentioned charged amino acids were observed at different concentrations ranging from 1 mM to 1 M (Figure 3.1) while for capped (N/C terminus) amino acids, ProCharTS was observed between 1-100 mM (Figure A1; Appendix II). The rise in absorbance with increasing concentrations were observed at selected multiple wavelengths and were found to be linearly related. This linear increase in the absorbance with increasing concentration negates the origin of such absorbance from any aggregate or agglomerates of amino acids.

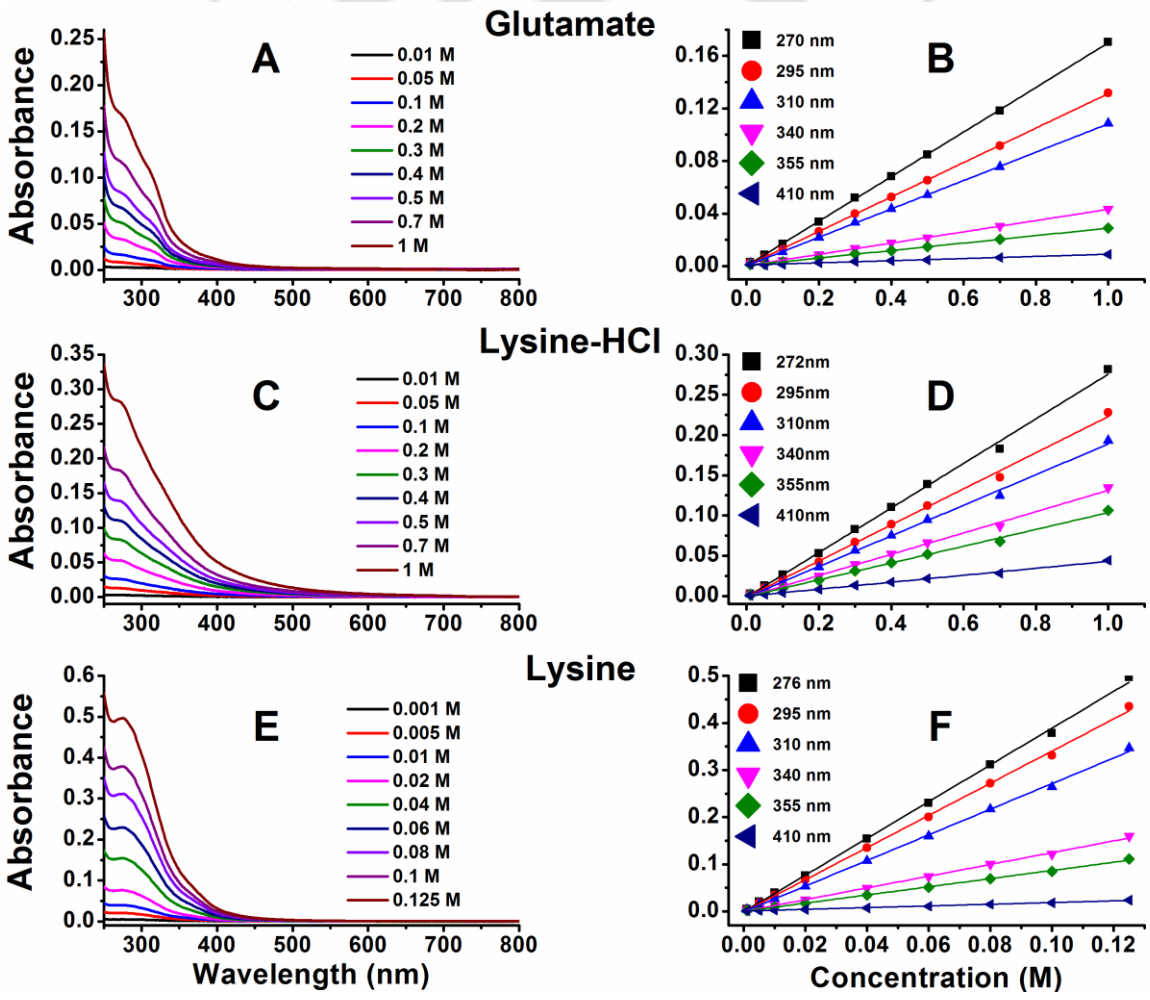

Figure 3.1: Absorption spectra for different concentrations of Glutamate, Lysine·HCl and Lysine are shown in panel **A**, **C** and **E**, respectively. Absorbance of Glutamate (**B**), Lysine·HCl (**D**) and Lysine **(F)** at selected wavelengths are plotted against different concentrations. The solid lines in panel **B**, **D** and **F** are the linear fit obtained for the rise in absorbance with increasing concentration at the given wavelengths. The following are the peak absorption wavelength values for Lysine: 276 nm, Lysine·HCl: 272 nm and Glutamate: 270 nm.

3.2.2 ProCharTS observed among amino acids are emissive in nature

All the amino acids under this study were explored for the luminescence at different excitation wavelengths ranging from 280 nm to 500 nm. To our surprise, they were found to be luminescent even at λ_{ex} 500 nm. However, the luminescence intensity at the longer excitation wavelengths are much lower than at shorter excitation wavelengths (Figure 3.2 A, C, E). Moreover, peak emission wavelengths are shifted towards red side with increasing excitation wavelengths as shown in Figure 3.2 B, D, F. Similar observations were made for the capped Lysine·HCl/Glutamic acid (Figure A2; Appendix II). The observed excitation-wavelength-dependent luminescence could be due to the presence of different charge transfer states (CT) as reported recently for photoluminescence from ligand-decorated silicon nanoparticles (SiNPs) (Shen et al 2018) or due to the presence of different emissive species that are selectively excited at different wavelengths.

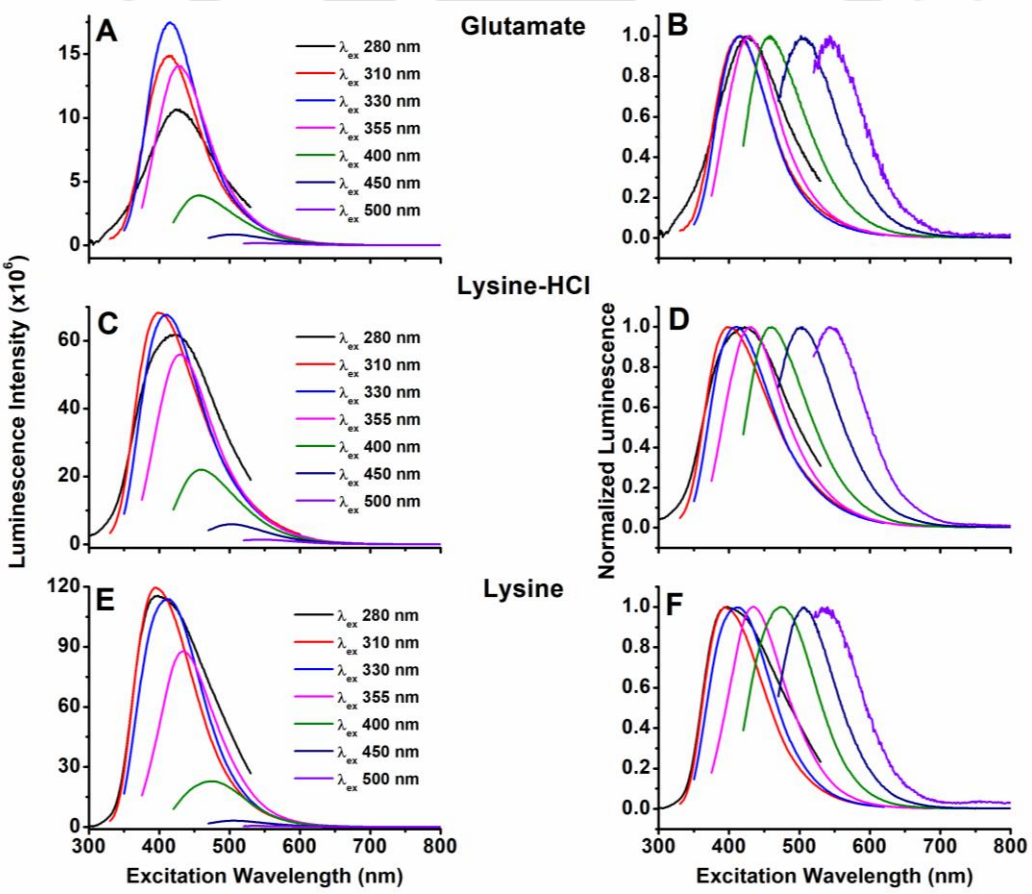

Figure 3.2: Luminescence spectra at different excitation wavelengths for Glutamate, Lysine·HCl and Lysine are shown in panel **A**, **C** and **E**, respectively. Normalized luminescence spectra of Glutamate, Lysine·HCl and Lysine are shown in **B**, **D** and **F** respectively. All the excitation were done with 2 nm slit width and emission was collected with 15 nm slit width. Concentration used were 300 mM for Lys·HCl and Glutamate while 30 mM for Lysine.

3.2.3 Luminescence from charge transfer states in amino acids mirrors the change in ProCharTS absorbance

Next, we explored the concomitant change in ProCharTS absorption to those observed for the associated luminescence. For this, the change in ionization state of Lysine·HCl was studied both by the ProCharTS absorbance and luminescence (Figure 3.3a). Similarly, the effect of ionic strength was also studied as shown in Figure 3.3b. The decrease in ProCharTS absorbance was corroborated by a decrease in luminescence in presence of 0.1 N NaOH and HCl (Figure 3.3a).

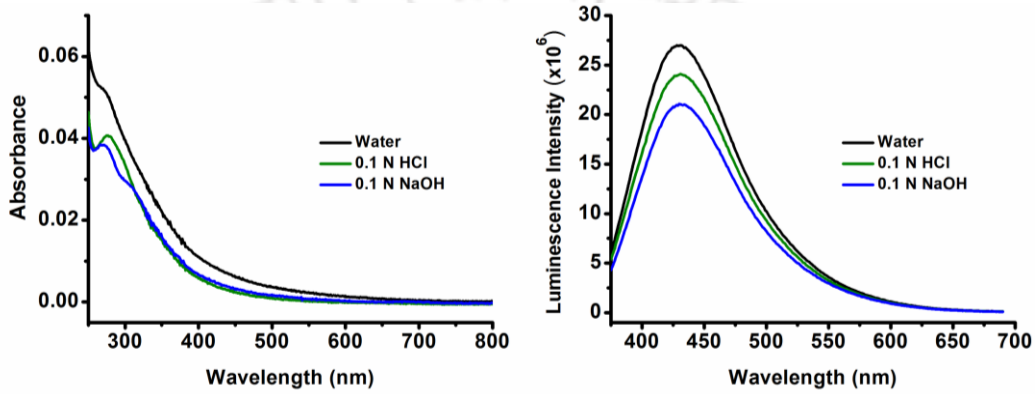

Figure 3.3a: Left panel shows the absorbance spectra of Lysine·HCl while the right panel shows the luminescence spectra for the identical samples. Concentration used was 150 mM for Lysine·HCl. For luminescence, all samples were excited at 355 nm with slit width of 2 nm and emission was collected with 15 nm of slit width.

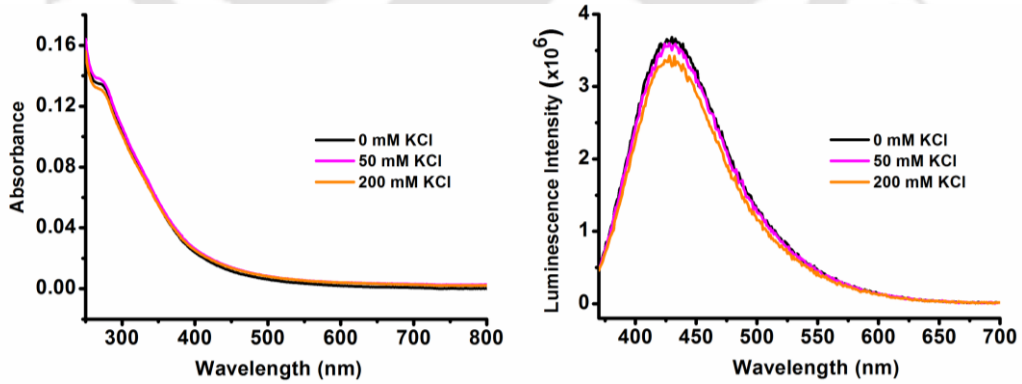

Figure 3.3b: Left panel shows the absorbance spectra of Lysine·HCl while the left panel shows the luminescence spectra for the identical samples. Concentration used were 500 mM for Lysine·HCl. For luminescence, all samples were excited at 355 nm with slit width of 1 nm and emission was collected with 3 nm of slit width.

On the other hand, with change in ionic strength almost no effect was observed in ProCharTS absorption of Lysine·HCl, which is again mirrored by luminescence spectra. Hence, for both

the cases the effect of change in solvent conditions was well reflected in both the absorbance as well as luminescence. This shows the sensitivity of both the ProCharTS absorbance and the luminescence arising from the charge transfer states towards any change in the solvent condition. Similar results were obtained for glutamate (data not shown).

3.2.4 Effect of addition of equimolar concentrations of Lysine·HCl and Glutamate

Equal concentrations of Lysine·HCl and Glutamate were mixed to determine the effect of oppositely charged amino acids on the ProCharTS absorption and luminescence. This was done at two different concentrations as shown in Figure 3.4.

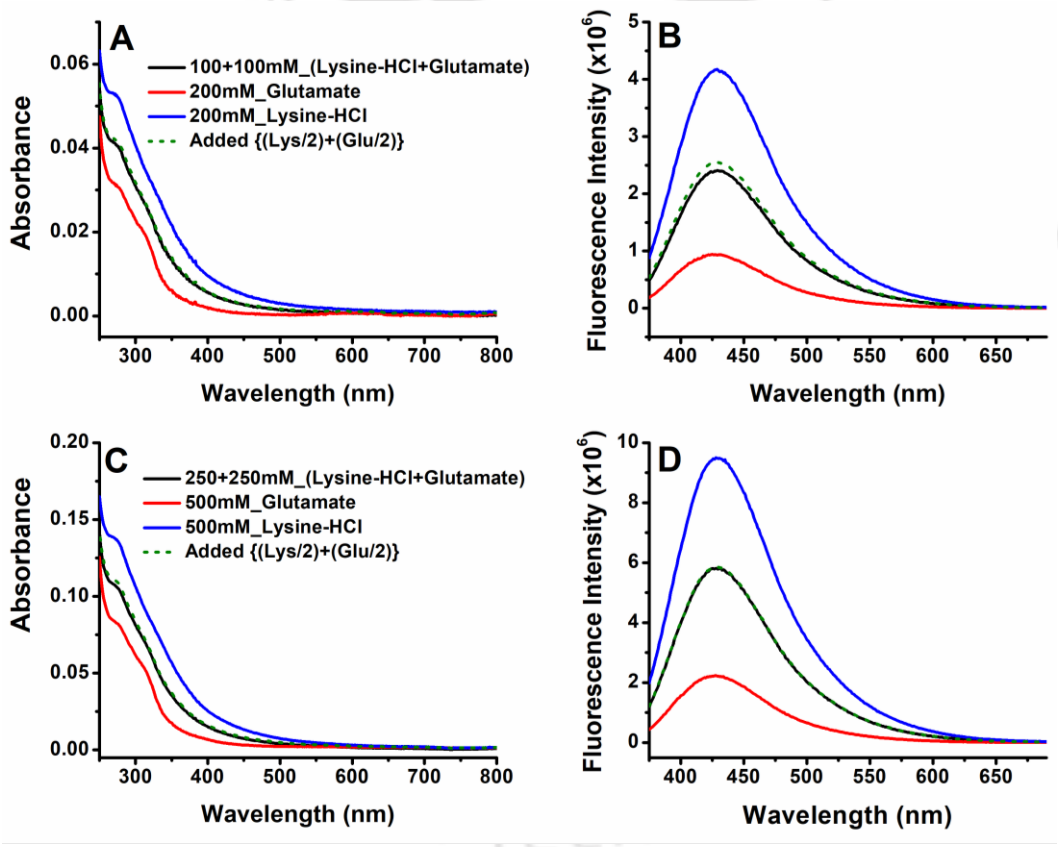

Figure 3.4: Panel **A** and **B** shows the absorbance and luminescence, respectively for the Lysine·HCl, Glutamate and 1:1 mix of Lysine·HCl and Glutamate at 200 mM. Similarly, **C** and **D** shows the ProCharTS absorbance and luminescence, respectively but at 500 mM concentrations. For luminescence (**B** and **D**) collection, samples were excited at 355 nm with 2 nm of slit width and emission was collected with 15 nm of slit width.

For both the concentrations, the manually added spectra almost overlaps the spectra obtained for the 1:1 mixture of Lysine·HCl and Glutamate. This was observed for both in ProCharTS

absorbance and luminescence. This clearly demonstrates the additive effect of the mixture and it removes suspicion of any synergistic effects.

With the above information, it is clear that the non-aromatic and charged amino acids do show luminescence properties. Apart from this mere observation, it is also evident that the luminescence from the charge transfer states are quite precise to reflect the phenomena observed by ProCharTS absorption. Moreover, luminescence being more sensitive than absorbance, it is more likely to get more meaningful and sensitive information about charge transfer transitions that would not be possible by absorption studies. Thus, it would be worth exploring this phenomenon in reference to proteins rich in charged amino acid residues. This would not only provide an insight to the luminescence features of charged, non-aromatic amino acids but also provide a clue behind the origin of intrinsic luminescence observed from monomeric proteins.

3.2.5: Selection of different proteins rich in charged residues

For the above mentioned reasons, multiple proteins were selected which are not only rich in charged amino acid residues but also belonged to different structural classes. That is, selected protein includes, natively folded protein, human serum albumin (HuSA), intrinsically disordered protein (IDP), α-Synuclein and intrinsically disordered region (IDR) of human c-Myc PEST fragments (PEST wt and its Trp mutant, PEST M1). The composition of these proteins are shown in Table 3.1 and the protein sequence is shown in section 2.2, Figure 2.11. These proteins are studied in parallel to the charged, non-aromatic amino acids (Lysine, Lysine·HCl and Glutamate) to unravel the role of charged amino acids in the origin of intrinsic luminescence from the monomeric proteins.

Protein	Nature of protein	Total amino acids	D	E	K	H	R	% of charged residues
PEST wt	IDR	77	6	13	1	7	0	35.1
PEST M1	IDR	78	6	13	1	7	0	34.6
α-Synuclein	IDP	140	6	18	15	1	0	28.6
HuSA	Folded	585	36	61	59	16	22	33.2

Table 3.1: The table displays the abundance of different charged amino acids in the selected proteins under this study.

3.2.6: Absorbance and extinction coefficient of different proteins and amino acids

Figure 3.5 shows the absorbance spectra of different proteins and amino acids selected for the study. It can be clearly seen that the amino acids have a profound absorption in the spectra region where ideally only the aromatic amino acids are considered to absorb (inset of Figure 3.5). Moreover, Trp containing proteins, HuSA & PEST M1 and Tyr containing protein, α-Synuclein shows the typical characteristic peak in the spectral region between 250 nm to 325 nm. Beyond 325 nm, where the absorbance from any aromatic amino acid is not observed, there is considerable absorbance among all the samples.

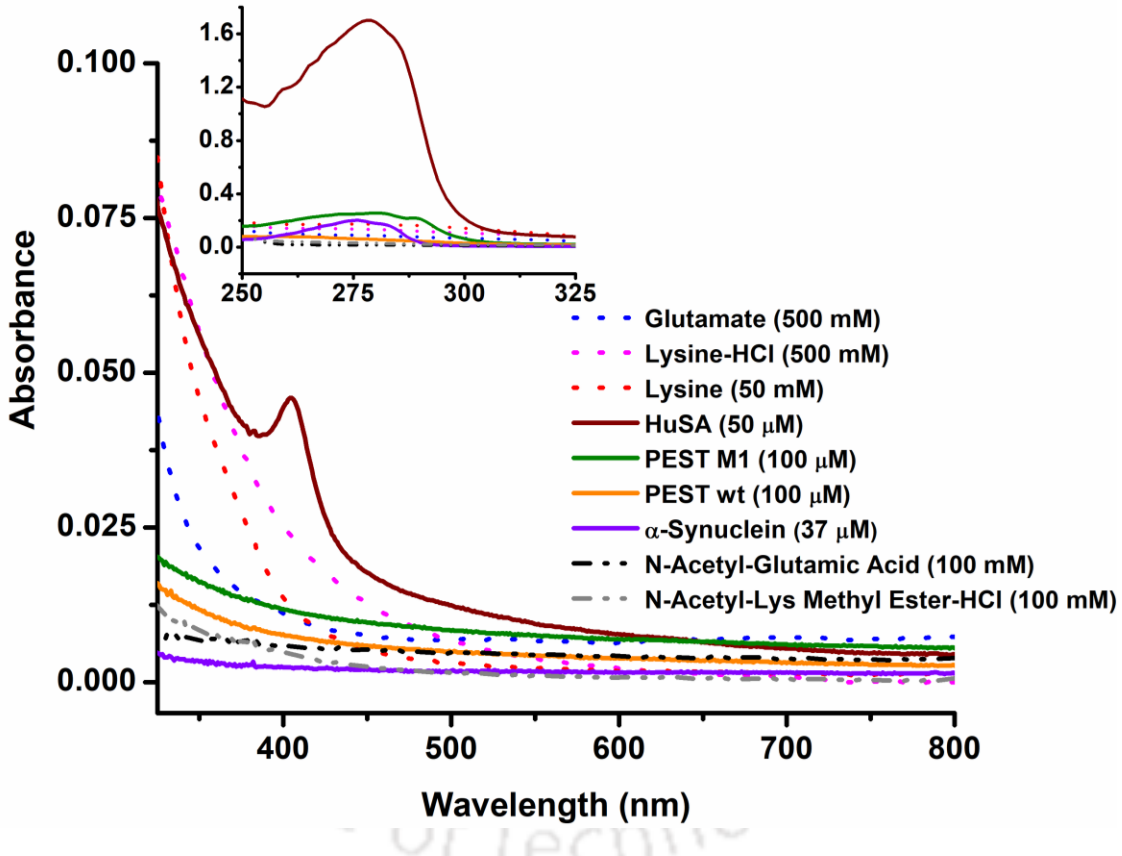

Figure 3.5: Absorbance spectra of different amino acids and proteins in the range of 325-800 nm. Inset shows the absorbance in the range of 250-325 nm. Each molecule of protein is considered as single entity for the sake of calculating protein concentration, not its constituent amino acids.

A more clear picture is provided by the extinction coefficient data for the above samples. From the Figure 3.6, it is quite clear that the extinction coefficient of amino acids are negligible as compared to proteins. This could be attributed to the spatial proximity of charged residues in proteins. In protein, the amino acids are held together by the peptide bond and within a folded structure of protein, the probability of getting one or more charged

residues in close proximity to another is maximized. This would result in higher ProCharTS transition probabilities. On the other hand, amino acids as singular entity have this probability to its minimum, resulting in much lower extinction coefficient. It should be noted that the extinction coefficient of capped-Lysine·HCl follows closely to that of Lysine·HCl. On the other hand, capped-Glutamic acid are observed to have higher extinction coefficient than that of uncapped Glutamate (monosodium salt of glutamic acid), as suggested previously (Prasad et al 2017). However, similar extinction coefficient of capped and un-capped Lysine·HCl signifies that the charge at the amino/carboxyl terminals of amino acids has little or no role in ProCharTS, while the charge on the side chains are the key player in charge transfer transitions.

As suggested above, the extinction coefficient of the natively folded protein, HuSA is maximum followed by the IDRs (PEST M1 and PEST wt) and IDP, α-Synuclein. Higher values of extinction coefficient for PEST M1 and wt compared to α-Synuclein can be credited to the higher content of charged residues, ~35 % versus ~28%.

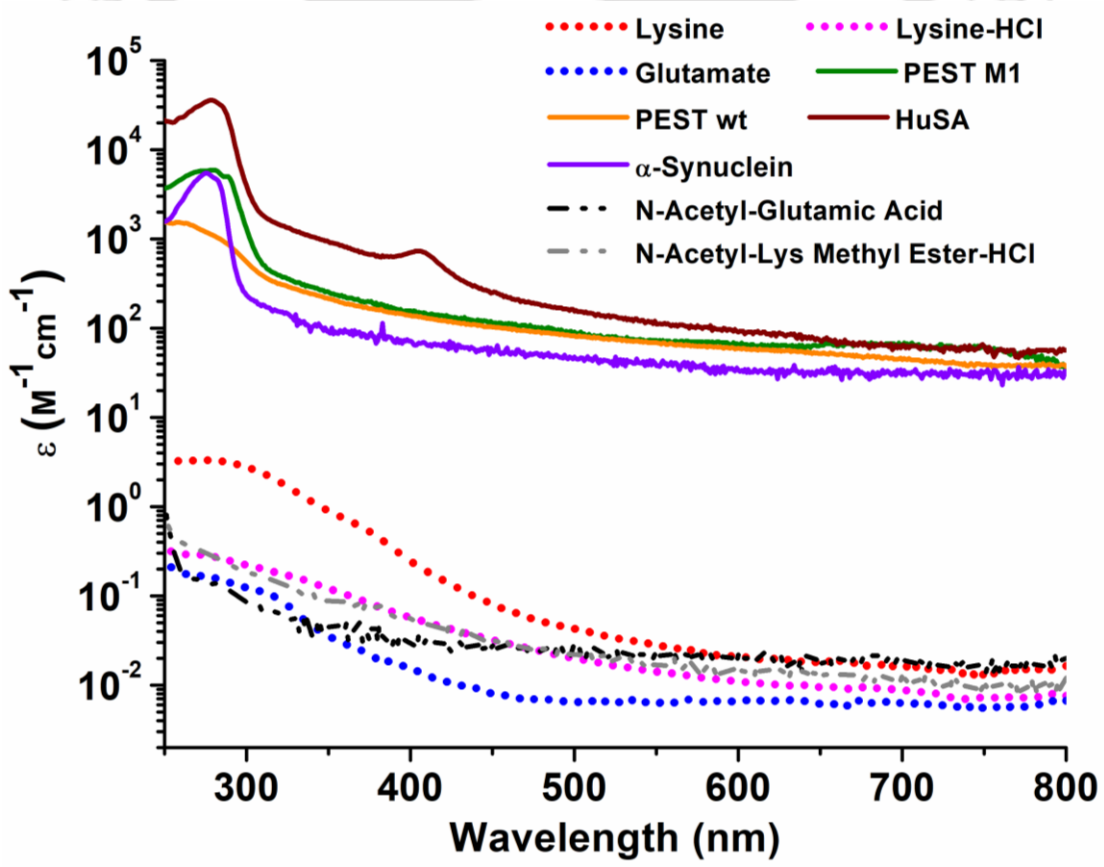

Figure 3.6: Extinction coefficient of different amino acids and proteins are presented in a logirathmic scale The presented values are an average of at least three-four independent measurements. The following are the peak values, PEST M1 (280 nm), PEST wt (250 nm), HuSA (278 nm and 404 nm), α-synuclein (276 nm).

3.2.7 ProCharTS observed from monomeric proteins

To ascertain that the ProCharTS observed from the proteins are arising from the monomeric entities, simplest of the experiments was done. Absorbance spectra of different proteins were recorded at different concentrations and relationship between the increasing concentration and absorption value was determined. As shown in Figure 3.7, the linear relationship between the observed absorbance with increasing concentration demonstrates the origin of ProCharTS from the monomeric proteins. This linearity was observed at multiple wavelengths between 325 – 600 nm for both HuSA and α-Synuclein. For remaining two proteins (PEST wt and PEST M1), Ansari and coworkers have already reported this linear relationship previously (Ansari et al 2018).

The linearity is only shown for wavelengths beyond 325 nm to avoid any contributions from any of the aromatic amino acids. A slight offset in linearity of α-Synuclein might have crept in because of the noisy absorption data. Higher concentration could have avoided the noisy data but we were limited by the availability of the protein.

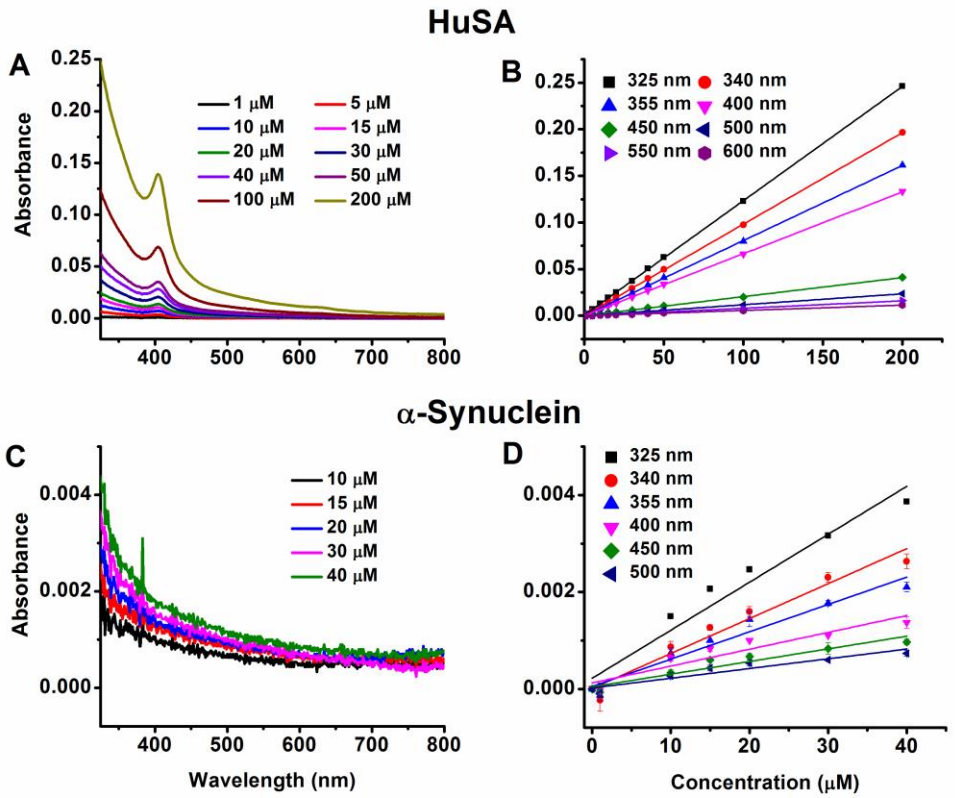

Figure 3.7: Absorption spectra for different concentrations of HuSA (with a peak value at 404 nm) and α-synuclein are shown in panel **A** and **C**, respectively. Absorbance of HuSA (**B**) and α-Synuclein (**D**) at selected wavelengths are plotted against different concentrations. The solid lines are the linear fit for the rise in absorbance with increasing concentration at the given wavelength.

3.2.8 Emission spectra of different proteins and amino acids

Here for this section, emission spectra of all the proteins and amino acids were collected at different excitation wavelength, λ_{ex} 280 nm, 310 nm, 340 nm, 355 nm, 370 nm and 410 nm. Proteins with Trp (HuSA and PEST M1) are excluded for 280 and 310 nm excitation while the protein with Tyr (α-Synuclein) was excluded for 280 nm excitation wavelength in order to avoid contributions from any aromatic amino acids.

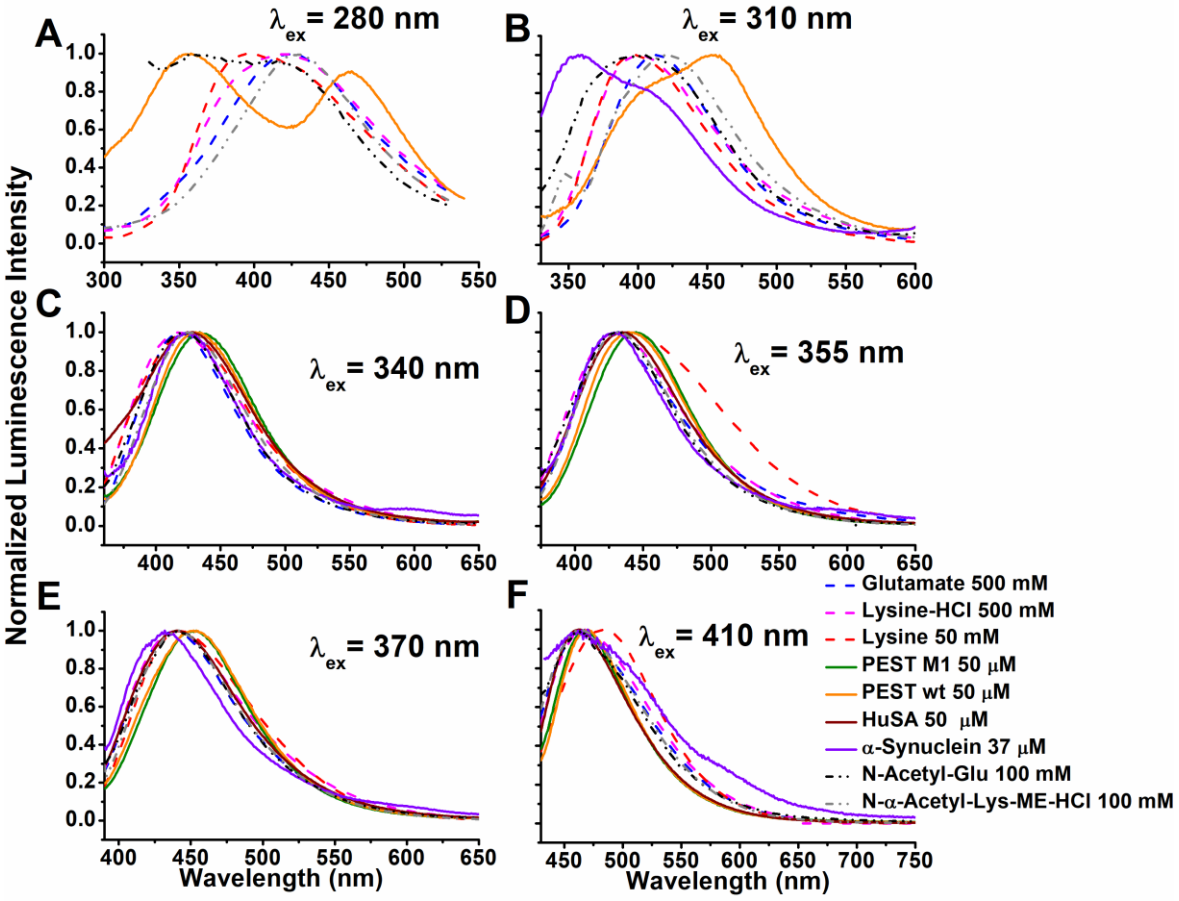

Figure 3.8: Normalized emission spectra of different proteins and amino acids at different excitation wavelengths.

For λ_{ex} 280 nm, the emission maxima for Lysine, Lysine·HCl and Glutamate are at 393 nm, 420 nm and 426 nm, respectively (Figure 3.8A) while PEST wt shows two distinct emission peaks at 358 nm and 466 nm. Capped-Lysine·HCl displays the emission maxima at 429 nm while capped-Glutamic acid shows two emission maxima, one at 361 and other at 422 nm.

For λ_{ex} 310 nm, Lysine, Lysine·HCl and Glutamate have emission maxima at 398 nm, 401 nm and 413 nm, respectively. On the other hand, proteins, α-Synuclein and PEST wt displays emission spectra with a peak value at 359 nm and 453 nm, respectively (Figure

3.8B). Both the proteins also shows a shoulder at 400 nm (α-Synuclein) and 407 nm (PEST wt). Capped-Lysine·HCl and capped-Glutamic acid displays the emission maxima at 421 nm and 406 nm, respectively.

From the Figure 3.8, it is quite clear that the spread of emission maxima are quite large among different samples for λ_{ex} 280 nm (~71 nm apart between 358 nm for PEST wt to 429 nm for capped-Lysine·HCl) and λ_{ex} 310 nm (~94 nm apart between 359 nm for α-Synuclein to 453 nm for PEST wt). For rest of the excitation wavelengths, λ_{ex} 340 nm, 355 nm, 370 nm and 410 nm, the emission maxima are more overlapping. For λ_{ex} 340 nm, the emission maxima are enveloped between 417 – 434 nm while for λ_{ex} 355 nm, 370 nm and 410 nm, the emission peaks are between 430 – 445 nm, 432 – 454 nm and 463 – 485 nm, respectively. Hence, the spread of emission maxima are within a difference of 17, 15, 22 and 22 nm for λ_{ex} 340, 355, 370 and 410 nm, respectively. Taken together, the emission maxima beyond the λ_{ex} 310 nm, are more overlapping and this narrowing gap between the emission maxima of proteins and amino acids suggests a common origin for the spectra.

3.2.9 Excitation spectra of different proteins and amino acids

For the emission spectra shown in Figure 3.8, it is quite evident that the emission maxima is between 410 nm to 490 nm whether the samples were excited at 340, 355, 370 or 410 nm. Hence, to reveal the excitation bands, excitation spectra were collected at three different emission maxima wavelengths, that is at 425 nm, 450 nm and 480 nm. All the excitation spectra are displayed in Figure 3.9.

When excitation spectra was collected at fixed emission wavelength of 425 nm, the excitation bands for amino acids were found to be around 330 nm (maxima of excitation spectra for Glutamate, Lysine·HCl and Lysine were found to be at 335, 329 and 331 nm, respectively). In addition, for proteins, it was between 349 – 356 nm (Figure 3.9A). The capped-Glutamic acid and capped-Lysine·HCl has the maxima of excitation at 339 nm and 347 nm, respectively.

For excitation spectra collected at fixed emission wavelength of 450 nm, the excitation band for amino acids were found around 350 nm (Glutamate ~341 nm, Lysine·HCl ~357 nm, Lysine ~349 nm, capped-Glutamic acid ~352 nm and capped-Lysine·HCl ~355 nm) while for proteins it was between 350 – 365 nm (Figure 3.9B).

For fixed emission wavelength of 480 nm, excitation bands for amino acids were found to be ~360 nm (Glutamate ~357 nm, Lysine·HCl ~365 nm, Lysine ~363 nm, capped-Glutamic acid ~364 nm and capped-Lysine·HCl ~359 nm) while for protein it was found to be between 358 – 372 nm (Figure 3.9C).

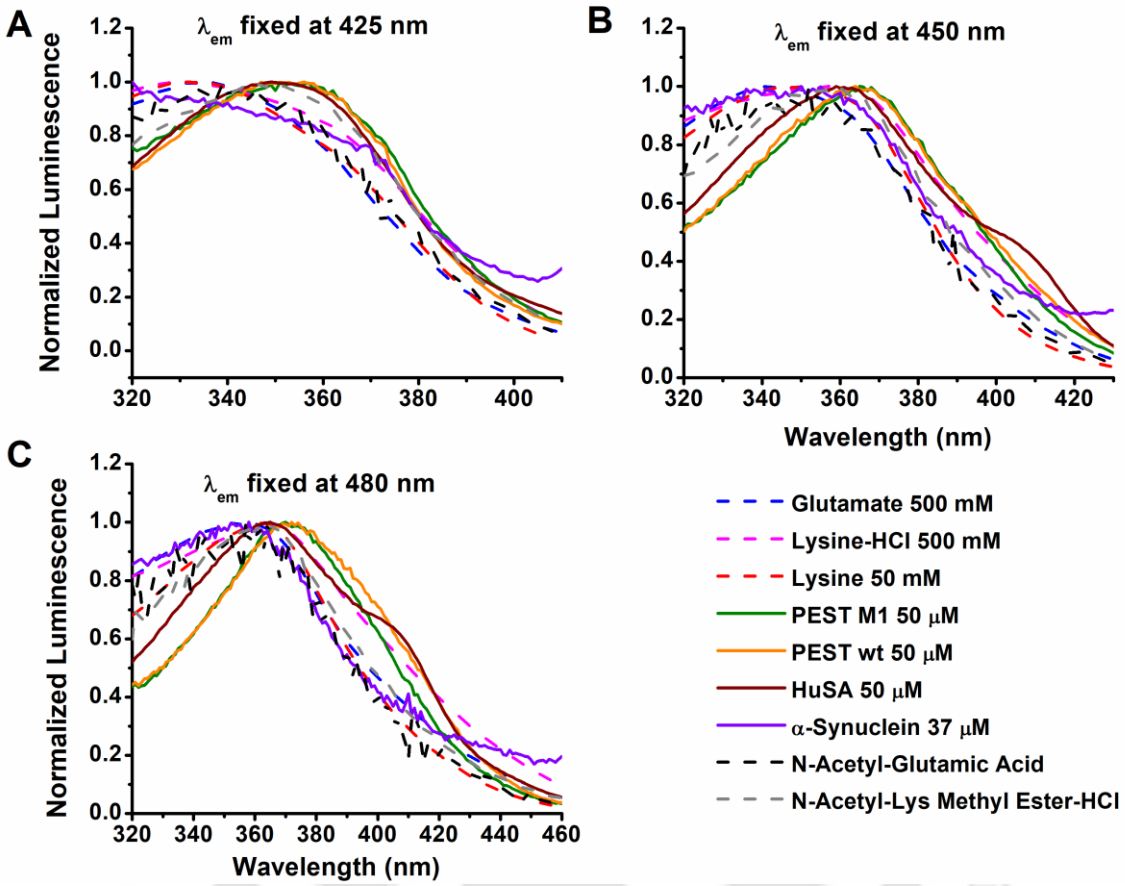

Figure 3.9: Normalized excitation spectra obtained for different proteins and amino acids at (**A**) 425 nm, (**B**) 450 nm and (**C**) 480 nm.

Hence, from the above observations it could be concluded that the excitation bands responsible for the observed emissions among amino acids are in the range of 330 – 360 nm and for proteins, excitation bands lie between 350 – 370 nm.

3.2.10 Stokes shift

As evident from the Figure 3.10, the variability in Stokes shift is huge between the amino acids (~12,000 cm^{-1}) and proteins (14,000—7000 cm^{-1}) when excited at 280 nm while for the excitation wavelengths 310, 340, 355, 370 and 410 nm, the Stokes shift appear comparable among all samples at the given excitation wavelength.

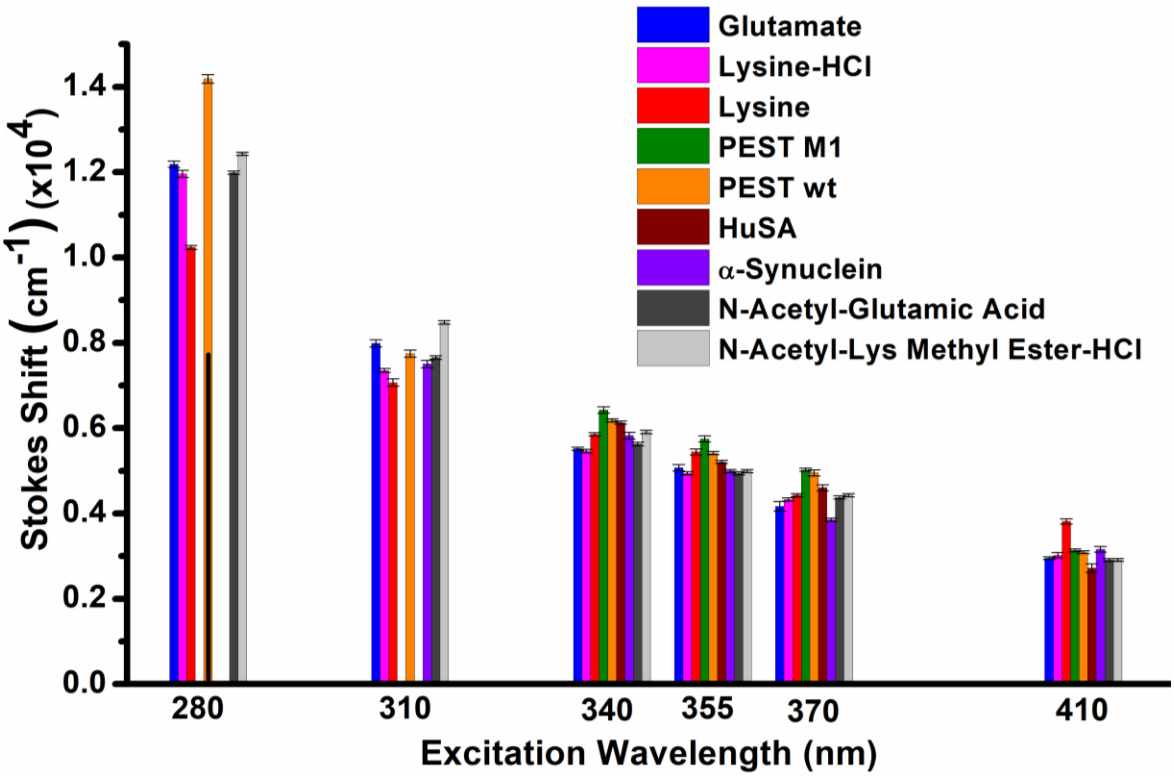

Figure 3.10: Stokes shift of different proteins and amino acids as a function of excitation wavelength. For 280 nm excitation, Stokes shift for first emission peak (Figure 3.8A) of PEST wt is represented as overlapping black bar with a value of 7781.3±33 cm^{-1}. Trp containing proteins are not included for λ_{ex} 280 nm and 310 nm while proteins containing Tyr are excluded for λ_{ex} 280 nm. For capped-Glutamic acid, Stokes shift for second emission peak is represented for λ_{ex} 280 nm.

Further, a decreasing trend in the Stokes shift is also noticeable with increasing excitation wavelength. For amino acids, Stokes shift has decreased from >10,000 cm^{-1} to >3,000 cm^{-1} when excitation wavelength is changed form 280 nm to 410 nm. In case of proteins, similar trend was observed but from 310 nm excitation onwards (i.e. Stokes shift has decreased from ~7,000 cm^{-1} to ~3,000 cm^{-1} when excitation is changed from 310 nm to 410 nm). This clearly shows a different behavior in the region of 280 nm for the set of proteins under this study (although the Trp containing proteins (PEST M1 and HuSA) has been excluded for this plot). The similarity in Stokes shift among all the amino acids and proteins at excitation wavelengths higher than 300 nm, makes a case for similar phenomena behind the emission from charged amino acids and proteins rich in charged amino acids. However, the change in Stokes shift with increasing excitation wavelength should be noted which does not follow the Kasha's rule (Kasha 1950). This could be attributed to the intramolecular charge transfer (Demchenko et al 2017, Scuppa et al 2011) as well as to the formation of different charge transfer states (Shen et al 2018).

Moreover, the huge Stokes shift observed among these charged amino acids gives an impression of substantial change in the dipole moment in the excited state of these molecules. For example, Trp exposed to water upon excitation at 280 nm shows emission peak ~348 nm (Teale & Weber 1957) with a Stokes shift of about ~7,000 cm^{-1}. In contrast to such aromatic amino acids, these charged amino acids show much greater values, >10,000 cm^{-1}. These further hints upon the higher sensitivity of luminescence arising from charge transfer states towards the polarity of the solvent.

3.2.11 Variation in luminescence yield with excitation wavelength

Luminescence yield of all the amino acids and proteins were determined at different excitation wavelengths (Figure 3.11). As their molar extinction coefficients and quantum yield (see later) are vastly different, they could not be compared for identical concentrations. The luminescence yield of the charged amino acids were found to be lower at longer excitation wavelength (as discussed in section 3.2.1). It can clearly be seen that the total yield among all the amino acids are maximum when excited at 280 nm with exception to Glutamate (Figure 3.11). The same has decreased for longer excitation wavelengths. Capped amino acids also follows the same trend. It should be noted that the luminescence yield has decreased steeply beyond λ_{ex} 355 nm. Here, 1:1 mixture of Lysine·HCl and Glutamate is also considered for the reason described in section 3.2.4.

Similar experiment was done with all the proteins. Among proteins, HuSA and PEST M1 were not included for λ_{ex} 280 nm and λ_{ex} 310 nm while α-Synuclein was excluded only for λ_{ex} 280 nm to avoid any contribution from aromatic amino acids. PEST wt has the maximum luminescence yield at λ_{ex} 280 nm and beyond λ_{ex} 280 nm, the luminescence yield kept on decreasing after a brief saturation between 300 – 355 nm. For α-Synuclein, luminescence yield was maximum for λ_{ex} 310 nm and for λ_{ex} 320 nm and 355 nm, it remained almost constant. Beyond λ_{ex} 355 nm, the luminescence yield of α-Synuclein has also decreased to a much lower value. A very similar pattern was observed in rest of the two proteins, HuSA and PEST M1. PEST M1 has the maximum yield at λ_{ex} 355 nm and the same has decreased over longer excitation wavelengths. HuSA shows maximum luminescence yield at λ_{ex} 330 nm followed by yield at λ_{ex} 355 nm and beyond, the luminescence yield has sharply decreased (Figure 3.11). Luminescence spectra of each of the proteins at different excitation wavelengths are shown in Appendix-II as Figure A3.

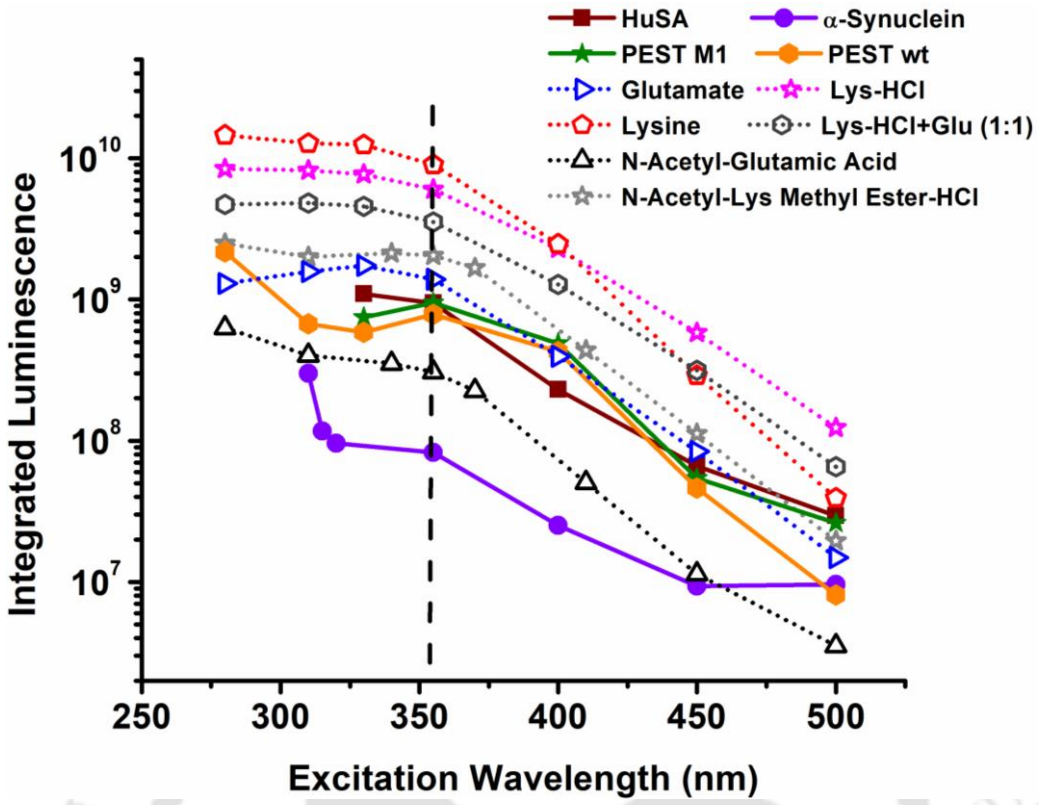

Figure 3.11: Integrated luminescence of different amino acids and proteins. All the samples were excited with 2 nm of slit width and emission was collected with 15 nm of slit width at the given excitation wavelength. Integrated luminescence was calculated for the emission spectral range containing >90% of luminescence for the given λ_{ex}. The concentration of different amino acids was 300 mM (Lysine·HCl and Glutamate), 30 mM (Lysine) and for mixed sample of Lysine·HCl + Glutamate, 150 mM of each. 100 mM each for the capped amino acids were used. Among proteins, 50 µM (PEST M1, PEST wt), 35 µM (α-synuclein) and 10 µM (HuSA) was used. The vertical dashed line represents the λ_{ex} (355 nm) used for the determination of linearity in luminescence and calculation of quantum yield among all samples.

From the above results, it is quite obvious that among all the samples the luminescence yield beyond λ_{ex} 355 nm is much lower. It can also be concluded that the common trend of decrease in luminescence yield with increasing λ_{ex} among all the amino acids and proteins suggests a common phenomenon responsible for the observed luminescence.

Since, the luminescence yield beyond λ_{ex} 355 nm is lower, the rest of the experiments like quantum yield calculation and observation of linearity in luminescence among all the proteins and amino acids were done at this excitation wavelength (355 nm). Further, our earlier work on Lysine·HCl luminescence (Homchaudhuri & Swaminathan 2001) also used this λ_{ex} for linearity studies. This selection has also an added advantage of automatically avoiding any contribution from aromatic amino acids present in proteins. Moreover, for the similar reason, luminescence lifetime was also observed at λ_{ex} 340 nm.

3.2.12 Quantum yield of different proteins and amino acids at 355 nm

Further, quantum yield of all the proteins and amino acids was calculated on excitation at 355 nm as described in Methods. The absorption and emission spectra used for the calculation of quantum yield of various proteins and amino acids is shown in Appendix II as Figure A4.

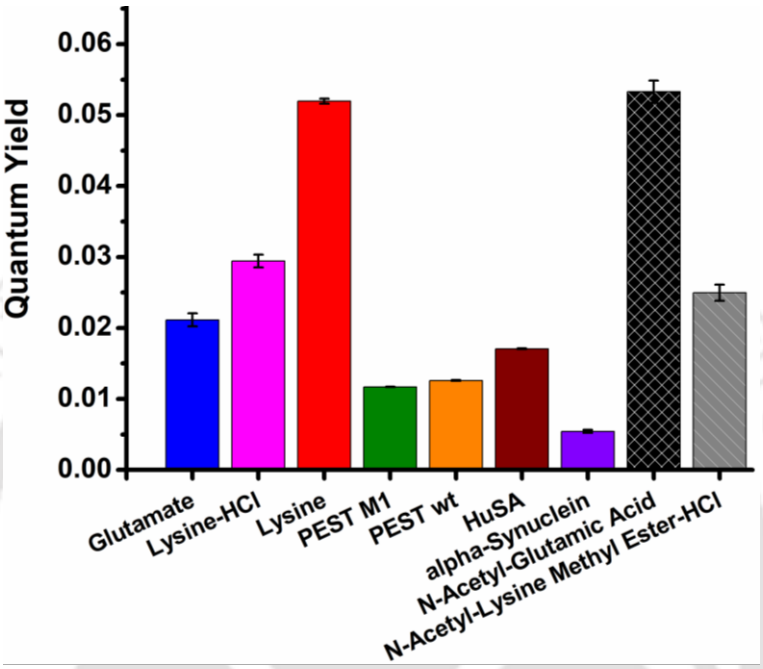

Figure 3.12: Quantum yield of different proteins and amino acids at 355 nm

Figure 3.12 shows the measured quantum yield of all the proteins and amino acids. Among different amino acids, Lysine has the highest quantum yield (0.051) followed by Lysine·HCl (0.029) and Glutamate (0.02). The observed quantum yield of capped-Glutamate (0.053) is very similar to that of Lysine. This could be due to similar molar absorptivity of pure Glutamic acid and pure Lysine (Prasad et al 2017). Moreover, capped-Lysine·HCl has quantum yield (0.025) similar to that of Lysine·HCl. The quantum yields of all the proteins are lower than amino acids. Among proteins, HuSA has the highest quantum yield (0.017) followed by PEST wt (0.012) and PEST M1 (0.011). α-Synuclein possess the lowest quantum yield among all proteins with values of 0.0056.

It is also surprising to note that in spite of higher extinction coefficient of proteins their quantum yield are lower than the amino acids. Additionally, the quantum yields observed here are significantly lower than the conventional fluorophore viz. Trp present in proteins which is ~0.14 (Eftink 1991, Eftink et al 1995).

However, the extinction coefficient (Figure 3.6), excitation (Figure 3.9) and emission (Figure 3.8) spectra, Stokes shift (Figure 3.10) and quantum yield (Figure 3.12) observed for capped amino acids are found to be similar to uncapped ones. This implies that there is a minimal or negligible role of charges at amino/carboxyl terminals in the origin of charge transfer transitions. This further strengthens the idea that the major contribution in CT transitions comes from the interplays of charged side chains present in these amino acids.

3.2.13 Linearity in luminescence at λ_{ex} 355 nm

The very first point to check if any luminescence observed from amino acids or proteins under this study is originating from oligomeric or aggregated species. Because several other groups have reported that, such emissions may originate from the oligomeric states of proteins (Bhattacharya et al 2017), crystals or protein aggregates (Chan et al 2013, Shukla et al 2004, Tikhonova et al 2018). To confirm this, linearity in absorbance with increasing concentrations was determined at multiple wavelengths (shown in section 3.2.7) while for luminescence, this was done at λ_{ex} 355 nm. Luminescence observed at λ_{ex} 355 nm among all amino acids proteins and proteins were found to be linear with their increasing concentrations (Figure 3.13 and 3.14).

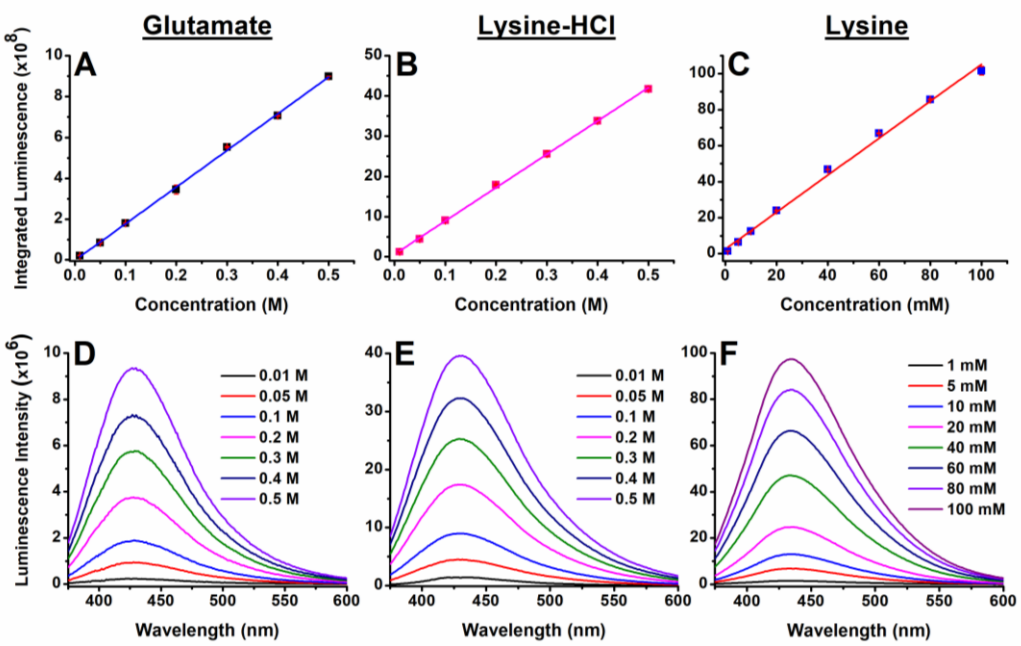

Figure 3.13: Upper panel shows the linearity in luminescence yield while lower panel shows the respective luminescence spectra (λ_{ex} 355 nm) at different concentrations of Glutamate, Lysine·HCl and Lysine.

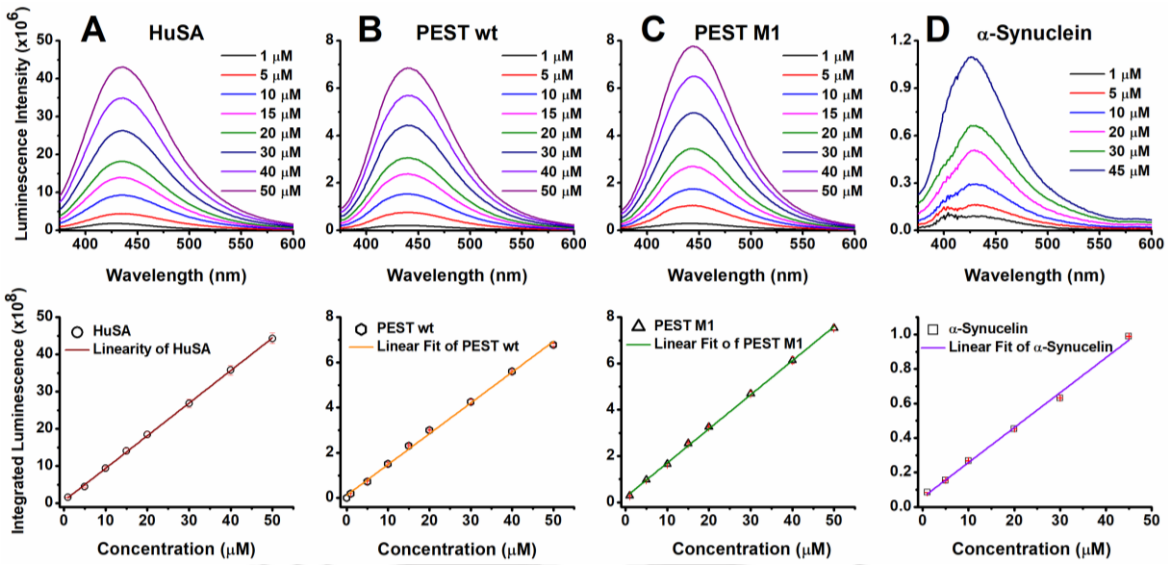

Figure 3.14: Column **A** to **D** shows the luminescence spectra of HuSA, PEST wt, PEST M1 and α-Synuclein, respectively. For each protein, rise in the integrated luminescence is fitted linearly with increasing concentration as shown in lower row. The λ_{emm} maxima are, 439 nm (PEST wt), 445 nm (PEST M1), 435 nm (HuSA), and 431 nm (α-Synuclein).

Linearity was observed with good R^2 value of > 0.99 and distinctive slopes (Table 3.2). The slope of the linearity plots are indicative of increase in luminescence for unit increase in concentration. Among amino acids, Lysine has the highest slope ($0.01x10^7$) followed by Lysine·HCl and Glutamate. Among proteins, the slope for the HuSA is maximum ($8.81x10^7$) followed by PEST M1, and PEST wt. The slope for α-Synuclein is lowest ($0.2x10^7$) among all proteins.

Sample	% charged amino acids	Slope ($x10^7$) (Intensity/μM)	Intercept ($x10^7$)	Adj. R^2	(QY_{355}* ε_{355}) (M^{-1} cm^{-1})
HuSA	33.3 (197)	8.8	4.7	0.999	14.96
PEST M1	34.6 (27)	1.5	1.7	0.998	2.75
PEST wt	35.1 (27)	1.4	1.2	0.997	2.56
α-Synuclein	28.6 (40)	0.2	0.4	0.993	0.48
Lysine	--	0.0103	26.6	0.995	0.042
Lysine·HCl	--	0.00083	6.5	0.999	0.0033
Glutamate	--	0.00018	-0.18	0.999	0.00068

Table 3.2: Parameters from linear fit deduced from Figure 3.14 and Figure 3.15. The values in parenthesis shows the total number of charged amino acids in the given protein. In the last column, product of quantum yield (Figure 3.12) and extinction coefficient (Figure 3.6) at 355 nm is shown.

As with absorption, the 3D fold of the protein appears to play a pivotal role in enhancing the luminescence arising from ProCharTS as HuSA shows the maximum slope for being a folded protein unlike the rest. The observed linearity also suggests that the luminescence is originating from the individual molecular entities not from any kind of intermolecular interaction or agglomerated species or oligomers of proteins. Moreover, the slopes (Table 3.2) reflect the population density of interacting charged amino acid side chains per monomer which is highest for HuSA and least for the amino acids.

3.2.14 Relationship between the luminescence and product of ε and Φ

To make a meaningful comparison between the luminescence observed from different proteins and amino acids, a simple parameter is calculated, that is the product of extinction coefficient (ε) and quantum yield (Φ). This term (ε x Φ) is directly proportional to the brightness of the fluorophore, accounting both for the amount of light absorbed and quantum efficiency of the fluorophore (Lavis & Raines 2008). The value of this parameter (ε_{355} x Φ_{355}) for different proteins and amino acids are displayed in Table 3.2. Here, the slopes obtained from the linearity in luminescence for different amino acids and proteins (Table 3.2) are plotted against brightness parameter; (ε_{355} x Φ_{355}) as shown in Figure 3.15.

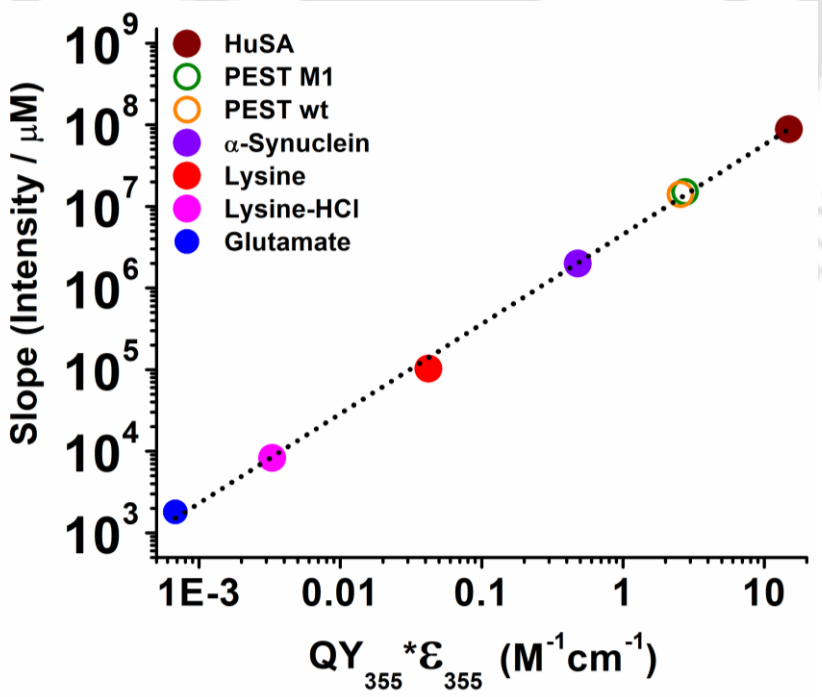

Figure 3.15: Plot of slope obtained from the linearity of luminescence (Table 3.2) versus the product of extinction coefficient and quantum yield (ε_{355} x Φ_{355}). Dotted line represents the linear fit with Adj. R^2 value of 0.99.

The linear relationship obtained above indicates that the reason behind the higher slope values among proteins is their higher extinction coefficient. Similarly, for amino acids the much lower values of their molar extinction coefficient are responsible for their lower slope values. This also reinforces the point that the quantum yield has a limited role in the contribution toward the luminescence, since the variability among the quantum yield is least among all the samples (0.005 to 0.05) in contrast to large variations in molar extinction coefficient (Figure 3.6).

3.2.15 Luminescence lifetime of protein charge transfer states

3.2.15.1 Luminescence lifetime at λ_{ex} 340 nm

3.2.15.1.1 Luminescence intensity decay observed at λ_{ex} 340 nm

Luminescence intensity decay of all the proteins and amino acids at λ_{ex} 340 nm are shown in Figure 3.16 along with their fit and fitted residuals. Panel A, B and C show the intensity decay of Lysine·HCl, Glutamate and Lysine respectively. It should be noted that in panel D of this figure, a 1:1 mixture of Lysine·HCl + Glutamate was analyzed to understand the additive effect on the luminescence lifetime of Lysine·HCl. The fluorescent intensity decays for rest of the proteins are displayed in panels E-H. Below each panel, the fitted residuals obtained from discrete analysis (for 3 exponential decay model, $i = 3$ in Eq. 2.52) are displayed. The decays profiles clearly reveal a multi-exponential nature of decay not only for amino acids but also for all the proteins. The decay curve of α-Synuclein should be noted to have a very short component, shorter than rest of the proteins. While the 1:1 mixture of Lysine·HCl and Glutamate, resembles similar to decay curve for individual amino acids.

3.2.15.1.2 Results of discrete analysis obtained for decay at λ_{ex} 340 nm

The results of discrete analysis are presented in Figure 3.17. All the amino acids and proteins display luminescence decays that fit best to three distinct lifetimes with varying amplitudes. Figure 3.17A shows the lifetime values for all the samples (for λ_{ex} 340 nm) which display an average short lifetime of ~1 ns followed by two longer lifetimes ~3 ns and >8 ns. This was consistent with all the samples. Figure 3.17B shows the amplitude values for the corresponding τ values in Figure 3.17A. This clearly shows that the very short component (τ_1) has the highest contribution to the decay (amplitude ≥ 0.6) among all the samples while the largest component (τ_3) has least contributions (amplitude value < 0.1).

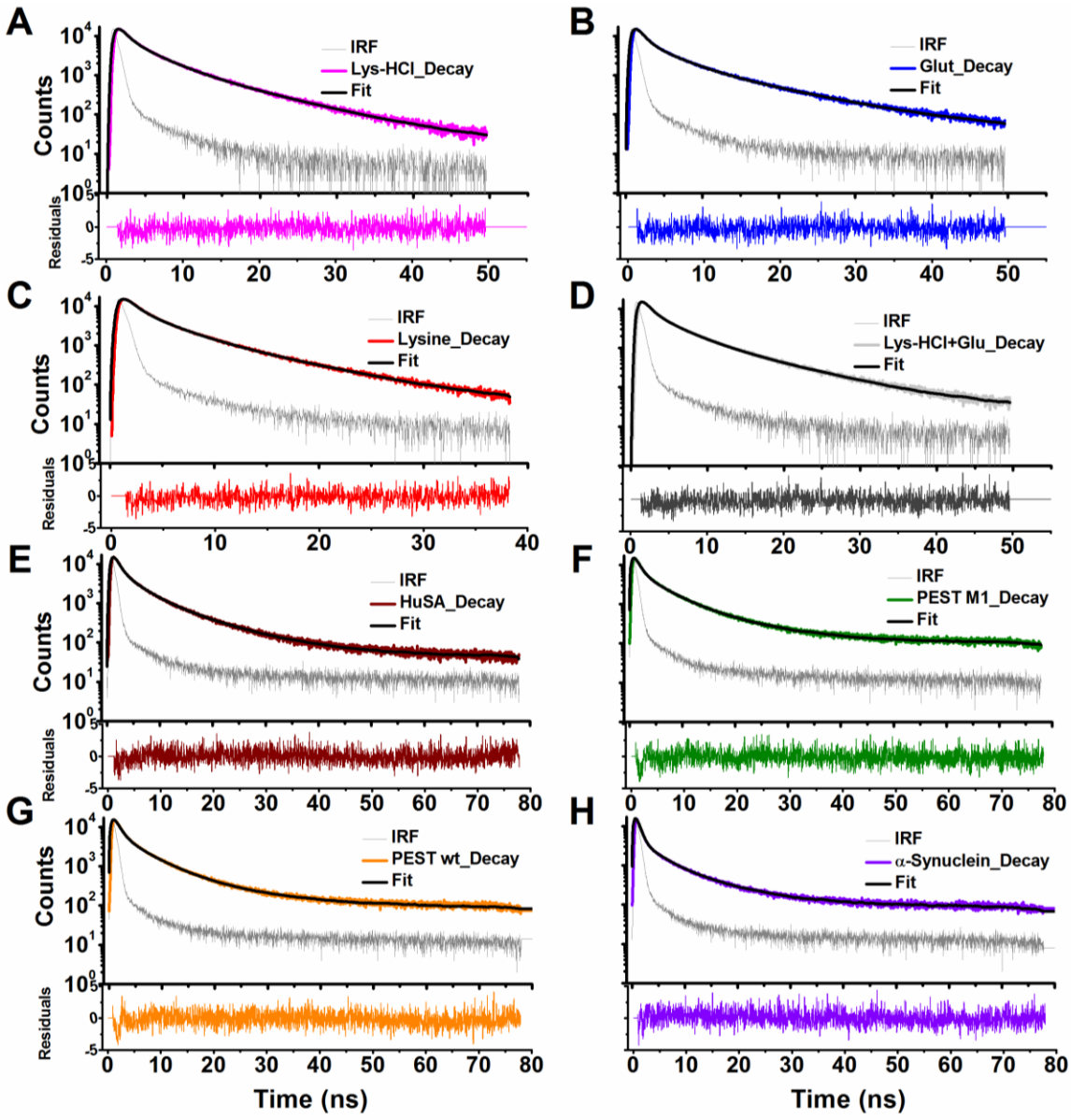

Figure 3.16: Luminescence intensity decay of different proteins and amino acids at 340 nm: All the samples were excited at 340 nm and data collection was done with 370 nm long-pass filter. All decays were fitted in three exponential model.

The mean lifetime (see Eq. 2.53) represents the area under the luminescence decay curve and is proportional to steady state luminescence intensity of the sample. The mean lifetime for all the samples are presented in Figure 3.18. The mean lifetime for Lysine·HCl (2.37±0.06 ns) is higher than Lysine (2.17±0.05 ns) and Glutamate (2.17±0.07 ns) while for the 1:1 mixture of Lysine·HCL and Glutamate an intermediate value (2.28±0.045 ns) was observed. Among proteins, PEST wt, PEST M1 and HuSA have similar mean lifetimes ~2 ns while α-Synuclein has a mean lifetime of 1.08±0.01 ns. The individual components and mean lifetime of all the proteins and amino acids are displayed in Table 3.3.

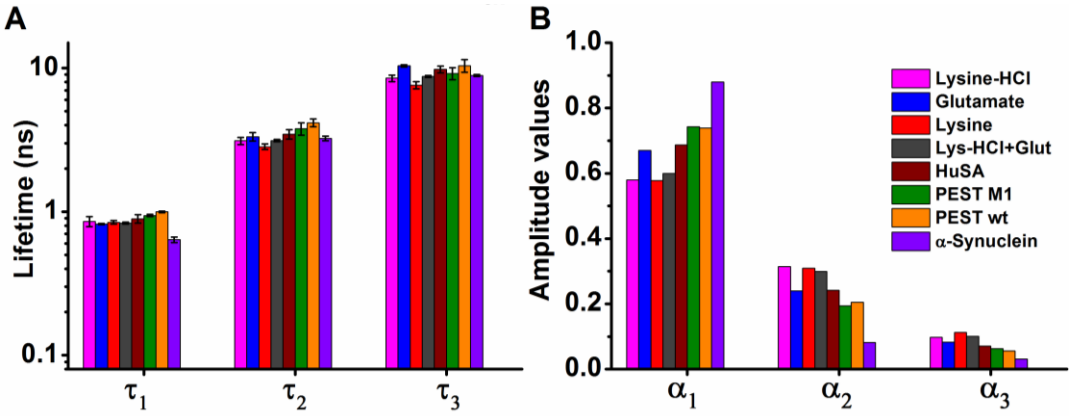

Figure 3.17: alpha (α) and tau (τ) values derived from three exponential decay fit: Panel **A** and **B** shows the tau and alpha values, respectively, obtained from 3 exponential fit for λ_{ex} 340 nm. The presented tau values are the average of 3-4 independent measurements while the alpha values are taken from the best fitted data.

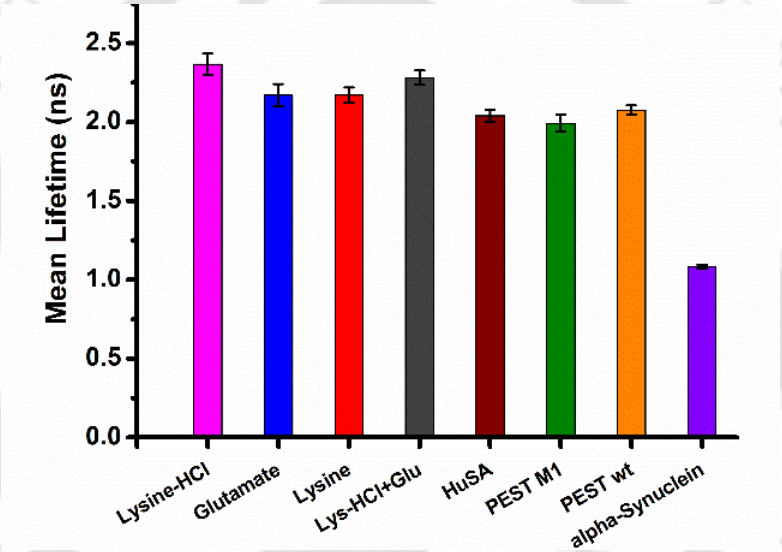

Figure 3.18: Mean luminescence lifetime of all the proteins and amino acids at λ_{ex} 340 nm.

Samples	τ_1	τ_2	τ_3	α_1	α_2	α_3	τ_{mean}	χ^2_R
Lysine·HCl	0.86 (0.07)	3.1 (0.17)	8.5 (0.44)	0.58	0.31	0.098	2.37 (0.07)	1.13
Glutamate	0.82 (0.01)	3.3 (0.22)	10.4 (0.19)	0.67	0.24	0.083	2.17 (0.07)	1.09
Lysine	0.84 (0.02)	2.8 (0.12)	7.6 (0.42)	0.58	0.31	0.113	2.17 (0.05)	1.07
Lys·HCl + Glutamate	0.83 (0.01)	3.1 (0.06)	8.8 (0.13)	0.6	0.29	0.101	2.28 (0.05)	1.13
HuSA	0.89 (0.06)	3.5 (0.27)	9.8 (0.52)	0.69	0.24	0.071	2.04 (0.04)	1.09
PEST M1	0.94 (0.02)	3.8 (0.37)	9.2 (0.9)	0.74	0.19	0.063	1.99 (0.05)	1.16
PEST wt	0.99 (0.01)	4.2 (0.26)	10.4 (1.03)	0.74	0.2	0.056	2.08 (0.03)	1.16
α-Synuclein	0.64 (0.03)	3.2 (0.11)	8.9 (0.14)	0.88	0.08	0.031	1.08 (0.01)	1.17

Table 3.3: Parameters obtained from three exponential fit for the fluorescence intensity decay observed at λ_{ex} 340 nm. Values in the parenthesis (for $\tau_{1\text{-}3}$ and τ_{mean}) indicates the standard deviation observed in 3 independent measurements while the $\alpha_{1\text{-}3}$ are represented from the best fit.

3.2.15.1.3 Results of MEM analysis obtained for decay at λ_{ex} 340 nm

In Figure 3.19 lifetime distribution plots obtained from MEM analysis for luminescence decays observed at λ_{ex}, 340 nm are shown.

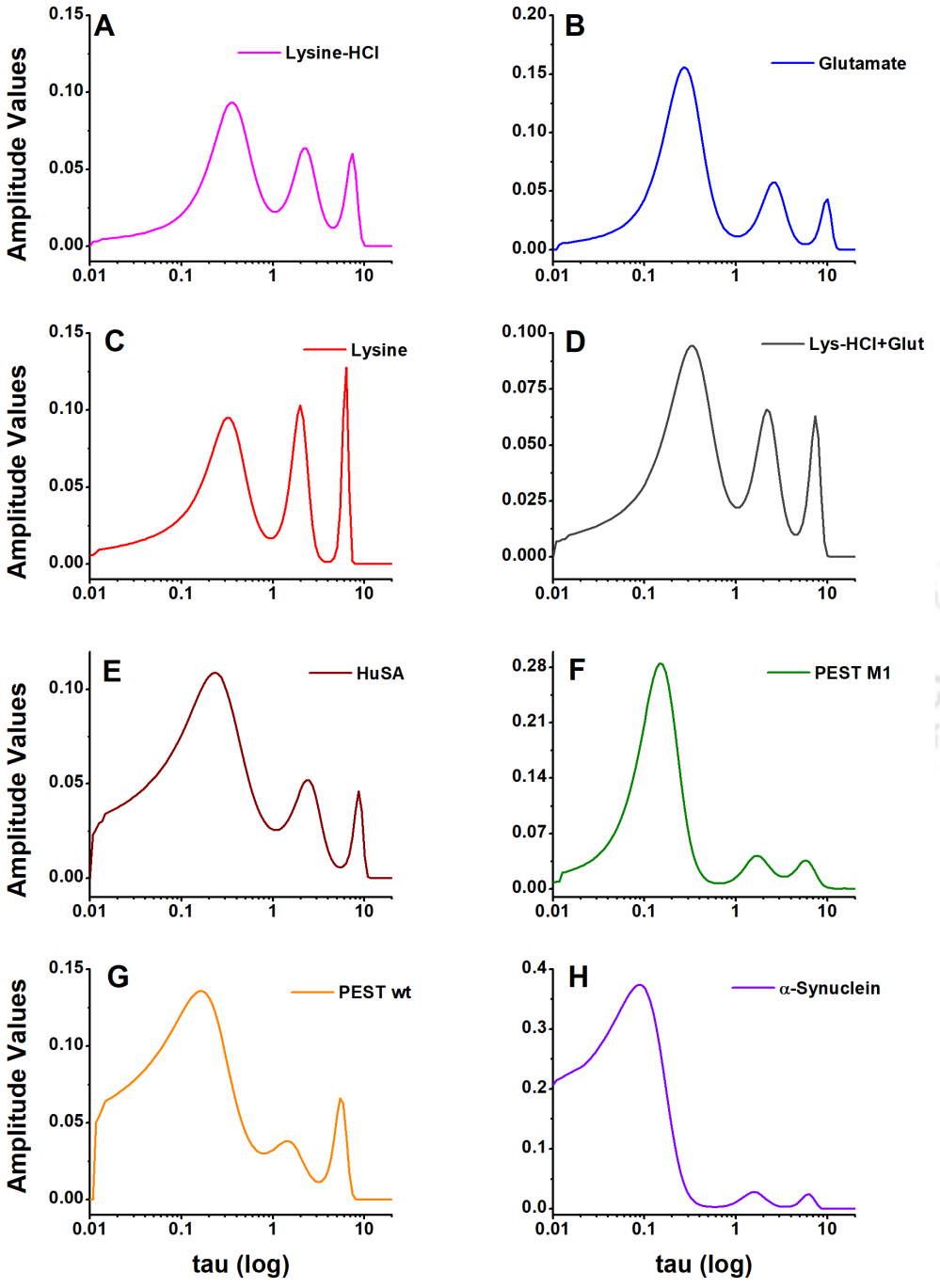

Figure 3.19: Lifetime distributions obtained from MEM analysis for the luminescence intensity decay observed at λ_{ex}, 340 nm. Residuals of the fit are displayed in Figure 3.24

MEM analysis revealed three well resolved distributions (three peaks corresponding to three different lifetimes) with varying amplitudes for each sample. The shortest component is ~0.3

ns among all amino acids while for HuSA, PEST M1 and PEST wt it is ~0.2 ns and for α-Synuclein it is ~0.1 ns. The longest component for all the amino acids and HuSA around 8-10 ns while for PEST wt, PEST M1 and α-Synuclein, this value is between 5-6 ns. The intermediate component is >2 ns for all the amino acids and HuSA while for rest of the proteins (PEST wt, PEST M1 and α-Synuclein) this component is >1 ns. It should be noted that the shortest component has a very broad distribution and maximal amplitude than rest of the two components while the longest component has the least contribution. This feature is consistent with the discrete analysis where the shortest lifetime component (τ_1) had the maximum contribution (α_1) and the longest component (τ_3) has least contribution (α_3). Figure 3.19D displays the lifetime distribution obtained for the 1:1 mixture of Lysine·HCl and Glutamate which is more similar to the distribution of Lysine·HCl alone rather than solely Glutamate. This observation is also similar to the discrete analysis (Figure 3.17).

3.2.15.2 Luminescence lifetime at λ_{ex} 295 nm

3.2.15.2.1 Luminescence intensity decay observed at λ_{ex} 295 nm

For λ_{ex} 295, the luminescence intensity decay profile of all the amino acids and proteins (except Trp containing proteins, PEST M1 and HuSA) are presented in Figure 3.20. The residuals obtained from discrete analysis (for 3 exponential model) for each decay is presented below each panel. Randomness in the residuals show the fits for the decay are well suited for the selected model. A very short component can be observed from decay itself for PEST wt, which is not present in the decay for rest of the samples. Here also, a 1:1 mixture of Lysine·HCl and Glutamate was analyzed for their additive effects on the luminescence lifetime.

3.2.15.2.2 Results of discrete analysis obtained for decay at λ_{ex} 295 nm

In Figure 3.21, lifetime values obtained from discrete analysis for all the samples are displayed for λ_{ex} 295 nm. In this case also, all the samples displayed three distinct lifetimes with different amplitudes. The smallest component (τ_1; < 1 ns) has the highest contribution while the other two components are of ~3 ns (τ_2) and > 6 ns (τ_3), respectively. Among the largest components (τ_3), Glutamate and PEST wt displays the highest value of > 11 ns (Figure 3.21A) while for rest of the samples, it lies between 6-10 ns. Figure 3.21B shows the contribution (amplitude values) for each components (τ) displayed in Figure 3.21A. For PEST wt, the contribution (α_1) from smallest component (τ_1) is exceptionally high while the

contribution (α_2) from the intermediate component (τ_2) is least among all the samples. This outlier behavior is reflected as the least mean lifetime among all the samples (Figure 3.22)

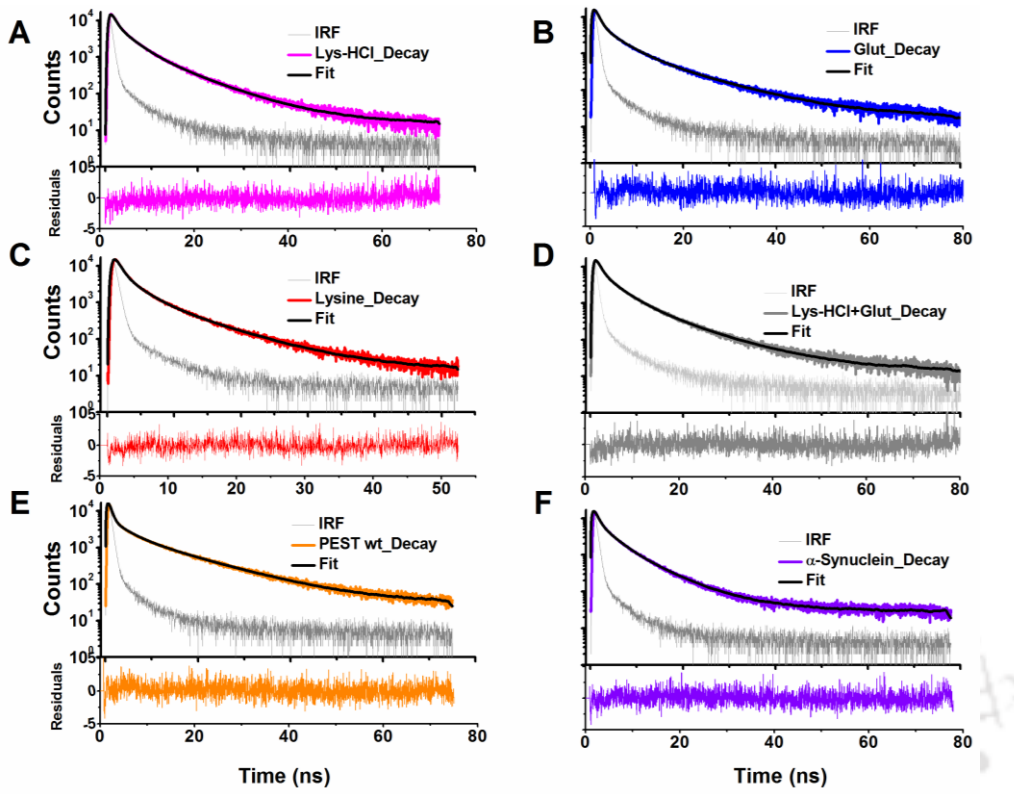

Figure 3.20: Luminescence intensity decay of different proteins and amino acids at 295 nm: All the samples were excited at 295 nm and data collection was done with 320 nm long-pass filter. All decays were fitted in three exponential model.

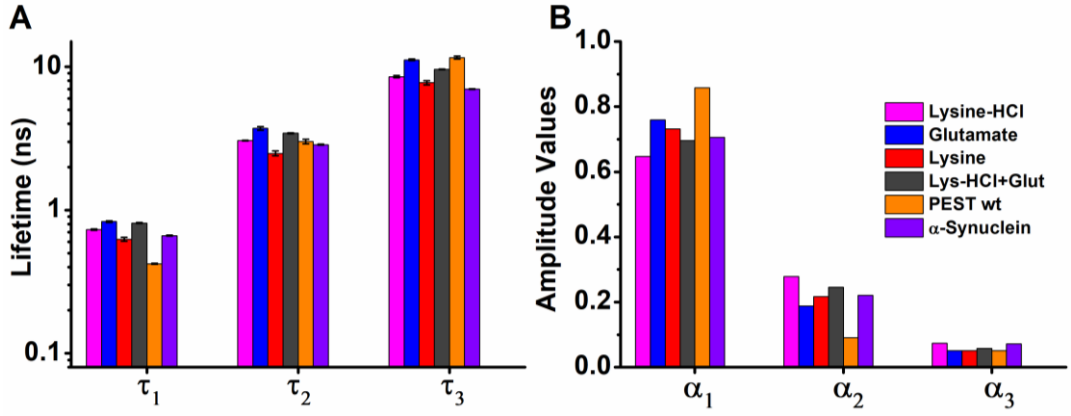

Figure 3.21: alpha (α) and tau (τ) values derived from three exponential decay fit: Panel **A** and **B** shows the tau and alpha values, respectively, obtained from 3 exponential fit for λ_{ex} 295 nm. The presented tau values are the average of 3-4 independent measurements while the alpha values are taken from the best fitted data.

For λ_{ex} 295 nm, the mean lifetime of Lysine·HCl, Glutamate and Lysine are 1.96±0.01 ns, 1.87±0.01 ns and 1.35±0.02 ns, respectively. However, the 1:1 mixture has surprisingly the

same mean lifetime (1.96±0.01 ns) as of Lysine·HCl. PEST wt has a mean lifetime of 1.26±0.02 ns and α-Synuclein has a mean lifetime of 1.62±0.02 ns (Figure 3.22). Similar to the observation made for λ_{ex} 340 nm, Lysine·HCl in this case also holds the highest mean lifetime amongst all. The individual components and mean lifetime of all the proteins and amino acids are displayed in Table 3.4.

The mean lifetime of these charged, non-aromatic amino acids are much less than what is generally observed for aromatic amino acids like Trp. For Trp in aqueous environment, the mean lifetime is ~3.1 ns (Lakowicz 2013, Rayner & Szabo 1978) while for Lysine·HCl it is determined to be ~1.9 ns. Lower luminescence lifetime indicates a lower quantum yield for these charged, non-aromatic amino acids. The same has been observed as shown in section 3.2.12.

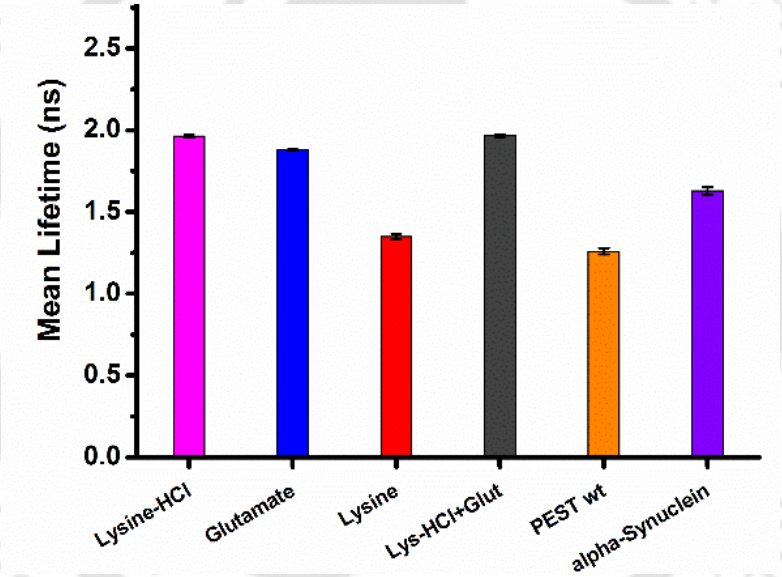

Figure 3.22: Mean luminescence lifetime of all the proteins and amino acids at λ_{ex} 295 nm

Samples	τ_1	τ_2	τ_3	α_1	α_2	α_3	τ_{mean}	χ_R^2
Lysine·HCl	0.73 (0.01)	3.1 (0.02)	8.5 (0.15)	0.65	0.28	0.074	1.96 (0.01)	1.15
Glutamate	0.83 (0.01)	3.7 (0.01)	11.2 (0.15)	0.76	0.19	0.051	1.88 (0.01)	1.11
Lysine	0.63 (0.02)	2.5 (0.09)	7.7 (0.27)	0.73	0.22	0.051	1.35 (0.02)	1.14
Lys·HCl + Glut	0.81 (0.01)	3.4 (0.03)	9.6 (0.06)	0.69	0.25	0.058	1.97 (0.01)	1.13
PEST wt	0.42 (0.01)	3.0 (0.11)	11.6 (0.26)	0.86	0.09	0.051	1.26 (0.02)	1.17
α-Synuclein	0.66 (0.01)	2.9 (0.02)	7.0 (0.03)	0.70	0.22	0.072	1.63 (0.02)	1.11

Table 3.4: Parameters obtained from three exponential fit for the fluorescence intensity decay observed at λ_{ex} 295 nm. Values in the parenthesis (for $\tau_{1\text{-}3}$ and τ_{mean}) indicates the standard deviation observed in 3 independent measurements while the $\alpha_{1\text{-}3}$ are represented from the best fit.

3.2.15.2.3 Results of MEM analysis obtained for decay at λ_{ex} 295 nm

For λ_{ex} 295 nm also, all the samples (except PEST M1 and HuSA for this λ_{ex}) display three distributions i.e. three different lifetimes with varying amplitudes (Figure 3.23). The shortest component for Lysine·HCl and Lysine is > 0.2 ns while for Glutamate its 0.1 ns. For PEST wt and α-Synuclein, the shortest component is < 0.1 ns. The second component with a peak value ≥ 2 ns is observed for Lysine·HCl, Lysine and PEST wt while Glutamate and α-Synuclein have this peak value > 1 ns. For the third component, Lysine·HCl, Lysine and PEST wt has the peak value between 8-10 ns while Glutamate and α-Synuclein have the peak value between 5-6 ns. These all results are comparable to the results of discrete analysis, where the contribution (α_1) from the first component (τ_1) is maximum amongst all the samples. When 1:1 mixture of Glutamate and Lysine·HCl is compared to the individual amino acids, the mixture resembles more of like the Lysine·HCl.

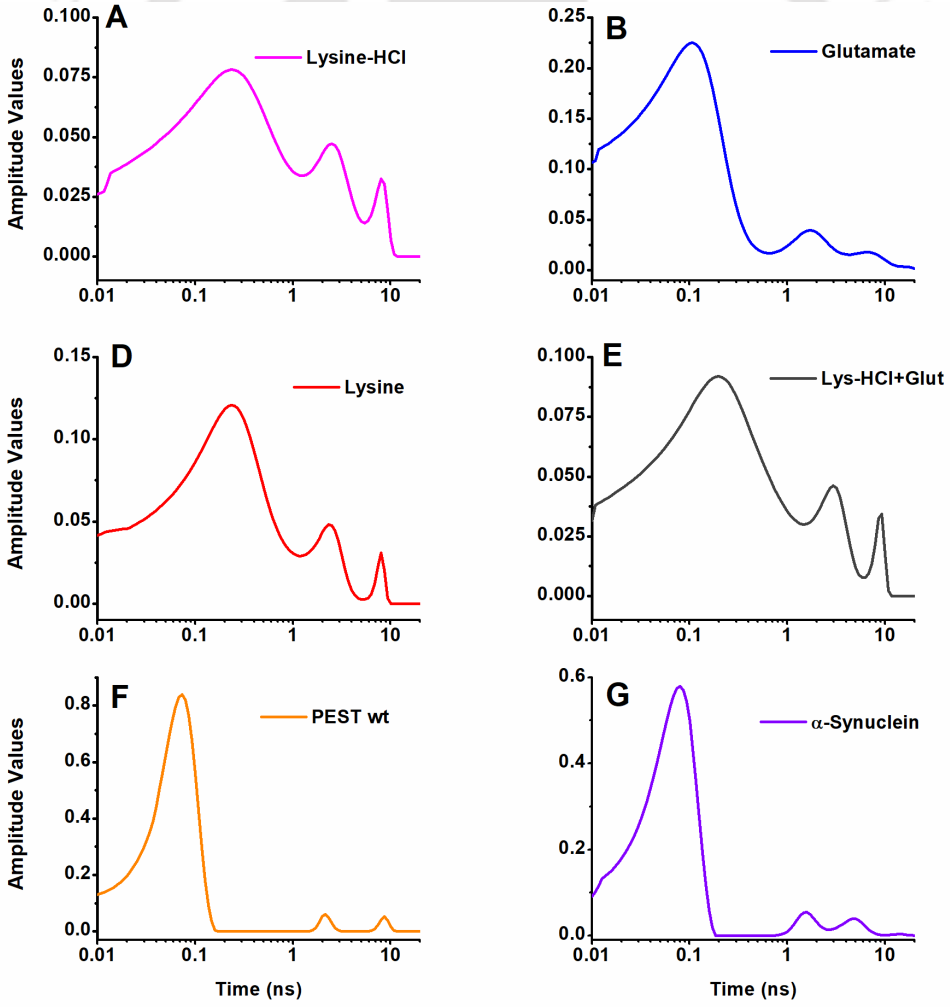

Figure 3.23: Lifetime distributions obtained from MEM analysis for the luminescence intensity decay observed at λ_{ex}, 295 nm. Residuals of the fit are displayed in Figure 3.25.

Overall, the distribution of first component obtained for λ_{ex} 295 nm is much broader as compared to the distributions obtained for λ_{ex} 340 nm. Apart from this, the distributions obtained for λ_{ex} 295 nm are more shifted towards the lower timescale (specially the first component) as compared to those obtained for λ_{ex} 340 nm. This shift of distribution toward the lower timescale can be interpreted for smaller mean lifetime than those obtained for λ_{ex} 340 nm. Similar results were shown by discrete analysis in Figure 3.18 and 3.22. Apart from this, the fair degree of similarity among distributions obtained across all the amino acids and proteins underscores the role of a common origin.

The residuals to evaluate the goodness of fit for MEM analysis is given in Figure 3.24 for λ_{ex} 340 nm and Figure 3.25 for λ_{ex} 295 nm.

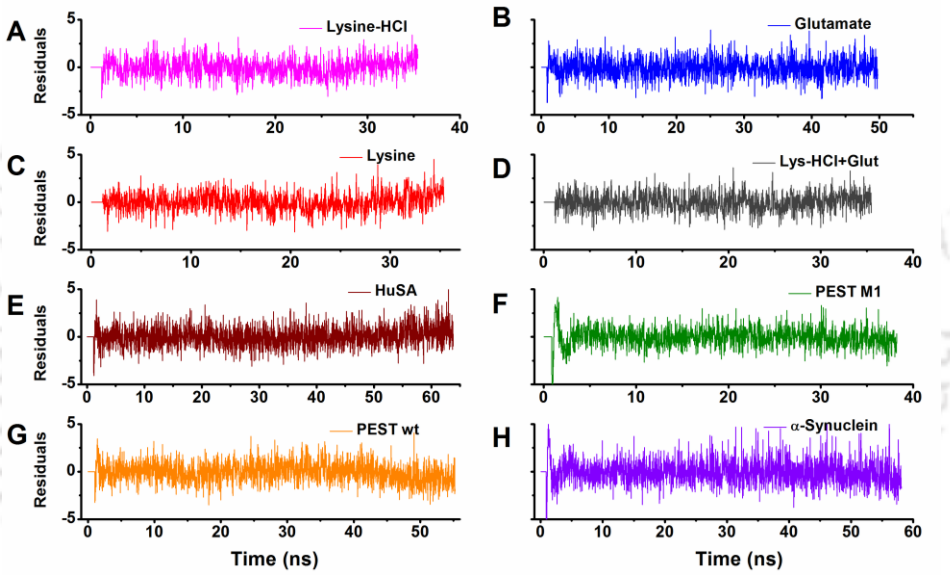

Figure 3.24: Residuals obtained from MEM analysis done for luminescence intensity decay at λ_{ex} 340 nm

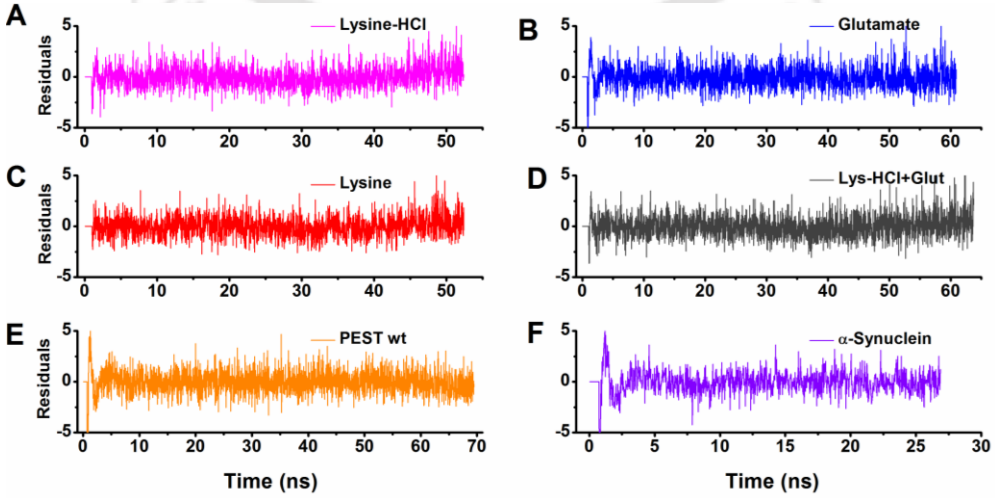

Figure 3.25: Residuals obtained from MEM analysis done for luminescence intensity decay at λ_{ex} 295 nm

3.3 Conclusions

a) The charged amino acids are luminescent in nature in their monomeric forms. Luminescence yield decreases with increasing excitation wavelength.

b) The proteins rich in charged amino acids do show intrinsic luminescence in their monomeric states apart from their aromatic spectral signatures.

c) The luminescence arising from these charge transfer states have lower quantum yield as well as low luminescence lifetime indicating a lower efficiency/rate of charge recombination.

d) The huge Stokes shift observed among all the amino acids and proteins are indicative of the considerable change in the excited state dipole moment resulting in more sensitivity towards solvent polarity.

e) Extinction coefficient has a major role to play behind the origin of observed luminescence intensities apart from the minor contribution from quantum yield.

f) The similarity between charged, non-aromatic amino acids and proteins for the observed emission spectra, excitation spectra, Stokes shift, luminescence lifetime and lifetime distributions suggests a common origin of the observed intrinsic luminescence, which is charge recombination luminescence.

Chapter 4

Human Serum Albumin (HuSA): A model protein to investigate ProCharTS

4.1 Introduction

Human serum albumin (HuSA) is one of the most studied proteins for its structure (Rabbani & Ahn 2019, Sugio et al 1999), function (Fanali et al 2012) and its binding capabilities toward a variety of ligands and drug molecules (Fasano et al 2005, Ghuman et al 2005, Quinlan et al 2005, Varshney et al 2010, Zhong et al 2000). HuSA contains 585 amino acids (Meloun et al 1975) and harbors ~33 % of charged residues in its sequence.

The presence of charged, polar groups and electrostatic interactions control important aspects of protein structure and function (Simonson 2003). For example, charged amino acids like arginine, histidine and lysine at several positions in HuSA are important from its functional and physiological aspects (Barnaby et al 2011, Jacobsen 1978, Kaneko et al 2011, Watanabe et al 2000). The N-terminus DAHK amino acid sequence has been known to bind many metal ions like Co, Cu and Ni (Quinlan et al 2005). Apart from this, this protein is also supposed to have an enhanced surface charge distribution at neutral pH (Lošdorfer Božič & Podgornik 2017) which is rendered by the presence of solvent exposed side chains of charged residues.

The richness of charged residues in HuSA has lured us to investigate this protein for ProCharTS. Since, ProCharTS depends upon the interplay of charged amino acids in close proximity and HuSA being abundant in charged residues, could serve as a model protein to study ProCharTS. Previously, HuSA was reported to show an unusual UV-Vis absorption spectra beyond 325 nm which was speculated to arise from the 7 pairs of lysine in close proximity by some unknown mechanism (Homchaudhuri & Swaminathan 2004). Later it was confirmed that the reason behind such an observation could be photoinduced charge transfer which are now termed as ProCharTS (Prasad et al 2017). Apart from lysine, other charged amino acids like glutamate, aspartate, histidine and arginine are also likely to be involved in the proposed protein charge transfer transitions (Mandal et al 2018). Moreover, the extinction coefficient of HuSA in the spectral region between 325 to 800 nm was found to be higher as compared to those proteins with less charged residues (Prasad et al 2017). This further put forward the abundance of charged residues and their proximity as a pre requisite for the charge transfer transitions.

The factors or the chemical environment that can affect the proximity of charge residues or can affect the charge itself can bring about a change in the ProCharTS. In another words,

the mere change in pH and ionic strength or perturbation of folded structure of protein could bring about a change in the probabilities of charge transfer transitions. And, this is the motive of the current chapter to illustrate the effects of above said conditions on the ProCharTS of HuSA.

To achieve this, absorption-based studies on HuSA was done to reveal how the change in pH and ionic strength can alter the ProCharTS. Unfolding studies were also performed in presence of Gdn·HCl to understand the importance of proximity of side chain of charged residues behind the origin of ProCharTS. In addition to absorption-based studies, luminescence from charge transfer states are also investigated to display how the luminescence from charge transfer transitions can uniquely corroborate and interpret the above results.

In the later part of the chapter, intrinsic luminescence from charge transfer states of HuSA molecules are presented. Since, there were report upon the origin of intrinsic fluorescence from oligomeric HuSA molecules (Bhattacharya et al 2017, Bhattacharya et al 2014); the luminescence from HuSA was investigated in more detail. To ascertain that the observed luminescence is originating from the monomeric HuSA molecules and not from any kind of aggregated or oligomeric entities, steady-state anisotropy measurements using Dansyl labelled HuSA were performed. Additionally, linear relationship between the increasing luminescence intensity versus increasing concentrations was also established to strengthen our assumption.

4.2 Results and Discussions

4.2.1 Effect of pH and ionic strength on ProCharTS of HuSA

To study the effects of counter ions on ProCharTS of HuSA, the absorbance spectra of 10 µM of HuSA was recorded in presence of 200 mM KCl and 50 mM phosphate buffer while to evaluate the effect of ionization, absorption spectra were recorded in presence of 0.1 N NaOH and 0.1 N HCl. Similarly, the luminescence spectra was also collected for the identical samples to evaluate the concomitant changes in luminescence intensity (Figure 4.1).

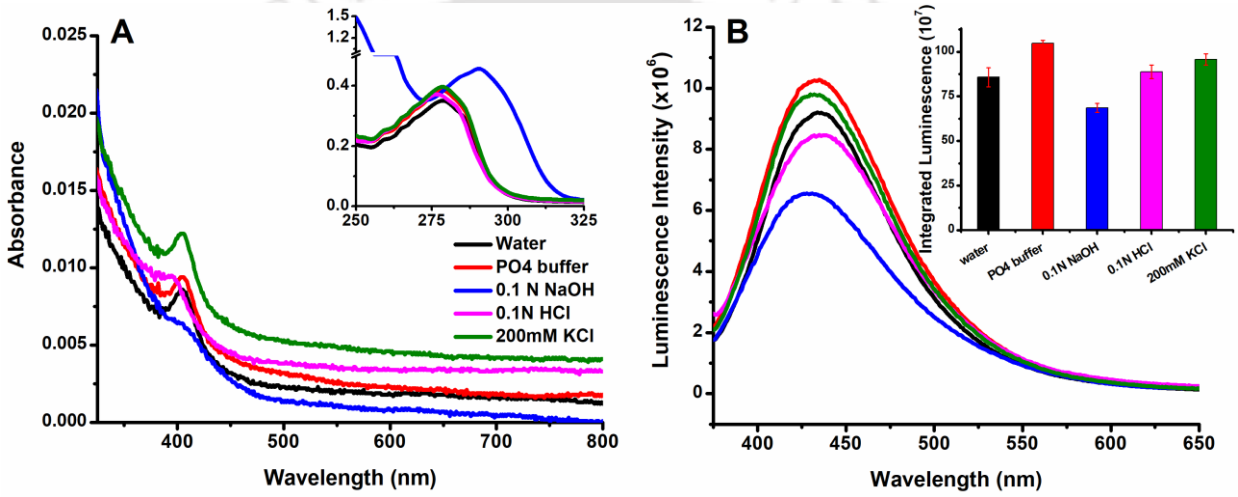

Figure 4.1: Panel **A** shows the ProCharTS in the range of 325-800 nm while the inset shows the change in absorbance contributed by aromatic amino acids. Break is provided between 0.5-1.0. Panel **B** shows the luminescence of HuSA, excited at 355 nm with slit width of 2 nm and 15 nm for emission collection. The inset in panel B shows the integrated luminescence. The concentration of HuSA used was 10 µM.

As evident from Figure 4.1, the presence of high salt (0.2 M KCl) tends to enhance the ProCharTS. This could be due to greater compactness and increased stability of the protein in presence of high salt (Ballou et al 1944, Nishimura et al 2001). However, the presence of counter ions like PO_4^-, K^+, Na^+ or Cl^- could also shield the COO^- or NH_3^+ in proteins affecting the ProCharTS. In this regard, multivalent anions like PO_4^{3-} appears more effective in shielding than K^+ and Cl^-. This is evident from the decreased ProCharTS in presence of phosphate buffer as compared to those in presence of KCl.

At lower pH (0.1 N HCl), the Glutamate side chains are neutralized while the Lysine side chains would remain in NH_3^+ form which can undergo peptide backbone to sidechain charge transfer transitions. Since these transitions are low energy transitions, higher ProCharTS are

observed at longer wavelengths. However, in presence of NaOH, pH reaches ~13.0, which causes the ionization of phenol hydroxyl in tyrosine (Alexander Ross et al 2002) resulting in the shift of absorption spectra as observed in the inset of Figure 4.1A. The higher concentration of hydroxyl groups neutralizes the Lysine side chain (probably by accepting extra H from terminal NH_3^+) interrupting the Lysine–Lysine and Lysine–Glutamate interaction, causing much lower transition probabilities at longer wavelength. The higher Glutamate–Glutamate interaction at this pH is revealed by the higher ProCharTS observed at lower wavelength ~325 nm. The value of absorption at this wavelength is much higher than the value obtained for deionized water.

On the other hand, the changes observed among the luminescence spectra very much reflects a similar trend as observed for absorbance. In this case also, the effect of counter ions tend to increase the luminescence intensity while at higher pH, the luminescence intensity has decreased (Figure 4.1B). These concomitant changes in absorption and luminescence suggests that the phenomenon responsible for the observed luminescence is indeed the charge transfer transitions. Apart from this, a slight blue shift in emission maxima (compared to emission maxima in presence of deionized water) is also observed in presence of NaOH and KCl. The enhanced compactness in presence of high salt and structural perturbation at higher pH could be the reason behind this. These observations suggests that the luminescence from charge transfer states are sensitive towards the solvent polarity and environmental effects (See chapter 6).

4.2.2 Prevalence of luminescence from charge transfer states in HuSA

The luminescence observed from the HuSA (as shown in chapter 3) is quite prevalent in the spectral region where no aromatic amino acids are expected to show any fluorescence. In case of HuSA, the luminescence was observed even when excited towards the red region i.e. even at λ_{ex} 600 nm. However, the luminescence yields are quite lower at longer excitation wavelengths, as shown in Figure 4.2A,C while the normalized luminescence at different excitation wavelengths are displayed in Figure 4.2B.

The observed luminescence clearly shows that there is a dependence of excitation wavelength upon the observed luminescence. Thus, the luminescence here does not follow the Kasha's rule (Kasha 1950). However, this anti-Kasha rule do suggests the role intramolecular charge transfer (Demchenko et al 2017, Scuppa et al 2011). Apart from this,

such an observation also points towards the emissions from different charge transfer states (De los Reyes et al 2015, Shen et al 2018).

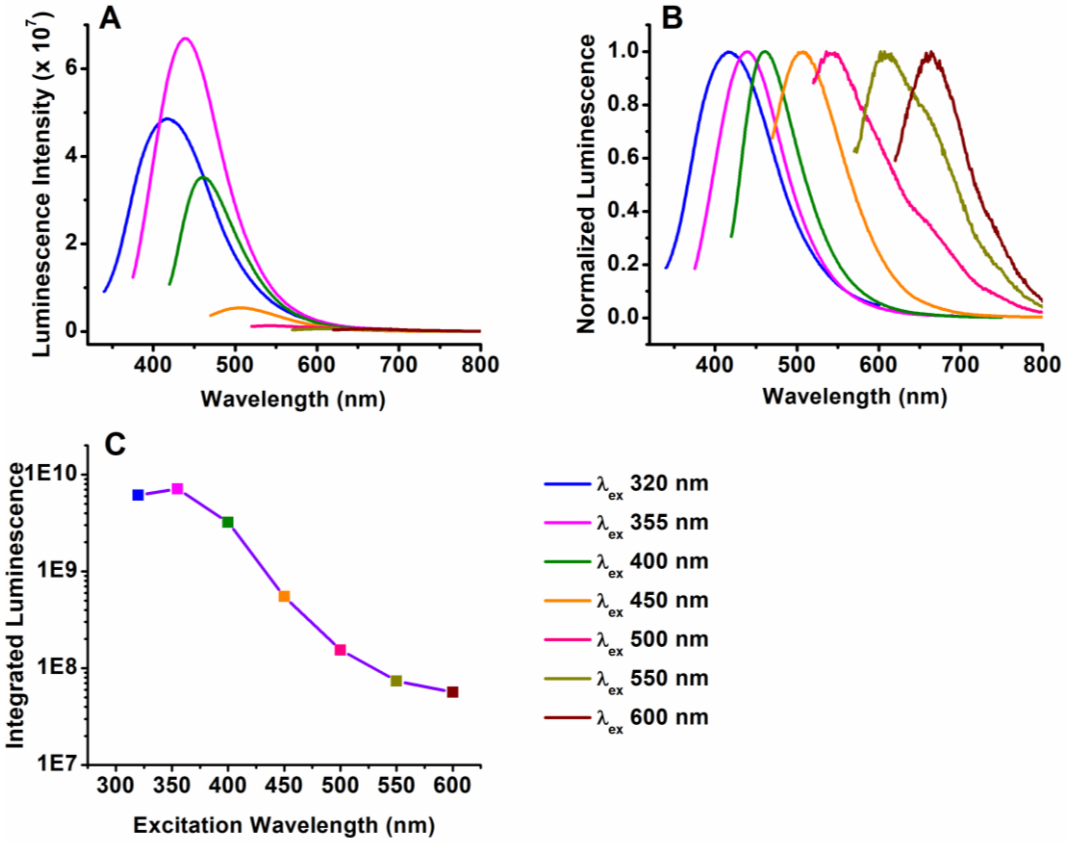

Figure 4.2: Panel **A** and **B** shows the luminescence and normalized luminescence intensity, respectively collected for HuSA at different λ_{ex}. Panel **C** shows the integrated luminescence at different λ_{ex}. All the samples were excited with slit width of 2 nm and emission was collected with slit width of 15 nm. The concentration of HuSA used was 100 µM.

4.2.3 Intrinsic luminescence observed from monomeric HuSA

Luminescence from HuSA was observed for different concentrations ranging from 0.5 µM to 120 µM at λ_{ex} 355 nm (Figure 4.3). To confirm whether the luminescence observed from HuSA molecules are arising from monomeric protein, a plot of total luminescence yield versus concentration was made. A linear relationship was observed between the increase in luminescence intensity with increasing concentration. The Adj. R^2 of obtained linear fit was 0.999 with a slope value of 1.01×10^7 (Intensity/µM). This linear relationship indicates that the luminescence observed are indeed from monomeric HuSA molecules in the concentration range 0.5 – 120 µM. This result is in agreement to the linearity observed in last chapter for the change in absorbance of HuSA with increasing concentration (Figure 3.7AB).

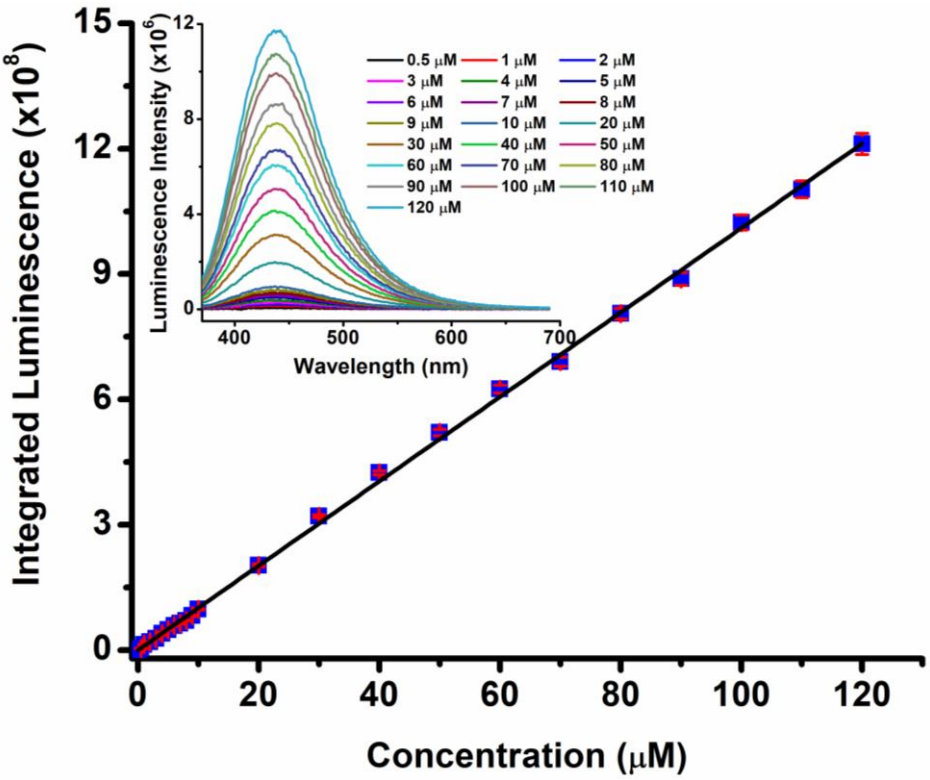

Figure 4.3: Linearity in luminescence is observed for the concentration range from 0.5 μM to 120 μM. Integrated luminescence intensity is linearly fitted with increasing concentration. Inset shows the luminescence spectra of different concentrations of HuSA. All the spectra were collected by excitation at 355 nm with 1 nm of excitation slit width and 5 nm of slit was used for emission collection.

Further, to confirm this finding, steady-state anisotropy of Dansyl-labelled HuSA was done. Dansyl chloride (1-dimethylamino-5napthylsulfonyl chloride) is an excellent probe for fluorescence polarization measurements (Lakowicz 2013). It is an amine reactive fluorophore and can react with the free amino groups of proteins. Once labelled to protein, an increase in absorption at 340 nm could be observed which corresponds to the Dansyl absorption after conjugation with protein (Levi & González Flecha 2003). Figure 4.4 shows the normalized absorption spectra of Dansyl-HuSA (HuSA labelled with Dansyl) and unlabeled HuSA. The increased absorption at ~340 nm for Dansyl-HuSA as compared to HuSA, indicates the success of labeling. The obtained Dansyl-HuSA had the dye per protein ratio of ~0.6.

For the anisotropy measurements, 0.1 μM of Dansyl-HuSA was mixed with 5 and 10 μM of unlabeled HuSA while 25, 50 and 100 μM of unlabeled HuSA contained 1 μM of Dansyl-HuSA. Fluorescence intensity of Dansyl-HuSA and the mixture of Dansyl-HuSA and free unlabeled HuSA is presented in Figure 4.5A. The normalized fluorescence spectra is presented in Figure 4.5B. The emission maxima was found to be ~415 nm among all the

samples when excited at 340 nm, indicating that the labelled Dansyl probe is buried inside the protein away from the aqueous environment.

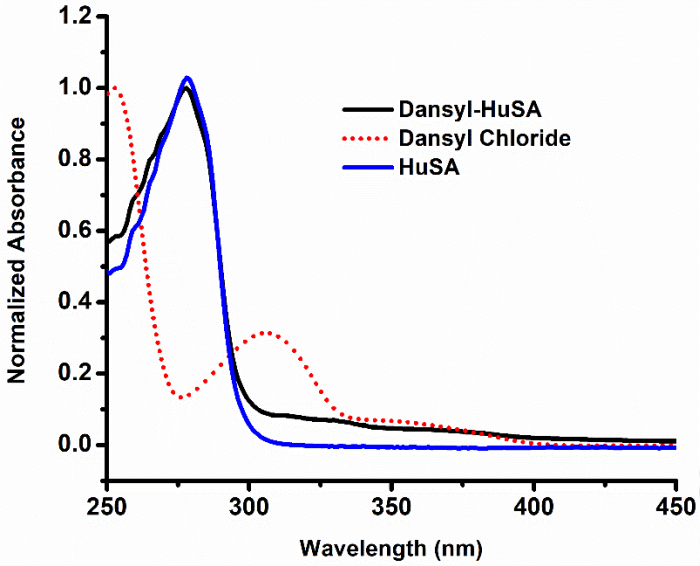

Figure 4.4: Normalized absorption spectra of Dansyl labelled HuSA compared with unlabelled HuSA and free Dansyl Chloride. Dye per protein (D/P) ratio obtained for labelled HuSA was 0.59.

It is obvious from the Figure 4.5A that the fluorescence intensity of mixture of Dansyl-HuSA and unlabeled HuSA is higher than Dansyl-HuSA and the same increases with increasing concentration of unlabeled HuSA. This should not happen since the concentration of Dansyl-HuSA is constant for the mixture containing either 5 µM or 10 µM of unlabeled HuSA (contained Dansyl-HuSA=0.1 µM; dashed line) or for the mixture containing 25-100 µM of unlabeled HuSA (contained Dansyl-HuSA=1 µM; solid lines). This anomalous increase in the fluorescence intensity (even when the concentration of extrinsic fluorophore is constant) suggests the contribution of intrinsic luminescence from HuSA at λ_{ex} 340 nm (as described in Chapter 3, HuSA shows luminescence at λ_{ex} 340 nm). The change in spectral shape (increasing FWHM with increasing concentration of unlabeled HuSA) in Figure 4.5B is also an evidence for the same. These findings will be discussed in details in the forthcoming Chapter 5.

The steady-state anisotropy of all the samples were collected at λ_{ex} 340 nm. Figure 4.6 shows the steady-state anisotropy value of Dansyl-HuSA in presence of different concentrations of unlabeled HuSA molecules. The value of steady-state anisotropy (r_{ss}) for only Dansyl-HuSA was 0.255±0.003. When 5 µM of unlabeled HuSA was added, the value remained almost constant ~0.256. Similarly, with addition of excess of unlabeled HuSA up to 100 µM, a nominal change in r_{ss} was observed, with a value of 0.266±0.002.

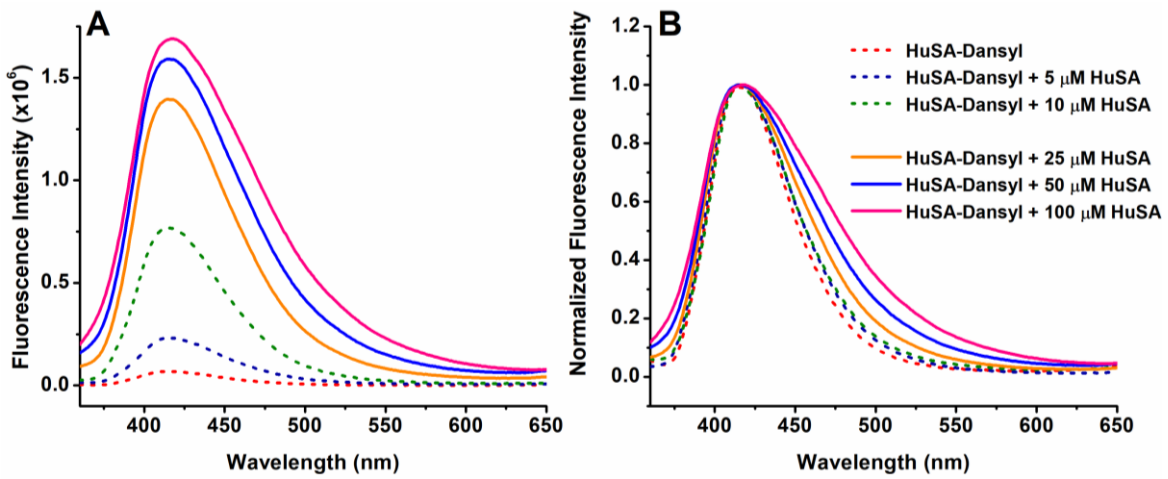

Figure 4.5: Panel **A** shows the steady state fluorescence of Dansyl-labelled HuSA excited at 340 nm with slits width of 5 nm for excitation and emission was collected with 10 nm of slit width. For fluorescence measurements, 0.1 µM (dashed line) of HuSA-Dansyl was mixed with 5 µM and 10 µM of unlabelled HuSA and for 25, 50 and 100 µM of unlabelled HuSA, 1 µM of HuSA-Dansyl (solid lines) was mixed. Panel **B** shows the normalized fluorescence spectra presented in panel A.

With the slightest possibility of aggregation or oligomerization of HuSA, the r_{ss} value should have gone to much higher values than observed in our experiments. The nominal increase in r_{ss} value negates the possibility of intermolecular interactions leading to any oligomer or aggregate formation. This suggests that the HuSA molecules at these concentrations are predominantly in the monomeric form.

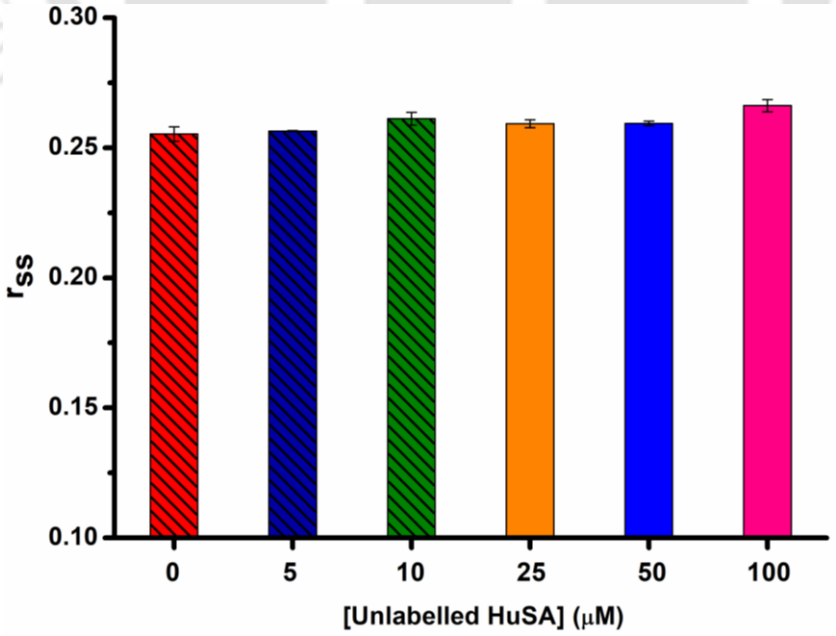

Figure 4.6: Steady-state anisotropy (r_{ss}) values of HuSA-Dansyl in presence of different concentration of unlabeled HuSA. Excitation was done at 340 nm and emission was collected at 415 nm. Dashed bar contains 0.1 µM of HuSA-Dansyl while rest of the sample contained 1 µM of HuSA- Dansyl.

4.2.4 Unfolding of HuSA decreases ProCharTS

HuSA was unfolded in presence of Gdn·HCl (3 M and 6 M) and effect of protein unfolding on the ProCharTS was studied. The very first thing to be done was to ascertain the unfolding of HuSA in presence of Gdn·HCl. This was done in two different ways. First, a slight blue shift in the absorption maximum of aromatic amino acids was observed (Inset of Figure 4.7) which is an indication of its exposure to aqueous environment upon unfolding (Schmid 2001). Secondly, large red shift in the fluorescence spectrum of the buried tryptophan residues (Eftink 1994, Ervin et al 2000) was observed (Figure 4.8), is an evidence of HuSA unfolding.

As observed in Figure 4.7, the unfolding caused by the Gdn·HCl resulted in the decrease of ProCharTS in HuSA. The decrease was maximum for the 6 M Gdn·HCl as compared to 3 M and natively folded HuSA. This decrease in ProCharTS can be interpreted in terms of loss of proximity between the side chains of charged residues in the protein. The proximity, which was present in a natively folded protein, is lost upon unfolding owing to decrease in the photo-induced charge transfer transitions, which finally resulted in the decrease of ProCharTS. Similar results were obtained earlier also upon unfolding of calf thymus histone (Homchaudhuri & Swaminathan 2004).

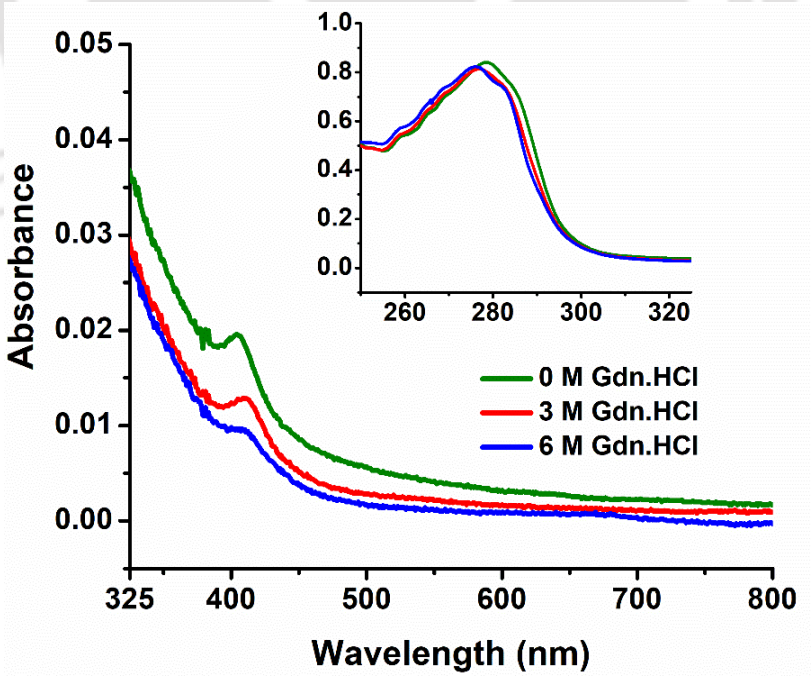

Figure 4.7: Comparison of ProCharTS of 25 µM natively folded and unfolded HuSA. A small peak is at 404 nm (folded protein) and 408 nm for unfolded protein is observed. Inset shows the absorption in the spectral region between 250–325 nm.

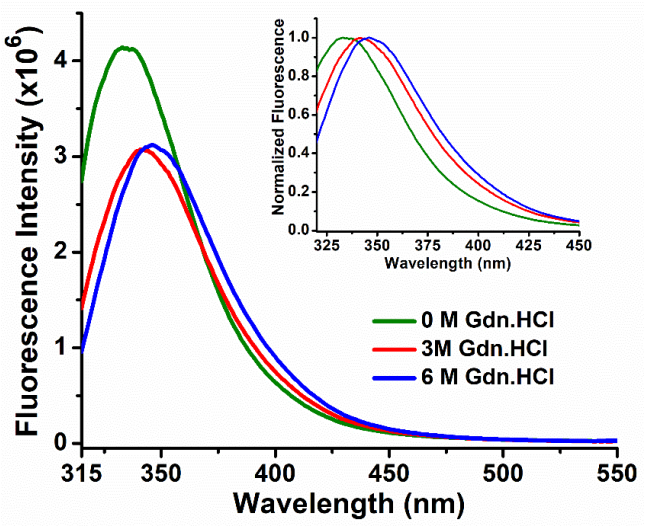

Figure 4.8: Fluorescence spectra of 25 μM HuSA excited at 295 nm with slit width of 2 nm and emission was collected with slit width of 5 nm. Inset shows the normalized emission spectra. Emission maxima has changed from 333 nm (0 M) to 346 nm (6 M).

Next, we explored the luminescence arising from charge transfer states in HuSA at λ_{ex} 355 nm. Similar to the observations made for ProCharTS absorbance, the luminescence intensity of HuSA has decreased upon unfolding. The decrease in luminescence was maximum for the 6 M Gdn·HCl as compared to natively folded HuSA (Figure 4.9). However, unlike tryptophan, in this case almost no shift in the emission maxima was observed (inset of Figure 4.9). This may arise if there is no major change in exposure of charged residues to water happens with addition of Gdn·HCl.

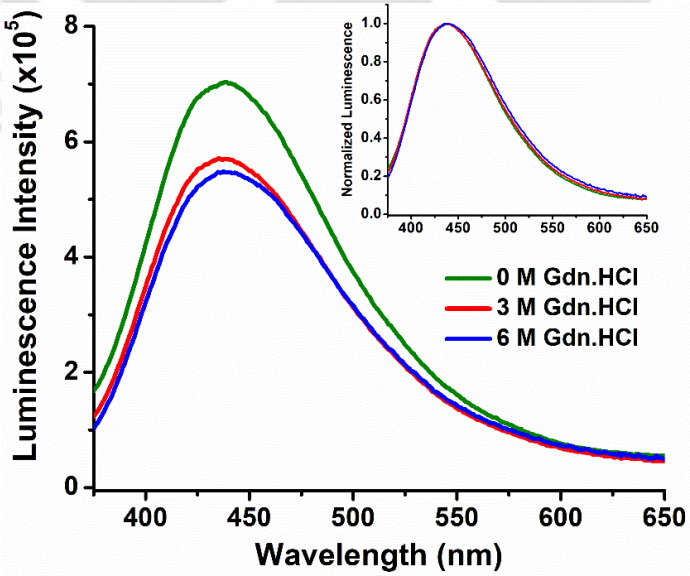

Figure 4.9: Fluorescence spectra of 25 μM HuSA excited at 355 nm with slit width of 2 nm and emission was collected with a slit width of 15 nm. Inset shows the normalized emission spectra. Emission maxima has changed from 339 nm (0 M) to 338 nm (6 M).

Further, time-resolved luminescence studies were done to understand the effect of unfolding on the luminescence lifetime of charge transfer states of HuSA. The time resolved studies were done at λ_{ex} 340 nm. Figure 4.10 represents the luminescence intensity decay of HuSA under different concentrations of Gdn·HCl.

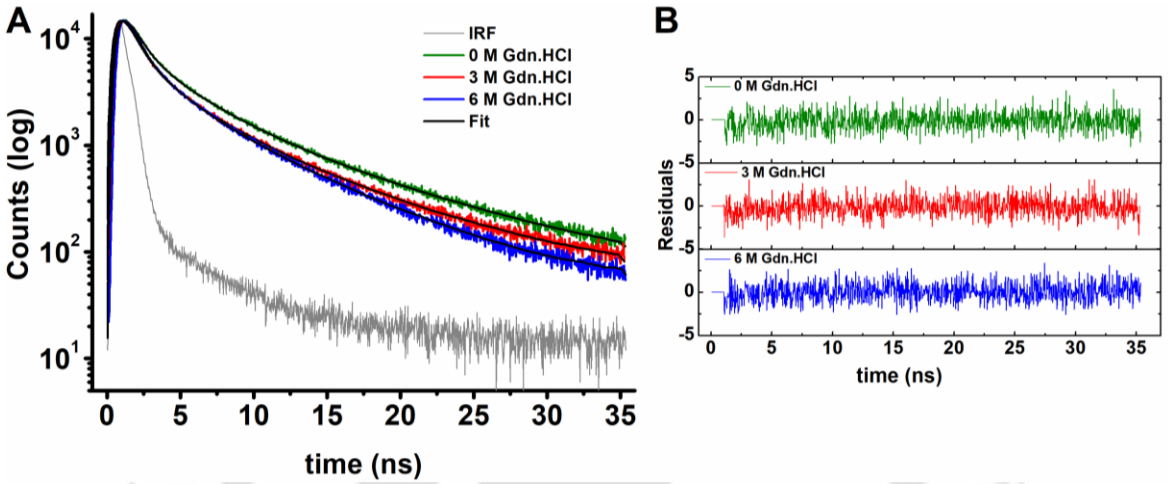

Figure 4.10: Time resolved luminescence decay of HuSA (25 μM) at λ_{ex} 340 nm. Emission was collected with 370 nm long-pass filter. Panel **A** shows the decay and fit while the panel **B** shows the residuals for the three exponential fit.

As observed in Figure 4.10A, the luminescence intensity decay of HuSA in both the native and unfolded conditions displays a multi exponential decay curve, which are fitted well in three exponential model. The goodness of fit can be observed from the randomness in the fitted residuals as shown in Figure 4.10B. The fitted parameters for luminescence intensity decay of HuSA in presence of 0, 3 and 6 M of Gdn·HCl are displayed in Table 4.1 and Figure 4.11.

Sample	α_1	α_2	α_3	τ_1 (ns)	τ_2 (ns)	τ_3 (ns)	τ_{mean} (ns)	χ_R^2
0 M	0.653	0.253	0.094	0.77 (0.04)	2.90 (0.08)	8.48 (0.26)	2.06 (0.05)	1.08
3 M	0.704	0.209	0.087	0.76 (0.03)	2.90 (0.15)	8.03 (0.32)	1.76 (0.03)	1.01
6 M	0.684	0.214	0.103	0.56 (0.05)	2.05 (0.13)	6.13 (0.16)	1.49 (0.06)	1.08

Table 4.1: Fitted parameters obtained from 3 exponential fit for luminescence intensity decay of HuSA in presence of Gdn·HCl. The presented tau values are the average of 4 independent measurements while the alpha values are taken from the best fitted data. Values in parenthesis displays the standard deviation calculated from 4 independent measurements.

The individual α, τ and mean lifetime values of HuSA in absence of Gdn·HCl are very similar to those observed in Chapter 3. The mean lifetime (Figure 4.11C) of HuSA has

decreased from 2.06±0.05 ns to 1.49±0.06 ns in presence of 6 M Gdn·HCl. This decrease is contributed mainly from the decrease of individual tau values ($\tau_{1\text{-}3}$), since the alpha value ($\alpha_{1\text{-}3}$) remains almost constant among all the samples (Figure 4.11AB).

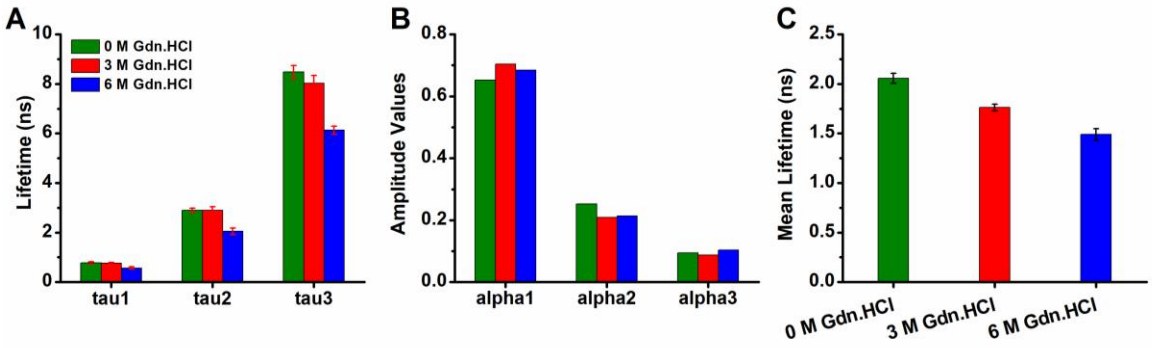

Figure 4.11: Panel **A** and **B** shows the tau and alpha values, respectively, obtained from 3 exponential fit for HuSA under different concentrations of Gdn.HCl. The presented tau values are the average of 4 independent measurements while the alpha values are taken from the best fitted data. Section **C** presents the mean lifetime for the same samples.

Further, to validate the results of discrete analysis, MEM (Maximum Entropy Method) analysis was also done. The distributions obtained from MEM analysis and residuals from the MEM fit are represented in Figure 4.12.

Similar to the results of discrete analysis, three distributions of lifetime were found among all the samples validating the 3 exponential model used to fit the data. The distribution corresponding to highest and second highest lifetime lifetime (τ_3 and τ_2) has shifted to the lower side for 6 M Gdn·HCl. This shift is from ~3 ns to ~2 ns for second largest component and from ~8 ns to ~6 ns for largest component (Figure 4.12A).

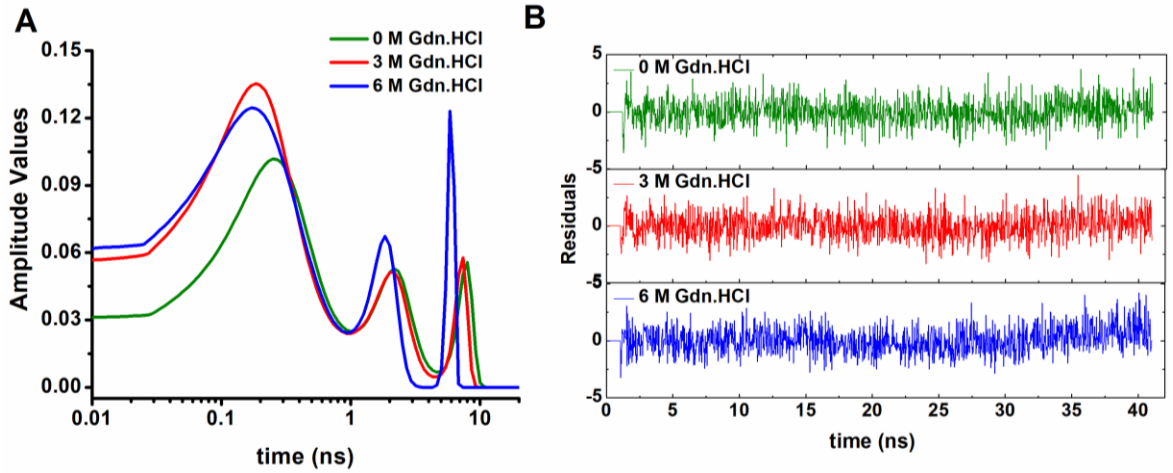

Figure 4.12: Panel **A** shows the lifetime distributions obtained from the MEM analysis while panel **B** shows the residuals for the MEM fit.

However, the smallest component (τ_1) has the maximum contribution among all the samples. Taken together, the shift of all the three distributions towards the lower timescale suggests a smaller mean lifetime of HuSA in unfolded state. Hence, all the changes observed in MEM analysis are quite similar to those obtained from the discrete analysis.

It should be noted that the decrease in mean lifetime implies a decrease in quantum yield of ProCharTS luminescence with unfolding in presence of Gdn·HCl. This may perhaps be due to decrease in charge recombination efficiency.

As a conclusion, the unfolding of HuSA causing the loss of proximity between the side chains of charged residues resulted in lower probabilities of charge transfer transitions. This in turn caused a decrease in ProCharTS absorption as well as luminescence observed from charge transfer states. Further, unfolding resulted in a lower quantum yield from ProCharTS emission. Therefore, ProCharTS could be used to detect the structural transitions in protein devoid of any aromatic amino acids but rich in charged residues.

4.3 Conclusions

a) ProCharTS absorption intensities are sensitive to changes in pH and ionic strength and so are the luminescence from charge transfer states.

b) Luminescence from charge transfer states in HuSA are emissive all the way up to λ_{ex} 600 nm. However, the yields at longer excitation wavelengths are much lower.

c) Intrinsic luminescence from HuSA molecules are observed from their monomeric states as revealed by steady-state anisotropy measurements and linearity with concentration in luminescence and absorbance plots.

d) ProCharTS is sensitive to the three-dimensional proximity of side chains among charged residues for the charge transfer transitions to happen. Loss of proximity, as in the case of protein unfolding, can decrease ProCharTS substantially.

Chapter 5

Effect of ProCharTS on extrinsic and intrinsic fluorescent probes in proteins

5.1 Introduction

The broad absorption range of ProCharTS spanning throughout the UV-Visible spectrum provides an immense opportunity to reveals its effects on the various intrinsic as well as extrinsic probes. Since, prerequisite for energy transfers as observed in Förster resonance energy transfer (FRET) is the overlap of donor emission band with the absorption band of acceptor molecule (Forster 1946, Stryer & Haugland 1967), ProCharTS can potentially interact with other fluorophores due to its wide spread absorption range. However, the phenomena involved under this study, protein charge transfer spectra (ProCharTS) cannot be approximated towards the involvement of a defined fluorophore as in FRET. Here, the chromophores are believed to be the selective arrangements of interacting amino acids in close proximity (Prasad et al 2017). Nevertheless, a similar phenomenon could possibly be studied.

Previously, it has been reported that the charged residues (Lys, Glu, Arg, Asp, and any N- and C-terminus residue) in the vicinity of tryptophan in proteins can affect the fluorescence of tryptophan (Vivian & Callis 2001) by shifting the emission maxima. This contribution from the charged residues were suspected to be originating from long-range nature of Coulomb interactions. Moreover, charged residues like Glu, Arg and Asp were reported to quench the Trp fluorescence in proteins (Chen & Barkley 1998) which was suspected to be achieved by the excited-state electron transfer. This was found to be highly dependent upon the proximity and orientation of the amino acid side chains towards the indole ring. However, the energy transfer to/from the charge transfer states are not well explored in case of proteins except for a few instances among bacteriochlorophyll proteins (Wahadoszamen et al 2014).

Here in the present chapter, we have tried to understand the effect charged residues in proteins and charged, non-aromatic amino acids on some typical fluorophores like tryptophan and Dansyl.

The Trp analogue, NATA (N-acetyl-L-Tryptophanamide) was selected as a model for intrinsic chromophore (Trp) in proteins. Since, it was observed (in Chapter 3) that the charged, non-aromatic amino acids, Glutamate and Lysine have maximum luminescence when excited in the UV region; their plausible effects on the steady-state fluorescence and fluorescence lifetime of NATA could be studied. Similarly, the consequences of charged

protein (PEST wt) on the fluorescence lifetime of NATA were also investigated. Finally, the effects of charged residues present in proteins (with no aromatic amino acids) upon the fluorescence lifetime of Trp was studied. This was accomplished by a comparative study of PEST wt and its mutant, PEST M1 (with an inserted Trp).

The origin of multiple lifetime of Trp are supposed to be primarily due to emission from two nearly identical electronic absorption transitions (^1L_a and ^1L_b state) of Trp (Valeur & Weber 1977) or due to the presence of rotameric structures about the C_α – C_β bonds (Ghisaidoobe & Chung 2014, Pan & Barkley 2004). This study could provide an alternate insight toward the origin of multi exponential decay of Trp in proteins, dependent upon the contributions from charged residues in protein.

On the other hand, extrinsic fluorophore, Dansyl is studied for change in various photo-physical characteristics mainly the steady-state fluorescence and fluorescence lifetime when labelled to a protein (HuSA) rich in charged amino acids and in excess presence of such charged proteins. As shown in Chapter 4, the change in spectral shape and intensity of Dansyl-HuSA at λ_{ex} 340 nm in presence of unlabeled HuSA, are further investigated in this chapter to evaluate any concomitant change in fluorescence lifetime.

These studies can help understand the effects of charged residues upon both the extrinsic and intrinsic protein fluorophores, providing a clue towards the phenomenon of energy transfer with ProCharTS as acceptor and presence of an additional chromophore like ProCharTS in the protein.

5.2 Results and Discussions

5.2.1 Effect of ProCharTS on fluorescence of an extrinsic probe, Dansyl

Dansyl (1-dimethylamino-5napthyl sulfonyl chloride) is one of the most commonly used fluorescent probes to label proteins mainly for the polarization studies. It is highly sensitive towards the solvent polarity and has a fluorescence lifetime of ~10 ns (Lakowicz 2013, Weber 1952).

To explore the effects of ProCharTS on this extrinsic probe, Dansyl was labelled to the HuSA protein and steady-state and time-resolved fluorescence studies were performed. Being amine reactive, Dansyl is conjugated to an un-protonated NH_2 group of one of the 59 Lysine residues or on the N-terminus of HuSA. Site-specific labelling was not required for the type of study involved. Often in protein aggregation investigations, a tiny amount of dansyl-labelled protein is mixed with excess of unlabeled protein. We wanted to investigate the consequences of such additions with HuSA.

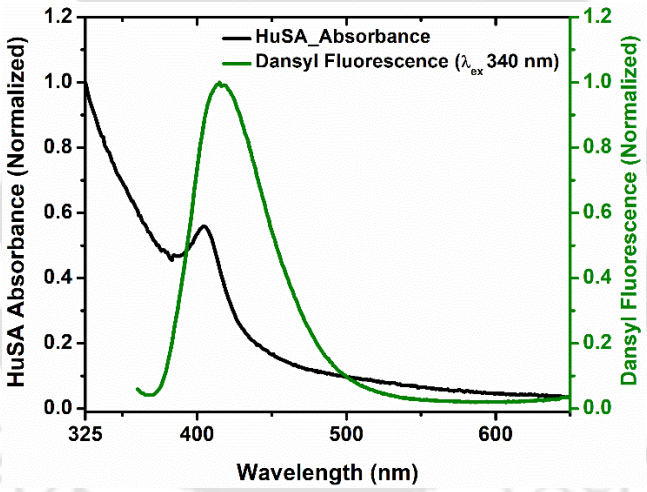

Figure 5.1: Normalized absorption of HuSA is displayed in black cure while the normalized fluorescence of Dansyl-HuSA at λ_{ex} 340 nm is shown in olive curve. A small peak in absorbance of HuSA is observed at 404 nm. The emission maxima for the fluorescence from Dansyl-HuSA is at 415 nm.

As, discussed in the Chapter 4, the anomalous increase in the fluorescence intensity of Dansyl-HuSA at λ_{ex} 340 nm with increasing concentration of unlabeled HuSA (concentration of Dansyl-HuSA being constant) was suspected to arise from the charge transfer states of HuSA itself. Since, the ProCharTS of HuSA overlaps the emission spectra of Dansyl, (as shown if Figure 5.1) there could be a possibility of energy transfer from the excited state Dansyl moiety to the charge-transfer states of HuSA. Under these

circumstances, there should be eminent effects on the fluorescence of the Dansyl in presence and excess presence of HuSA molecules.

As observed from the Figure 5.2, there is a regular increase in the FWHM (full width at half maximum) of the normalized fluorescence spectra of Dansyl-HuSA in presence of increasing concentration of unlabeled HuSA. The FWHM for Dansyl-HuSA was calculated to be ~60 nm, which increases to ~ 71 nm, and ~91 nm in presence of 25 µM and 100 µM of unlabeled HuSA, respectively. Moreover, the luminescence spectra of HuSA at λ_{ex} 340 nm has FWHM of ~132 nm. This increasing FWHM with increasing concentration of unlabeled HuSA molecules suggests a definite contribution of HuSA ProCharTS luminescence in the observed fluorescence of Dansyl. Perhaps owing to larger molar absorptivity and fluorescence quantum yield of dansyl probe, the dansyl emission appears to dominate the emission in the mixture.

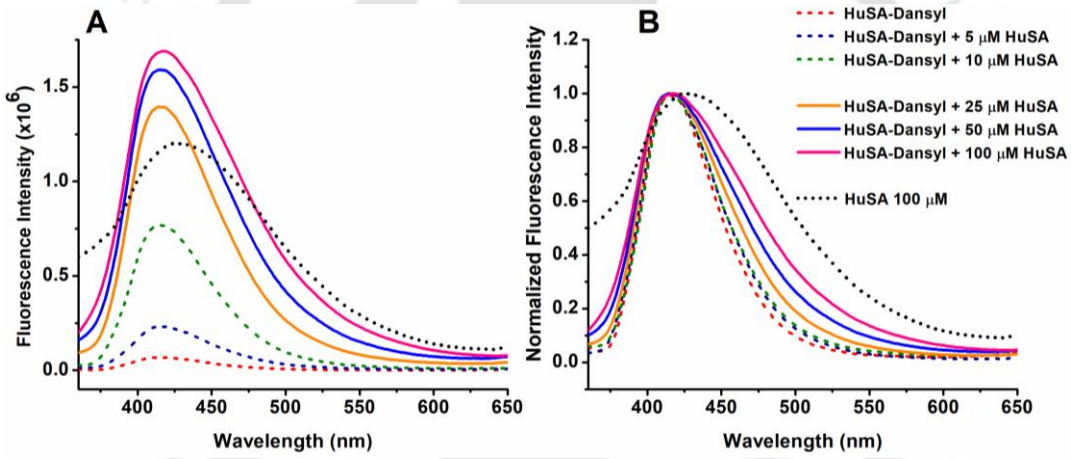

Figure 5.2: Panel **A** and **B** shows the fluorescence spectra and normalized fluorescence, respectively for Dansyl-HuSA at λ_{ex} 340 nm in presence of different concentration of unlabeled HuSA. Dashed and solid lines indicates the presence of 0.1 and 1 µM HuSA-Dansyl, respectively in the mixture. Dotted line represents the luminescence of HuSA under similar conditions.

With pronounced effects on the steady-state fluorescence measurements, time-resolved studies were also done to evaluate the effects on the fluorescence lifetime of the Dansyl. This was achieved by analyzing the identical samples for fluorescence intensity decay at λ_{ex} 340 nm.

Figure 5.3 displays the fluorescence intensity decay of Dansyl-HuSA in presence of different concentrations of unlabeled HuSA. It is clear from the intensity decay curve that the decay indeed is multi-exponential in nature. All the decays were well fitted in the 3 exponential model. The residuals obtained from fit are displayed in the Appendix-III as Figure A1 and

the fitted parameters (α and τ) are displayed in the Figure 5.4 and τ_{mean} in Figure 5.5 and Table 5.1.

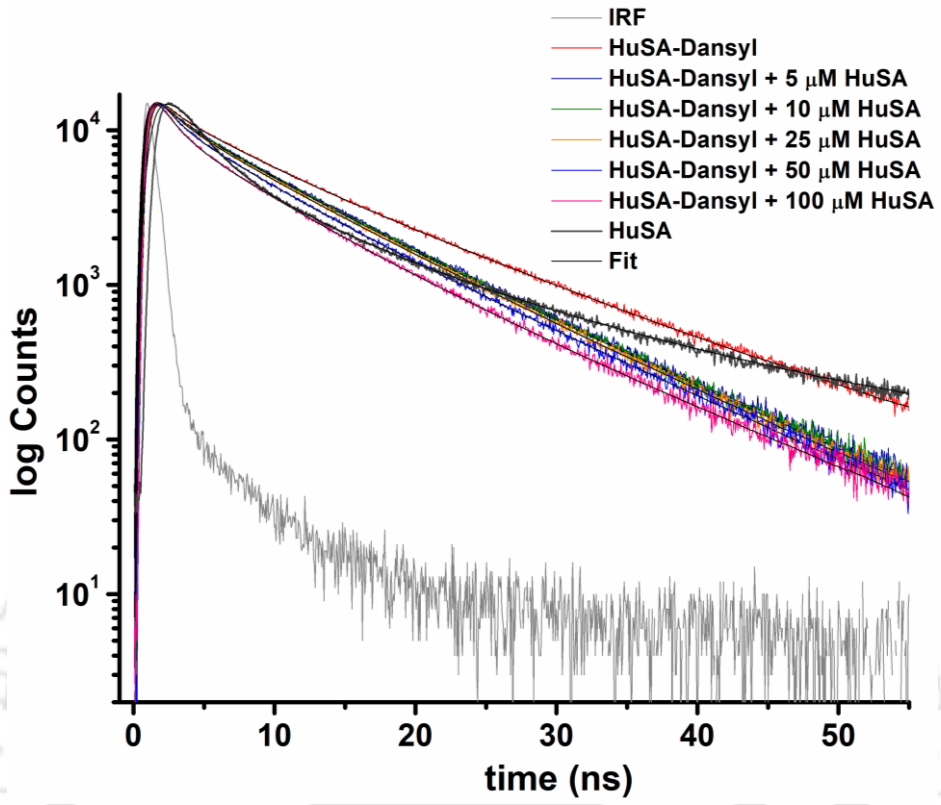

Figure 5.3: Fluorescence intensity decay curve of Dansyl-HuSA in presence of different concentrations of unlabeled HuSA. Black lines shows the fitted curve for three exponential model. Samples were excited at λ_{ex} 340 nm and emission was collected with 370 nm long-pass filter. Residuals of fit are shown in Appendix-III as Figure A1.

The individual component (τ_3) for Dansyl-HuSA has a value of 11.98±0.13 ns, which displays the lifetime of Dansyl fluorophore with highest contribution (α_1) among all the samples (Figure 5.4B). This component has decreased to ~10 ns upon addition of unlabeled HuSA and remained almost constant for rest of the samples. The value of this component (τ_3) observed for HuSA is 8.48±0.26 ns.

The values of τ_1, τ_2 and τ_3 remained almost same among all the samples except for pure HuSA (Figure 5.4B). Therefore, the decrease in mean lifetime (τ_{mean}) as observed in Figure 5.5 can be attributed to the changes in the amplitude values (Figure 5.4A). As evident from Figure 5.4A, the contribution (α_3) from the largest component (τ_3) has continuously decreased while the contribution (α_1) from smallest component (τ_1) has concomitantly increased with increasing concentration of unlabeled HuSA. This mirrored change in contributions from the largest (τ_3) and the smallest components (τ_1) has driven the change

in calculated mean lifetime from 6.53±0.35 ns (for Dansyl-HuSA) to 4.44±0.09 ns (for Dansyl-HuSA+100 µM HuSA), whereas the mean lifetime for HuSA was 2.06±0.05 ns. This clearly implies apparent quenching of Dansyl conjugated HuSA in presence of increasing concentrations of free HuSA.

Sample	α_1	α_2	α_3	τ_1 (ns)	τ_2 (ns)	τ_3 (ns)	τ_{mean} (ns)	χ_R^2
Dansyl-HuSA	0.275	0.295	0.43	0.7546 (0.16)	4.672 (0.29)	11.98 (0.13)	6.53 (0.35)	1.048
+ 5 µM HuSA	0.278	0.234	0.489	1.079 (0.18)	5.109 (0.28)	10.096 (0.22)	6.01 (0.31)	1.084
+ 10 µM HuSA	0.345	0.265	0.39	0.929 (0.04)	5.145 (0.14)	10.242 (0.05)	5.598 (0.1)	1.105
+ 25 µM HuSA	0.34	0.257	0.403	0.995 (0.17)	4.832 (0.15)	10.076 (0.05)	5.51 (0.26)	1.035
+ 50 µM HuSA	0.42	0.27	0.31	1.016 (0.16)	4.946 (0.51)	10.319 (0.27)	4.96 (0.2)	1.112
+ 100 µM HuSA	0.483	0.285	0.233	1.138 (0.07)	5.312 (0.33)	10.786 (0.28)	4.44 (0.09)	1.23
HuSA	0.653	0.253	0.094	0.77 (0.04)	2.9 (0.08)	8.48 (0.26)	2.06 (0.05)	1.08

Table 5.1: Fitted parameters obtained from 3 exponential fit for the decay curves displayed in Figure 5.3. The values in parenthesis represents the standard deviation from three independent measurements. The α values are displayed from the best obtained fit.

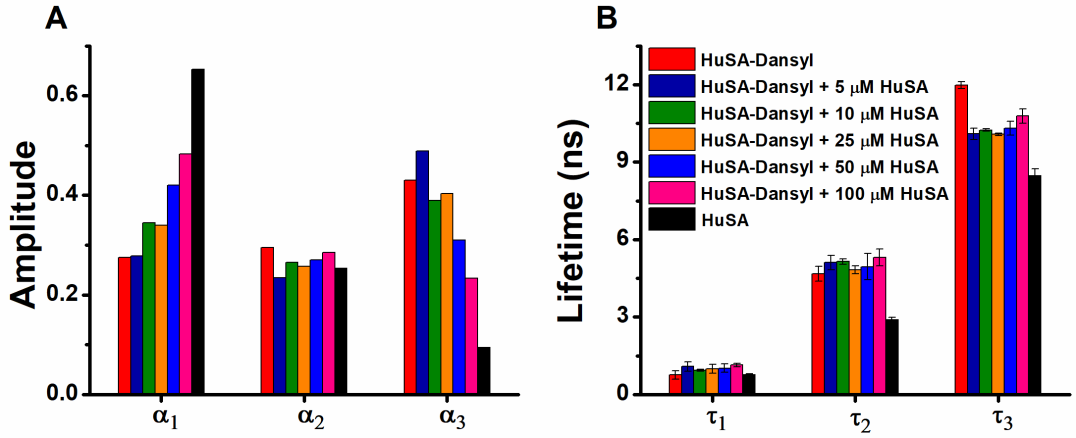

Figure 5.4: Panel **A** and **B** shows α and τ value, respectively obtained from 3 exponential fit. The presented τ values are the average of 3 independent measurements while the α values are taken from the best fitted data.

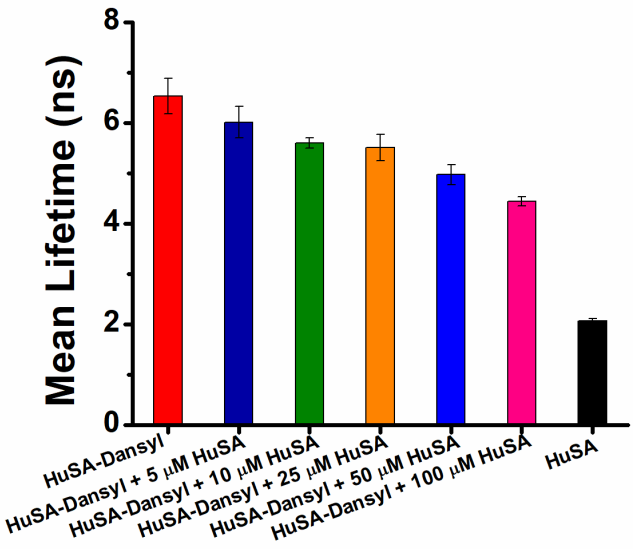

Figure 5.5: Mean lifetime of Dansyl-HuSA in presence of different concentrations of unlabeled HuSA

With the gradual addition of higher concentrations of unlabeled HuSA, the values of α_1 and α_3 for different mixed samples of Dansyl-HuSA, resembles more of like the HuSA. This clearly suggests the influence of HuSA on the fluorescence of Dansyl since HuSA is also intrinsically luminescent at λ_{ex} 340 nm, where the Dansyl probes are excited.

Further, to validate the above results, MEM analysis was also done. The three distributions obtained from MEM analysis (Figure 5.6) validates the 3 exponential model used for the discrete analysis. For Dansyl-HuSA, the highest contribution is for the largest component ~12 ns, which has shifted to ~10 ns (similar to discrete analysis) for rest of the samples. The increase in the amplitude of shortest lifetime component and concomitant decrease in the amplitude of longest lifetime component are also evident with increasing concentrations of unlabeled HuSA (Figure 5.6A-F). However, HuSA displays a broad distribution, where the smallest component has the largest amplitude while the largest lifetime component is ~8 ns (Figure 5.6G). These observations and changes are all consistent with those revealed from discrete analysis. The residuals obtained for the MEM fit are displayed in Appendix-III as Figure A2.

From the above observations, it is clear that the luminescence from charge transfer states of HuSA significantly affects the fluorescence of Dansyl probe. Certainly, the effect is more pronounced in presence of higher concentrations of unlabeled HuSA. Overall, the addition of free HuSA gives an impression of apparent quenching.

However, the decrease in the α_3 values suggests a change in the microenvironment associated with ~12 ns component. This could be attributed to the intramolecular

interactions between the Dansyl probe and side chain residues of protein involved in charge transfer transitions.

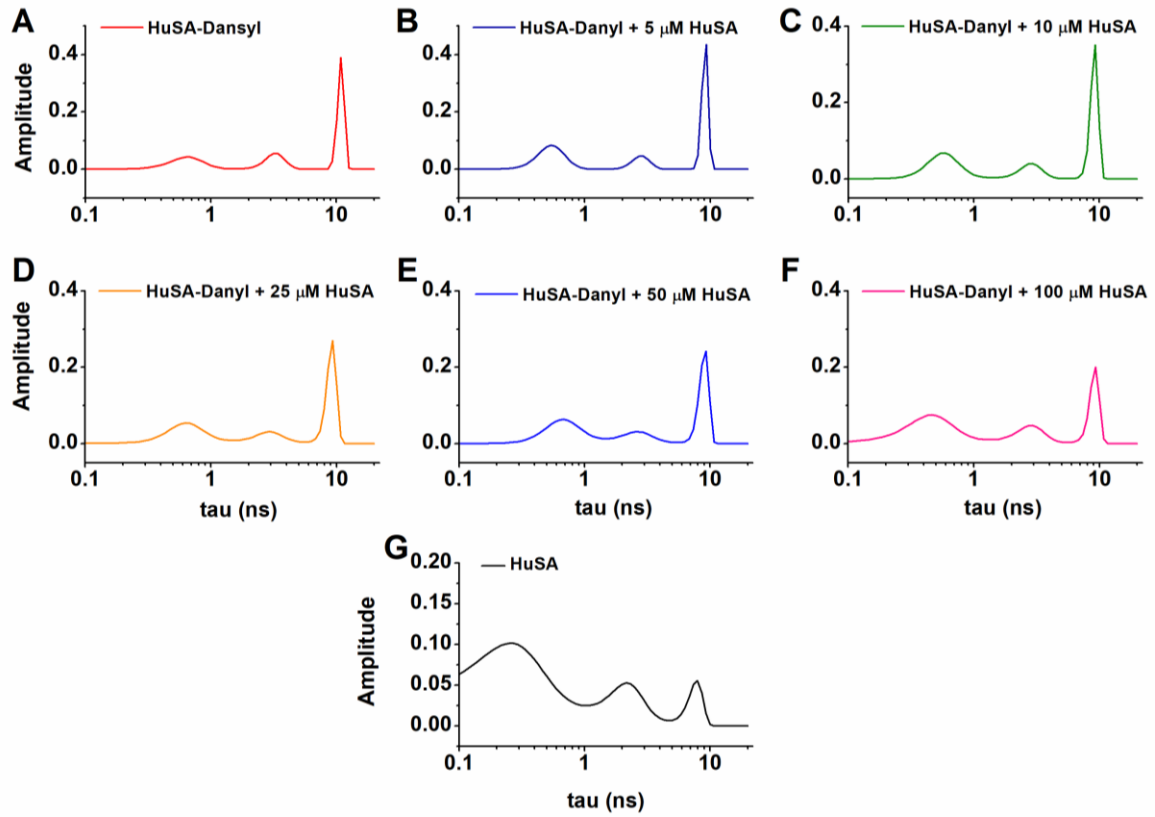

Figure 5.6: Lifetime distributions obtained from MEM analysis for Dansyl-HuSA in presence of different concentrations of unlabeled HuSA. Residuals for the fit are shown in Appendix-III as Figure A2.

Observations made with the same probe, labelled to a protein with significantly lesser-charged amino acids in its sequence (hen egg white lysozyme; ~21% vs 33% for HuSA), showed a similar value (12.14 ns) for largest component (τ_3) (Table 5.2) (Homchaudhuri et al 2006). The other components (τ_1 and τ_2) are also quite similar for the two Dansyl labelled proteins, listed in Table 5.2. These similarities do show the absence of explicit energy transfer but the drastically different amplitude values also indicates the different microenvironments in which the Dansyl probe is present. Here, the charged residues in HuSA appear to drastically diminish the amplitude of longest lifetime component of Dansyl probe while concomitantly increasing the remaining amplitudes.

Now, the intriguing question is why the change in the amplitude of the largest and smallest components are observed upon addition of unlabeled HuSA. The answer lies with the luminescence contributions from the HuSA itself. HuSA also has similar lifetime values and lifetime distributions as of Dansyl (Table 5.1). Thus, it can be concluded that the

fluorescence properties of extrinsic probes, like Dansyl could change when labelled to a protein harboring high percentage of charged residues. In that case, the charge transfer states in protein can modulate the fluorescence from such extrinsic fluorophores by adding up their own contributions to the total luminescence arising from the sample.

Protein	α_1	α_2	α_3	τ_1 (ns)	τ_2 (ns)	τ_3 (ns)	τ_{mean} (ns)	χ_R^2
Dansyl-HuSA	0.275	0.295	0.43	0.75 (0.16)	4.67 (0.29)	11.98 (0.13)	6.53 (0.35)	0.998
Dansyl-HEWL*	0.02	0.06	0.92	0.96	5.03	12.14	14.48	1.4

Table 5.2: Fitted parameters obtained from 3 exponential decay fit of two different proteins. The values in parenthesis indicates the standard deviations from three independent measurements. Asterisk (*) marked data is taken from (Homchaudhuri et al 2006).

5.2.2 Effect of ProCharTS on the fluorescence of intrinsic probe

To study the effects of ProCharTS on intrinsic probe, the design of the experiment was kept easy to maneuver and control. For this, analogue of Trp, NATA was selected as a model for the intrinsic Trp emission from proteins (Ray et al 2008) while to recreate ProCharTS, different amino acids (Lysine, Lysine·HCl and Glutamate) are utilized. This was done after taking into account the difficulty in creating ProCharTS in full-length protein. On the other hand, the flexibility in controlling ProCharTS by altering the concentration of charged amino acids would be an easier and artificial way to recreate ProCharTS in the surrounding of Trp in NATA. However, in the later parts of this section, similar studies are done utilizing protein rich in charge residues, PEST wt (sequence shown in Figure 2.11AB).

5.2.2.1 Effect of Lysine on the fluorescence of NATA

Steady-state fluorescence of NATA at λ_{ex} 295 nm was observed to decrease in presence of Lysine (Figure 5.7A). However, the absolute decrease in the fluorescence intensity is quite minimal (Figure 5.7B; unshaded bars). It should be noted that in order to specifically collect the signals from the spectral region of maximal fluorescence of NATA, integrated fluorescence from steady-state measurements were calculated only between 320-360 (unshaded bars) nm (similarly for time resolved studies a band-pass filter (340±20 nm) was used). On the other hand, the increase in the FWHM of the fluorescence spectra and net integrated fluorescence (shaded bars) indicates the contribution from the luminescence of Lysine (at λ_{ex} 295 nm Lysine show intrinsic luminescence).

Further, time resolved fluorescence studies were performed under identical conditions to reveal the effect of luminescence from charge transfer states in Lysine on the fluorescence lifetime of NATA. Figure 5.8 displays the fluorescence intensity decay of NATA in presence of different concentrations of Lysine. Although, the NATA is expected to show mono-exponential decay (Boens et al 2007), but in presence of Lysine it deviated from this trend. For mono-exponential fit, bad residuals for the fit and higher χ_R^2 are obtained (Figure 5.8) but the same are fitted well in bi-exponential model (Figure 5.9).

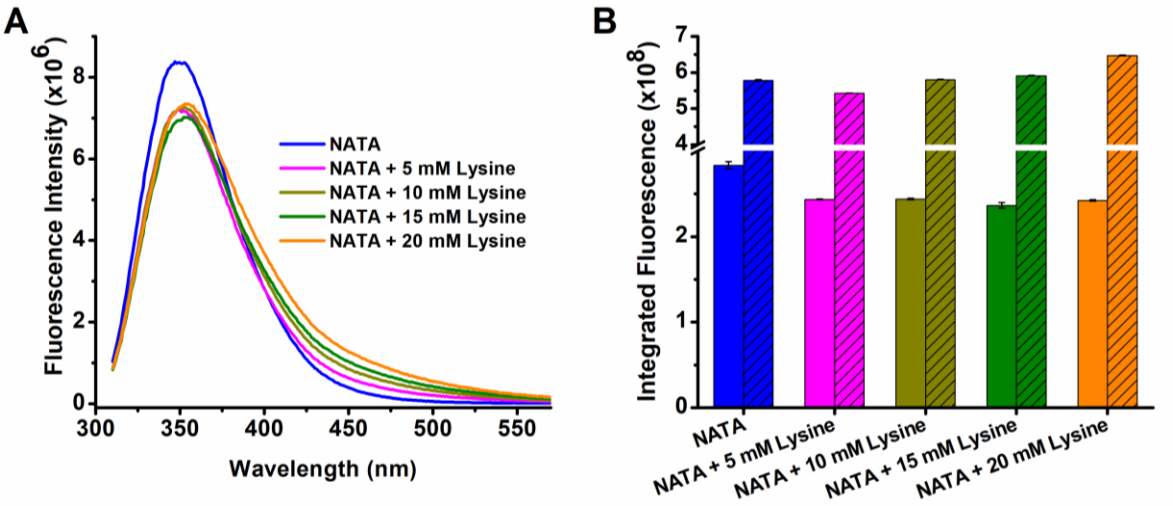

Figure 5.7: Panel **A** shows the fluorescence intensity of 20 µM NATA at λ_{ex} 295 nm in presence of different concentrations of Lysine. Panel **B** shows the integrated fluorescence calculated between 320-360 nm (unshaded bars) and 320-560 nm (shaded bars). Break in panel B is provided between 3–4 x 10^8.

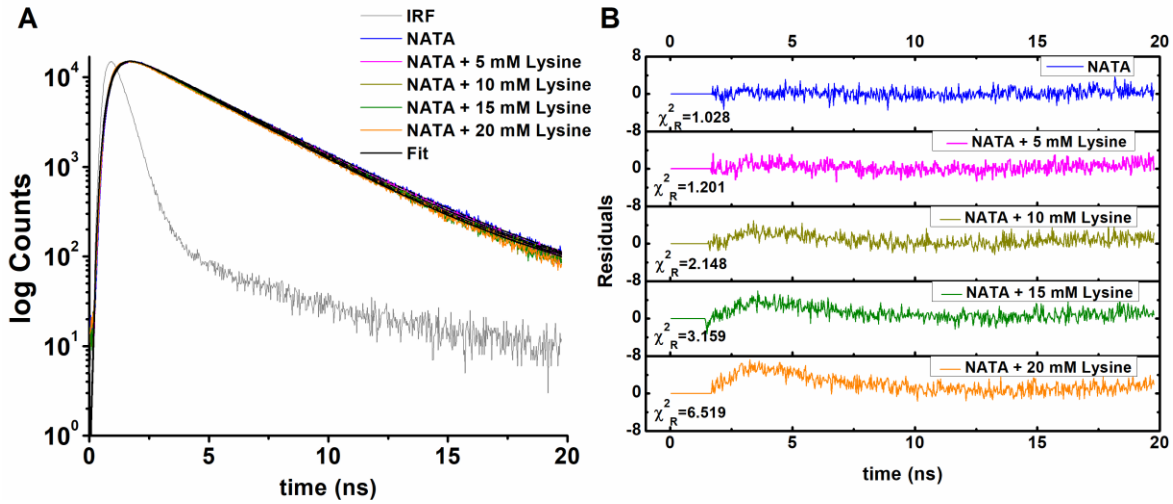

Figure 5.8: Panel **A** shows the fluorescence intensity decay and 1 exponential fit for 20 µM NATA at λ_{ex} 295 nm in presence of different concentration of Lysine. Panel **B** shows the residuals from the fit. Emission was collected using 340±20 nm band pass filter.

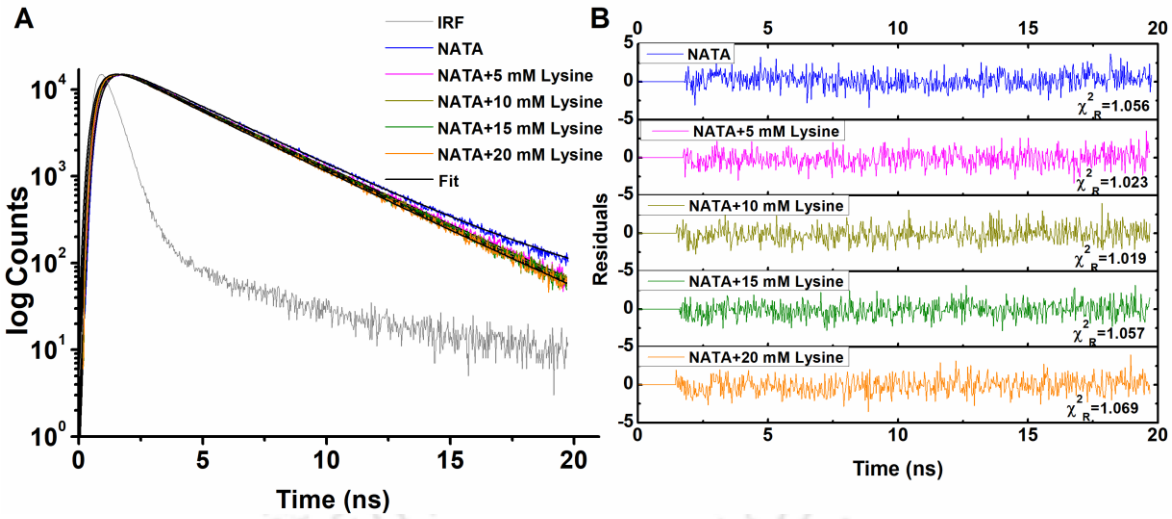

Figure 5.9: Panel **A** shows the fluorescence intensity decay and 2 exponential fit for 20 µM NATA in presence of different concentration of Lysine. Panel **B** shows the residuals from the 2 exponential fit. NATA is fitted in 1 exponential model. Emission was collected using 340±20 nm band pass filter.

The fitted parameters are displayed in Table 5.3. It is clear from the table, that there is an increase in the contribution (α_1) from the longer component (τ_1) and decreased contributions (α_2) form shorter component (τ_2) when the concentration of Lysine was increased from 5 mM to 20 mM. However, τ_1 is almost constant (between 3.49-3.45 ns) while a slight decrease in τ_2 was observed (from 2.44 ns to 2.28 ns). The change observed in α values derived a minor change in the mean lifetime of the NATA in presence of Lysine. Mean lifetime changed from 3.01 ±0.003 ns to 2.87±0.006 ns (Table 5.3).

Sample	α_1	α_2	τ_1 (ns)	τ_2 (ns)	τ_{mean} (ns)	χ_R^2
NATA	1	-	3.06 (0.02)	-	-	1.056
+ 5 mM Lysine	0.504	0.496	3.49 (0.05)	2.44 (0.05)	3.01 (0.003)	1.023
+ 10 mM Lysine	0.634	0.366	3.36 (0.01)	2.12 (0.02)	2.95 (0.008)	1.019
+ 15 mM Lysine	0.615	0.385	3.46 (0.17)	2.29 (0.21)	2.92 (0.005)	1.057
+ 20 mM Lysine	0.620	0.380	3.45 (0.13)	2.28 (0.15)	2.87 (0.006)	1.069

Table 5.3: Fitted parameters obtained from 2 exponential fit of fluorescence intensity decay of NATA in presence of Lysine. Values in parenthesis indicates the standard deviation from 3 independent measurements. The α values are taken from the best fitted data. NATA is fitted in 1 exponential model.

The result from the discrete analysis are validated by MEM analysis. For lower concentration (5 mM) of Lysine, only one distribution was observed while for rest of the concentrations two distributions were obtained. Surprisingly, distribution at lower time scale (~0.5 ns) revealed by MEM was not resolved by the discrete analysis. However, both the

lifetimes (τ_1 and τ_2) revealed from discrete analysis are enveloped within single distribution (between 2-4 ns) in MEM (Figure 5.10).

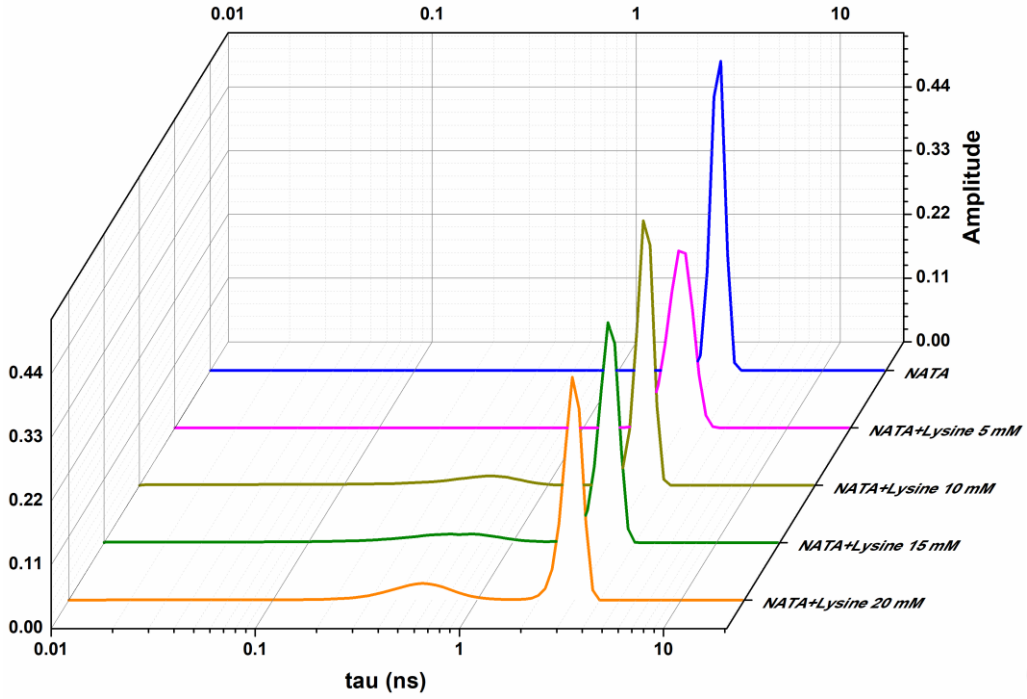

Figure 5.10: Lifetime distributions obtained for NATA in presence of Lysine. Residuals from the fit are displayed in Appendix-III as Figure A3.

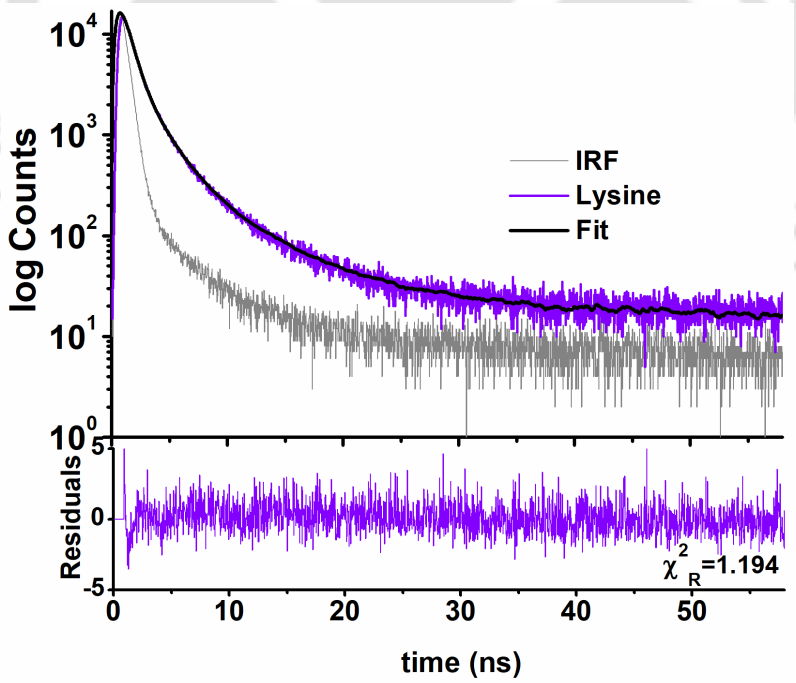

Figure 5.11: Luminescence intensity decay of Lysine at λ_{ex} 295 nm and its 3 exponential fit. Emission collected using 340±20 nm band pass filter. Lower panel displays the residuals obtained from the fit.

Sample	α_1	α_2	α_3	τ_1 (ns)	τ_2 (ns)	τ_3 (ns)	τ_{mean} (ns)	χ_R^2
Lysine	0.835	0.155	0.010	0.495 (0.07)	1.78 (0.02)	6.37 (0.47)	0.75 (0.06)	1.194

Table 5.4: Fitted parameters obtained from the 3 exponential fit of Lysine at λ_{ex} 295 nm. The values in the parenthesis displays the standard deviation calculated from 3 independent measurements. The α values are taken from the best fit.

The appearance of second smaller component in MEM analysis could be due to the influence of Lysine which is more prominent at higher concentrations. Similar smaller component (0.495 ns) is revealed from the luminescence decay analysis of Lysine under similar conditions (Figure 5.11 and Table 5.4). This adds to the fact that the presence of Lysine does affect the fluorescence decay of NATA, changing its mono-exponential nature.

5.2.2.2 Effect of Lysine·HCl on the fluorescence of NATA

Similar to the above studies, fluorescence of NATA was observed in presence of different concentrations of Lysine·HCl. The steady state fluorescence indicates a similar decrease in the fluorescence intensity of NATA with increasing concentration of Lysine·HCl (Figure 5.12A and unshaded bars in Figure 5.12B). However, the appearance of higher intensities beyond 375 nm (Figure 5.12A) and slight increase in the net integrated fluorescence (shaded bars in Figure 5.12B) indicates the contributions from Lysine·HCl, which increases with increasing concentrations of Lysine·HCl.

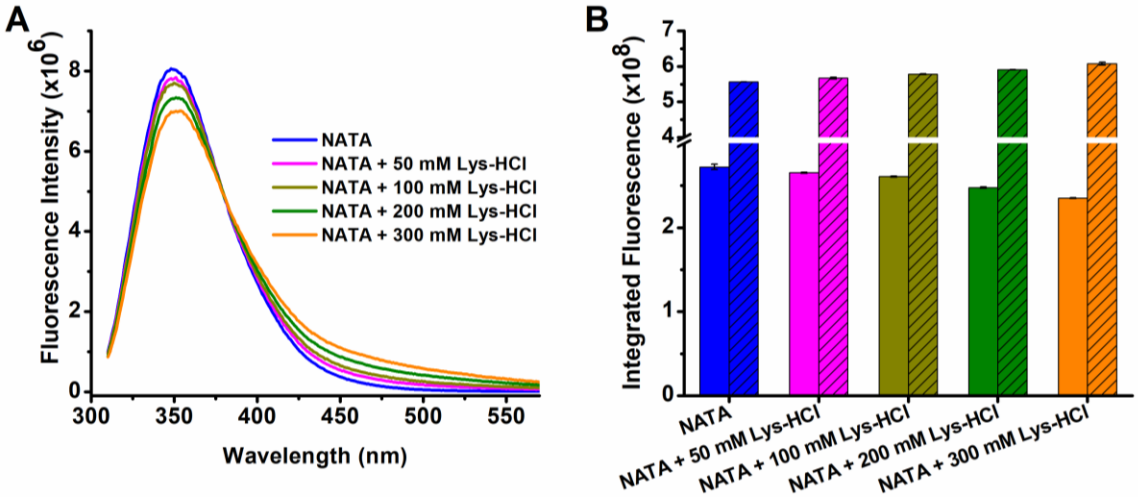

Figure 5.12: Panel **A** shows the fluorescence intensity of 20 µM NATA at λ_{ex} 295 nm in presence of different concentrations of Lysine·HCl. Panel **B** shows the integrated fluorescence calculated between 320-360 nm (unshaded bars) and 320-560 nm (shaded bars). Break in panel B is provided between 3–4 x 10^8.

Time-resolved studies of identical samples displays a deviation from the mono-exponential decay of NATA in presence of Lysine·HCl (when fitted in 1 exponential model, bad residuals with higher reduced chi square values are obtained as represented in Figure 5.13). The same are well fitted in 2 exponential model (Figure 5.14).

Fitting in 2 exponential model, reveals a decrease in the τ_2 value (from 2.61 to 2.43 ns) and a concomitant increase in the τ_1 value (from 3.74 to 4.01 ns) when the concentrations of Lysine·HCl was increased from 50 mM to 300 mM (Table 5.5). The contribution (α_1) from the longer component (τ_1) has decreased while the contribution (α_2) from shorter component (τ_2) has increased on increasing the concentration of Lysine·HCl. The increasing concentration of Lysine·HCl, favored the micro-environment where NATA and Lysine·HCl can be considered to interact leading to the quenching of fluorescence from NATA. This quenching brought about a decrease in the mean lifetime of NATA from ~3 ns to 2.65 ns (Table 5.5).

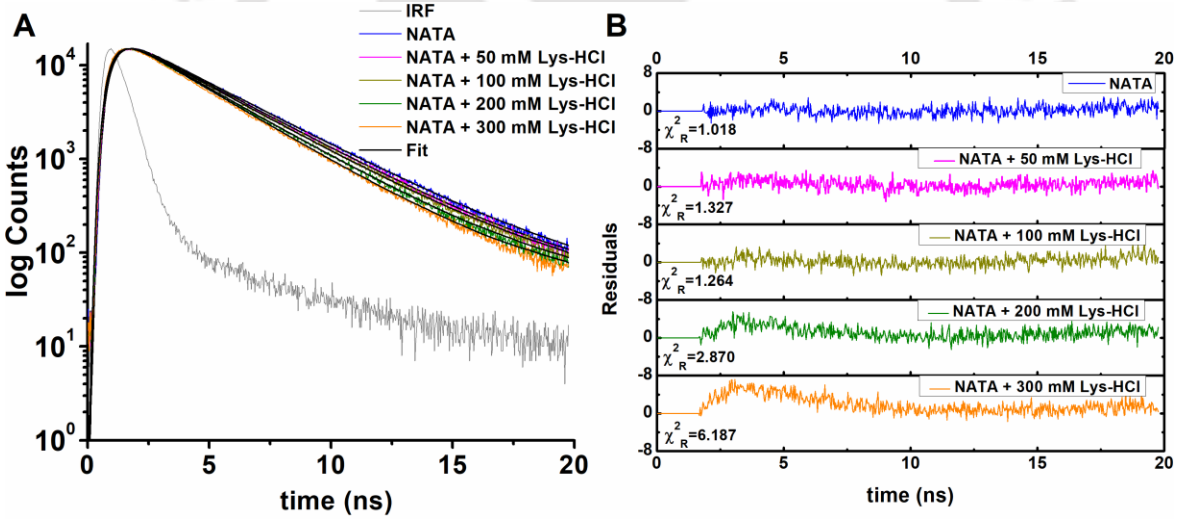

Figure 5.13: Panel **A** shows the fluorescence intensity decay and 1 exponential fit for 20 µM NATA at λ_{ex} 295 nm in presence of different concentration of Lysine·HCl. Panel **B** shows the residuals from the fit. Emission was collected using 340±20 nm band pass filter.

Further, MEM analysis also revealed similar changes in the lifetime distribution (Figure 5.15). Here also, the two lifetimes (τ_1 and τ_2) are enveloped under a single distribution while at higher concentrations of Lysine·HCl (100-300 mM) a smaller component ~0.6 ns is resolved which are absent in discrete analysis. Again, this component is very similar to the smallest component (τ_1) with highest contribution (α_1), as obtained from the decay of Lysine·HCl (Figure 5.16 and Table 5.6). This supports the evidence of contributions to the fluorescence of NATA from the luminescence of Lysine·HCl at λ_{ex} 295 nm. Apart from this,

a slight shift of the major distribution in MEM towards the lower time scale suggests a decrease in the lifetime of NATA, as inferred from the discrete analysis. Hence, the presence of Lysine significantly affects the fluorescence of NATA as revealed by the steady-state and time-resolved studies.

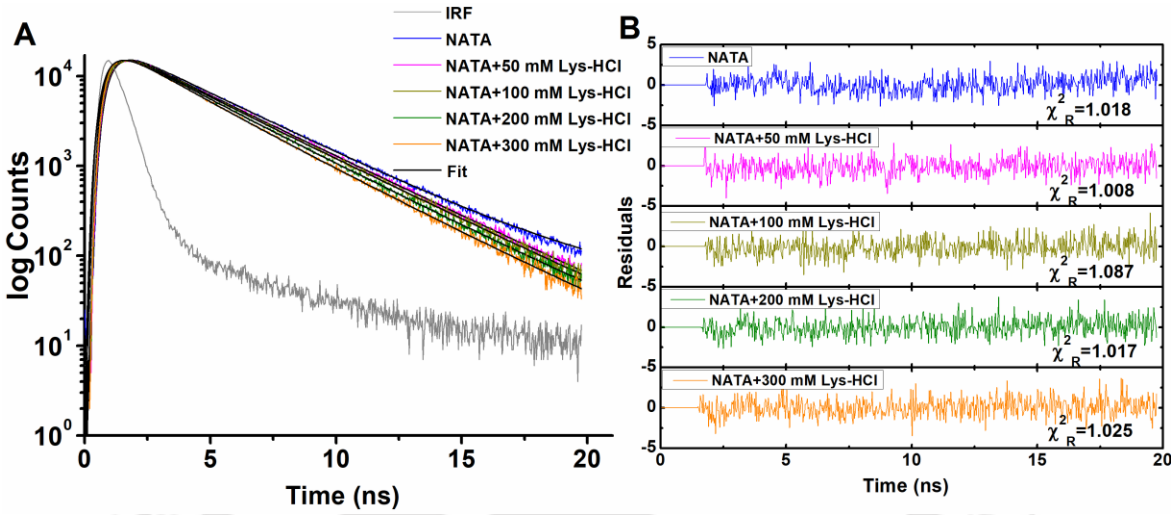

Figure 5.14: Panel **A** shows the fluorescence intensity decay and 2 exponential fit for 20 µM NATA in presence of different concentration of Lysine·HCl. Panel **B** shows the residuals from the 2 exponential fit. NATA is fitted in 1 exponential model. Emission was collected using 340±20 nm band pass filter.

Sample	α_1	α_2	τ_1 (ns)	τ_2 (ns)	τ_{mean} (ns)	χ^2_R
NATA	1	-	3.07 (0.01)	-	-	1.081
+ 50 mM Lys·HCl	0.353	0.647	3.74 (0.17)	2.61 (0.09)	2.99 (0.009)	1.008
+ 100 mM Lys·HCl	0.285	0.715	3.98 (0.22)	2.64 (0.07)	2.92 (0.013)	1.087
+ 200 mM Lys·HCl	0.161	0.839	4.14 (0.10)	2.56 (0.02)	2.77 (0.005)	1.017
+ 300 mM Lys·HCl	0.149	0.851	4.01 (0.04)	2.43 (0.01)	2.65 (0.003)	1.025

Table 5.5: Fitted parameters obtained from 2 exponential fit of fluorescence intensity decay of 20 µM NATA in presence of Lysine·HCl. Values in parenthesis indicates the standard deviation from 3 independent measurements. The α values are taken from the best fitted data. NATA is fitted in 1 exponential model.

5.2.2.3 Effect of Glutamate on the fluorescence of NATA

Similarly, the fluorescence of NATA was observed in presence of different concentrations of Glutamate. In this case, up to 500 mM of Glutamate was analyzed for its effect on the fluorescence of NATA. Since, the luminescence contribution of Glutamate at λ_{ex} 295 nm is far less than that of Lysine or Lysine·HCl, the effect on the steady-state fluorescence spectra of NATA is visible only as a steep decrease along the peak emission of NATA contrary to Lysine and Lysine·HCl (Figure 5.17AB). Additionally, no change in FWHM of fluorescence

spectra was observed in this case. However, close observation beyond 425 nm shows the effect of Glutamate where 500 mM Glutamate has highest counts than rest of the samples (Figure 5.17A).

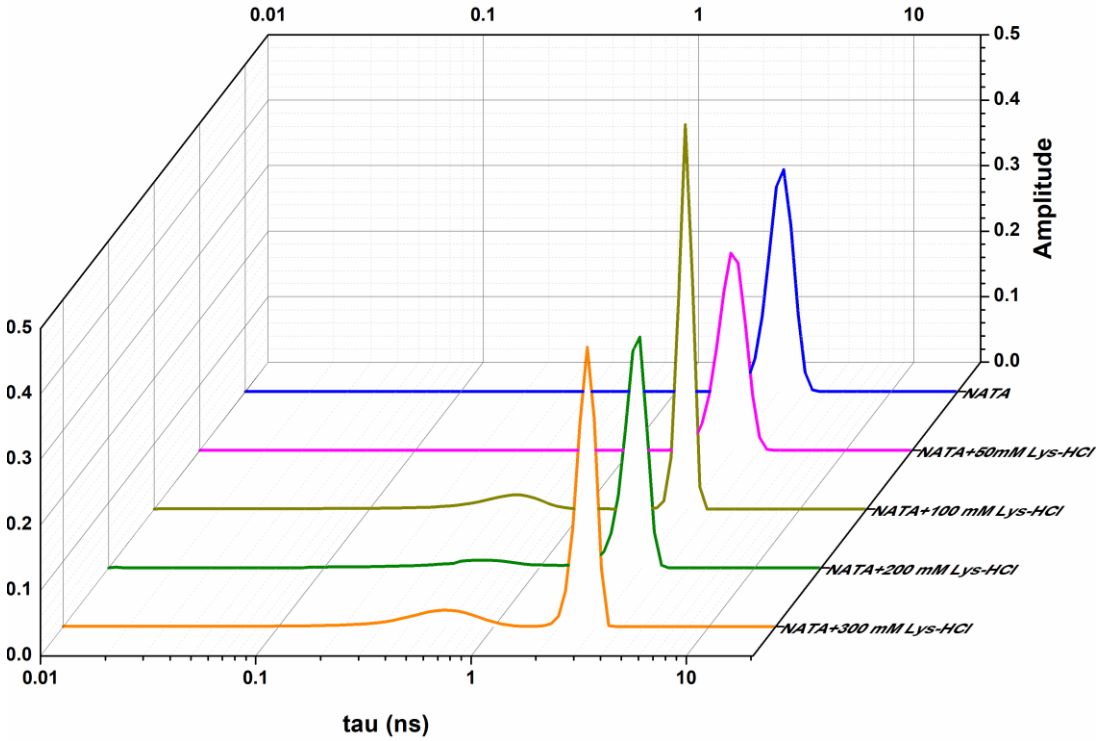

Figure 5.15: Lifetime distributions obtained for NATA in presence of Lysine·HCl. Residuals from the fit are displayed in Appendix-III as Figure A4.

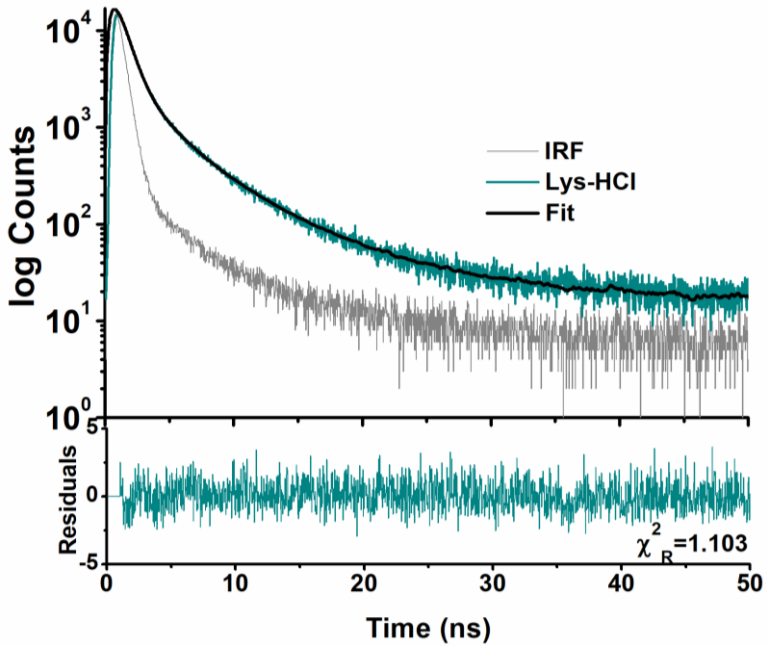

Figure 5.16: Luminescence intensity decay of Lysine·HCl at λ_{ex} 295 nm and its 3 exponential fit. Emission collected using 340±20 nm band pass filter. Lower panel displays the residuals obtained from the fit.

Sample	α_1	α_2	α_3	τ_1 (ns)	τ_2 (ns)	τ_3 (ns)	τ_{mean} (ns)	χ_R^2
Lysine·HCl	0.903	0.085	0.012	0.67 (0.02)	2.48 (0.27)	6.61 (0.98)	0.89 (0.02)	1.103

Table: 5.6: Fitted parameters obtained from the 3 exponential fit of Lysine·HCl at λ_{ex} 295 nm. The values in the parenthesis displays the standard deviation calculated from 3 independent measurements. The α values are taken from the best fit.

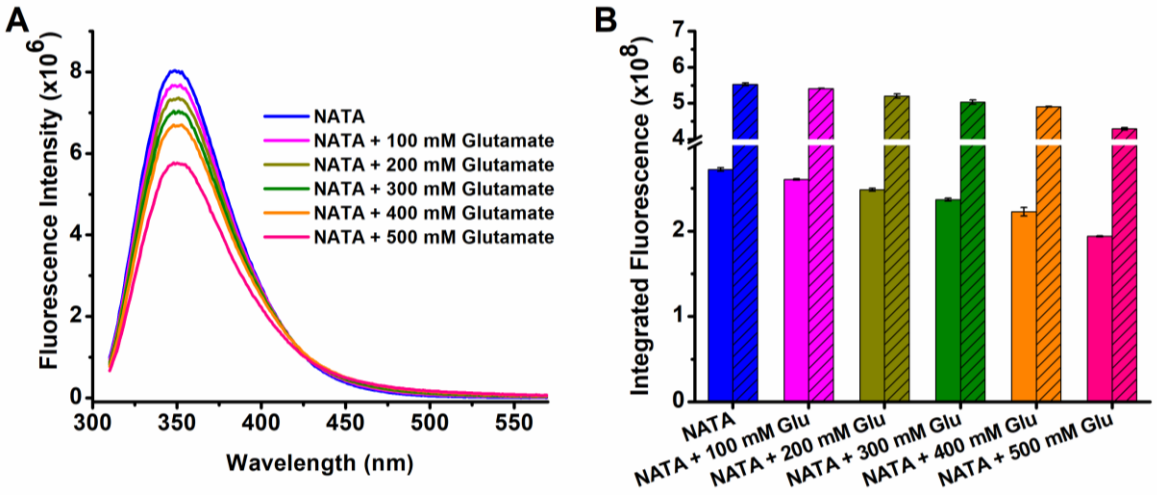

Figure 5.17: Panel **A** shows the fluorescence intensity of 20 µM NATA at λ_{ex} 295 nm in presence of different concentrations of Glutamate. Panel **B** shows the integrated fluorescence calculated between 320-360 nm (unshaded bars) and 320-560 nm (shaded bars). Break in panel B is provided between 3–4 x 10^8.

Time resolved fluorescence studies for the above mentioned samples followed a similar 2 exponential decay (Figure 5.19) as observed in above sections in presence of Lysine and Lysine·HCl. Similarly, it could not be fitted in 1 exponential model (Figure 5.18).

A different trend was observed in the fitted parameters as compared to those in presence of Lysine or Lysine·HCl. In this case, both the components (τ_1 and τ_2) tend to increase nominally with increasing concentrations of Glutamate. τ_1 has increased from 3.35 ns to 3.75 ns while τ_2 has increased from 2.29 ns to 2.36 ns when the concentration of glutamate was increased from 100 mM to 500 mM. However, the contribution form the first component (τ_1) has decreased from 0.596 to 0.134 while for second component (τ_2), it has increased from 0.404 to 0.866 (Table 5.7). With decrease in the contribution (α_1) of larger component (τ_1) and concomitant increase in the contribution (α_2) from shorter component (τ_2), the mean lifetime has decreased from 2.95 ns in presence of 100 mM to 2.56 ns in presence of 500 mM Glutamate.

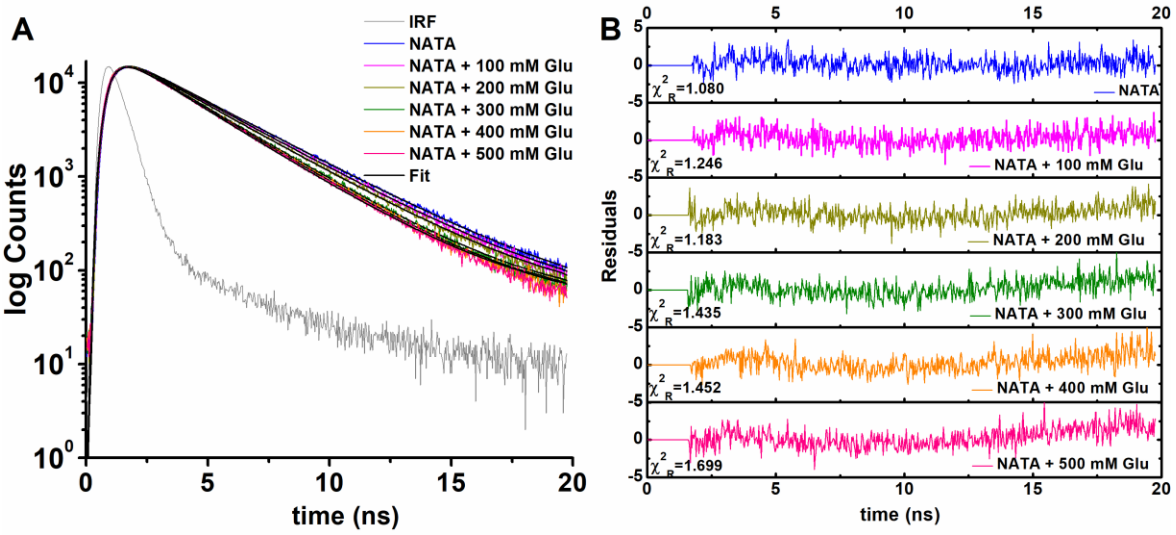

Figure 5.18: Panel **A** shows the fluorescence intensity decay and 1 exponential fit for 20 µM NATA at λ_{ex} 295 nm in presence of different concentration of Glutamate. Panel **B** shows the residuals from the fit. Emission was collected using 340±20 nm band pass filter.

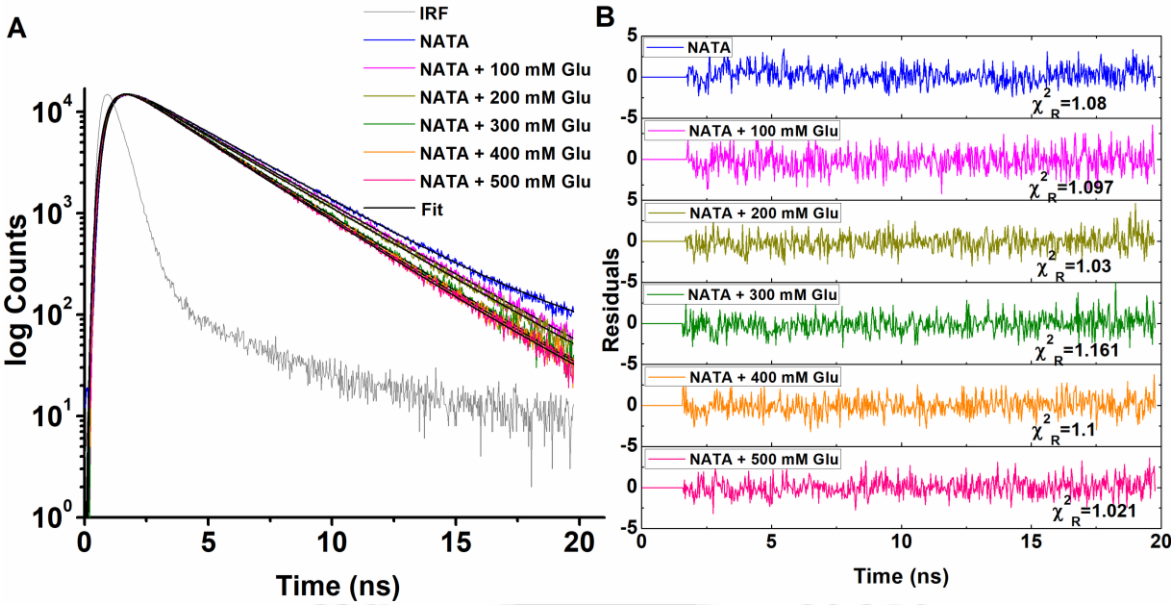

Figure 5.19: Panel **A** shows the fluorescence intensity decay and 2 exponential fit for 20 µM NATA in presence of different concentration of Glutamate. Panel **B** shows the residuals from the 2 exponential fit. NATA is fitted in 1 exponential model. Emission was collected using 340±20 nm band pass filter.

The results of discrete analysis are again validated by the MEM analysis. Similar to the distributions obtained for NATA in presence of Lysine and Lysine·HCl, here also both the components (τ_1 and τ_2 corresponding to discrete analysis) are found to be enveloped within a single distribution (Figure 5.20). However, NATA in presence of Glutamate do not show any distribution on the lower lifetime scale even at higher concentrations of Glutamate. This can be expected as no signal was collected for Glutamate 'alone' during experiment under

similar conditions, probably due to its lower quantum yield than Lysine or Lysine·HCl at λ_{ex} 295 nm. Apart from this, a very small shift in distributions towards the lower time scale can be observed. This hints upon the marginal decrease in the mean lifetime of NATA in presence of given concentrations of Glutamate (Figure 5.20).

Sample	α_1	α_2	τ_1 (ns)	τ_2 (ns)	τ_{mean} (ns)	χ_R^2
NATA	1	-	3.04 (0.01)	-	-	1.08
+ 100 mM Glutamate	0.596	0.404	3.35 (0.03)	2.29 (0.07)	2.95 (0.007)	1.097
+ 200 mM Glutamate	0.572	0.428	3.30 (0.02)	2.22 (0.04)	2.84 (0.008)	1.03
+ 300 mM Glutamate	0.247	0.726	3.40 (0.06)	2.37 (0.04)	2.68 (0.005)	1.161
+ 400 mM Glutamate	0.183	0.817	3.66 (0.02)	2.37 (0.01)	2.61 (0.004)	1.1
+ 500 mM Glutamate	0.134	0.866	3.75 (0.04)	2.36 (0.01)	2.56 (0.004)	1.021

Table 5.7: Fitted parameters obtained from 2 exponential fit of fluorescence intensity decay of 20 µM NATA in presence of Glutamate. Values in parenthesis indicates the standard deviation from 3 independent measurements. The α values are taken from the best fitted data. NATA is fitted in 1 exponential model.

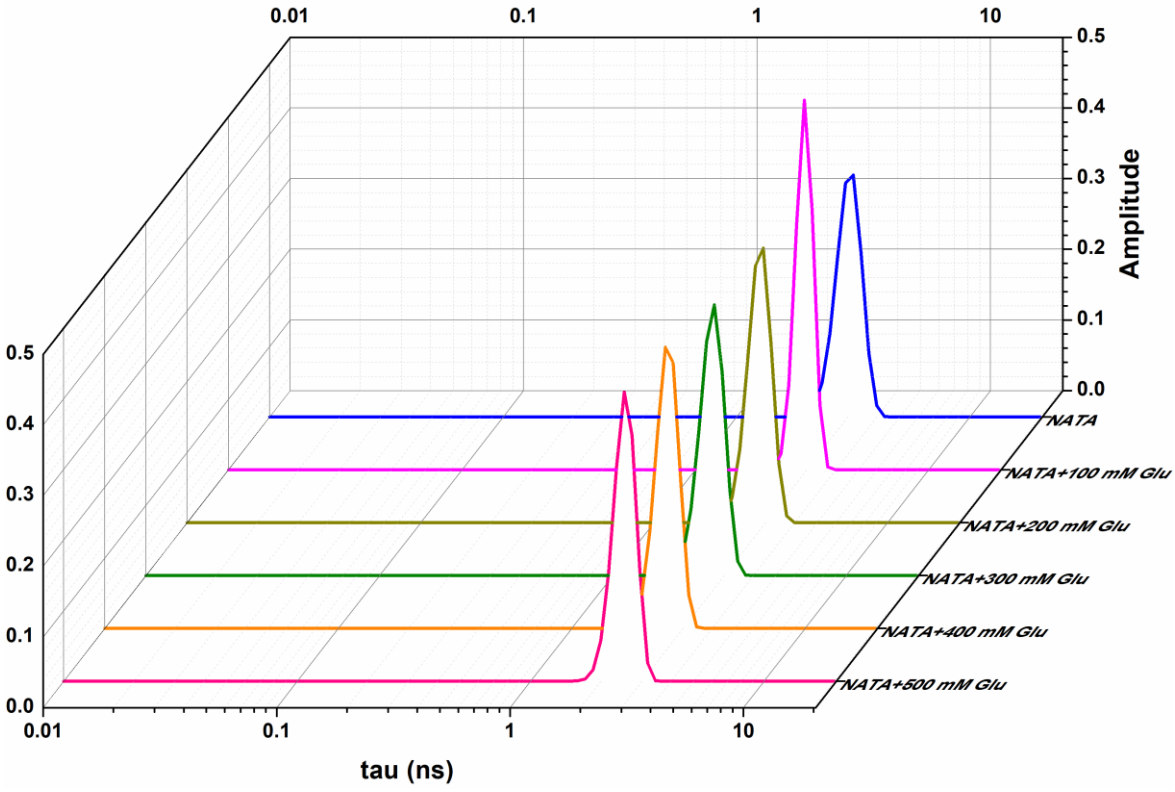

Figure 5.20: Lifetime distributions obtained for NATA in presence Glutamate. Residuals from the fit are displayed in Appendix-III as Figure A5.

As observed above, the decrease in the mean lifetime values in presence of all the amino acids, Lysine, Lysine·HCl and Glutamate do present a scenario of quenching of fluorescence

from NATA. Here, the charged amino acids acts like the quencher. To get further insights, Stern-Volmer plot was generated for the given range of concentrations for each of the charged amino acids as shown in Figure 5.21. It clearly reveals the dynamic quenching of fluorescence from NATA. The value of bimolecular quenching (k_q) constant is highest for Lysine ($1.07x10^9$ $M^{-1}s^{-1}$) followed by Lysine·HCl ($1.72x10^8$ $M^{-1}s^{-1}$) and Glutamate ($1.38x10^8$ $M^{-1}s^{-1}$). This indicates that the Lysine in the proximity of indole ring can efficiently quench the fluorescence of tryptophan.

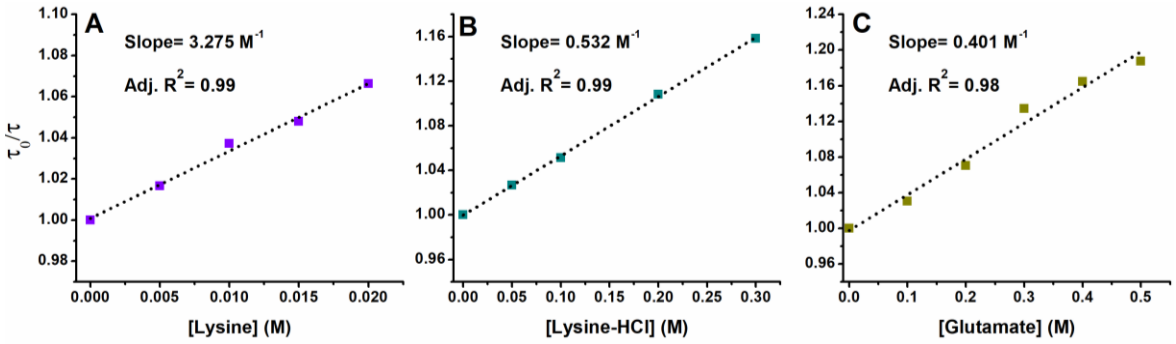

Figure 5.21: Stern-Volmer plot for quenching of fluorescence of NATA in presence of **A**) Lysine, **B**) Lysine·HCl and **C**) Glutamate. Here, τ is mean lifetime observed in presence of amino acids and τ_0 is the lifetime of NATA in absence of any amino acid. The dotted black line represents the obtained linear fit.

Similar studies were done by quenching 3-methyl indole in presence of different amino acids (Chen & Barkley 1998) which clearly states the role of side chains behind the observed quenching. The reported mechanism of quenching was excited-state electron/proton transfer between the side chains and indole ring.

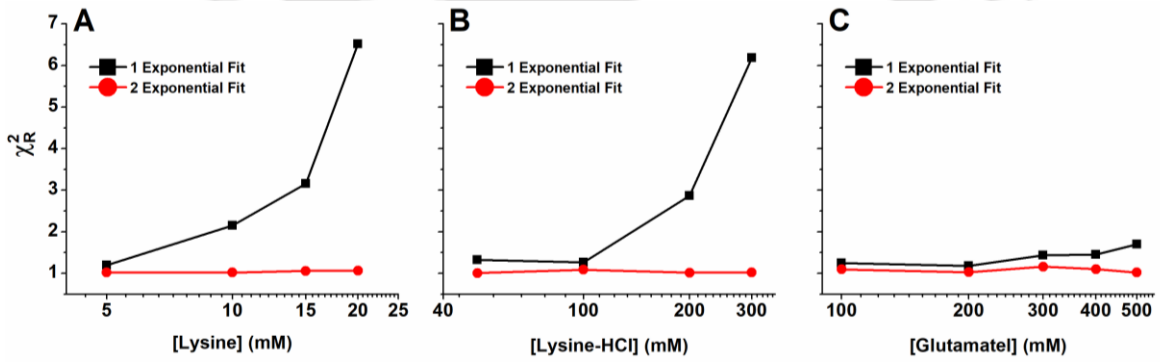

Figure 5.22: Values of χ_R^2 are plotted against concentration of amino acids in which the decay of NATA was observed and fitted in either mono or bi-exponential model.

However, under this study not only the quenching but also deviation from the mono-exponential decay of NATA is observed. Figure 5.22 shows the values of χ_R^2 obtained from fitted decay of NATA (in presence of different amino acids) in both mono and bi-exponential

models. Figure 5.8, 5.13, 5.18 and 5.22 show that the extent of deviation from mono-exponential decay (χ_R^2) is most for Lysine and Lysine·HCl compared to Glutamate. This is consistent with least luminescence contribution from Glutamate. On the other hand, quenching observed under this study indicates the presence of single class of fluorophores (referred to linear Stern-Volmer plot) accessible to amino acids as quenchers. Hence, the application of two exponential model to fit the decay cannot be explained, unless the contributions from charge amino acids are considered. This is further confirmed by the appearance of another smaller component (~0.5 ns and ~0.6 ns; Figure 5.10 and 5.15, respectively) from MEM analysis, which are also revealed to be the most prominent component in sole amino acids (Table 5.4 and 5.6). Therefore, this could probably suggests one of the reasons behind the origin of multi-exponential decay of Trp in proteins.

5.2.2.4 Effect of charged residues in protein on the fluorescence of NATA

In the previous sections, effect of charged, non-aromatic amino acids were observed upon the fluorescence of NATA. In this section similar studies have been done but in presence of protein instead of amino acids. Protein utilized here is PEST wt, which harbors ~35% charged residues with only one Phenylalanine in its sequence. Time resolved fluorescence studies were done in presence of 0 to 250 µM of PEST wt. Up to 50 µM of PEST wt, the fluorescence intensity decay of NATA was fitted properly in 1 exponential model (Figure A6 in Appendix-III) while for 100 µM and above they are well fitted in two exponential model (Figure 5.23). The parameters obtained from the fit are displayed in Table 5.8.

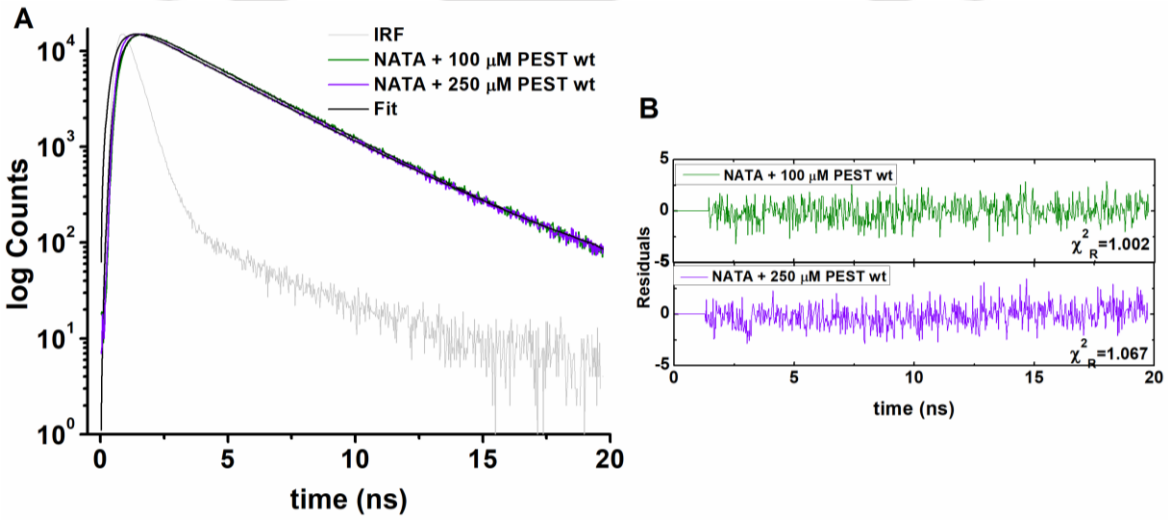

Figure 5.23: Panel **A** shows the fluorescence intensity decay and 2 exponential fit for 20 µM NATA in presence of different concentration of PEST wt. Panel **B** shows the residuals from the 2 exponential fit. Emission was collected using 340±20 nm band pass filter.

Sample	α_1	α_2	τ_1 (ns)	τ_2 (ns)	τ_{mean} (ns)	χ_R^2
NATA	1	-	3.03 (0.01)	-	-	1.004
+ 50 µM PEST wt	1	-	2.96 (0.003)	-	-	1.031
+ 100 µM PEST wt	0.082	0.918	4.03 (0.03)	2.90 (0.08)	2.97 (0.004)	1.002
+ 250 µM PEST wt	0.204	0.796	3.76 (0.04)	2.72 (0.03)	2.93 (0.008)	1.067

Table 5.8: Parameters obtained from the fit. NATA and (NATA + 50 µM PEST wt) is fitted in 1 exponential model while others are fitted in 2 exponential model. Values in parenthesis indicates the standard deviation from 3 independent measurements. The α values are taken from the best fitted data.

With increase in the concentration of PEST wt (100 µM and above), the smaller component (τ_2) representing the fluorescence lifetime of NATA decreases to 2.72 ns and a new longer component (τ_1) appears at ~4 ns. Apart from this, the contribution (α_1) from the longer component (τ_1) increased to 0.2 in presence of 250 µM PEST wt. The new component (τ_1) with higher lifetime is very similar to that of observed with mutant of PEST wt with an inserted Trp (Section 5.2.2.5; Figure 5.25). The other component (τ_2) has decreased similarly as observed in presence of Lysine and Lysine·HCl. Mean lifetime however, has remained fairly steady at ~2.9 ns.

MEM analysis reveals similar distribution obtained for NATA in presence of charged amino acids. Both the components observed from discrete analysis seemed to be enveloped in a single distribution (Figure 5.24). Another distribution observed in presence of highest concentration of PEST wt at ~0.3 ns, was not resolved by the discrete analysis.

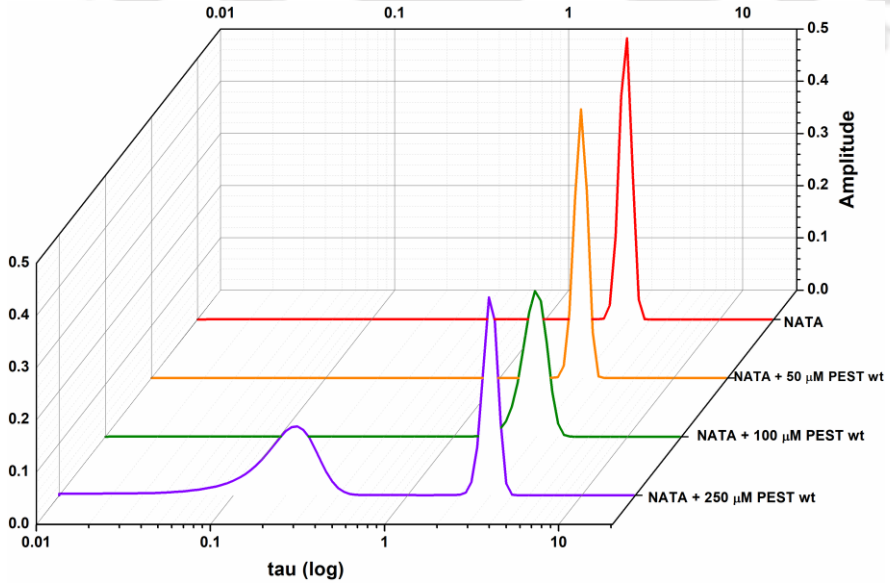

Figure 5.24: Lifetime distributions obtained for NATA in presence PEST wt. Residuals for the fit are shown in Appendix-III as Figure A7.

The mono exponential decay of NATA deviated only in presence of higher concentration (≥ 100 µM - 250 µM) of PEST wt. This concentration of protein reflects ~3 mM to 7 mM charged residues in the protein, which is similar to the concentration of charged amino acids studied above, although local concentration of charged residues will be quite high. These all suggests that the presence of charged amino acids in the vicinity of indole can affect the fluorescence of Trp. This effect can be visualized by the decrease in the fluorescence lifetime of NATA as well as by generation of a second component or by giving rise to the multi-exponential decay of Trp. The main reason for changes in Trp decay, in this case is the contribution of ProCharTS luminescence arising from PEST wt.

5.2.2.5 Effect of inserted Trp on the ProCharTS luminescence of PEST wt

The effect of ProCharTS on the fluorescence of Trp would not be significant due to its lower quantum yield (as discussed in Chapter 3). However, this was analyzed by a comparative study of PEST wt and PEST M1, a mutant with an inserted Trp on the C-terminus. The fluorescence intensity decay of both proteins at λ_{ex} 295 nm reveals a three exponential decay (Figure 5.25 and Table 5.9).

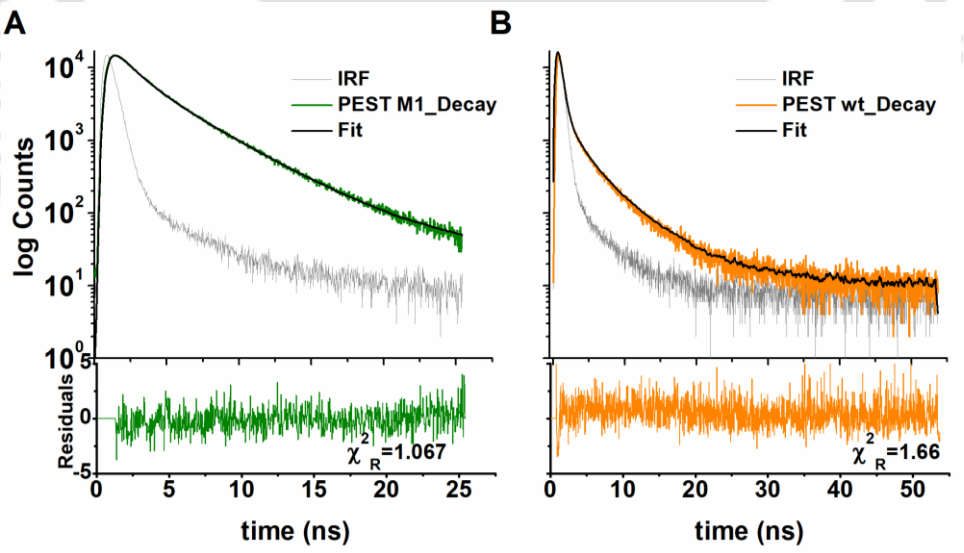

Figure 5.25: Panel **A** and **B** shows the fluorescence intensity decay and 3 exponential fit for PEST M1 and PEST wt, respectively at λ_{ex} 295 nm. Lower panel displays the residuals from the fit. Emission was collected using 340±20 nm band pass filter.

τ_3 representing the lifetime of Trp with a value ~3.8 ns (Table 5.9), is higher than the values generally observed for Trp exposed to solvent. Here, PEST M1 being an IDR, the Trp is supposed to be exposed to the solvent. This increase in the lifetime is very similar to those observed for the increase in lifetime of NATA in presence of Glutamate (Table 5.7). Thus,

the role of Glutamate can be postulated since the site of insertion of Trp in PEST M1 is rich in Glutamate residues (C-terminus is rich in His and Glu; Figure 2.11A). Apart from this, the other two lifetimes are 0.33 ns (τ_1) and 1.48 ns (τ_2). On the other hand, PEST wt also displays three exponential decay with a very fast component as observed from the decay itself. In this case, the smallest component (τ_1) has the largest contribution while the other two components have least contributions (Table 5.9).

Sample	α_1	α_2	α_3	τ_1 (ns)	τ_2 (ns)	τ_3 (ns)	τ_{mean} (ns)	χ_R^2
PEST M1	0.405	0.332	0.263	0.33 (0.04)	1.48 (0.09)	3.8 (0.07)	1.57 (0.07)	1.067
PEST wt	0.973	0.021	0.006	0.172 (0.01)	1.19 (0.04)	5.6 (0.23)	0.238 (0.02)	1.66

Table 5.9: Parameters obtained from the 3 exponential fit. Values in parenthesis indicates the standard deviation from 3 independent measurements. The α values are taken from the best fitted data.

Lifetime distributions obtained from the MEM analysis also revealed similar values as displayed in Appendix-III as Figure A8.

From the above observations, it can be inferred that the presence of Glutamate in the vicinity of Trp can affect its fluorescence lifetime and can give raise to the multi-exponential decay of Trp in proteins. The exact changes in Trp fluorescence intensity decay depends on the nature of the charge environment in the immediate surroundings of indole fluorophore.

5.3 Conclusions

a) Any extrinsic chromophore sharing the spectral region of luminescence overlapping with absorption and luminescence arising from charge transfer states could be affected if labelled to a protein rich in charged amino acids
b) The presence of charged side chains of amino acids in the proximity of indole ring can alter the fluorescence lifetime of NATA, generally by quenching it to lower values.
c) Similarly, ProCharTS can affect the fluorescence of intrinsic chromophore, Trp in proteins rich in charged residues
d) The deviation of fluorescence intensity decay of NATA from mono to bi-exponential in presence of charged amino acids can partly explain the multi-exponential decay kinetics of Trp in proteins

Chapter 6

ProCharTS: A label-free approach to detect aggregation of hen egg white lysozyme (HEWL)

6.1 Introduction

Protein aggregation is one of the most common cause for the amyloidosis (Aguzzi & O'Connor 2010, Fink 1998, Sipe 1992). Protein amyloids are symptoms of various diseases like type 2 diabetes, Alzheimer's, Parkinson's, Huntington's and prion disease (Aguzzi & Calella 2009, Ashraf et al 2014, Kumar et al 2016, Mukherjee et al 2015, Mukherjee & Soto 2017, Olzscha et al 2011, Pedersen & Heegaard 2013, Ross & Poirier 2005). The understanding of the mechanism and pathways of protein aggregation and their easier detection at earlier stages would certainly help developing methods and techniques to curb it. In this regard, a number of proteins have been investigated and lysozyme is one such model protein for amyloid research (Swaminathan et al 2011).

Hen egg white lysozyme (HEWL) is a small protein with 129 amino acids (Canfield 1963), sharing ~60% sequence identity to that of the human lysozyme. This similarity stirred the investigations on the aggregation of HEWL once the point mutation induced systemic amyloidosis among human lysozyme were reported in 1993 (Pepys et al 1993). HEWL is intensely investigated for aggregation under various conditions like alkaline pH (Hameed et al 2007, Homchaudhuri et al 2006, Ravi et al 2014b, Sophianopoulos & Van Holde 1961, Sophianopoulos & Van Holde 1964), acidic pH (Arnaudov & de Vries 2005, Chaari et al 2015, Hill et al 2009, Krebs et al 2000, Mishra et al 2007), in presence of ethanol (Goda et al 2000) and guanidine hydrochloride (Vernaglia et al 2004).

The *in-vitro* detection of protein aggregates at early stages are difficult and mature amyloid fibrils are generally detected by the various molecular probes like Thioflavin-T (ThT), Congo Red (Maezawa et al 2008) and 1-anilinonapthelene-8-sulfonate (Ladiwala et al 2011). Apart from this, traditional techniques like, Atomic Force Microscope (AFM), Transmission Electron Microscope (TEM), Circular Dichroism (CD) and Fourier Transform Infrared Spectroscopy (FTIR) are routinely utilized in monitoring prefibrillar protein aggregates (Gregoire et al 2012, Nilsson 2004). However, the detection of oligomers by ThT assays are insensitive (Lee et al 2011) and suffers fluorescence self-quenching (Lindberg et al 2017). Apart from this, intrinsic chromophore like Trp fluorescence are of limited utility for monitoring aggregation (Swaminathan et al 1994).

In the present chapter, we have utilized ProCharTS to detect the oligomerization and fibrillation of HEWL under alkaline as well as acidic conditions. Since ProCharTS intensity

is highly dependent upon the proximity of charged residues (Prasad et al 2017), intermolecular events like protein aggregation, involving formation of new intermolecular contacts between the aggregating protein chains, could be tracked utilizing ProCharTS as an intrinsic label-free tool. Apart from this, inhibition of HEWL aggregation in presence of iodoacetamide (Ravi et al 2014a) were also done to crosscheck the ability of ProCharTS to detect aggregation. Further, the sensitivity of ProCharTS in detecting protein aggregates were compared to that of ThT assays.

Later in the chapter, luminescence arising from the protein aggregates are explored. Several groups have reported upon the intrinsic fluorescence arising from the oligomeric (Bhattacharya et al 2017, Bhattacharya et al 2014) as well as protein amyloid fibrils (Chan et al 2013, del Mercato et al 2007, Tikhonova et al 2018). Such fluorescence from protein oligomers and protein fibrils are termed intrinsic fluorescence (Chan et al 2013, del Mercato et al 2007, Pinotsi et al 2013) or intrinsic deep-blue/blue fluorescence (Bhattacharya et al 2017, Tikhonova et al 2018). There are different hypothesis behind their origin including electron/charge transport (Bhattacharya et al 2017, del Mercato et al 2007), proton transfer (Pinotsi et al 2016), or due to oxidation of amino acids (Tikhonova et al 2018). However, similar blue auto-fluorescence has also been reported for monomeric proteins and individual amino acids where carbonyl double bonds are considered as the source for auto-fluorescence (Niyangoda et al 2017).

Here in this chapter, luminescence from the HEWL aggregates are observed and are evaluated as emissions from charge transfer states of ProCharTS. Moreover, a unique blue shift in the luminescence spectra specifically from amyloid fibrils are observed. Apart from this, the quantum yield and luminescence lifetime of HEWL oligomers and fibrils formed under acidic conditions are also reported. Taken together, the detection of protein aggregates based on protein charge transfer spectra (ProCharTS) and a simpler way to differentiate between the oligomers and fibrils, based upon the shift in the luminescence spectra at λ_{ex} >300 nm, are demonstrated in this chapter.

6.2 Results and Discussions

6.2.1: Detection of HEWL aggregates by ProCharTS

6.2.1.1 ProCharTS of HEWL aggregates formed at alkaline pH

HEWL aggregates formed at pH 12.2 shows an increase in the ProCharTS absorption intensity with increasing monomeric concentration (Figure 6.1). The gradual increase in the absorption spectra is due to increased intermolecular contacts between the side chains of charged residues in aggregates as compared to monomers. The concentration dependence of increase is because of the likelihood of forming larger size HEWL aggregates at higher concentrations compared to lower (Ravi et al 2014b). Further to ascertain whether the increase in ProCharTS intensity arises solely from the formation of HEWL aggregates, we proceeded to arrest HEWL aggregation at alkaline pH by adding iodoacetamide, which retards the aggregation process by inhibiting intermolecular disulfide bond formation (Ravi et al 2014a).

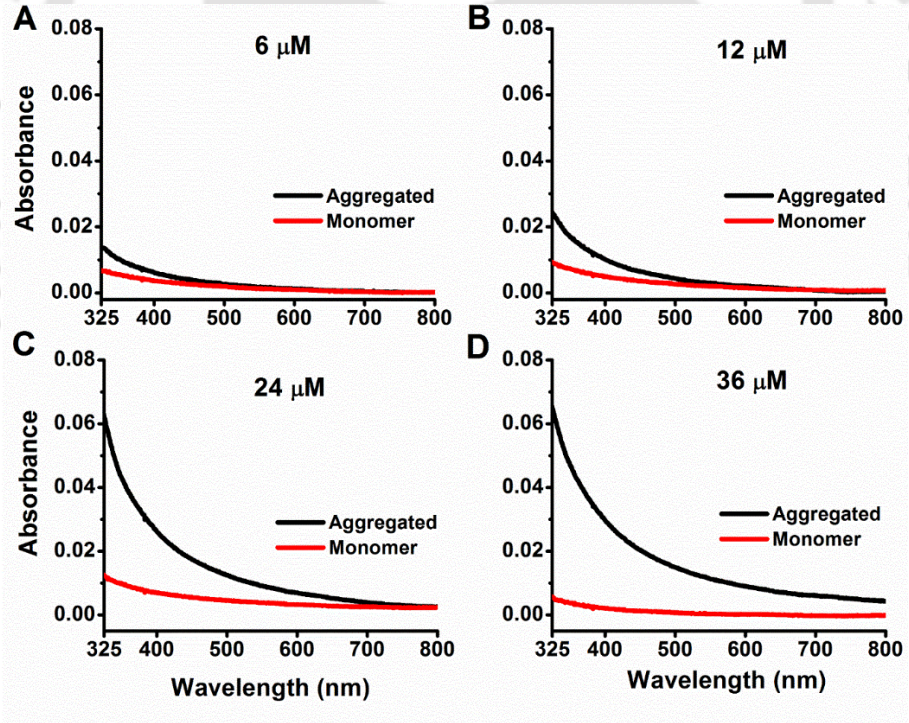

Figure 6.1: ProCharTS of HEWL aggregates formed at alkaline pH: ProCharTS for HEWL aggregates incubated at alkaline pH (12.2) for 10 days are shown alongside the freshly prepared monomer at identical concentrations. The spectra of (**A**) 6 µM, (**B**) 12 µM, (**C**) 24 µM and (**D**) 36 µM HEWL aggregates are shown.

In absence of iodoacetamide, the increase in absorption is evident with increasing time from day 6 to day 10. A decrease in absorption for day 8 and 10 could be due to proteolysis at

alkaline pH (Figure 6.2A). Moreover, the change in spectral shape for 9 and 10 day old aggregates, could be due to restructuring of the aggregates probably affecting the nature of molecular contacts giving rise to ProCharTS absorption. In presence of iodoacetamide, a negligible increase in the ProCharTS absorption was observed (Figure 6.2B) implying a sharp decline in the population and density of intermolecular contacts between charged residues in HEWL aggregates. This is supported by the fact that weaker protein-protein interactions were observed in presence of iodoacetamide (Ravi et al 2014a). Thus, the concentration and time dependent increase in the ProCharTS and its decline in presence of iodoacetamide appears to be directly tracking the formation of HEWL aggregates.

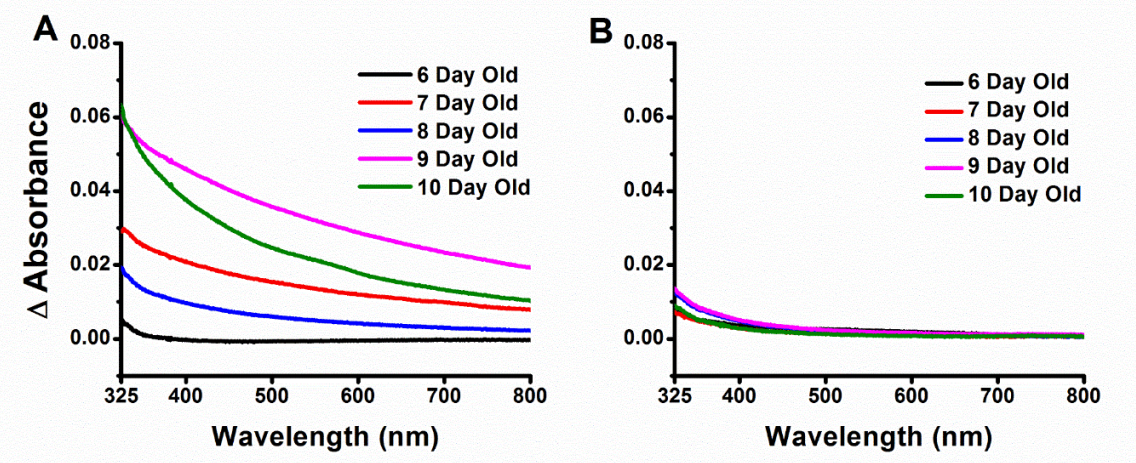

Figure 6.2: Effect of inhibition of HEWL aggregation at pH 12.2 on ProCharTS. Panel **A** and **B** shows the ProCharTS of HEWL aggregates in absence and presence of Iodoacetamide, respectively. The aggregates (12 μM) were transferred to 0.1 M sodium bicarbonate buffer (pH 9.3) before recording the spectra

6.2.1.2 ProCharTS of HEWL aggregates formed at acidic pH

The aggregates formed at acidic pH are of different makeup and specifically at pH 2 it forms fibrillar structure (Arnaudov & de Vries 2005, Brudar & Hribar-Lee 2019, Chaari et al 2015, Krebs et al 2000). This fact is supported by the higher ThT fluorescence at pH 2 (Figure 6.3C). The increase in the ProCharTS was observed with increasing age of aggregates formed at either pH 5 or pH 2 (Figure 6.3AB). However, with day 3 onwards the aggregation seems to saturate for pH 2 (Figure 6.3A) which is also reflected by the similar ThT fluorescence for day 3-5 (Figure 6.3C). The similar behavior of ProCharTS and ThT fluorescence suggests the potential of ProCharTS in detecting protein aggregation.

In case of pH 5, although the ThT fluorescence remained almost constant (Figure 6.3D), the ProCharTS increased for the subsequent days (Figure 6.3C). This could be due to the formation of oligomers at this pH, which are not sensitive to the ThT (Lee et al 2011) assay

but at the same time their presence and growth is tracked by the ProCharTS. In this case, ProCharTS seems to be more sensitive than ThT in detection of oligomeric aggregates.

Since the aggregates formed at pH 2 are fibrillar and compact in nature, more intermolecular contacts and higher probabilities of proximity between the charged residues are possible. Due to this, ProCharTS observed for aggregates at pH 2 are higher than that of pH 5 (Figure 6.3AB).

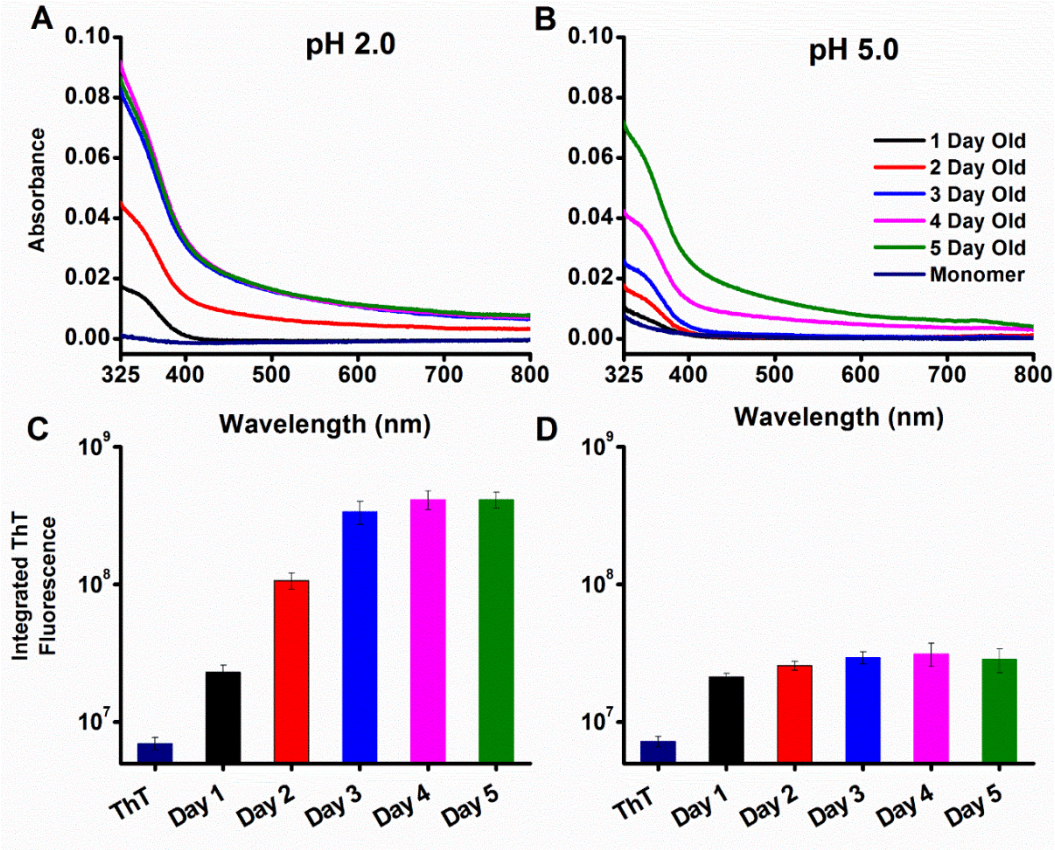

Figure 6.3: Panel **A** and **B** shows the ProCharTS of aggregates (100 µM) formed at pH 2 and 5, respectively. Panel **C** and **D** shows the ThT fluorescence in presence of aggregates formed at pH 2 and 5, respectively.

Further, we verified the sensitivity of ProCharTS for detecting protein aggregates in a wavelength dependent manner and compared it to ThT assay. Figure 6.4 shows the change in ProCharTS at different absorption wavelengths between 300-700 nm. As evident from the ThT assay for aggregates formed at pH 2, a similar saturation from day 3 onwards was also observed in ProCharTS (Figure 6.4A) at all the selected wavelengths. The aggregates formed at pH 5, shows a continuous increase in the ProCharTS (Figure 6.4B) while the ThT fluorescence remained the same (Figure 6.3D). This suggests a higher sensitivity of ProCharTS in detecting oligomeric aggregates and on the other hand, it is equally sensitive in detecting fibrillar aggregates. Apart from this, ProCharTS at lower wavelengths seems to

be more sensitive in detecting aggregates probably due to the higher extinction coefficient at lower wavelength region (Figure 6.5). Here in the case of HEWL, the interference from the absorption of aromatic amino acids could contaminate and dominate the ProCharTS at wavelengths <325 nm but in case of aggregating proteins devoid of any aromatic amino acids, this could be more beneficial and applicable.

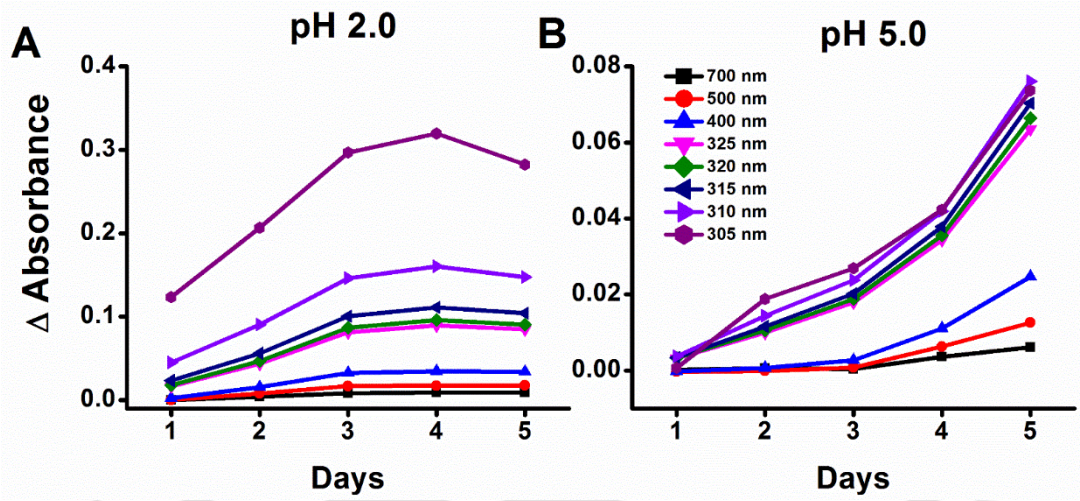

Figure 6.4: Panel **A** and **B** displays the change in absorbance as a function of the incubation period for different wavelengths among the HEWL aggregates formed at pH 2.0 and pH 5.0, respectively.

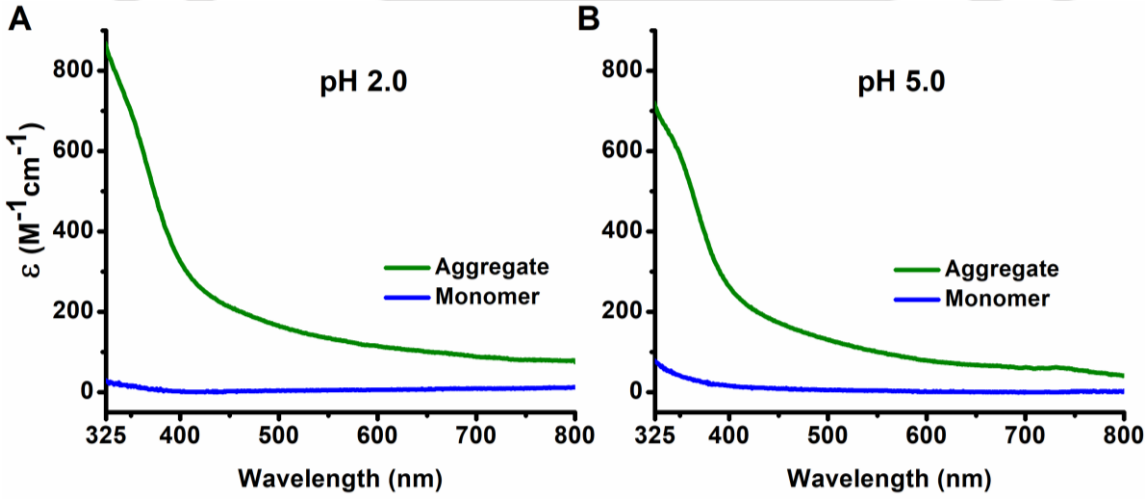

Figure 6.5: Panel **A** and **B** shows the extinction coefficient of 5 day old HEWL aggregate formed at pH 2 and 5, respectively. The reported extinction coefficients are averages of three independent measurements. Monomer was freshly prepared at the same pH.

The higher extinction coefficient of HEWL aggregates as compared to monomers (Figure 6.5) demonstrates a much higher density of side chains of charged residues in close proximity involved in charge transfer transitions. This observation motivated us to explore the luminescence properties of these aggregates particularly in the spectral region away from excitation band of aromatic amino acids.

6.2.2: Intrinsic Luminescence from HEWL aggregates

The HEWL aggregates formed at acidic pH were investigated for their intrinsic luminescence. The luminescence spectra are presented in Figure 6.6. Here, the aggregation periods are extended to 12 day for pH 2 and up to 8 days for pH 5. With increasing incubation period, the luminescence intensity of aggregates increased for both the pH (Figure 6.6AB). This increase in luminescence intensity is consistent with the increase in the ProCharTS observed for the aggregates (Figure A1 and A2 in Appendix-IV). The observed luminescence could arise from charge transfer states in aggregating proteins.

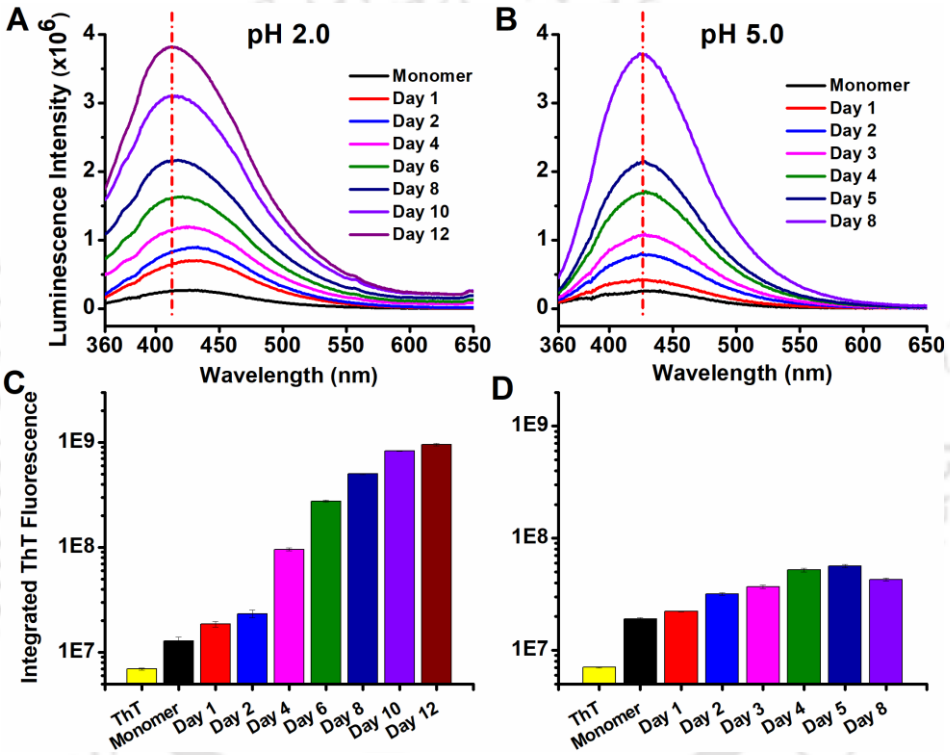

Figure 6.6: Panel **A** and **B** shows the luminescence spectra of different day old 100 µM HEWL aggregates formed at pH 2 and 5, respectively at λ_{ex} 340 nm. Lower panels **C** and **D** shows the integrated ThT fluorescence for HEWL aggregates at pH 2 and 5, respectively. The vertical dashed line in upper panels shows peak of emission maxima corresponding to the oldest day aggregate. All emission spectra are corrected for inner filter effect.

Similar to the observations made for the ProCharTS absorption, here also the luminescence from the charge transfer states of aggregates seems to be more sensitive in detecting the oligomeric aggregates while equally sensitive in detecting the fibrillar aggregates. This fact is clear due similar trend of ThT fluorescence as observed above in Figure 6.3. ThT fluorescence for aggregates formed at pH 2 has a concomitant increment with time, which is mirrored by a gradual rise in the luminescence intensity (Figure 6.6 AC). However, for

aggregates formed at pH 5, the ThT fluorescence is almost constant from day 4 onwards but a gradual increase in the luminescence intensity is observed (Figure 6.6 BD).

Apart from this, another striking feature observed in Figure 6.6A is the blue shift in the emission maxima of the older aggregates as compared to monomer. The same was absent for aggregates at pH 5 (Figure 6.6A). The blue shift could be due to sequestering of the side chains of charged residues involved in charge transfer transitions away from the solvent, within the compact fibrillar structure of aggregates. The Stokes shift was observed to decrease from 5882.2 ± 78.3 to 5139.8 ± 5.1 cm^{-1} for aggregates at pH 2. However, at pH 5, minimal decrease in Stokes shift from 5937.5 ± 77.9 to 5826.9 ± 9 cm^{-1} was observed (Figure 6.7).

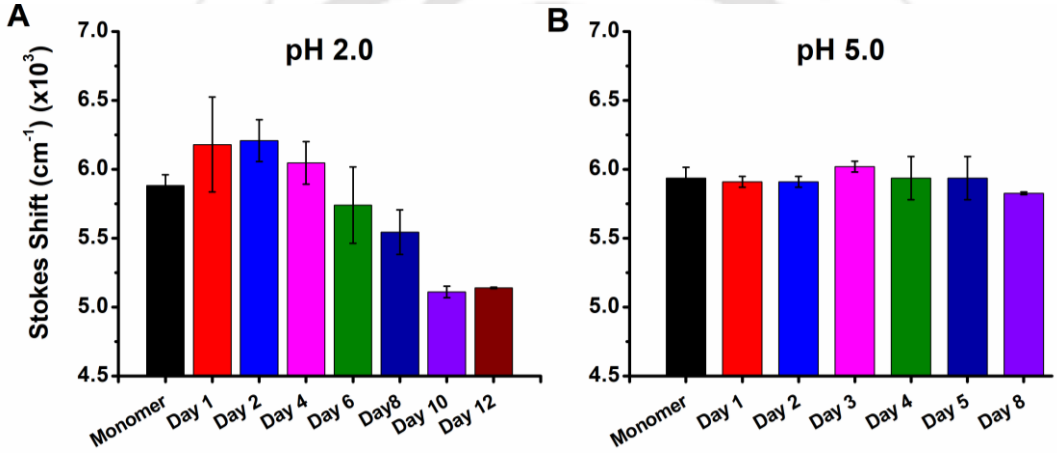

Figure 6.7: Panel **A** and **B** shows the Stokes shift observed in the luminescence spectra of HEWL aggregates formed at pH 2 and 5, respectively. All the samples were excited at λ_{ex} 340 nm.

Further, to confirm the above observation, the aggregates at pH 2 were excited at two different excitation wavelengths, that is, at 330 and 355 nm. For both the excitation wavelengths, there was a substantial shift towards the lower wavelength (Figure 6.8). For λ_{ex} 330 nm, the Stokes shift decreased from 6148.3 ± 82.5 to 5458.3 ± 43.6 cm^{-1}, while for λ_{ex} 355 nm, the observed change was from 5206.9 ± 37.3 to 5020.7 ± 75.8 cm^{-1}. With respect to monomer, ~11-12% change in Stokes shift was observed for aggregates at pH 2.0 at λ_{ex} 330 and 340 nm, while for λ_{ex} 355 nm the change was ~ 4%. However, with respect to lowest to highest change in Stokes shift, ~20% change was observed at λ_{ex} 330 and 340 nm while for λ_{ex} 355 nm ~10% change was observed. Contrary to pH 2, aggregates formed at pH 5 have much less change in the Stokes shift as compared to the monomers at pH 5 as well as with respect to their overall change in Stokes shift (Figure A3, Appendix-IV).

It should be noted that the Stokes shift initially increased (as observed for Day 1 or 2) then gradually decreases with increasing incubation period. The initial increase as compared to monomers could be due to the presence of loosely packed oligomers (Breydo & Uversky 2014) at the initial stages of aggregation where the side chains of charged residues involved in charge transfer transitions are exposed to solvent and can undergoes solvent relaxation of charge transfer states. However, during the process of maturation and fibril formation, the compaction of fibrillar structure could have caused their sequesterization away from the solvent, leading to decrease in Stokes shift.

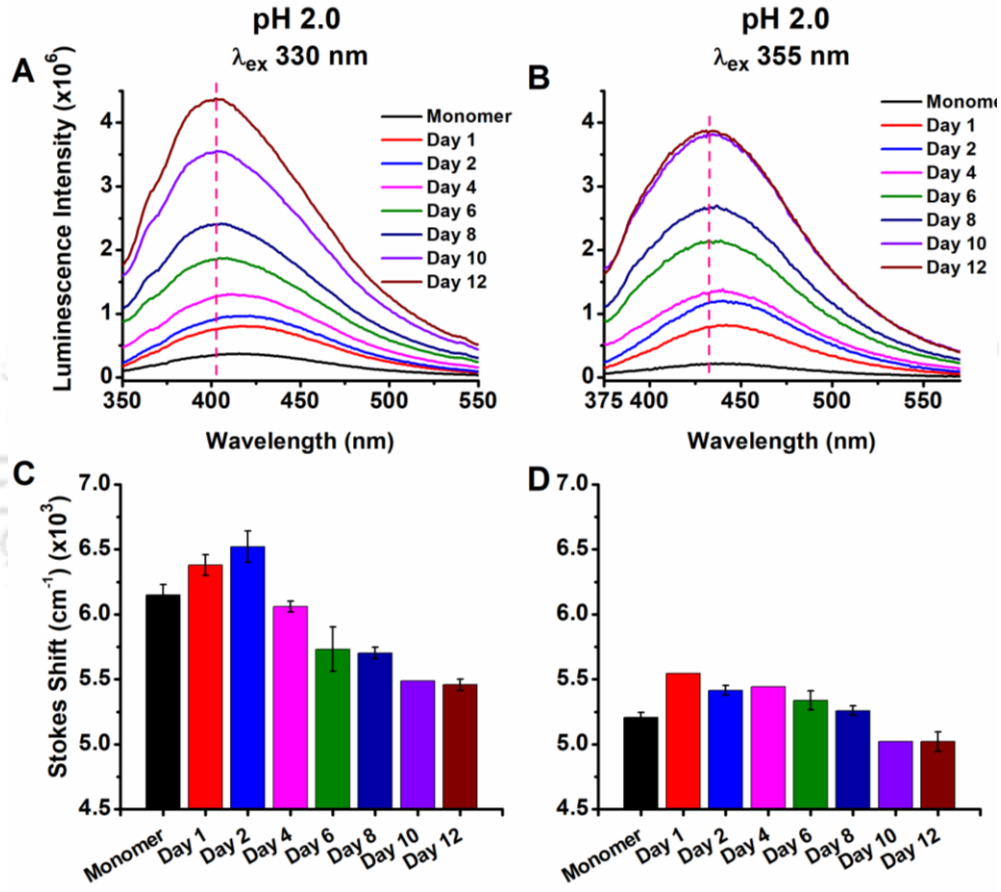

Figure 6.8: Panel **A** and **B** shows the luminescence intensity of HEWL aggregates (100 µM) formed at pH 2 for excitation wavelengths of 330 nm and 355 nm, respectively. The lower panels show the change in Stokes shift obtained for λ_{ex} 330 nm (**C**) and λ_{ex} 355 nm (**D**). The vertical dashed line in upper panels shows peak of emission maxima corresponding to the oldest day aggregate. Samples were excited with slit width of 1 nm for λ_{ex} 355 nm and 2 nm for λ_{ex} 330 nm. Emission was collected with slit width of 5 nm. All emission spectra are corrected for inner filter effect.

Further, this observation was compared to the intrinsic Trp fluorescence from the HEWL aggregates formed at pH 2. Figure 6.9A shows the fluorescence intensity of Trp at λ_{ex} 295 nm. The fluorescence intensity tends to decrease with increasing time. Moreover, the

emission spectra displays a red shift in its emission maxima, implying the exposure of Trp upon the onset of aggregation and fibril formation. In this case, the Stokes shift has increased from 3823.3 ± 64.3 cm^{-1} to 4834.8 cm^{-1}.

Comparatively, the luminescence intensity at λ_{ex} ≥330 nm increases with incubation period while for Stokes shift, initial increases is followed by a decrease. However, in case of Trp excitation (λ_{ex} 295), Stokes shift has a tendency to increase and later saturate. Since, solvent relaxation is more on exposure to water the decrease in Stokes shift at λ_{ex} ≥330 nm is indeed surprising. This implies that a non-polar group like Trp is more exposed to water compared to charged side chains in HEWL aggregates that are 12 days old. Moreover, any concern about the effect of evaporation behind the increase in luminescence of aggregates with time can also be negated. Since, it would have caused a similar time dependent increase in Trp fluorescence, which actually has decreased (Figure 6.9A).

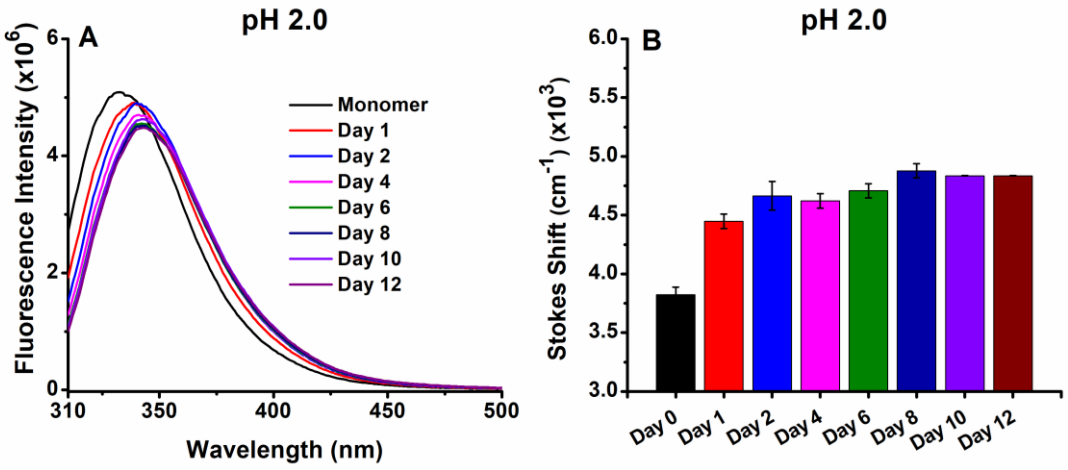

Figure 6.9: Panel **A** displays the fluorescence intensity of different day old aggregates formed at (λ_{ex} 295 nm) pH 2. Panel **B** displays the change in Stokes shift among different day old aggregates. 10 µM HEWL aggregates were used for these measurements.

Further, quantum yield of the HEWL aggregates formed at pH 2 were calculated at λ_{ex} 355 nm. It was surprising to observe that in spite of increasing luminescence intensity at λ_{ex} 355 (Figure 6.8B), the quantum yield of older day aggregates were significantly lower than that of monomers (Figure 6.10). The absorbance and luminescence intensity of all the aggregates used for the quantum yield calculation are displayed in Appendix-IV as Figure A4.

The quantum yield for the monomer is 0.022 ± 0.001 while for the aggregates it has decreased to ~0.0094 on Day 1 that further increases slightly to 0.0129 ± 0.0001 for Day 2. From Day 4 onwards it remained fairly constant with a value between 0.0114- 0.0124. The

initial decrease in quantum yield on Day 1 could be due to the quenching from formation of loosely packed oligomers, as discussed above. Upon the formation of fibrillar structure, where the side chains of charged residues involved in charge transfer transitions are more of stable within the maturing fibrils, the quantum yield has slightly increased as compared to Day 1 (Figure 6.10).

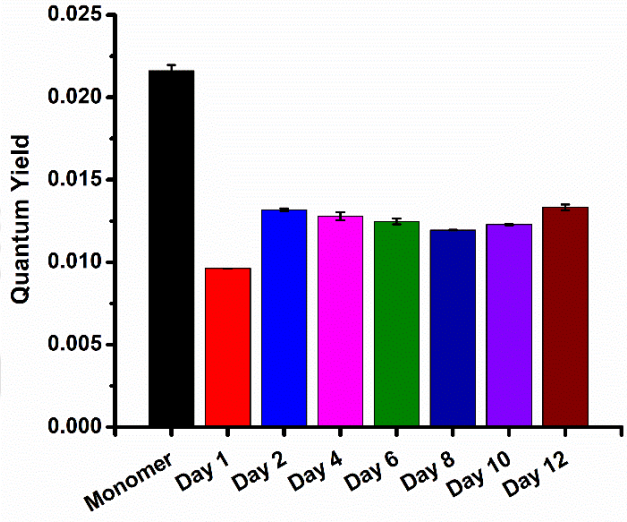

Figure 6.10: Quantum yield at λ_{ex} 355 nm for different day old aggregates formed at pH 2.

Higher luminescence intensity for aggregates in spite of having lower quantum yield than their monomeric counterparts could be attributed to the higher extinction coefficient of HEWL aggregates (Figure 6.5). This observation is similar to those observed in Chapter 3, where it was shown that the proteins with lower quantum yield but much higher extinction coefficient have larger slopes for the change in luminescence intensity with increasing concentration. (Figure 3.15 and Table 3.2). Hence, the increase in the luminescence of HEWL aggregates could directly be linked to their higher extinction coefficient.

Further, to validate the decrease in the quantum yield of HEWL upon aggregation, the luminescence lifetime of HEWL monomers and aggregates were compared at λ_{ex} 340 nm. For comparison, the luminescence intensity decay of HEWL monomers and 8 day old aggregates formed at either of pH are considered and displayed in Figure 6.11.

Luminescence intensity decay of monomers and aggregates are both fitted in three exponential model. As observed from the Figure 6.11, the lifetime of aggregates are lower than that of monomers. The fitted parameters are displayed in Table 6.1 and Table 6.2 for pH 2 and pH 5, respectively.

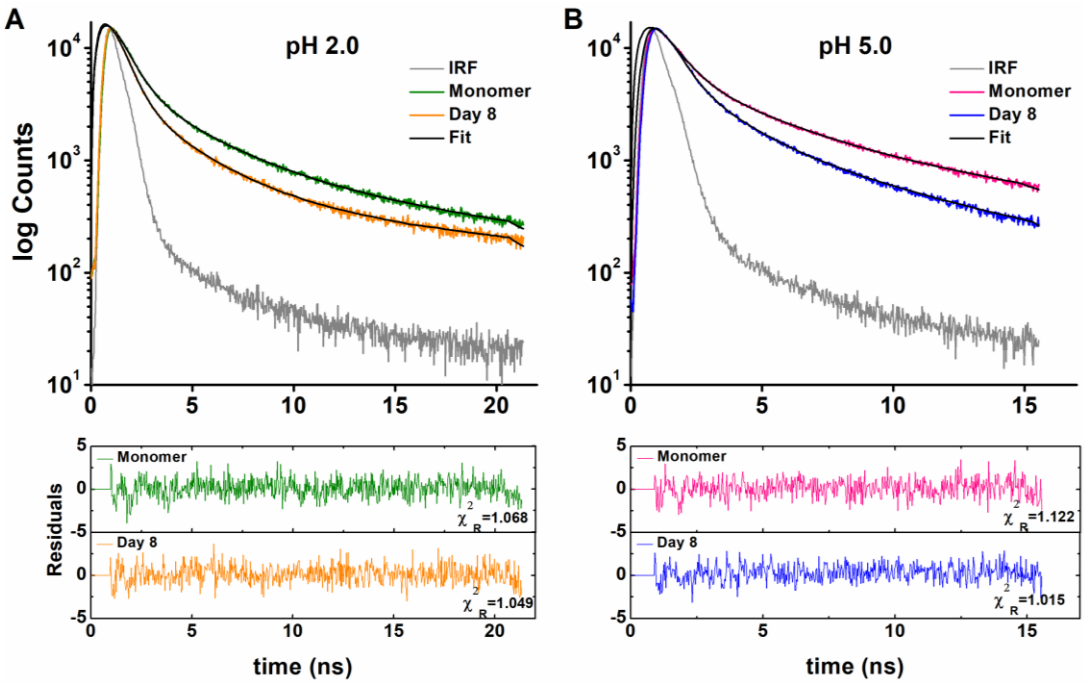

Figure 6.11: Luminescence intensity decay (λ_{ex} 340 nm) and its 3 exponential fit are displayed for HEWL monomers and aggregates (100 µM) at pH 2 (**A**) and pH 5 (**B**). The lower panel shows residuals obtained from the 3 exponential fit.

Sample	α_1	α_2	α_3	τ_1 (ns)	τ_2 (ns)	τ_3 (ns)	τ_{mean} (ns)	χ_R^2
Monomer	0.820	0.160	0.021	0.69 (0.007)	2.89 (0.19)	14.50 (0.37)	1.304 (0.00)	1.068
Day 8	0.882	0.105	0.013	0.56 (0.009)	2.56 (0.057)	17.17 (2.79)	0.94 (0.029)	1.049

Table 6.1: Fitted parameters obtained from 3 exponential fit for the HEWL monomers and Day 8 aggregate formed at pH 2.0. The values in the parenthesis for tau represents the standard deviation obtained from two independent measurements while alpha values are taken from the best-fitted data.

Sample	α_1	α_2	α_3	τ_1 (ns)	τ_2 (ns)	τ_3 (ns)	τ_{mean} (ns)	χ_R^2
Monomer	0.782	0.170	0.048	0.66 (0.01)	2.61 (0.23)	10.56 (0.69)	1.44 (0.10)	1.122
Day 8	0.816	0.149	0.035	0.50 (0.10)	2.10 (0.33)	7.78 (0.81)	0.96 (0.11)	1.015

Table 6.2: Fitted parameters obtained from 3 exponential fit for the HEWL monomers and Day 8 aggregate formed at pH 5.0. The values in the parenthesis for tau represents the standard deviation obtained from two independent measurements while alpha values are taken from the best-fitted data.

At pH 2, the first two components (τ_1 and τ_2) for aggregates are slightly lower than that of monomer. Apart from this, the contributions (α_1) from the smallest component (τ_1) has also

increased in case of aggregates. These collectively brought down the mean lifetime of aggregates to 0.94 ± 0.029 ns as compared to monomers, 1.304 ns (Table 6.1). However, the largest component (τ_3) with least contribution (α_3) has further decreased in case of aggregates (α_3=0.013) due to which its effect on the mean lifetime could not be observed.

In case of aggregates formed at pH 5, all the components (τ_{1-3}) are smaller than those of monomers (Table 6.2). Also the contribution (α_1) from the smallest component (τ_1) among aggregates has increased. These collectively resulted in the smaller mean lifetime of HEWL aggregates (1.44 ± 0.01 ns) than monomers (0.96 ± 0.11 ns).

The decreased mean lifetime of aggregates obtained both at pH 2 and 5 supports the observed lower values of quantum yield for aggregates than their corresponding monomers (Figure 6.10). This in turn confirms the crucial role of extinction coefficient behind the enhanced luminescence observed for HEWL aggregates.

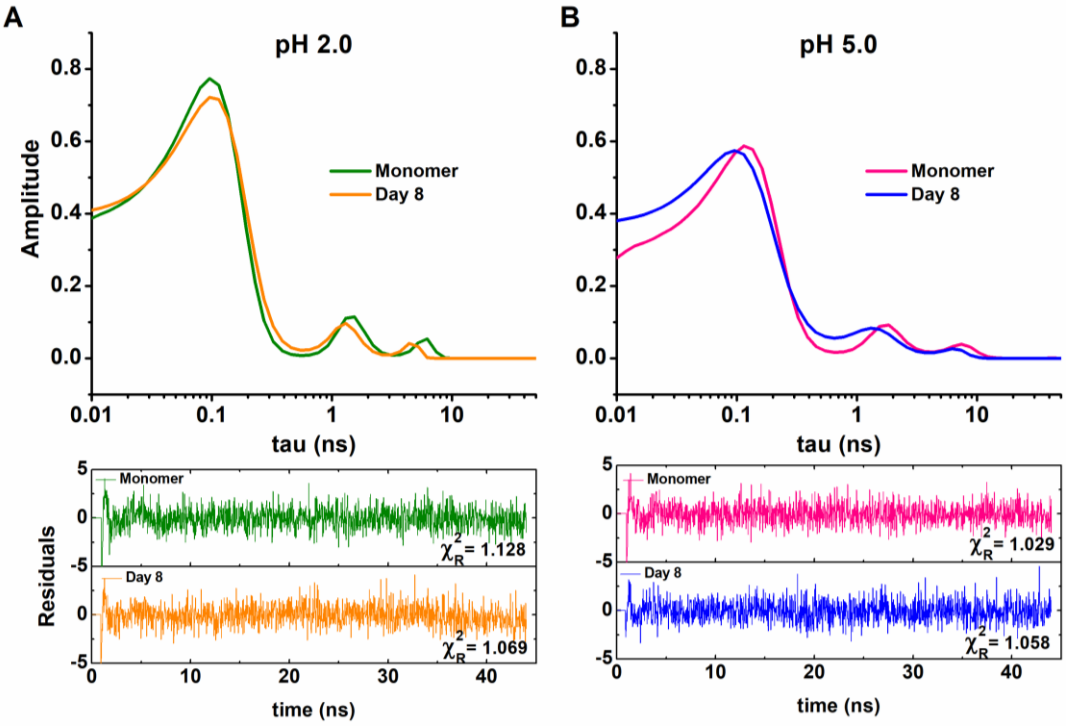

Figure 6.12: Panel **A** and **B** shows the lifetime distributions obtained from MEM analysis for the monomer and aggregates (100 µM) at pH 2 and 5, respectively. Lower panels display the fitted residuals.

The observations made by the discrete analysis were further validated by the MEM analysis. The lifetime distributions obtained for the samples at both pH displays three distributions for both the monomer and 8 day old aggregate (Figure 6.12). However, the distributions of the aggregate are shifted on the lower time scale for the two larger components in case of

pH 2 while for all the components for aggregates at pH 5. These shifts towards the lower timescale for the individual components suggests an overall decrease in the lifetime of the aggregates, similar to those observed in discrete analysis.

Although the lifetime and quantum yield of aggregates are lower than that of the monomers, the gradual rise in their luminescence intensity adds up to the evidence towards the major role of extinction coefficient. Thus, the higher luminescence observed for HEWL aggregates could predominantly be due to increase in their extinction coefficient. To sum up, the luminescence form HEWL aggregates observed and reported here could be due to the emissions from charge transfer states (with inefficient charge recombination) and ProCharTS is the major reason behind the observed absorption spectra for HEWL aggregates beyond 325 nm.

6.3 Conclusions

a) ProCharTS can track the growth of protein aggregates from UV-Vis absorption spectrum as a label-free tool, given the protein is rich/moderately rich in charged residues

b) ProCharTS are more sensitive in detecting early oligomers and are equally sensitive in detecting fibrillar aggregates as compared to ThT

c) The intrinsic luminescence from aggregates could be due to the transitions from charge transfer states at λ_{ex} >325 nm

d) Concomitant rise in intrinsic luminescence from aggregates with increasing incubation period could also be used to track the growth of aggregates

e) The increase in luminescence with the age of aggregates happens in spite of decrease in quantum yield and luminescence lifetime, implying the contribution of rising extinction coefficient that increases with the growth of oligomers and are maximum for the fibrils

f) The blue shift observed in the intrinsic luminescence from aggregates at λ_{ex} >325 nm are a sign of onset of maturation of oligomers into fibrils or simply the presence of fibril with charged residues that are shielded from water.

Chapter 7

Thesis Summary & Future Directions

7.1: Thesis Summary

The whole thesis revolved around the central theme of photo-induced electron transfer involving side chains of charged residues and peptide backbone in proteins, its consequent absorption spectra, ProCharTS and luminescence from charge transfer states. The solutions of pure charged amino acids (Lysine, Lysine·HCl, Glutamate and their capped derivatives) and selected proteins rich in charged residues display similar excitation and emission spectra apart from showing significant ProCharTS. However, their drastically different extinction coefficients clearly demonstrated the crucial role of proximity of interacting side chains towards charge transfer transitions. Apart from this, similarity in their Stokes shift, quantum yield and luminescence lifetime suggests towards the common origin and that could be charge recombination luminescence. The lower quantum yield and luminescence lifetime hints towards the lower rates of charge recombination. Moreover, the extinction coefficient are found to be the major contributor towards the origin of luminescence from charge transfer states. It is again worth noting that such luminescence are sensitive towards the solvent polarity owing to their huge Stokes shift.

Since, the observed luminescence are excitation wavelength dependent and possess significant presence in UV-Visible region, they are found to modulate the fluorescence of other chromophores sharing the same spectral region. It was found that the charged residues in the vicinity of indole not only quenched the fluorescence lifetime of Trp but also changed the decay kinetics of excited state population. This could be one of the reasons behind the multi-exponential decay of Trp in proteins. Similarly, the effect of intrinsic luminescence from charge transfer states was also observed to modulate the fluorescence of an extrinsic fluorophore, Dansyl labelled to protein, HuSA which is moderately rich in charged residues.

Further, the ProCharTS was found to be suitable in monitoring protein unfolding as well as protein aggregation. Both the molecular events revealed insight on the dependence of ProCharTS on the proximal distance between the interacting side chains as well as their population and density at any given condition. The decrease in Stokes shift observed for luminescence (at $\lambda_{ex} \geq 330$ nm) from fibrillar HEWL aggregates hold the assumption of their (ProCharTS luminescence) sensitivity towards the solvent polarity. Finally, the increase in luminescence from HEWL aggregates with time was observed in spite of decrease in their luminescence lifetime and quantum yield, which signifies the major contribution of extinction coefficient in the origin of such intrinsic luminescence.

7.2: Future Directions

The sensitivity of ProCharTS towards the proximal distance between the interacting side chains of charged residues, presence of counter ions, pH and polarity of the solvent makes it a promising tool to investigate several other molecular processes like Protein-Protein interactions, Protein-Ligand interactions, detection of post-translation modification like phosphorylation in proteins, Protein-DNA/RNA interactions and several others. Apart from this, ProCharTS could also be used in detection of heavy metals using proteins that can bind metal ions triggering some structural changes in protein. As shown in this work, ProCharTS could also serve as a label-free tool to study structural changes in proteins like intrinsically disordered proteins (IDPs).

Apart from the charged amino acids considered in this work (Lysine and Glutamate), remaining charged amino acids, Asp, Arg and His and protein rich in these charged amino acids could also be explored for similar intrinsic luminescence properties. This would further establish the phenomena of charge transfer transitions in proteins.

Another ambitious step would be developing ways to increase the quantum yield of luminescence arising from charge transfer states. With this possibility, certainly the applications of ProCharTS would expand from mere UV-Visible spectroscopy to other fields like microscopy.

Appendix

Appendix-I

Reagents prepared for estimation of protein by Lowry Method:

Reagent I is prepared by mixing the following two solutions

A. 50 mL of 2% sodium carbonate mixed with 50 ml of 0.1 N NaOH solution

Na_2CO_3	1 gm
NaOH	0.2 gm

B. 10 mL of 1.56% copper sulphate solution mixed with 10 mL of 2.37% sodium potassium tartarate solution

$KNaC_4H_4O_6.4H_2O$	0. 237 gm
$CuSO_4.5H_2O$	0.156 gm

The above mentioned solutions were mixed, 2 mL of (B) with 100 ml of (A) to obtain Reagent I

Reagent II was prepared by mixing Folin's reagent with equal volume of water. This solution was stored in dark.

Both reagents I and II were freshly prepared just before the experiments.

Appendix-II

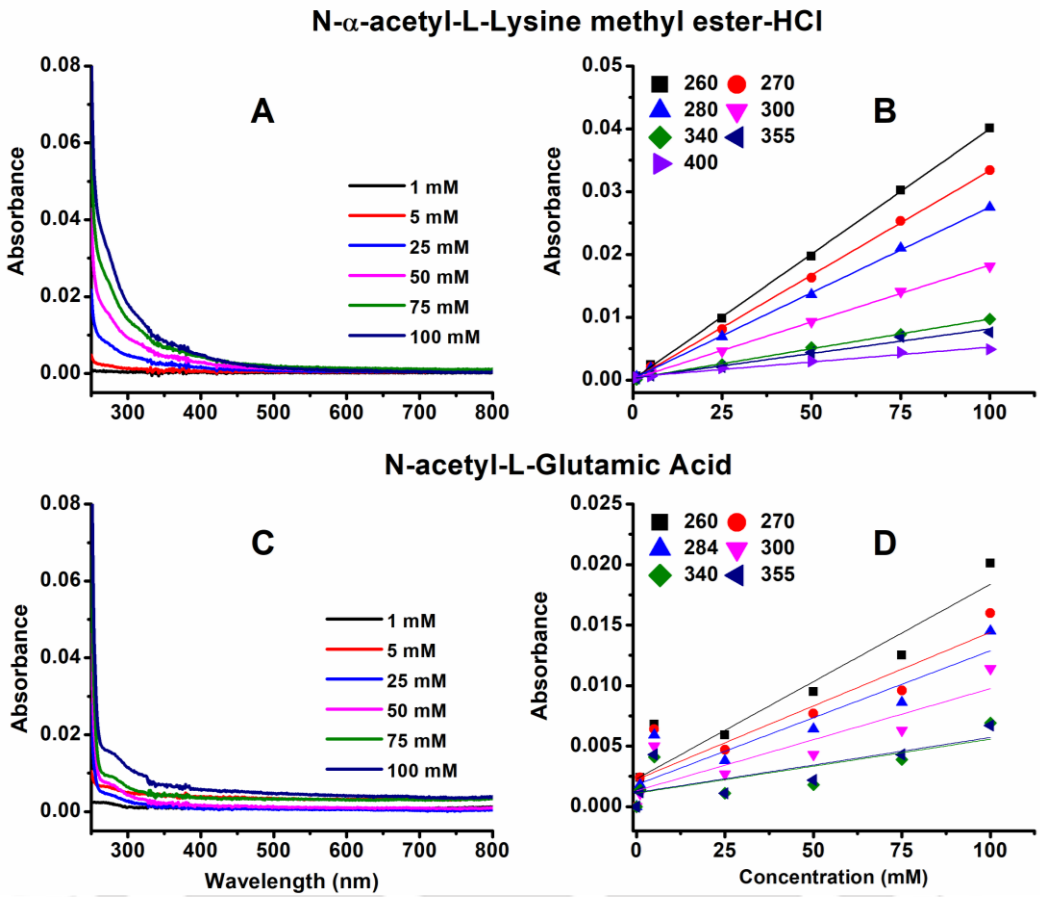

Figure A1: Absorption spectra for different concentrations of N-α-acetyl-L-lysine methyl ester·HCl (capped-Lysine·HCl) and N-acetyl-L-glutamaic acid (capped-Glutamic acid) are shown in panel **A** and **C,** respectively. Absorbance of capped-Lysine·HCl (**B**) and capped-Glutamic acid (**D**) at selected wavelengths are plotted against different concentrations. The solid lines in panel **B** and **D** are the linear fits obtained for the rise in absorbance with increasing concentration at the given wavelengths. Lower concentrations of these amino acids (as compared to uncapped ones in Figure 3.1) are used due to expensive nature of capped Lysine·HCl and due to lower solubility of capped-Glutamic acid.

Appendix-II

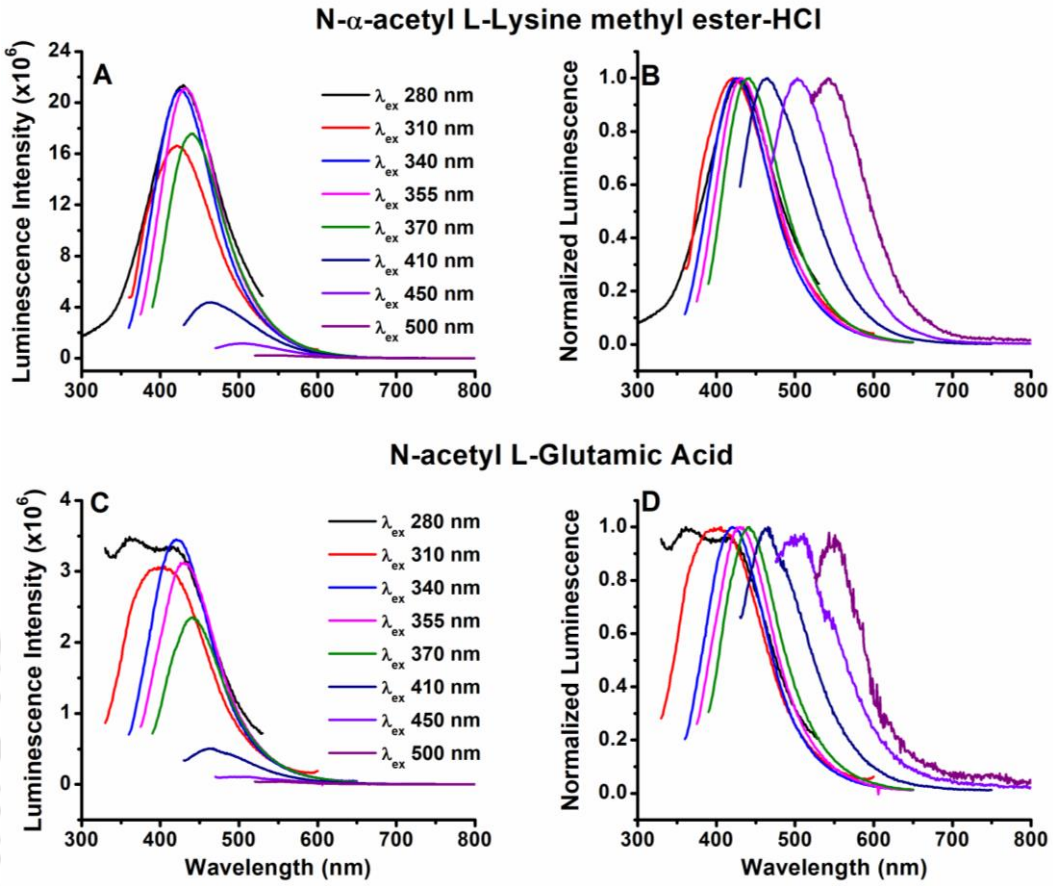

Figure A2: Luminescence spectra at different excitation wavelengths for capped-Lysine·HCl and capped-Glutamic acid are shown in panel **A** and **C**, respectively. Their normalized luminescence spectra are shown in **B** and **D,** respectively. All the excitation were done with 2 nm slit width and emission was collected with 15 nm slit width. Concentration used were 100 mM each for capped Lysine·HCl and capped Glutamic acid.

Appendix-II

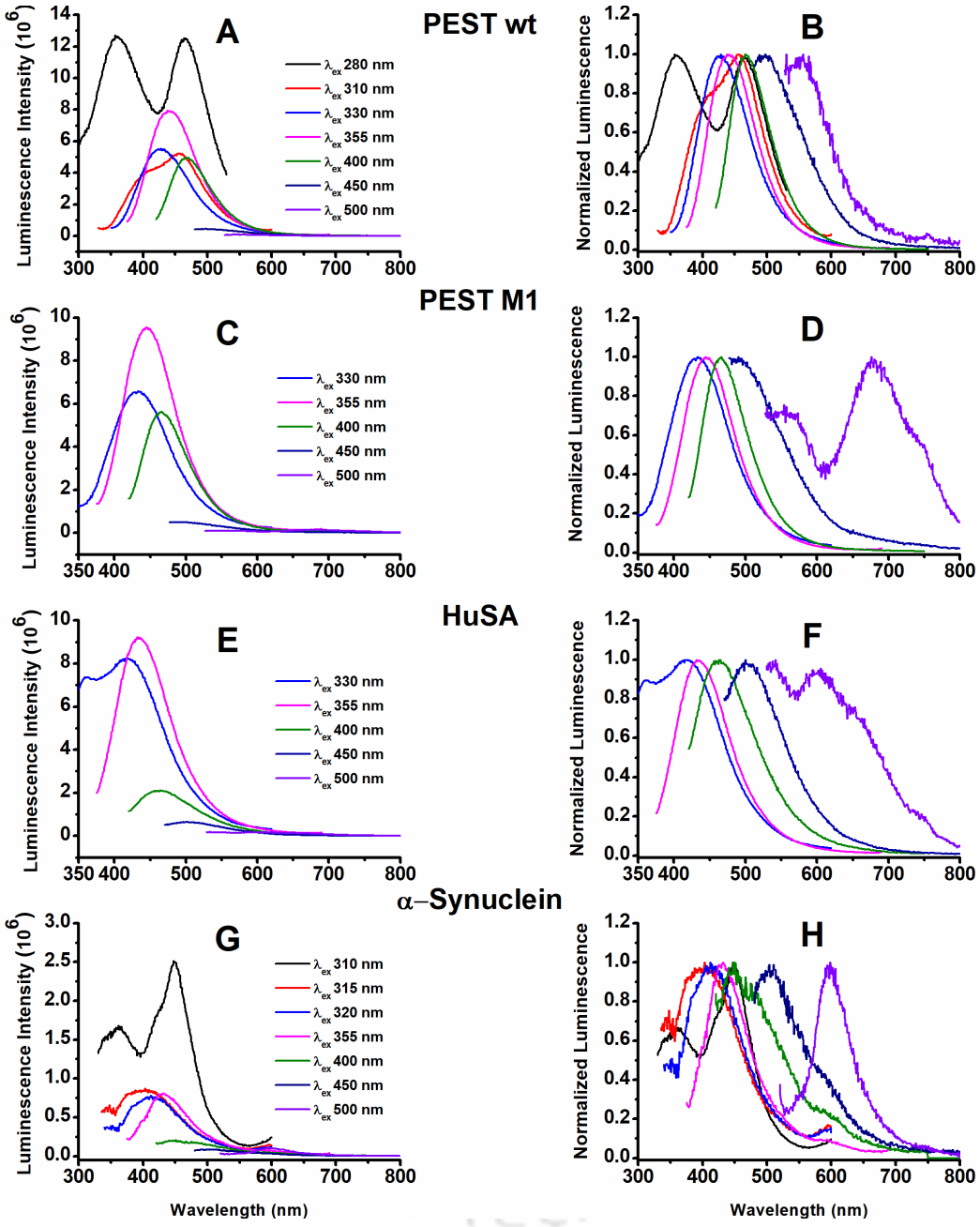

Figure A3 : Luminescence spectra at different excitation wavelengths for PEST wt, PEST M1, HuSA and α-Synuclein are shown in panel **A**, **C**, **E** and G, respectively. Normalized luminescence spectra for the same are shown in **B**, **D**, **F** and **H**, respectively. All the excitation were done with 2 nm slit width and emission was collected with 15 nm slit width. Concentrations used were 50 µM for PEST M1 and PEST wt, 10 µM of HuSA and 35 µM of α-Synuclien.

Appendix-II

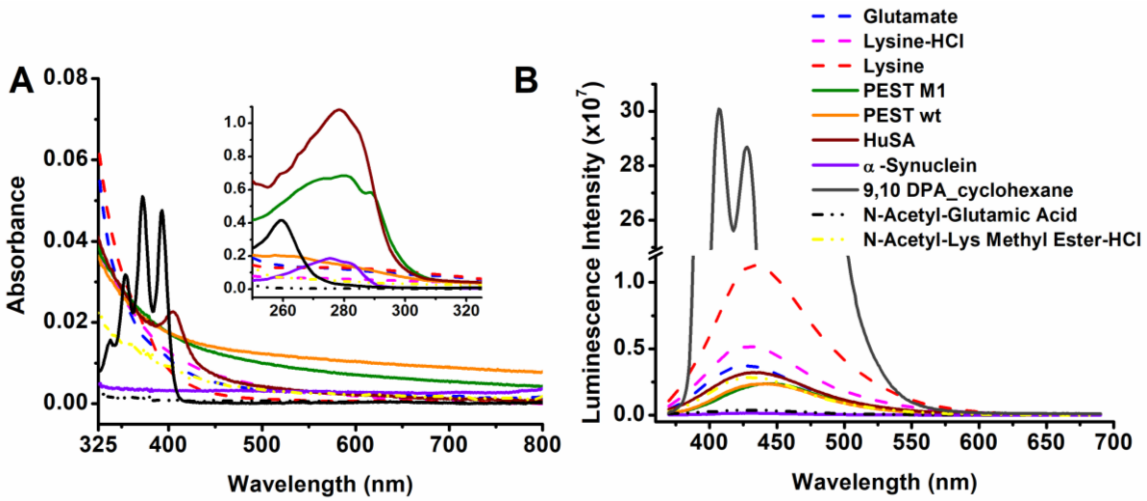

Figure A4: Panel **A** and **B** shows the absorbance and luminescence spectra, respectively for all the amino acids and proteins utilized in the quantum yield calculations. Luminescence spectra was collected for λ_{ex} 355 nm between 370-690 nm using excitation slit width of 1 nm and emission slit width of 5 nm. Inset in panel A shows the absorbance in the spectral region of 250 -325 nm. Break provided in panel **B** is between $1.2x10^7$ to $24.9x10^7$.

Appendix-III

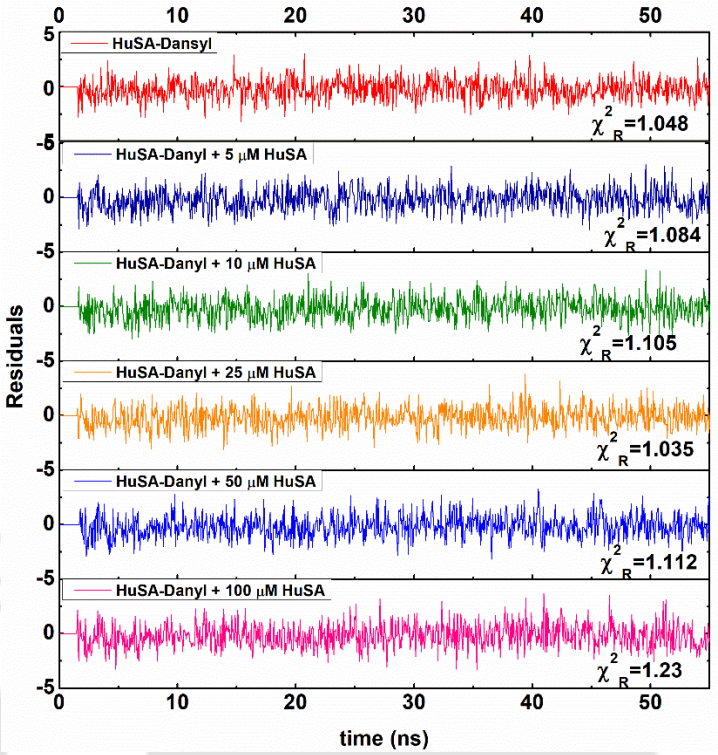

Figure A1: Residuals for 3 exponential fit obtained for fluorescence intensity decay of Dansyl-HuSA displayed in Figure 5.3

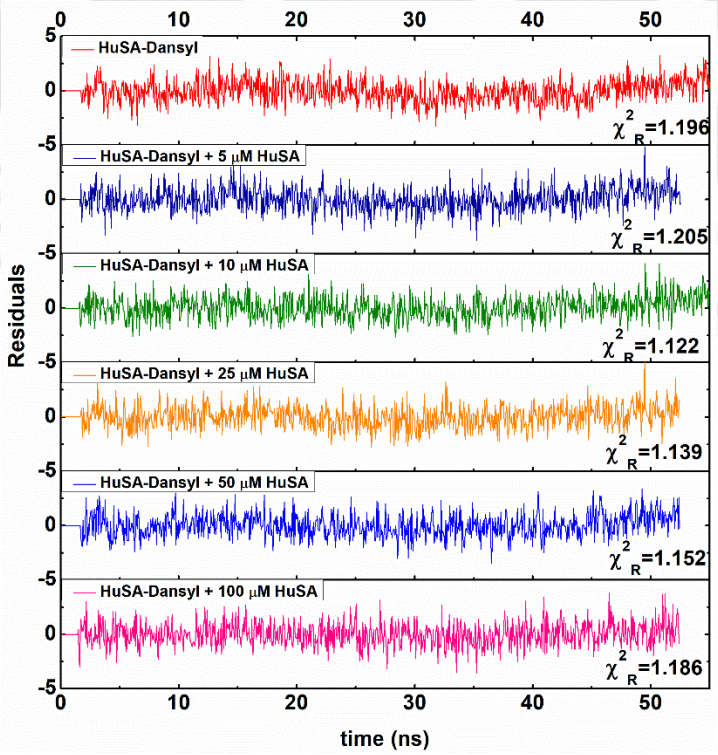

Figure A2: Residuals obtained from MEM fit for Dansyl-HuSA in presence of different concentrations of HuSA shown in Figure 5.6.

Appendix-III

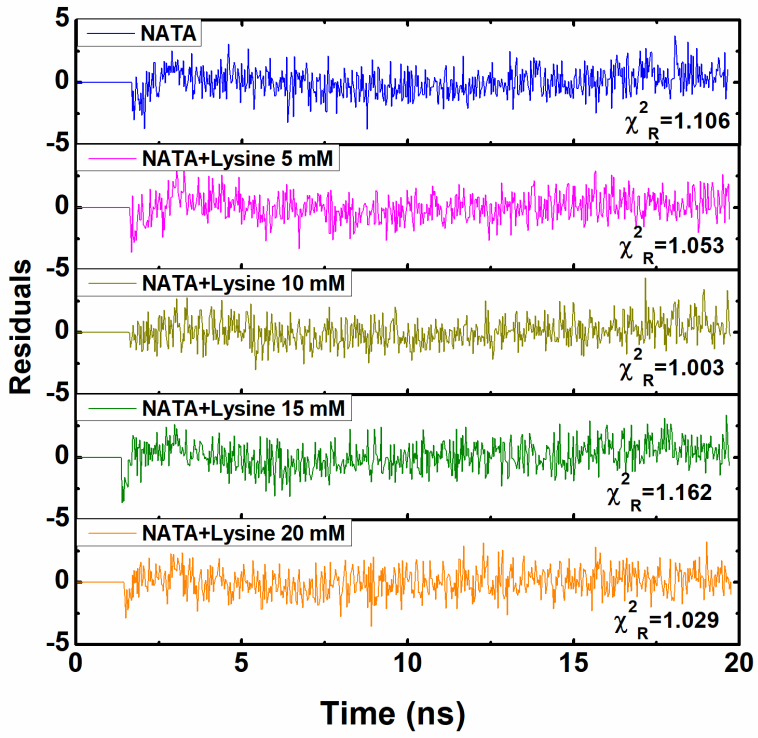

Figure A3: Residuals obtained from the MEM analysis done for fluorescence intensity decay of NATA in presence of Lysine (Figure 5.10).

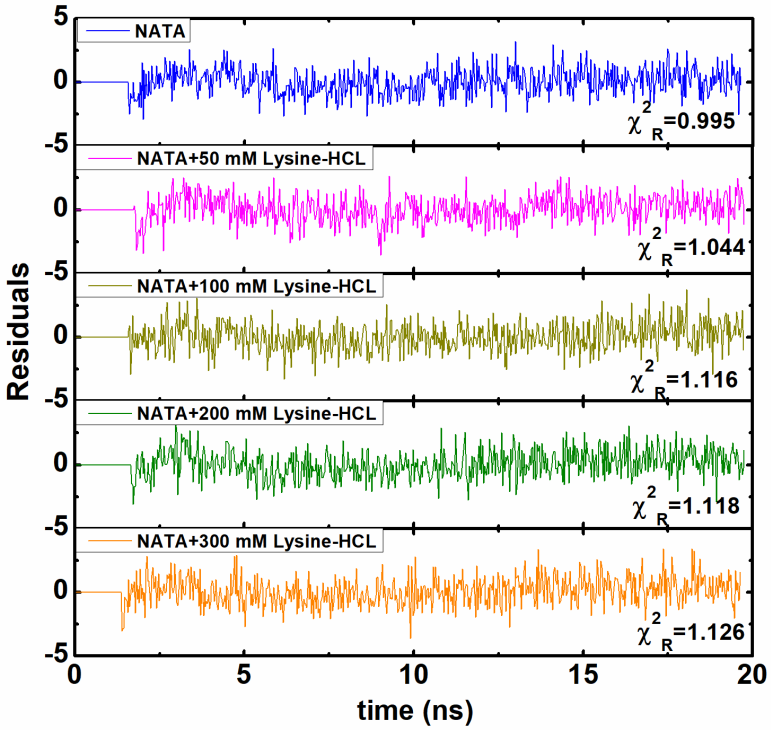

Figure A4: Residuals obtained from the MEM analysis done for fluorescence intensity decay of NATA in presence of Lysine·HCl (Figure 5.15).

Appendix-III

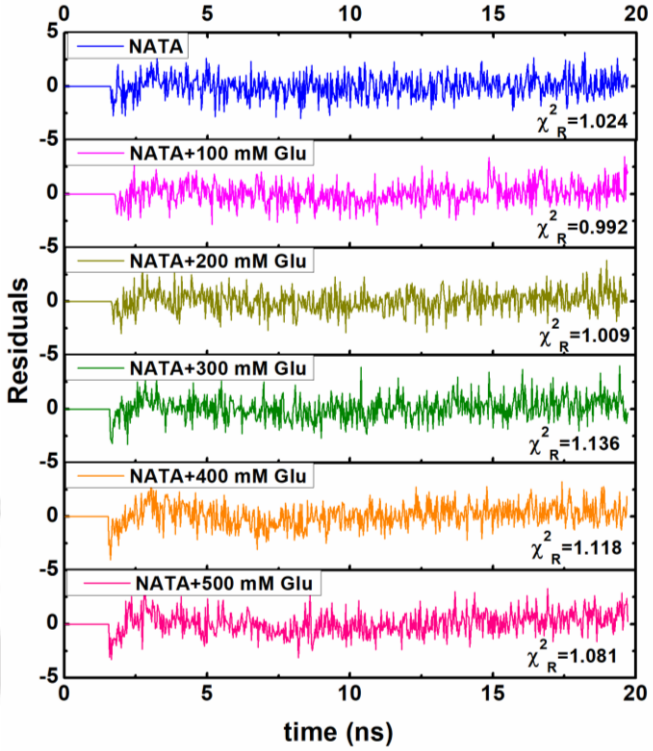

Figure A5: Residuals obtained from the MEM analysis done for fluorescence intensity decay of NATA in presence of Glutamate (Figure 5.20).

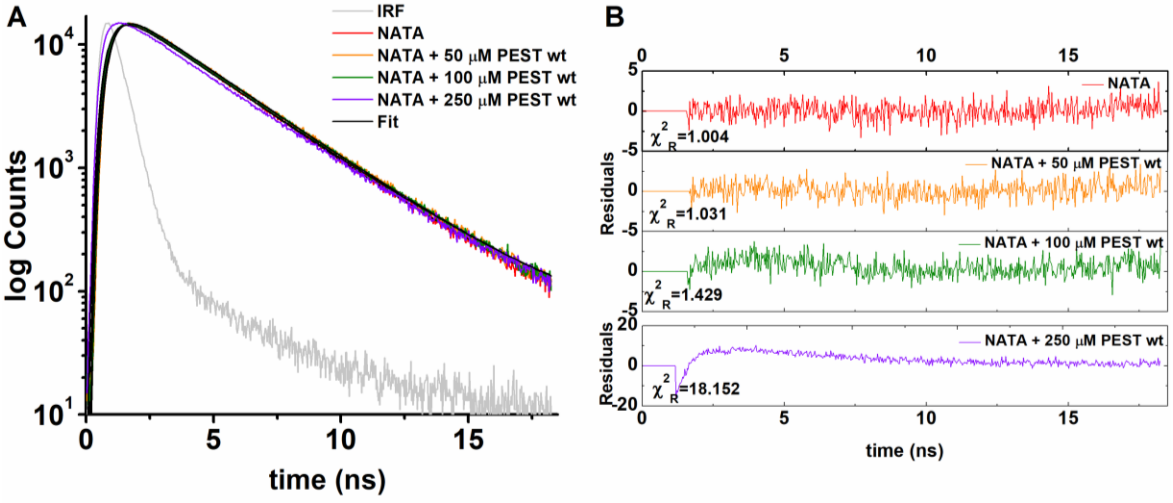

Figure A6: Panel **A** shows the fluorescence intensity decay and 1 exponential fit for 20 μM NATA at λ_{ex} 295 nm in presence of different concentration of PEST wt. Panel **B** shows the residuals from the fit. Emission was collected using 340±20 nm band pass filter.

Appendix-III

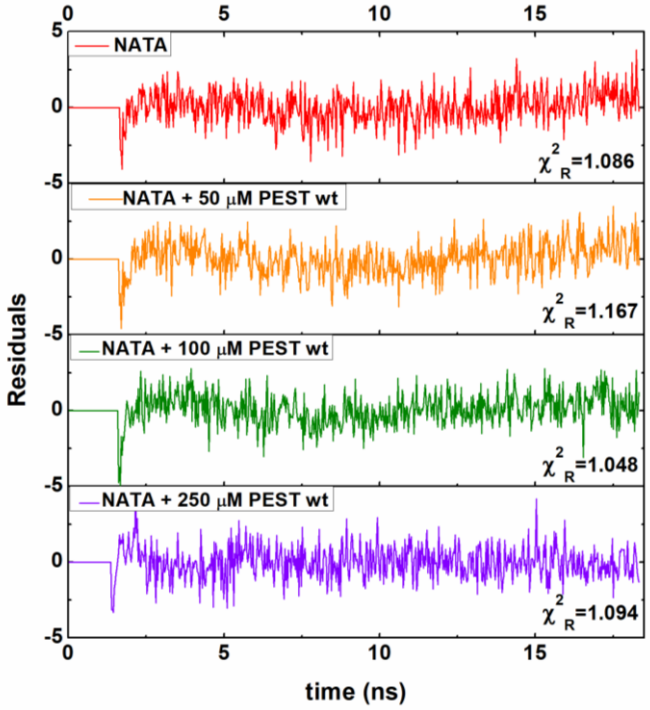

Figure A7: Residuals obtained from the MEM analysis done for fluorescence intensity decay of NATA in presence of PEST wt (Figure 5.24).

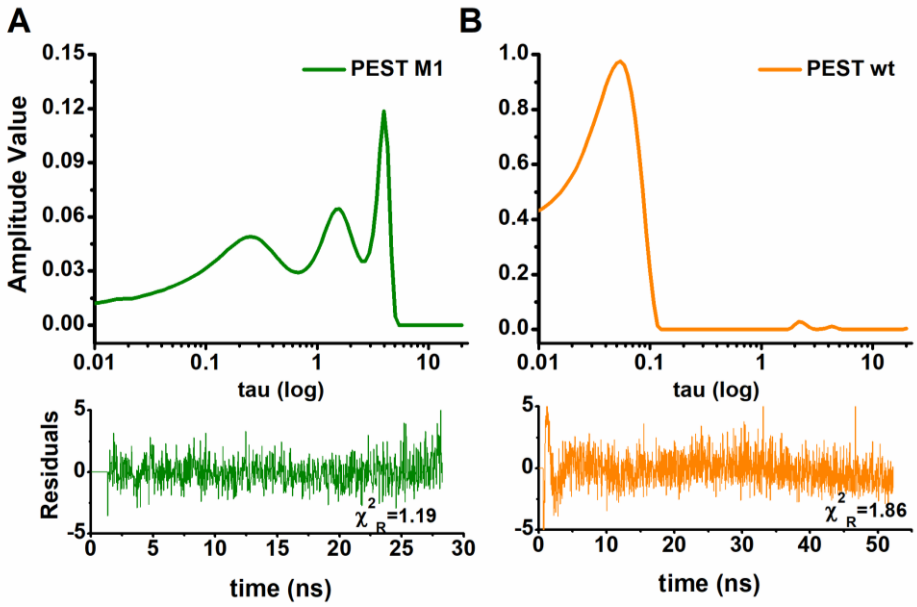

Figure A8: Lifetime distributions obtained for **A**) PEST M1 and **B**) PEST wt at λ_{ex} 295 nm. NATA in presence PEST wt. Panel **A** shows the distribution while the panel **B** shows the residuals obtained from the MEM fit. Emission was collected using 340±20 nm band pass filter.

Appendix-IV

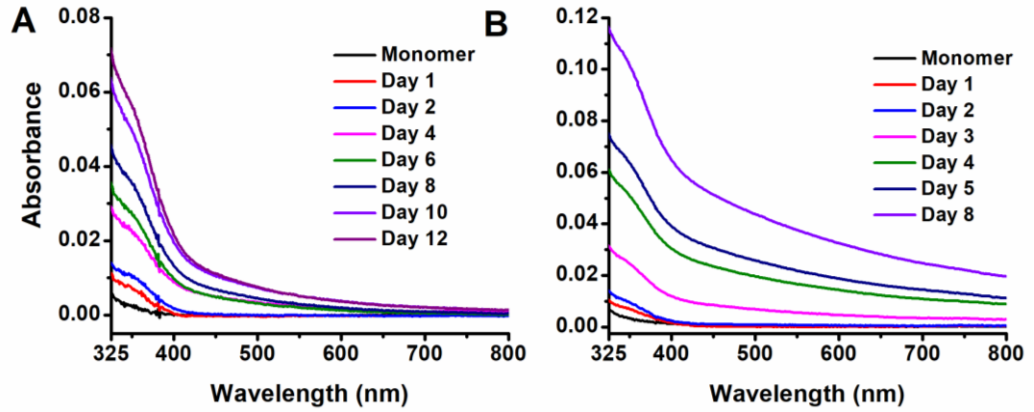

Figure A1: Panel **A** and **B** shows the ProCharTS of HEWL aggregates (100 µM) formed at pH 2 and 5, respectively.

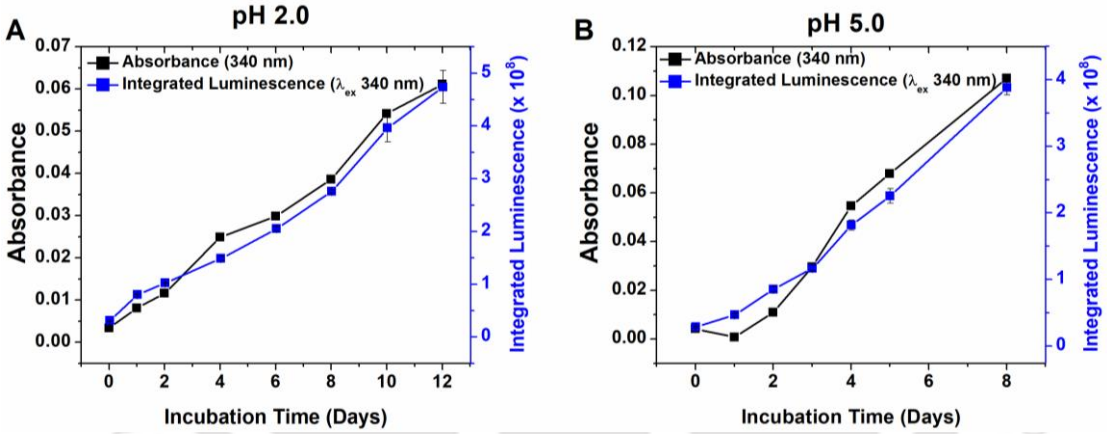

Figure A2: Panel **A** and **B** shows the change in absorbance at 340 nm and integrated luminescence at λ_{ex} 340 nm for HEWL aggregates (100 µM) formed at pH 2.0 and 5.0, respectively.

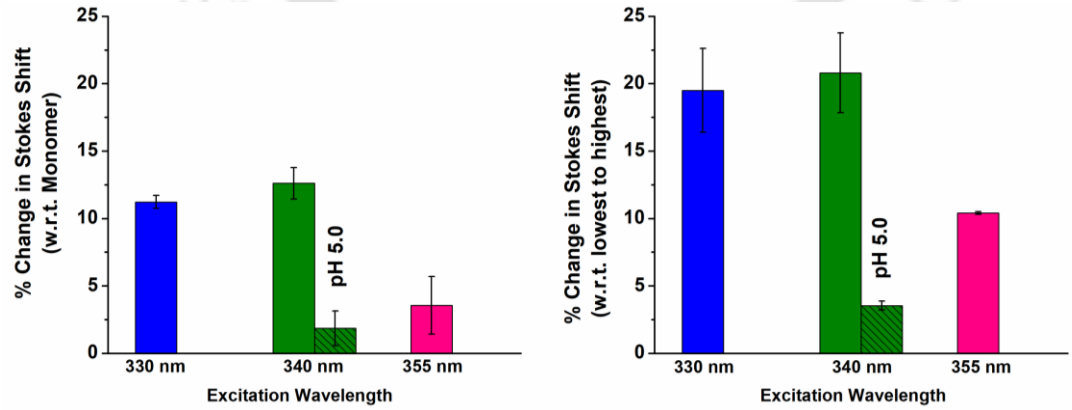

Figure A3: Percentage change in Stokes shift of HEWL aggregates formed at pH 2. Left panel shows the change with respect to monomer while the right one displays the change respect to the lowest change observed at the given excitation wavelength. The respective change observed for aggregates at pH 5 are shown in dashed bar.

Appendix-IV

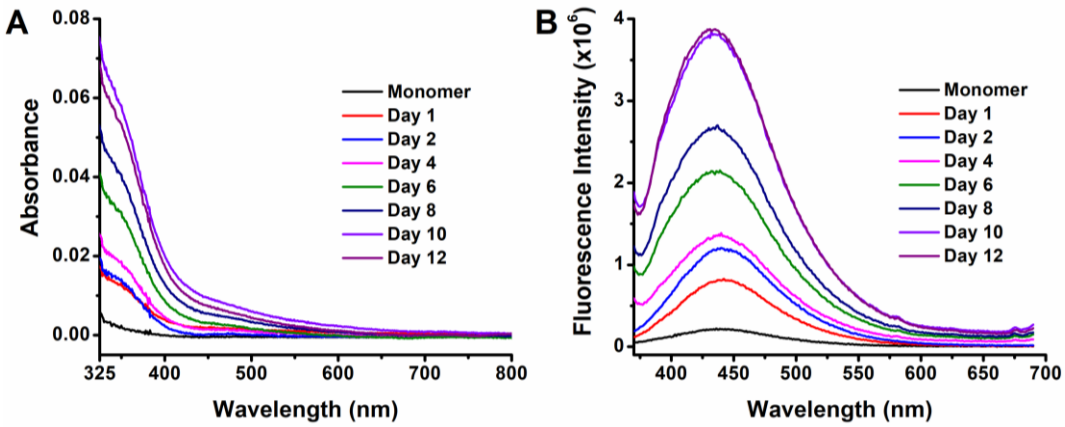

Figure A4: Panel **A** and **B** shows the absorbance and luminescence spectra (λ_{ex} 355 nm), respectively for different day old aggregates at pH 2 used for calculation of quantum yield at λ_{ex} 355 nm. All emission spectra are corrected for inner filter effect.

List of Publications & Conferences

List of Publications:

1. Ansari M. Z.; Kumar A.; Ahari D.; Priyadarshi A.; Lolla P.; Bhandari R.; Swaminathan R. 2018. Protein Charge Transfer Absorption Spectra: An Intrinsic Probe to Monitor Structural and Oligomeric Transitions in Proteins. *Faraday Discussions* 207: 91–113
2. Kumar A.; Ahari D.; Priyadarshi A.; Ansari M. Z.; Swaminathan R. (in press). Weak Intrinsic Luminescence in Monomeric Proteins Arising from Charge Recombination. *The Journal of Physical Chemistry B* (DOI: 10.1021/acs.jpcb.9b10071)
3. Kumar A.; Alom E. S.; Priyadarshi A.; Ahari D.; Swaminathan R. Role of ProCharTS in the Origin of Multi-Exponential Decay of Trp in Proteins. (*Manuscript under preparation*)
4. Kumar A.; Singh A.; Swaminathan R. Easy Detection of Protein Aggregates and Amyloid Fibrils using Intrinsic Luminescence from Charge Transfer States in Proteins. (*Manuscript under preparation*)

List of conference papers:

1. Ansari, M. Z.; Kumar, A.; Ahari, D.; Priyadarshi, A.; Lolla, P.; Bhandari, R.; Swaminathan, R. 2018. Protein Charge Transfer Absorption Spectra: An Intrinsic Probe to Monitor Structural and Oligomeric Transitions in Proteins. *Biophysical Journal* 114: 586a (DOI: 10.1016/j.bpj.2017.11.3208)
2. Kumar, A.; Ahari, D.; Priyadarshi, A.; Ansari, M. Z.; Swaminathan, R. 2020. Weak Intrinsic Luminescence in Monomeric Proteins Arising from Charge Recombination, *Biophysical Journal*, 118: 468a (DOI: 10.1016/j.bpj.2019.11.2600)
3. Kumar, A.; Alom, E. S.; Priyadarshi, A.; Ahari, D.; Ansari, M. Z.; Swaminathan, R.; 2020. Unraveling the Origin of Multi-Exponential Fluorescence Intensity Decay of Tryptophan in Proteins, *Biophysical Journal*, 118: 469a (DOI: 10.1016/j.bpj.2019.11.2604)

List of national conferences attended:

1. Kumar A, Ahari D, Ansari MZ, Swaminathan R. Intrinsic fluorescence from Protein Charge Transfer States: Photochemical Features. Poster presented at Research Concleave'19, IIT Guwahati, March 2019
2. Kumar A, Ahari D, Ansari MZ, Swaminathan R. Emission arising from Protein Charge Transfer absorption among charged amino acids and protein rich in charged amino acids. Poster presented at FCS-2018, JNU, New Delhi, November 2018
3. Kumar A, Swaminathan R. Label free approach for the detection of protein aggregation. Oral presentation delivered at FCS-2017, IIT Guwahati, December 2017
4. Kumar A, Ansari MZ, Ahari D, Swaminathan R. Unraveling molecular identity of aggregated proteins and intrinsically disordered proteins using MALDI-TOF. Poster presented at ICSIMR, IIT Guwahati, June 2017
5. Kumar A, Javadi M, Kunnumakkara AB, Swaminathan R. HEWL nanoparticles: Nanocarrier for Cancer Therapy. Presented poster at OWLS-2016, TIFR Mumbai, March 2016
6. Kumar A, Swaminathan R. Single molecule approach towards understanding HEWL aggregation. Poster presented at 7th Bangalore Microscopy Course, NCBS Bangalore, September 2015
7. Attended workshop on Microscopy at Bangalore Microscopy Course, at NCBS Bangalore, September 20th – 27th, 2015
8. Kumar A, Mallick B, Swaminatha R. Single molecule detection of HEWL aggregation using TIFR microscopy. Poster presented at FluoRA-2014 at IISER Pune, December 2014

References

Aguzzi A, Calella AM. 2009. Prions: Protein Aggregation and Infectious Diseases. *Physiological Reviews* 89: 1105-52

Aguzzi A, O'Connor T. 2010. Protein aggregation diseases: pathogenicity and therapeutic perspectives. *Nature Reviews Drug Discovery* 9: 237

Ahn M, Hagan CL, Bernardo-Gancedo A, De Genst E, Newby FN, et al. 2016. The Significance of the Location of Mutations for the Native-State Dynamics of Human Lysozyme. *Biophysical Journal* 111: 2358-67

Alexander Ross JB, Laws WR, Rousslang KW, Wyssbrod HR. 2002. Tyrosine Fluorescence and Phosphorescence from Proteins and Polypeptides In *Topics in Fluorescence Spectroscopy*, ed. JR Lakowicz, pp. 1-64. Boston, MA: Springer US

Aliverti A, Curti B, Vanoni MA. 1999. Identifying and Quantitating FAD and FMN in Simple and in Iron-Sulfur-Containing Flavoproteins In *Flavoprotein Protocols*, ed. SK Chapman, GA Reid, pp. 9-23. Totowa, NJ: Humana Press

Ansari MZ, Kumar A, Ahari D, Priyadarshi A, Lolla P, et al. 2018. Protein charge transfer absorption spectra: an intrinsic probe to monitor structural and oligomeric transitions in proteins. *Faraday Discussions* 207: 91-113

Ardito F, Giuliani M, Perrone D, Troiano G, Lo Muzio L. 2017. The crucial role of protein phosphorylation in cell signaling and its use as targeted therapy. *International journal of molecular medicine* 40: 271-80

Arikuma Y, Nakayama H, Morita T, Kimura S. 2010. Electron Hopping over 100 Å Along an α Helix. *Angewandte Chemie International Edition* 49: 1800-04

Arnaudov LN, de Vries R. 2005. Thermally Induced Fibrillar Aggregation of Hen Egg White Lysozyme. *Biophysical Journal* 88: 515-26

Ashraf GM, Greig NH, Khan TA, Hassan I, Tabrez S, et al. 2014. Protein misfolding and aggregation in Alzheimer's disease and Type 2 Diabetes Mellitus. *CNS & neurological disorders drug targets* 13: 1280-93

Aubert C, Mathis P, Andr, xe, Eker PM, Brettel K. 1999. Intraprotein Electron Transfer between Tyrosine and Tryptophan in DNA Photolyase from Anacystis nidulans. *Proceedings of the National Academy of Sciences of the United States of America* 96: 5423-27

Ballou GA, Boyer PD, Luck JM, Lum FG. 1944. The heat coagulation of human serum albumin. *Journal of Biological Chemistry* 153: 589-605

Baranov LY, Schlag EW. 1999. New mechanism for facile charge transport in polypeptides. *Zeitschrift für Naturforschung A* 54: 387-96

Barbara PF, Meyer TJ, Ratner MA. 1996. Contemporary Issues in Electron Transfer Research. *The Journal of Physical Chemistry* 100: 13148-68

Barber J. 2009. Photosynthetic energy conversion: natural and artificial. *Chemical Society Reviews* 38: 185-96

Barnaby OS, Cerny RL, Clarke W, Hage DS. 2011. Comparison of modification sites formed on human serum albumin at various stages of glycation. *Clin Chim Acta* 412: 277-85

Berberan Santos MN, Valeur B. 2012. *Molecular Fluorescence: Principles and Applications, Second Edition*. Wiley-VCH.

Berg JM, Tymoczko JL, Stryer L. 2006. Biochemistry. 5th. *New York: WH Freeman* 38: 76

Berlin YA, Burin AL, Ratner MA. 2000. On the long-range charge transfer in DNA. *The Journal of Physical Chemistry A* 104: 443-45

Bevington PR, Robinson DK, Bunce G. 1993. Data Reduction and Error Analysis for the Physical Sciences, 2nd ed. *American Journal of Physics* 61: 766-67

Bhattacharya A, Bhowmik S, Singh AK, Kodgire P, Das AK, Mukherjee TK. 2017. Direct Evidence of Intrinsic Blue Fluorescence from Oligomeric Interfaces of Human Serum Albumin. *Langmuir* 33: 10606-15

Bhattacharya A, Prajapati R, Chatterjee S, Mukherjee TK. 2014. Concentration-Dependent Reversible Self-Oligomerization of Serum Albumins through Intermolecular β-Sheet Formation. *Langmuir* 30: 14894-904

Blankenship RE, Prince RC. 1985. Excited-state redox potentials and the Z scheme of photosynthesis. *Trends in Biochemical Sciences* 10: 382-83

Blankenship RE. 1994. Protein structure, electron transfer and evolution of prokaryotic photosynthetic reaction centers. *Antonie van Leeuwenhoek* 65: 311-29

Blankenship RE. 2014. *Molecular mechanisms of photosynthesis*. John Wiley & Sons.

Boens N, Qin W, Basarić N, Hofkens J, Ameloot M, et al. 2007. Fluorescence Lifetime Standards for Time and Frequency Domain Fluorescence Spectroscopy. *Analytical Chemistry* 79: 2137-49

Bolton JR, Archer MD. 1991. Basic Electron-Transfer Theory In *Electron Transfer in Inorganic, Organic, and Biological Systems*, pp. 7-23: American Chemical Society

Bolton JR, Mataga N, McLendon G. 1991. Introduction to Electron Transfer in Inorganic, Organic, and Biological Systems In *Electron Transfer in Inorganic, Organic, and Biological Systems*, pp. 1-6: American Chemical Society

Brash DE. 1997. Sunlight and the onset of skin cancer. *Trends in Genetics* 13: 410-14

Braslavsky SE. 2007. Glossary of terms used in photochemistry, (IUPAC Recommendations 2006). *Pure and Applied Chemistry* 79: 293-465

Breton J, Martin JL, Migus A, Antonetti A, Orszag A. 1986. Femtosecond spectroscopy of excitation energy transfer and initial charge separation in the reaction center of the photosynthetic bacterium *Rhodopseudomonas viridis*. *Proceedings of the National Academy of Sciences* 83: 5121

Brettel K, Byrdin M. 2010. Reaction mechanisms of DNA photolyase. *Current Opinion in Structural Biology* 20: 693-701

Breydo L, Uversky VN. 2014. Chapter 1 - Molecular Mechanisms of Protein Misfolding In *Bio-nanoimaging*, ed. VN Uversky, YL Lyubchenko, pp. 1-14. Boston: Academic Press

Broo A, Larsson S. 1991. Electron transfer in azurin and the role of aromatic side groups of the protein. *The Journal of Physical Chemistry* 95: 4925-28

Brouwer Albert M. 2011. Standards for photoluminescence quantum yield measurements in solution (IUPAC Technical Report). In *Pure and Applied Chemistry*, pp. 2213

Brudar S, Hribar-Lee B. 2019. The Role of Buffers in Wild-Type HEWL Amyloid Fibril Formation Mechanism. *Biomolecules* 9: 65

Brüne D, Andrade-Navarro MA, Mier P. 2018. Proteome-wide comparison between the amino acid composition of domains and linkers. *BMC Research Notes* 11: 117

Bürgi J, Xue B, Uversky VN, van der Goot FG. 2016. Intrinsic Disorder in Transmembrane Proteins: Roles in Signaling and Topology Prediction. *PLOS ONE* 11: e0158594

Butler J, Land EJ, Prütz WA, Swallow AJ. 1982. Charge transfer between tryptophan and tyrosine in proteins. *Biochimica et Biophysica Acta (BBA) - Protein Structure and Molecular Enzymology* 705: 150-62

Calatayud JM, Zamora LL. 2013. Spectrophotometry | Pharmaceutical Applications☆ In *Encyclopedia of Analytical Science (Third Edition)*, ed. P Worsfold, C Poole, A Townshend, M Miró, pp. 249-62. Oxford: Academic Press

Canfield RE. 1963. The Amino Acid Sequence of Egg White Lysozyme. *Journal of Biological Chemistry* 238: 2698-707

Cantor CR, Schimmel PR. 1980. *Biophysical chemistry: Part II: Techniques for the study of biological structure and function*. W. H. Freeman and Company.

Cascarina SM, Ross ED. 2018. Proteome-scale relationships between local amino acid composition and protein fates and functions. *PLOS Computational Biology* 14: e1006256

Chaari A, Fahy C, Chevillot-Biraud A, Rholam M. 2015. Insights into Kinetics of Agitation-Induced Aggregation of Hen Lysozyme under Heat and Acidic Conditions from Various Spectroscopic Methods. *PLOS ONE* 10: e0142095

Chai B-h, Zheng J-m, Zhao Q, Pollack GH. 2008. Spectroscopic Studies of Solutes in Aqueous Solution. *The Journal of Physical Chemistry A* 112: 2242-47

Chan FTS, Kaminski Schierle GS, Kumita JR, Bertoncini CW, Dobson CM, Kaminski CF. 2013. Protein amyloids develop an intrinsic fluorescence signature during aggregation. *Analyst* 138: 2156-62

Charneski CA, Hurst LD. 2013. Positively Charged Residues Are the Major Determinants of Ribosomal Velocity. *PLOS Biology* 11: e1001508

Chen RF. 1968. Dansyl labeled proteins: Determination of extinction coefficient and number of bound residues with radioactive dansyl chloride. *Analytical Biochemistry* 25: 412-16

Chen X, Luo W, Ma H, Peng Q, Yuan WZ, Zhang Y. 2018. Prevalent intrinsic emission from nonaromatic amino acids and poly(amino acids). *Science China Chemistry* 61: 351-59

Chen Y, Barkley MD. 1998. Toward Understanding Tryptophan Fluorescence in Proteins. *Biochemistry* 37: 9976-82

Cid M-M, Bravo J. 2014. *Structure Elucidation in Organic Chemistry: The Search for the Right Tools*. John Wiley & Sons.

Clement E, Corongiu G. 1982. Charge transfer in nucleic acids. *International Journal of Quantum Chemistry* 22: 213-21

Creed D. 1984. The Photophysics And Photochemistry Of The Near-Uv Absorbing Amino Acids–I. Tryptophan And Its Simple Derivatives. *Photochemistry and Photobiology* 39: 537-62

Dawson RMC, Elliott DC, Elliott WH, Jones KM. 2002. *Data for biochemical research*. Clarendon Press.

De los Reyes GB, Dasog M, Na M, Titova LV, Veinot JGC, Hegmann FA. 2015. Charge transfer state emission dynamics in blue-emitting functionalized silicon nanocrystals. *Physical Chemistry Chemical Physics* 17: 30125-33

de Graff Adam MR, Hazoglou Michael J, Dill Ken A. 2016. Highly Charged Proteins: The Achilles' Heel of Aging Proteomes. *Structure* 24: 329-36

Deisenhofer J, Epp O, Miki K, Huber R, Michel H. 1985. Structure of the protein subunits in the photosynthetic reaction centre of Rhodopseudomonas viridis at 3Å resolution. *Nature* 318: 618-24

del Mercato LL, Pompa PP, Maruccio G, Torre AD, Sabella S, et al. 2007. Charge transport and intrinsic fluorescence in amyloid-like fibrils. *Proceedings of the National Academy of Sciences* 104: 18019

Demchenko AP, Tomin VI, Chou P-T. 2017. Breaking the Kasha Rule for More Efficient Photochemistry. *Chemical Reviews* 117: 13353-81

Demchenko AP. 1986. Spectroscopic Properties of Protein Chromophores In *Ultraviolet Spectroscopy of Proteins*, ed. AP Demchenko, pp. 5-26. Berlin, Heidelberg: Springer Berlin Heidelberg

Demchenko AP. 2013. *Ultraviolet Spectroscopy of Proteins*. Springer Science & Business Media.

Eftink MR, Jia J, Hu D, Ghiron CA. 1995. Fluorescence Studies with Tryptophan Analogs: Excited State Interactions Involving the Side Chain Amino Group. *The Journal of Physical Chemistry* 99: 5713-23

Eftink MR. 1991. Fluorescence Techniques for Studying Protein Structure. *Methods of Biochemical Analysis*

Eftink MR. 1994. The use of fluorescence methods to monitor unfolding transitions in proteins. *Biophysical journal* 66: 482-501

Eley DD, Spivey DI. 1962. Semiconductivity of organic substances. Part 9.—Nucleic acid in the dry state. *Transactions of the Faraday Society* 58: 411-15

Ervin J, Sabelko J, Gruebele M. 2000. Submicrosecond real-time fluorescence sampling: application to protein folding. *Journal of Photochemistry and Photobiology B: Biology* 54: 1-15

Fanali G, di Masi A, Trezza V, Marino M, Fasano M, Ascenzi P. 2012. Human serum albumin: From bench to bedside. *Molecular Aspects of Medicine* 33: 209-90

Fasano M, Curry S, Terreno E, Galliano M, Fanali G, et al. 2005. The extraordinary ligand binding properties of human serum albumin. *IUBMB Life* 57: 787-96

Feraud K, Dunn MS, Kaplan J. 1935. Spectroscopic investigations of amino acids and amino acid derivatives I. Ultra-violet absorption spectra of *l*-Tyrosine, *dl*-Phenylalanine, and *l*-Tryptophane. *Journal of Biological Chemistry* 112: 323-28

Fink AL. 1998. Protein aggregation: folding aggregates, inclusion bodies and amyloid. *Folding and Design* 3: R9-R23

Forster T. 1946. Energiewanderung und Fluoreszenz. *Naturwissenschaften* 33: 166-75

Fox MA, Galoppini E. 1997. Electric Field Effects on Electron Transfer Rates in Dichromophoric Peptides: The Effect of Helix Unfolding. *Journal of the American Chemical Society* 119: 5277-85

Frieden E. 1975. Non-covalent interactions: Key to biological flexibility and specificity. *Journal of Chemical Education* 52: 754

Gade Malmos K, Blancas-Mejia LM, Weber B, Buchner J, Ramirez-Alvarado M, et al. 2017. ThT 101: a primer on the use of thioflavin T to investigate amyloid formation. *Amyloid* 24: 1-16

Galoppini E, Fox MA. 1996. Effect of the Electric Field Generated by the Helix Dipole on Photoinduced Intramolecular Electron Transfer in Dichromophoric α-Helical Peptides. *Journal of the American Chemical Society* 118: 2299-300

Galston AW. 1992. Photosynthesis as a Basis for Life Support on Earth and in Space. *BioScience* 42: 490-93

Gatto E, Porchetta A, Stella L, Guryanov I, Formaggio F, et al. 2008. Conformational Effects on the Electron-Transfer Efficiency in Peptide Foldamers Based on α,α-Disubstituted Glycyl Residues. *Chemistry & Biodiversity* 5: 1263-78

Genereux JC, Barton JK. 2010. Mechanisms for DNA Charge Transport. *Chemical Reviews* 110: 1642-62

Ghindilis AL, Atanasov P, Wilkins E. 1997. Enzyme-catalyzed direct electron transfer: Fundamentals and analytical applications. *Electroanalysis* 9: 661-74

Ghisaidoobe BA, Chung JS. 2014. Intrinsic Tryptophan Fluorescence in the Detection and Analysis of Proteins: A Focus on Förster Resonance Energy Transfer Techniques. *International Journal of Molecular Sciences* 15: 22518-38

Ghuman J, Zunszain PA, Petitpas I, Bhattacharya AA, Otagiri M, Curry S. 2005. Structural Basis of the Drug-binding Specificity of Human Serum Albumin. *Journal of Molecular Biology* 353: 38-52

Giese B, Eckhardt S, Lauz M. 2012. Electron Transfer in Peptides and Proteins. *Encyclopedia of Radicals in Chemistry, Biology and Materials*

Giese B. 2002a. Electron transfer in DNA. *Current Opinion in Chemical Biology* 6: 612-18

Giese B. 2002b. Long-Distance Electron Transfer Through DNA. *Annual Review of Biochemistry* 71: 51-70

Goda S, Takano K, Yamagata Y, Nagata R, Akutsu H, et al. 2000. Amyloid protofilament formation of hen egg lysozyme in highly concentrated ethanol solution. *Protein Sci* 9: 369-75

Gray HB, Winkler JR. 1996. Electron Transfer In Proteins. *Annual Review of Biochemistry* 65: 537-61

Gray HB, Winkler JR. 2001. Electron Transfer in Metalloproteins. *Electron Transfer in Chemistry*: 2-23

Gray HB, Winkler JR. 2010. Electron flow through metalloproteins. *Biochimica et Biophysica Acta (BBA) - Bioenergetics* 1797: 1563-72

Gregoire S, Irwin J, Kwon I. 2012. Techniques for Monitoring Protein Misfolding and Aggregation in Vitro and in Living Cells. *Korean J Chem Eng* 29: 693-702

Grinvald A, Steinberg IZ. 1974. On the analysis of fluorescence decay kinetics by the method of least-squares. *Analytical Biochemistry* 59: 583-98

Guptasarma P. 2008. Solution-state characteristics of the ultraviolet A-induced visible fluorescence from proteins. *Archives of Biochemistry and Biophysics* 478: 127-29

Gutmann F. 1997. *Charge transfer complexes in biological systems*. M. Dekker.

Hameed M, Ahmad B, Fazili KM, Andrabi K, Khan RH. 2007. Different Molten Globule-like Folding Intermediates of Hen Egg White Lysozyme Induced by High pH and Tertiary Butanol. *The Journal of Biochemistry* 141: 573-83

Hansen JC, Lu X, Ross ED, Woody RW. 2006. Intrinsic Protein Disorder, Amino Acid Composition, and Histone Terminal Domains. *Journal of Biological Chemistry* 281: 1853-56

Hartree EF. 1972. Determination of protein: A modification of the lowry method that gives a linear photometric response. *Analytical Biochemistry* 48: 422-27

Hill SE, Robinson J, Matthews G, Muschol M. 2009. Amyloid Protofibrils of Lysozyme Nucleate and Grow Via Oligomer Fusion. *Biophysical Journal* 96: 3781-90

Hof M. 2003. Basics of Optical Spectroscopy. *Handbook of Spectroscopy*

Holmlin RE, Dandliker PJ, Barton JK. 1997. Charge Transfer through the DNA Base Stack. *Angewandte Chemie International Edition in English* 36: 2714-30

Homchaudhuri L, Kumar S, Swaminathan R. 2006. Slow aggregation of lysozyme in alkaline pH monitored in real time employing the fluorescence anisotropy of covalently labelled dansyl probe. *FEBS Letters* 580: 2097-101

Homchaudhuri L, Swaminathan R. 2001. Novel Absorption and Fluorescence Characteristics of L-Lysine. *Chemistry Letters* 30:844-45

Homchaudhuri L, Swaminathan R. 2004. Near Ultraviolet Absorption Arising from Lysine Residues in Close Proximity: A Probe to Monitor Protein Unfolding and Aggregation in Lysine-Rich Proteins. *Bulletin of the Chemical Society of Japan* 77: 765-69

Hopfield JJ. 1974. Electron Transfer Between Biological Molecules by Thermally Activated Tunneling. *Proceedings of the National Academy of Sciences* 71: 3640

Horváth O, Stevenson KL. 1993. *Charge transfer photochemistry of coordination compounds*. Wiley-VCH.

Hoyer W, Antony T, Cherny D, Heim G, Jovin TM, Subramaniam V. 2002. Dependence of α-Synuclein Aggregate Morphology on Solution Conditions. *Journal of Molecular Biology* 322: 383-93

Hsiao C, Chou IC, Okafor CD, Bowman JC, O'Neill EB, et al. 2013. RNA with iron(II) as a cofactor catalyses electron transfer. *Nature Chemistry* 5: 525

Iakoucheva LM, Radivojac P, Brown CJ, O'Connor TR, Sikes JG, et al. 2004. The importance of intrinsic disorder for protein phosphorylation. *Nucleic Acids Research* 32: 1037-49

Jacobsen C. 1978. Lysine residue 240 of human serum albumin is involved in high-affinity binding of bilirubin. *Biochem J* 171: 453-59

Johnsen S, Lohmann KJ. 2008. Magnetoreception in animals feature article. *Physics Today* 61: 29

Jortner J, Bixon M, Langenbacher T, Michel-Beyerle ME. 1998. Charge transfer and transport in DNA. *Proceedings of the National Academy of Sciences* 95: 12759

Kai M, Takeda K, Morita T, Kimura S. 2008. Distance dependence of long-range electron transfer through helical peptides. *Journal of Peptide Science* 14: 192-202

Kaila Ville RI. 2018. Long-range proton-coupled electron transfer in biological energy conversion: towards mechanistic understanding of respiratory complex I. *Journal of The Royal Society Interface* 15: 20170916

Kaneko K, Chuang VTG, Minomo A, Yamasaki K, Bhagavan NV, et al. 2011. Histidine146 of human serum albumin plays a prominent role at the interface of subdomains IA and IIA in allosteric ligand binding. *IUBMB Life* 63: 277-85

Karnaukhova E, Rutardottir S, Rajabi M, Wester Rosenlöf L, Alayash AI, Åkerström B. 2014. Characterization of heme binding to recombinant α1-microglobulin. *Front Physiol* 5: 465-65

Kasha M. 1950. Characterization of electronic transitions in complex molecules. *Discussions of the Faraday Society* 9: 14-19

Kennelly PJ. 2014. Protein Ser/Thr/Tyr phosphorylation in the archaea. *Journal of Biological Chemistry* 289: 9480-87

Kirmaier C, Gaul D, DeBey R, Holten D, Schenck CC. 1991. Charge separation in a reaction center incorporating bacteriochlorophyll for photoactive bacteriopheophytin. *Science* 251: 922

Knowles P. 1985. Biological Spectroscopy. *Biochemical Society Transactions* 13: 535

Kratochvílová I, Vala M, Weiter M, Špérová M, Schneider B, et al. 2013. Charge transfer through DNA/DNA duplexes and DNA/RNA hybrids: Complex theoretical and experimental studies. *Biophysical Chemistry* 180-181: 127-34

Krebs MRH, Wilkins DK, Chung EW, Pitkeathly MC, Chamberlain AK, et al. 2000. Formation and seeding of amyloid fibrils from wild-type hen lysozyme and a peptide fragment from the β-domain 11Edited by P. E. Wright. *Journal of Molecular Biology* 300: 541-49

Kubař T, Elstner M. 2008. What Governs the Charge Transfer in DNA? The Role of DNA Conformation and Environment. *The Journal of Physical Chemistry B* 112: 8788-98

Kumar V, Sami N, Kashav T, Islam A, Ahmad F, Hassan MI. 2016. Protein aggregation and neurodegenerative diseases: From theory to therapy. *European Journal of Medicinal Chemistry* 124: 1105-20

Ladiwala ARA, Dordick JS, Tessier PM. 2011. Aromatic small molecules remodel toxic soluble oligomers of amyloid β through three independent pathways. *Journal of Biological Chemistry* 286: 3209-18

Lakowicz JR. 2013. *Principles of Fluorescence Spectroscopy*. Springer Science & Business Media.

Lam Q, Kato M, Cheruzel L. 2016. Ru(II)-diimine functionalized metalloproteins: From electron transfer studies to light-driven biocatalysis. *Biochim Biophys Acta* 1857: 589-97

Lascelles J. 1962. The chromatophores of photosynthetic bacteria. *Microbiology* 29: 47-52

Lavis LD, Raines RT. 2008. Bright ideas for chemical biology. *ACS Chem Biol* 3: 142-55

Law MJ, Linde ME, Chambers EJ, Oubridge C, Katsamba PS, et al. 2006. The role of positively charged amino acids and electrostatic interactions in the complex of U1A protein and U1 hairpin II RNA. *Nucleic acids research* 34: 275-85

Lee J, Culyba EK, Powers ET, Kelly JW. 2011. Amyloid-β forms fibrils by nucleated conformational conversion of oligomers. *Nat Chem Biol* 7: 602-09

Leggio C, Galantini L, Pavel NV. 2008. About the albumin structure in solution: cigar Expanded form versus heart Normal shape. *Physical Chemistry Chemical Physics* 10: 6741-50

Lever ABP. 1974. Charge transfer spectra of transition metal complexes. *Journal of Chemical Education* 51: 612

Levi V, González Flecha FL. 2003. Labeling of proteins with fluorescent probes: Photophysical characterization of dansylated bovine serum albumin. *Biochemistry and Molecular Biology Education* 31: 333-36

Li Y, Artés JM, Hihath J. 2016a. Long-Range Charge Transport in Adenine-Stacked RNA:DNA Hybrids. *Small* 12: 432-37

Li Y, Artés JM, Qi J, Morelan IA, Feldstein P, et al. 2016b. Comparing Charge Transport in Oligonucleotides: RNA:DNA Hybrids and DNA Duplexes. *The Journal of Physical Chemistry Letters* 7: 1888-94

Lin S, Jaschke PR, Wang H, Paddock M, Tufts A, et al. 2009. Electron transfer in the *Rhodobacter sphaeroide*s reaction center assembled with zinc bacteriochlorophyll. *Proceedings of the National Academy of Sciences* 106: 8537

Lindberg DJ, Wenger A, Sundin E, Wesén E, Westerlund F, Esbjörner EK. 2017. Binding of Thioflavin-T to Amyloid Fibrils Leads to Fluorescence Self-Quenching and Fibril Compaction. *Biochemistry* 56: 2170-74

Liu J, Chakraborty S, Hosseinzadeh P, Yu Y, Tian S, et al. 2014. Metalloproteins containing cytochrome, iron-sulfur, or copper redox centers. *Chemical reviews* 114: 4366-469

Livesey AK, Brochon JC. 1987. Analyzing the distribution of decay constants in pulse-fluorimetry using the maximum entropy method. *Biophysical journal* 52: 693-706

Lodish H, Berk A, Zipursky SL, Matsudaira P, Baltimore D, Darnell J. 2000. Molecular cell biology 4th edition. *National Center for Biotechnology Information, Bookshelf*

Longworth JW. 1971. Luminescence of Polypeptides and Proteins In *Excited States of Proteins and Nucleic Acids*, ed. RF Steiner, I Weinryb, pp. 319-484. Boston, MA: Springer US

Lošdorfer Božič A, Podgornik R. 2017. pH Dependence of Charge Multipole Moments in Proteins. *Biophysical Journal* 113: 1454-65

Lowry OH, Rosebrough NJ, Farr AL, Randall RJ. 1951. Protein measurement with the folin phenol reagent. *Journal of Biological Chemistry* 193: 265-75

Lubner CE, Knörzer P, Silva PJN, Vincent KA, Happe T, et al. 2010. Wiring an [FeFe]-Hydrogenase with Photosystem I for Light-Induced Hydrogen Production. *Biochemistry* 49: 10264-66

Maezawa I, Hong H-S, Liu R, Wu C-Y, Cheng RH, et al. 2008. Congo red and thioflavin-T analogs detect Aβ oligomers. *Journal of Neurochemistry* 104: 457-68

Maie K, Miyagi K, Takada T, Nakamura M, Yamana K. 2009. RNA-Mediated Electron Transfer: Double Exponential Distance Dependence. *Journal of the American Chemical Society* 131: 13188-89

Mandal I, Paul S, Venkatramani R. 2018. Optical backbone-sidechain charge transfer transitions in proteins sensitive to secondary structure and modifications. *Faraday discussions* 207: 115-35

Marcus RA. 1956a. Electrostatic Free Energy and Other Properties of States Having Nonequilibrium Polarization. I. *The Journal of Chemical Physics* 24: 979-89

Marcus RA. 1956b. On the Theory of Oxidation-Reduction Reactions Involving Electron Transfer. I. *The Journal of Chemical Physics* 24: 966-78

Marcus RA. 1993. Electron Transfer Reactions in Chemistry: Theory and Experiment (Nobel Lecture). *Angewandte Chemie International Edition in English* 32: 1111-21

Martin DR, Matyushov DV. 2017. Electron-transfer chain in respiratory complex I. *Scientific Reports* 7: 5495

May V, Khun O. 2011. Electron Transfer. *Charge and Energy Transfer Dynamics in Molecular Systems*: 309-433

Meech SR, Hoff AJ, Wiersma DA. 1986. Role of charge-transfer states in bacterial photosynthesis. *Proceedings of the National Academy of Sciences of the United States of America* 83: 9464-68

Meloun B, Moravek L, Kostka V. 1975. Complete amino acid sequence of human serum albumin. *FEBS letters* 58: 134-37

Mishra R, Sörgjerd K, Nyström S, Nordigården A, Yu Y-C, Hammarström P. 2007. Lysozyme Amyloidogenesis Is Accelerated by Specific Nicking and Fragmentation but Decelerated by Intact Protein Binding and Conversion. *Journal of Molecular Biology* 366: 1029-44

Mohamed R, Degac J, Helms V. 2015. Composition of Overlapping Protein-Protein and Protein-Ligand Interfaces. *PLOS ONE* 10: e0140965

Moser CC, Keske JM, Warncke K, Farid RS, Dutton PL. 1992. Nature of biological electron transfer. *Nature* 355: 796-802

Moughal Shahi AR, Domratcheva T. 2013. Challenges in Computing Electron-Transfer Energies of DNA Repair Using Hybrid QM/MM Models. *Journal of Chemical Theory and Computation* 9: 4644-52

Mukherjee A, Morales-Scheihing D, Butler PC, Soto C. 2015. Type 2 Diabetes as a Protein Misfolding Disease. *Trends in molecular medicine* 21: 439-49

Mukherjee A, Soto C. 2017. Prion-Like Protein Aggregates and Type 2 Diabetes. *Cold Spring Harbor Perspectives in Medicine* 7

Mulliken RS, Person WB. 1969. *Molecular complexes: a lecture and reprint volume*. Wiley-Interscience.

Nilsson MR. 2004. Techniques to study amyloid fibril formation in vitro. *Methods* 34: 151-60

Nishimura C, Uversky VN, Fink AL. 2001. Effect of Salts on the Stability and Folding of Staphylococcal Nuclease. *Biochemistry* 40: 2113-28

Niyangoda C, Miti T, Breydo L, Uversky V, Muschol M. 2017. Carbonyl-based blue autofluorescence of proteins and amino acids. *PLOS ONE* 12: e0176983

Olzscha H, Schermann SM, Woerner AC, Pinkert S, Hecht MH, et al. 2011. Amyloid-like Aggregates Sequester Numerous Metastable Proteins with Essential Cellular Functions. *Cell* 144: 67-78

Pace CN, Vajdos F, Fee L, Grimsley G, Gray T. 1995. How to measure and predict the molar absorption coefficient of a protein. *Protein Science* 4: 2411-23

Pan C-P, Barkley MD. 2004. Conformational Effects on Tryptophan Fluorescence in Cyclic Hexapeptides. *Biophysical Journal* 86: 3828-35

Pedersen JT, Heegaard NHH. 2013. Analysis of Protein Aggregation in Neurodegenerative Disease. *Analytical Chemistry* 85: 4215-27

Pepys MB, Hawkins PN, Booth DR, Vigushin DM, Tennent GA, et al. 1993. Human lysozyme gene mutations cause hereditary systemic amyloidosis. *Nature* 362: 553-57

Pinotsi D, Buell AK, Dobson CM, Kaminski Schierle GS, Kaminski CF. 2013. A Label-Free, Quantitative Assay of Amyloid Fibril Growth Based on Intrinsic Fluorescence. *ChemBioChem* 14: 846-50

Pinotsi D, Grisanti L, Mahou P, Gebauer R, Kaminski CF, et al. 2016. Proton Transfer and Structure-Specific Fluorescence in Hydrogen Bond-Rich Protein Structures. *Journal of the American Chemical Society* 138: 3046-57

Prűtz WA, Butler J, Land EJ, Swallow AJ. 1980. Direct demonstration of electron transfer between tryptophan and tyrosine in proteins. *Biochemical and Biophysical Research Communications* 96: 408-14

Prasad S, Mandal I, Singh S, Paul A, Mandal B, et al. 2017. Near UV-Visible electronic absorption originating from charged amino acids in a monomeric protein. *Chemical Science* 8: 5416-33

Prütz WA, Land EJ, Sloper RW. 1981. Charge transfer in peptides. Effects of temperature, peptide length and solvent conditions upon intramolecular one-electron reactions involving tryptophan and tyrosine. *Journal of the Chemical Society, Faraday Transactions 1: Physical Chemistry in Condensed Phases* 77: 281-92

Quick WP, Neuhaus HE. 1997. The regulation and control of photosynthetic carbon assimilation. pp. 41-62: Taylor and Francis

Quinlan GJ, Martin GS, Evans TW. 2005. Albumin: Biochemical properties and therapeutic potential. *Hepatology* 41: 1211-19

Rabbani G, Ahn SN. 2019. Structure, enzymatic activities, glycation and therapeutic potential of human serum albumin: A natural cargo. *International Journal of Biological Macromolecules* 123: 979-90

Rajski SR, Barton JK. 2001. How Different DNA-Binding Proteins Affect Long-Range Oxidative Damage to DNA. *Biochemistry* 40: 5556-64

Ravi VK, Goel M, Kotamarthi HC, Ainavarapu SRK, Swaminathan R. 2014a. Preventing Disulfide Bond Formation Weakens Non-Covalent Forces among Lysozyme Aggregates. *PLOS ONE* 9: e87012

Ravi VK, Swain T, Chandra N, Swaminathan R. 2014b. On the Characterization of Intermediates in the Isodesmic Aggregation Pathway of Hen Lysozyme at Alkaline pH. *PLOS ONE* 9: e87256

Rawtani D, Kuntmal B, Agrawal Y. 2016. Charge transfer in DNA and its diverse modelling approaches. *Frontiers in Life Science* 9: 214-25

Ray K, Chowdhury MH, Szmacinski H, Lakowicz JR. 2008. Metal-Enhanced Intrinsic Fluorescence of Proteins on Silver Nanostructured Surfaces toward Label-Free Detection. *The Journal of Physical Chemistry C* 112: 17957-63

Rayner DM, Szabo AG. 1978. Time resolved fluorescence of aqueous tryptophan. *Canadian Journal of Chemistry* 56: 743-45

Requião RD, Fernandes L, de Souza HJA, Rossetto S, Domitrovic T, Palhano FL. 2017. Protein charge distribution in proteomes and its impact on translation. *PLOS Computational Biology* 13: e1005549

Rochaix J-D. 2011. Regulation of photosynthetic electron transport. *Biochimica et Biophysica Acta (BBA) - Bioenergetics* 1807: 375-83

Ross CA, Poirier MA. 2005. What is the role of protein aggregation in neurodegeneration? *Nat Rev Mol Cell Biol* 6: 891-98

Ryzhkina IS, Sergeeva SY, Kiseleva YV, Timosheva AP, Salakhutdinova OA, et al. 2018. Self-organization and properties of dispersed systems based on dilute aqueous solutions of (S)- and (R)-lysine. *Mendeleev Communications* 28: 66-69

Ryzhkina IS, Sergeeva SY, Kiseleva YV, Timosheva AP, Salakhutdinova OA, et al. 2018. Self-organization and properties of dispersed systems based on dilute aqueous solutions of (S)- and (R)-lysine. *Mendeleev Communications* 28: 66-69

Saen-Oon S, Lucas MF, Guallar V. 2013. Electron transfer in proteins: theory, applications and future perspectives. *Physical Chemistry Chemical Physics* 15: 15271-85

Sancar A. 1994. Structure and function of DNA photolyase. *Biochemistry* 33: 2-9

Sancar A. 1996. DNA Excision Repair. *Annual Review of Biochemistry* 65: 43-81

Schlag EW, Sheu S-Y, Yang D-Y, Selzle HL, Lin SH. 2007. Distal Charge Transport in Peptides. *Angewandte Chemie International Edition* 46: 3196-210

Schmid F-X. 2001. Biological Macromolecules: UV-visible Spectrophotometry. *eLS*

Scuppa S, Orian L, Donoli A, Santi S, Meneghetti M. 2011. Anti-Kasha's Rule Fluorescence Emission in (2-Ferrocenyl)indene Generated by a Twisted Intramolecular Charge-Transfer (TICT) Process. *The Journal of Physical Chemistry A* 115: 8344-49

Seyedsayamdost MR, Xie J, Chan CTY, Schultz PG, Stubbe J. 2007. Site-Specific Insertion of 3-Aminotyrosine into Subunit α2 of E. coli Ribonucleotide Reductase: Direct Evidence for Involvement of Y730 and Y731 in Radical Propagation. *Journal of the American Chemical Society* 129: 15060-71

Seyedsayamdost MR, Yee CS, Reece SY, Nocera DG, Stubbe J. 2006. pH Rate Profiles of FnY356−R2s (n = 2, 3, 4) in Escherichia coli Ribonucleotide Reductase: Evidence that Y356 Is a Redox-Active Amino Acid along the Radical Propagation Pathway. *Journal of the American Chemical Society* 128: 1562-68

Shah A, Adhikari B, Martic S, Munir A, Shahzad S, et al. 2015. Electron transfer in peptides. *Chemical Society Reviews* 44: 1015-27

Shen X-B, Song B, Fang B, Jiang A-R, Ji S-J, He Y. 2018. Excitation-wavelength-dependent photoluminescence of silicon nanoparticles enabled by adjustment of surface ligands. *Chemical Communications* 54: 4947-50

Shukla A, Mukherjee S, Sharma S, Agrawal V, Radha Kishan KV, Guptasarma P. 2004. A novel UV laser-induced visible blue radiation from protein crystals and aggregates: scattering artifacts or fluorescence transitions of peptide electrons delocalized through hydrogen bonding? *Archives of Biochemistry and Biophysics* 428: 144-53

Simonson T. 2003. Electrostatics and dynamics of proteins. *Reports on Progress in Physics* 66: 737-87

Sipe JD. 1992. Amyloidosis. *Annual Review of Biochemistry* 61: 947-75

Siriwong K, Voityuk AA. 2012. Electron transfer in DNA. *Wiley Interdisciplinary Reviews: Computational Molecular Science* 2: 780-94

Sjulstok E, Olsen JMH, Solov'yov IA. 2015. Quantifying electron transfer reactions in biological systems: what interactions play the major role? *Scientific Reports* 5: 18446

Solov'yov IA, Ritz T, Schulten KJ, Hore PJ. 2014. A chemical compass for bird navigation In *Quantum effects in biology*, pp. 218-36: Cambridge University Press

Sophianopoulos AJ, Van Holde KE. 1961. Evidence for Dimerization of Lysozyme in Alkaline Solution. *Journal of Biological Chemistry* 236: PC82-PC83

Sophianopoulos AJ, Van Holde KE. 1964. Physical Studies of Muramidase (Lysozyme): II. pH-Dependent Dimerization. *Journal of Biological Chemistry* 239: 2516-24

Strümpfer J, Şener M, Schulten K. 2012. How Quantum Coherence Assists Photosynthetic Light-Harvesting. *The Journal of Physical Chemistry Letters* 3: 536-42

Stryer L, Haugland RP. 1967. Energy Transfer: A Spectroscopic Ruler. *Proceedings of the National Academy of Sciences of the United States of America* 58: 719-26

Sugio S, Kashima A, Mochizuki S, Noda M, Kobayashi K. 1999. Crystal structure of human serum albumin at 2.5 Å resolution. *Protein Engineering, Design and Selection* 12: 439-46

Swaminathan R, Krishnamoorthy G, Periasamy N. 1994a. Similarity of fluorescence lifetime distributions for single tryptophan proteins in the random coil state. *Biophysical Journal* 67: 2013-23

Swaminathan R, Periasamy N, Udgaonkar JB, Krishnamoorthy G. 1994. Molten Globule-like Conformation of Barstar: A Study by Fluorescence Dynamics. *The Journal of Physical Chemistry* 98: 9270-78

Swaminathan R, Periasamy N. 1996. Analysis of fluorescence decay by the maximum entropy method: Influence of noise and analysis parameters on the width of the distribution of lifetimes. *Proceedings of the Indian Academy of Sciences - Chemical Sciences* 108: 39

Swaminathan R, Ravi VK, Kumar S, Kumar MVS, Chandra N. 2011. Lysozyme: A model protein for amyloid research In *Advances in Protein Chemistry and Structural Biology*, ed. R Donev, pp. 63-111: Academic Press

Takada T, Otsuka Y, Nakamura M, Yamana K. 2011. Electron transfer through RNA: Chemical probing of dual distance dependence. *Bioorganic & Medicinal Chemistry* 19: 6881-84

Teale FW, Weber G. 1957. Ultraviolet fluorescence of the aromatic amino acids. *Biochem J* 65: 476-82

Tikhonova TN, Rovnyagina NR, Zherebker AY, Sluchanko NN, Rubekina AA, et al. 2018. Dissection of the deep-blue autofluorescence changes accompanying amyloid fibrillation. *Archives of Biochemistry and Biophysics* 651: 13-20

Tommos C, Valentine KG, Martínez-Rivera MC, Liang L, Moorman VR. 2013. Reversible Phenol Oxidation and Reduction in the Structurally Well-Defined 2-Mercaptophenol-α3C Protein. *Biochemistry* 52: 1409-18

Valeur B, Weber G. 1977. Resolution Of The Fluorescence Excitation Spectrum Of Indole Into The $1L_a$ And $1L_b$ Excitation Bands*. *Photochemistry and Photobiology* 25: 441-44

Varshney A, Sen P, Ahmad E, Rehan M, Subbarao N, Khan RH. 2010. Ligand binding strategies of human serum albumin: How can the cargo be utilized? *Chirality* 22: 77-87

Vernaglia BA, Huang J, Clark ED. 2004. Guanidine Hydrochloride Can Induce Amyloid Fibril Formation from Hen Egg-White Lysozyme. *Biomacromolecules* 5: 1362-70

Vivian JT, Callis PR. 2001. Mechanisms of Tryptophan Fluorescence Shifts in Proteins. *Biophysical Journal* 80: 2093-109

Vogler A, Kunkely H. 1993. Charge Transfer Excitation of Coordination Compounds. Generation of Reactive Intermediates In *Photosensitization and Photocatalysis Using Inorganic and Organometallic Compounds*, ed. K Kalyanasundaram, M Grätzel, pp. 71-111. Dordrecht: Springer Netherlands

Voityuk AA, Siriwong K, Rösch N. 2004. Environmental Fluctuations Facilitate Electron-Hole Transfer from Guanine to Adenine in DNA π Stacks. *Angewandte Chemie International Edition* 43: 624-27

Waddell WJ. 1956. A simple ultraviolet spectrophotometric method for the determination of protein. *The Journal of Laboratory and Clinical Medicine* 48: 311-14

Wagenknecht H-A. 2005. Principles and Mechanisms of Photoinduced Charge Injection, Transport, and Trapping in DNA. *Charge Transfer in DNA*: 1-26

Wahadoszamen M, Margalit I, Ara AM, van Grondelle R, Noy D. 2014. The role of charge-transfer states in energy transfer and dissipation within natural and artificial bacteriochlorophyll proteins. *Nature Communications* 5: 5287 1-7

Wall J, Murphy CL, Solomon A. 1999. [14] In vitro immunoglobulin light chain fibrillogenesis In *Methods in Enzymology*, pp. 204-17: Academic Press

Watanabe H, Tanase S, Nakajou K, Maruyama T, Kragh-Hansen U, Otagiri M. 2000. Role of Arg-410 and Tyr-411 in human serum albumin for ligand binding and esterase-like activity. *Biochemical Journal* 349: 813-19

Weber G. 1952. Polarization of the fluorescence of macromolecules. II. Fluorescent conjugates of ovalbumin and bovine serum albumin. *Biochem J* 51: 155-67

Weber S. 2005. Light-driven enzymatic catalysis of DNA repair: a review of recent biophysical studies on photolyase. *Biochimica et Biophysica Acta (BBA) - Bioenergetics* 1707: 1-23

Weinryb I, Steiner RF. 1971. The Luminescence of the Aromatic Amino Acids In *Excited States of Proteins and Nucleic Acids*, ed. RF Steiner, I Weinryb, pp. 277-318. Boston, MA: Springer US

Wetlaufer DB. 1963. Ultraviolet spectra Of Proteins and Amino Acids In *Advances in Protein Chemistry*, ed. CB Anfinsen, K Bailey, ML Anson, JT Edsall, pp. 303-90: Academic Press

Wierzbinski E, de Leon A, Davis KL, Bezer S, Wolak MA, et al. 2012. Charge Transfer through Modified Peptide Nucleic Acids. *Langmuir* 28: 1971-81

Wong ELS, Gooding JJ. 2006. Charge Transfer through DNA: A Selective Electrochemical DNA Biosensor. *Analytical Chemistry* 78: 2138-44

Wong JR, Shao F. 2017. Hole Transport in A-form DNA/RNA Hybrid Duplexes. *Scientific Reports* 7: 40293

Wörner HJ, Arrell CA, Banerji N, Cannizzo A, Chergui M, et al. 2017. Charge migration and charge transfer in molecular systems. *Structural Dynamics* 4: 061508

Xia D, Esser L, Tang W-K, Zhou F, Zhou Y, et al. 2013. Structural analysis of cytochrome bc1 complexes: Implications to the mechanism of function. *Biochimica et Biophysica Acta (BBA) - Bioenergetics* 1827: 1278-94

Yacoby I, Pochekailov S, Toporik H, Ghirardi ML, King PW, Zhang S. 2011. Photosynthetic electron partitioning between [FeFe]-hydrogenase and ferredoxin: $NADP^+$-oxidoreductase (FNR) enzymes in vitro. *Proceedings of the National Academy of Sciences* 108: 9396

Zhao N, Pang B, Shyu C-R, Korkin D. 2011. Charged residues at protein interaction interfaces: Unexpected conservation and orchestrated divergence. *Protein Science* 20: 1275-84

Zhong D, Douhal A, Zewail AH. 2000. Femtosecond studies of protein–ligand hydrophobic binding and dynamics: Human serum albumin. *Proceedings of the National Academy of Sciences* 97: 14056-61